

## Metallization of Polymers 2

# **Metallization of Polymers 2**

Edited by

**Edward Sacher**

*École Polytechnique  
Montréal, Québec, Canada*

**Springer-Science+Business Media, LLC**

Library of Congress Cataloging-in-Publication Data

---

Metallization of polymers 2/edited by Edward Sacher.

p. cm.

Proceedings of the Montréal Workshop on Polymer Metallization, held June 27–29, 2001, Montréal, Québec.

Includes bibliographical references and index.

ISBN 978-1-4613-5134-4 ISBN 978-1-4615-0563-1 (eBook)

DOI 10.1007/978-1-4615-0563-1

1. Metal coating—Congresses. 2. Polymers—Surfaces—Congresses. 3. Metallizing—Congresses. I. Sacher, Edward, 1934– II. Montréal Workshop on Polymer Metallization (2001: Montréal, Québec)

TA491 .M463 2002

668.9—dc21

2002022134

---

ISBN 978-1-4613-5134-4

©2002 Springer-Science+Business Media New York

Originally published by Kluwer / Plenum Publishers, New York in 2002

Softcover reprint of the hardcover 1st edition 2002

<http://www.wkap.nl/>

10 9 8 7 6 5 4 3 2 1

A C.I.P. record for this book is available from the Library of Congress

All rights reserved

No part of this book may be reproduced, stored in a retrieval system, or transmitted in any form or by any means, electronic, mechanical, photocopying, microfilming, recording, or otherwise, without written permission from the Publisher, with the exception of any material supplied specifically for the purpose of being entered and executed on a computer system, for exclusive use by the purchaser of the work.

## PREFACE

As the demands put on the polymer/metal interface, particularly by the microelectronics industry, become more and more severe, the necessity for understanding this interface, its properties and its limitations, becomes more and more essential. This requires a broad knowledge of, and a familiarity with, the latest findings in this rapidly advancing field.

At the very least, such familiarity requires an exchange of information, particularly among those intimately involved in this field. Communications among many of us in this area have made one fact quite obvious: the facilities provided by existing organizations, scientific and otherwise, do not offer the forum necessary to accomplish this exchange of information.

It was for this reason that Jean-Jacques Pireaux, Steven Kowalczyk and I organized the first **Metallization of Polymers**, a symposium sponsored by the American Chemical Society, which took place in Montréal, September 25–28, 1989; the Proceedings from that symposium were published as ACS Symposium Series **440**, (1990). It is this same perceived lack of a proper forum, and the encouragement of my colleagues, that prompted me to organize this meeting, so as to bring to the attention of the participants new instruments, materials, methods, advances, and, particularly, thoughts in the field of polymer metallization. The meeting was designed as a workshop, with time being made available throughout for discussion and for the consideration of new findings. Indeed, several of the papers in this volume discuss the recent finding of metal nanoclusters formed on initial deposition, and their behavior. How such clusters influence the subsequent formation of smooth metal layers has yet to be understood.

Several of the questions raised in the Preface to the first Proceedings, more than a decade ago, are still unanswered, and new ones have arisen. It is hoped that some answers will be provided by forums such as our Workshop.

Such forums need external support. With profound thanks, it is my pleasure to acknowledge the support of the following organizations:

The Dow Chemical Company;  
The École Polytechnique;  
Meridian Scientific Services;  
The Natural Sciences and Engineering Research Council of Canada;  
Nortel Networks;  
The Thin Film Research Group of the Université de Montréal/École Polytechnique.

Edward Sacher

# CONTENTS

## NEW INSTRUMENTATION

<b>1. Surface Analysis Using Confocal Raman Micro-spectroscopy .....</b>	<b>1</b>
C. Hyett, D.-Q. Yang, T.H. Ellis, and E. Sacher	
<b>2. Ellipsometric Characterization of the Optical Constants of Metals: Thin Film versus Nanoparticle .....</b>	<b>11</b>
D. Dalacu and L. Martinu	
<b>3. Ultra Thin Film Analysis Using the Thermo VG Scientifics Thetaprobe Instrument .....</b>	<b>23</b>
R.K. Champaneria and J. Wolstenholme	
<b>4. Nanoindentation of Microsprings and Microcantilevers .....</b>	<b>35</b>
M. Seto, B. Dick, and M. Brett	

## LOW PERMITTIVITY MATERIALS

<b>5. Physical and Interfacial Properties of Low Permittivity Polymers: Cyclotene, SiLK and Ultra-Low K .....</b>	<b>43</b>
D. Frye, J.J. Waeterloos, M. Simmonds, T. Stokich, and J. Im	
<b>6. Mechanical Properties of Cured Silk Low-K Dielectric Films .....</b>	<b>53</b>
J. Im, P.H. Townsend, J. Curphy, C. Karas, and E.O. Shaffer II	
<b>7. Plasma-Polymerized Fluoropolymer Thin Films for Microelectronic Applications .....</b>	<b>61</b>
M. Silverstein, R. Chen, E. Sacher, and L. Sandrin	

## POLYMER METALLIZATION

<b>8. Fundamental Aspects of Polymer Metallization .....</b>	<b>73</b>
F. Faupel, V. Zaporojchenko, T. Strunskus, J. Erichsen, K. Dolgner, A. Thran, and M. Keine	

<b>9. The Study of Copper Clusters on Dow Cyclotene and Their Stability . . . . .</b>	<b>97</b>
D.-Q. Yang and E. Sacher	
<b>10. Adsorption of Noble Metal Atoms on Polymers . . . . .</b>	<b>107</b>
V. Zaporojtchenko, J. Erichsen, J. Zekonyte, A. Thran, T. Strunskus, and F. Faupel	
<b>11. Nucleation and Growth of Vapor-Deposited Metal Films on Self- Assembled Monolayers Studied by Multiple Characterization Probes . . . . .</b>	<b>117</b>
A.V. Walker, G.L. Fisher, A.E. Hooper, T. Tighe, R. Opila, N. Winograd, and D.L. Allara	

## BARRIER LAYERS

<b>12. Morphological Investigations of Low-k Polymer/Diffusion Barrier Interfaces for IC Metallization . . . . .</b>	<b>127</b>
S. Sankaran and R.E. Geer	
<b>13. Chemistry in the Initial Formation of Nitride Barriers on Low-K Dielectrics . . . . .</b>	<b>141</b>
P. Abramowitz, J. Liu, M. Keine, P.S. Ho, and J. Im	
<b>14. Capabilities and Limitations of RBS to Characterize Hyper-Thin Silicon Compound on Various Polymeric Substrates . . . . .</b>	<b>153</b>
G. Dennler, A. Houdayer, P. Raynaud, Y. Segui, and M.R. Wertheimer	

## ADHESION ENHANCEMENT

<b>15. Surface Modifications by Ion-Assisted Reactions . . . . .</b>	<b>165</b>
S.K. Koh, J.S. Cho, S. Han, K.H. Kim, and Y.W. Beag	
<b>16. Plasma and VUV Pretreatments of Polymer Surfaces for Adhesion Enhancement of Electrolessly Deposited Ni or Cu Films . . . . .</b>	<b>191</b>
M. Romand, M. Charbonnier and, Y. Goepfert	
<b>Index . . . . .</b>	<b>207</b>

# SURFACE ANALYSIS USING CONFOCAL RAMAN MICRO-SPECTROSCOPY

C. Hyett, D.-Q. Yang, T.H. Ellis and E. Sacher\*

## 1. INTRODUCTION

Recent developments in instrumentation and the availability of several high quality commercial Raman microscopes have made Raman micro-spectroscopy an emerging tool for surface analysis. Specifically, confocal Raman micro-spectroscopy allows for near diffraction-limited spatial resolution, with the chemical and structural information of vibrational spectroscopy. Modern single-dispersion spectrographs with notch filters, permitting excellent spectral resolution while minimizing Rayleigh interference and maximizing the detected signal, are also important developments.

The ability of Raman spectroscopy to probe molecular structure, coupled with the spatial resolution and light gathering power of a microscope, has created a powerful tool for surface analysis. This technique constitutes a non-destructive method of obtaining chemical and morphological information from a variety of different composite materials, surfaces and thin films. Since the introduction of Raman microscopy techniques, its application to materials research has increased. The ability of the microscope to obtain chemical information from regions as small as  $1 \mu\text{m}^2$  makes Raman microscopy complementary to other microanalysis techniques, such as electron microscopy or x-ray microanalysis. The high spatial resolution is a definite advantage over infrared microscopy, which provides similar chemical information but is limited by lower attainable resolution ( $\sim 30 \mu\text{m}^2$  for a conventional globar system and  $\sim 10 \mu\text{m}^2$  for a synchrotron system).

---

\* C. Hyett and T. H. Ellis, Université de Montréal, Montréal, Québec, H3C 3J7. D.-Q. Yang and E. Sacher, École polytechnique, Montréal, Québec, H3C 3A7.

## 2. INSTRUMENTATION

### 2.1 Conventional Raman Microscopy

Using a microscope for the collection optics of a Raman spectrometer helps solve one of the major limitations of Raman spectroscopy: the inherently low intensity Raman scattering effect. The invention of the laser, an ideal excitation source for Raman spectroscopy, catalyzed a renaissance in Raman spectroscopy. Replacing the mercury arc lamps previously used with far more intense laser excitation sources greatly increased the detectable Raman signal. Lasers are also highly monochromatic sources of radiation, which greatly simplifies the instrumentation. While the introduction of laser sources overcame the inherently poor signal intensity of Raman scattered light, the use of microscope objectives, with their large solid angle field-of-view and high degree of focusing, allowed for more of the scattered light in a given region to be captured and to reach the detector<sup>1,2</sup>.

Microscope optical systems for Raman spectroscopy are directly linked to the non-intuitive observation that the Raman scatter intensity does not decrease with decreasing volume until the diffraction limit is approached<sup>2</sup>; instead, scatter intensity remains constant. A significant problem with Raman microscopy is the power density incident on the sample; without significant attenuation, standard laser sources will destroy the sample in a very short time. While lower powered lasers are required, the increase in efficiency of the collection optics more than makes up for this. Microscopes use faster optical systems, focus more light onto the sample and collect more scattered light than conventional Raman spectrometers.

### 2.2 Confocal Raman microscopy

Confocal microscopy was introduced to overcome some of the limitations of optical microscopy. A point source at the diffraction limit is focused onto the sample and the enlarged image is analyzed through a pinhole<sup>3</sup>. This technique allows much greater contrast and spatial resolution at the cost of reducing the image area down to a small part of the entire field-of-view. In order to capture the entire field-of-view, an XY-raster scan of the field can be performed, and a full 2-dimensional image is created through numerical analysis of the detector signals. Additionally, a 3-dimensional image can be created by optical sectioning, where the XY raster scans are performed sequentially with a Z-focus stage, and the resulting data cube is analyzed via numerical methods to recreate the optical image of the original object<sup>2</sup>.

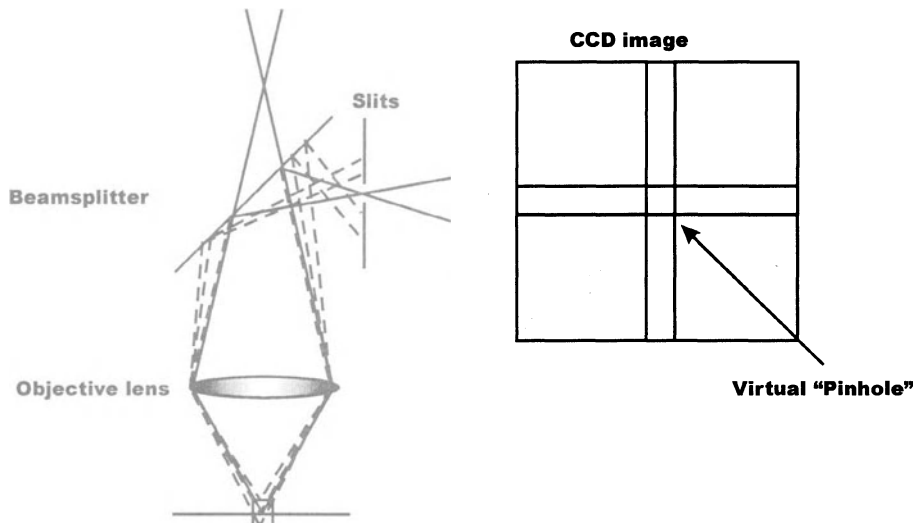


**Figure 1.** Confocal optical system of the Renishaw System 3000 Raman Microscope.

This has several effects which differentiate confocal optical systems from standard optical microscopes. The first is the spatial filtering effects of the combined pinhole and point source optical configuration. This spatial filtering also reduces the stray light background from out-of-focus regions of the sample. The net effect is that all the detected light arises from a thin layer close to the focal plane; any signals arising from regions which are out of focus are suppressed by the spatial filtering properties of the optical system. This spatial filtering is found in Figure 1, which shows the confocal arrangement in the Renishaw System 3000 Raman Microscope. This demonstrates how the pinhole and point source spatially filter the detected signal.

A problem with confocal systems in Raman microspectroscopy arises from the intense laser source, most of the intensity of which will be elastically backscattered (Rayleigh scatter) into the spectrograph. This Rayleigh line must be suppressed somehow in order to discriminate the weaker Raman scattering from this Rayleigh line. Recent developments in spectral filtering technology and multichannel detectors have allowed the commercialization of fully confocal Raman microscopes.

As can be seen in Figure 1, the system used in this paper differs slightly from the description of the confocal microscope given earlier: specifically, the lack of a pinhole either on the source or before the spectrometer. The system commercialized by Renishaw makes use of the collimation of the laser beam and the focusing ability of the microscope objectives to produce a point source (typical laser beam dimensions are 5-10  $\mu\text{m}$  in diameter). The collected light is then spatially filtered by a combination of the spectrometer slits and the charge-coupled device (CCD) area used; combining these two elements, which are already in the beam path, creates a "virtual pinhole" of about 20 $\times$ 40  $\mu\text{m}$ . This "virtual pinhole" minimizes the time-consuming optical calibrations often required to properly adjust the optical parameters of confocal systems.

### 3. APPLICATIONS TO SURFACE ANALYSIS

The use of confocal optical systems in Raman microspectroscopy offers several advantages and disadvantages for all types of Raman experiments. The first property which is important is that much of the light collected is rejected by the spatial filter; this is the price paid to increase the spatial resolution and depth discrimination. This also helps by reducing the amount of fluorescence interference that reaches the detector, since the Raman signal is more or less constant with decreasing volume but the fluorescence interference is proportional to the number of active molecules in the region probed. Thus decreasing the region probed decreases the number of interference sources, resulting in the more rapid decrease in the fluorescence background than in the Raman signal. The increased depth discrimination and spatial resolution with the confocal microscope is the greatest advantage of the confocal technique. When the analysis requires molecular information on the micron scale, few other techniques can provide the necessary information. Several confocal experiments carried out by our laboratory, and the system used, will be detailed here.

#### 3.1 System Information

Experiments were performed on a Renishaw RM 3000 Raman Microscope with confocal, imaging, variable temperature, and ultra-high resolution capabilities. The system has four laser sources in line: two Ar<sup>+</sup> lasers (488.0 nm and 514.5 nm), a He-Ne laser (632.8 nm), and a near-infrared diode laser (~785 nm). In almost all cases, the maximum incident power at the objective is about 1 mW. The spectrometer is coupled to a Leica DM LM industrial microscope with an XYZ mapping stage for confocal mapping experiments and a variety of objective lenses, including 100 $\times$  and 50 $\times$  high-power objectives for mapping work. The spectrometer has a single dispersion monochromator equipped with an 1800 lines/mm or 1200 lines/mm grating and an air-cooled CCD detector; the spectral resolution is 1.57 cm<sup>-1</sup> with the blue 488 nm laser and 1.65 cm<sup>-1</sup> with the green 514.5 nm laser (using the 1800 lines/mm grating). Very good confocal performance can be achieved with the virtual pinhole setup, combined with the argon lasers and the high magnification objectives.

#### 3.2 BCB Thin Films

Dow Cyclotene 3022, also known as BCB, is a low permittivity polymer. It has many desirable properties that make it a candidate for use in the new high-speed microelectronic devices necessary for use with III/V compound semiconductors. The material is furnished as a B-staged mesitylene solution that is spun on and, after solvent evaporation, undergoes a Diels-Alder reaction<sup>4</sup> on curing. Our studies on this material<sup>5</sup> concerned two questions. Which of the two possible Diels-Alder pathways was followed on cure and, since the B-staged material was cured in film form, did the presence of an excess energy at the solid surface (the surface tension) cause the reaction there to differ from that in the bulk? Our results, obtained by confocal Raman spectroscopy<sup>5</sup>, are summarized here.

The samples were furnished by Nortel Networks, Nep  an, Ontario, and were cured according to their specifications<sup>5</sup>. Cure consisted of a stepped bake cycle of the

B-staged film, in N<sub>2</sub>, to a temperature of 250°C before cooling to room temperature, still under N<sub>2</sub>. The sample thickness was ~1.3 μm on a silicon substrate.

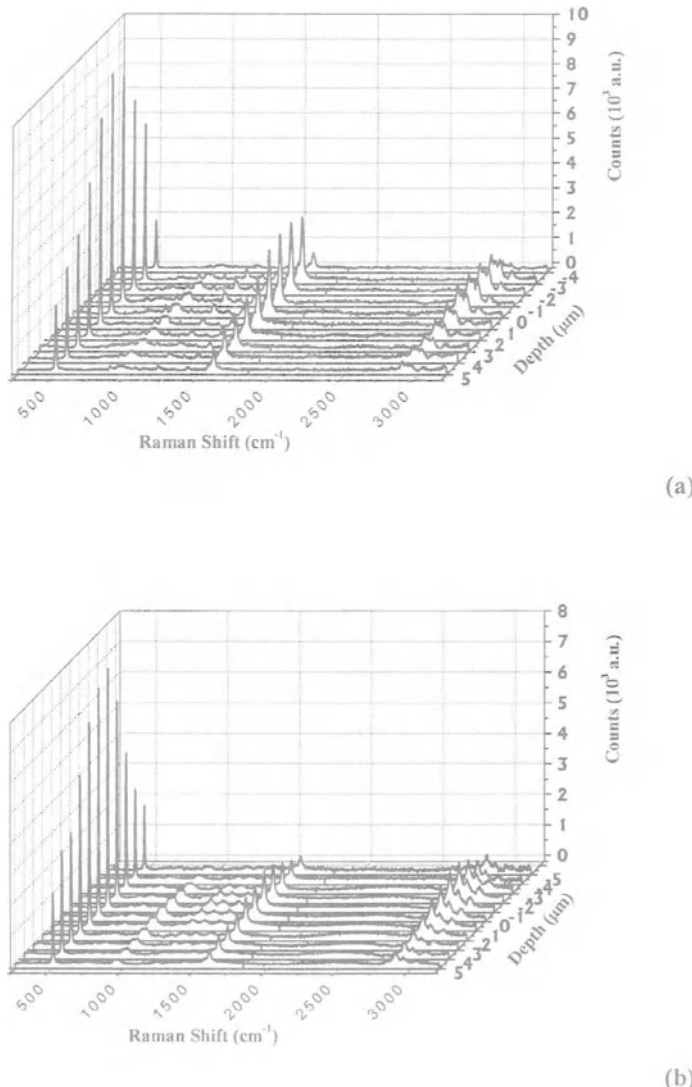


**Figure 2.** Confocal depth profiles of the (a) B-staged and (b) cured materials. These spectra were acquired with the 514.5 nm laser and a 50× objective, depth discrimination is approximately 2 μm and the Z stage was moved in 1 μm steps.

The depth profiles in Figure 2a and b show that neither the B-staged nor the fully cured films showed structural differences at either surface. While the B-staged material in Figure 2a is not expected to show any such differences, it is included to show the expected intensity variations of a uniform film. Figure 2b clearly shows that no new bands appear, nor do any bands already present disappear, as the Z direction is stepped to obtain the confocal profile. This tells us that, whichever pathway was followed, it was invariant across the entire sample thickness.

Of the two Diels-Alder pathways available for curing, they differ principally in that only one retains the aromaticity of the B-staged material. A comparison of Figure 2a and Figure 2b clearly shows that the aromatic skeletal stretching modes near  $1600\text{ cm}^{-1}$  are retained on cure, identifying the cure as the one which retains the aromaticity. This was subsequently confirmed<sup>5, 6</sup> by high-resolution photoacoustic FTIR and XPS studies.

### 3.3 Highly Oriented Pyrolytic Graphite (HOPG)

BCB is a crosslinked polymer with the surprising ability to extensively delocalize its electrons. Our efforts to understand the extent of surface damage to BCB caused by ion treatment required a model system whose structure was well known and well understood. For this, we turned to HOPG, which is also capable of extensive electron delocalization. To accomplish this, we used confocal Raman spectroscopy, with the focus at the outer surface. In this way, we were able to identify surface peaks, and how they changed on ion treatment. A simplifying factor comes from the fact that, having no polar groups, the vibrational peaks exhibited by HOPG are exclusively due to lattice phonons. For this study<sup>7</sup>, we used a high purity type ZYA sample of HOPG, purchased from SPI, Inc., cleaved with adhesive tape just prior to each experiment.

HOPG damage on ion bombardment<sup>8-13</sup> is due to the disruption of the well-ordered aromatic sheet structure at the sample surface, and its conversion to a more disordered system. This entails the partial loss of orbital hybridization and the accompanying reduction of electron delocalization<sup>7</sup>. As seen in Figure 3, several changes at the HOPG surface are manifested on  $\text{Ar}^+$  ion treatment (2 kV, 30 min.). In Figure 3a, the Raman-active  $E_{2g}$  mode at  $1581\text{ cm}^{-1}$  (referred to as G in the literature) decreases, and new modes appear at 1327 ( $D_1$ ), 1367 ( $D_2$ ) and  $1620\text{ cm}^{-1}$  ( $D'$ ). In Figure 3b, the modes at 2690 ( $2D_1$ ), 2734 ( $2D_2$ ) and 3245 ( $2D'$ )  $\text{cm}^{-1}$  all decrease on  $\text{Ar}^+$  ion treatment. Additionally, the appearance of a new band at  $2970\text{ cm}^{-1}$  ( $D_1 + D'$ ) corresponds to the decrease in the intensity for the 2690, 2734 and 3245  $\text{cm}^{-1}$  bands.

Both our data and those in the literature show six bands for undamaged HOPG, one fundamental and five overtone/combinations. After damaging the surface these bands all decrease in intensity and four “new” bands appear. These four bands are predicted by maxima in the phonon density of states calculations<sup>14</sup> for graphite crystals, but their fundamental transitions are forbidden by the Raman selection rules in undamaged HOPG.

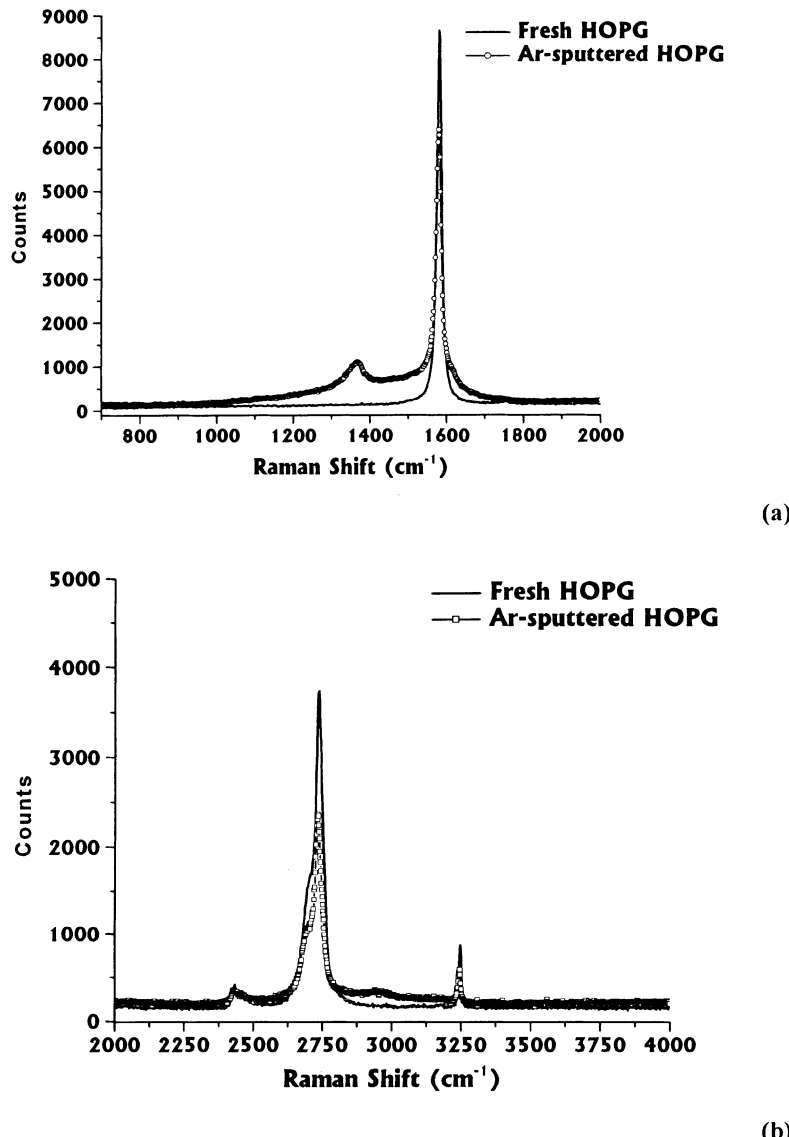


**Figure 3.** Spectra of fresh and Ar-sputtered materials showing the spectral changes at the (a) 500-2000 cm<sup>-1</sup> fundamental region and the (b) 2000-4000 cm<sup>-1</sup> overtone region.

The sudden appearance of these bands indicates that crystal symmetry is broken upon irradiation, accounting for the appearance of these previously forbidden transitions as well as the intensity loss of the other bands. If the crystal symmetry is altered in

localized regions those regions then give rise to a different spectroscopic signature. Previous studies have shown that when the crystal is irradiated at higher fluences there is a much greater loss of order, which results in the complete transformation of the Raman spectrum.

We have also used confocal Raman<sup>7</sup> to study the chemical interaction, if any, of HOPG and sputtered Cu (4 Å, 1 Å/min, 2 kV Ar<sup>+</sup>). Figure 4 shows that both Ar<sup>+</sup> and Cu produce the same sort of surface damage; the absence of new peaks indicates a lack of Cu-C bond formation. This lack of Cu-C bond formation, even for energetically deposited Cu, was confirmed by XPS<sup>7</sup>. Thus, the effect of both these highly energetic ions on the HOPG surface is the same: the HOPG lattice is disrupted. The slight differences in peak intensity suggest that the Cu is better at surface disruption.

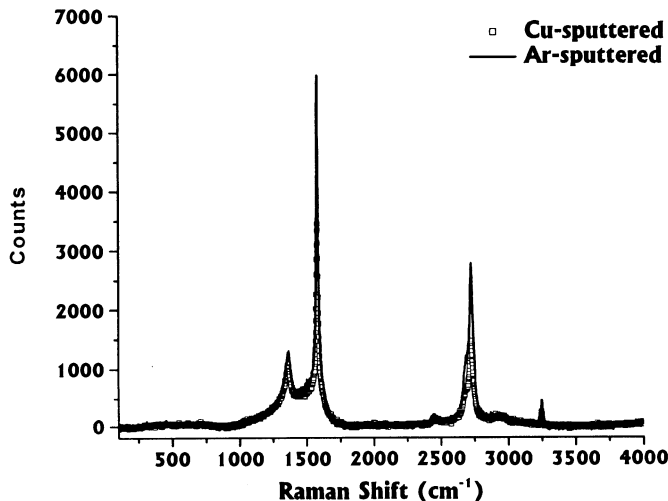


**Figure 4.** Spectra showing the Ar- and Cu-sputtered HOPG surfaces.

SRIM simulations<sup>15</sup> show that the projected ranges for Ar<sup>+</sup> and Cu are 40 and 5 Å, respectively. The fact that their effects can be seen by confocal Raman, despite the expected optical skin depth of 700 Å for the 488 nm laser line, underlines the extremely high surface sensitivity of this technique.

#### 4. CONCLUSIONS

Confocal Raman microspectroscopy is a powerful tool for materials science and for the characterization of surfaces, and is applicable to a wide range of materials and thin films. Our group has successfully used this technique to study the homogeneity of

polymer thin films created through a solid-state curing process, currently used in the manufacturing of microelectronic devices. Employing a model system, we have also successfully used this technique to understand more about the chemical changes occurring at a surface on high-energy ion treatment of the material.

## 5. REFERENCES

1. P. Hendra, C. Jones and C. Warnes, Fourier Transform Raman Spectroscopy: Instrumentation and Chemical Applications; (Ellis Horwood Ltd., New York, 1991).
2. G. Turrell and J. Corset, Raman Microscopy: Developments and Applications; (Academic Press, New York, 1996).
3. M. Minsky, Memoir on Inventing the Confocal Scanning Microscope, Scanning 10, 128 (1988).
4. R. A. Kirchhoff and K. Bruza, Benzocyclotenes in Polymer Synthesis, Progress in Polymer Science 18, 85 (1993).
5. S. Poulin, D.-Q. Yang, E. Sacher, C. Hyett and T. H. Ellis, The Surface Structure of Dow Cyclotene 3022, as Determined by Photoacoustic FTIR, confocal Raman and photoelectron spectroscopies, Applied Surface Science 165, 15-22 (2000).
6. D.-Q. Yang, S. Poulin, E. Sacher and C. Hyett, Interfacial reaction between evaporated copper and Dow Cyclotene 3022, Applied Surface Science 165, 116-126 (2000).
7. D.-Q. Yang and E. Sacher, s-p Hybridization in Highly Oriented Pyrolytic Graphite Before and After Modification by Argon Ions and Copper Deposition, Physical Review B (Submitted), .
8. B. S. Elman, M. S. Dresselhaus, G. Dresselhaus, E. W. Maby and H. Mazurek, Raman scattering from ion implanted graphite, Physical Review B 24, 1027 (1981).
9. B. S. Elman, M. Shayegan, M. S. Dresselhaus, H. Mazurek and G. Dresselhaus, Structural characterization of ion-implanted graphite, Physical Review B 25, 4142 (1982).
10. K. Nakamura, M. Fujitsuka and M. Kitajima, Disorder-induced line broadening in first order Raman scattering from graphite, Physical Review B 41, 12260 (1990).
11. K. Nakamura and M. Kitajima, Real-time Raman measurements of graphite under Ar+ irradiation, Applied Physics Letters 59, 1550 (1991).
12. K. Nakamura and M. Kitajima, Ion-irradiation effects on the phonon correlation length of graphite studied by Raman spectroscopy, Physical Review B 45, 78 (1992).
13. K. G. Nakamura and M. Kitajima, Time-resolved Raman measurements of a graphite surface under ion irradiation, Surface Science 283, 255 (1993).
14. M. Maeda, Y. Kuramoto and C. Horie, Phonon Dispersion Relations of Graphite, Journal of the Physical Society of Japan 47, 337 (1979).
15. JFZ IBM-Web Homepage 1/98 (Yorktown, October 1, 1999);  
<http://www.research.ibm.com/ionbeams/home.htm#Home:%20SRIM%20Installation>.

# ELLIPSOMETRIC CHARACTERIZATION OF THE OPTICAL CONSTANTS OF METALS: THIN FILM VERSUS NANOPARTICLE

Dan Dalacu and Ludvik Martinu\*

## 1. INTRODUCTION

The characterization of the optical constants of metals is extensive and dates back many decades.<sup>1</sup> Particular emphasis has been placed on gold, with calculations of the dielectric function performed using both photometric<sup>2,3</sup> (reflection and transmission) and ellipsometric<sup>4-8</sup> measurements. Depending on the type of sample being measured (thin film or bulk), the deposition method used, and the post-deposition annealing, slightly different optical constants have been determined. The dependence of the optical constants on the details of the sample preparation arises from variations in the microstructural characteristics of the samples. Different grain morphologies will affect the surface roughness, void content, strain-induced lattice deformation, and electron scattering, all of which will affect the calculations of the dielectric function of the metal,  $\epsilon_m$ .<sup>9</sup>

In this article, ellipsometry will be employed to determine the optical constants of gold. Ellipsometry is inherently an oblique incidence measurement so that a single measurement suffices for the calculation of  $\epsilon$ , unlike reflection and transmission (these are usually measured at normal incidence where both components of the light are equivalent). Ellipsometry is also less sensitive to macroscopic surface scattering since a ratio of intensities is measured, as opposed to photometry where the measured absolute intensities will be affected by light loss due to scattering out of the field of the detector.<sup>10</sup>

The optical constants will be determined first for a thin film of gold. The influence of surface films and grain boundary material on the calculated  $\epsilon_m$  will be demonstrated. By explicitly including these in the calculation of  $\epsilon_m$  through the use of effective medium theories<sup>11</sup> (EMTs), it will be shown how the true optical constants can be recuperated. Second, the optical constants of an ensemble of gold clusters with nanometer dimensions

---

\* Dan Dalacu, Institute for Microstructural Sciences, National Research Council, Ottawa, Ontario, Canada, K1A 0R6. Ludvik Martinu, École Polytechnique de Montréal, P.O. Box 6079, Station Centre-Ville, Montréal, Québec, Canada, H3C 3A7.

will be determined. Two types of nanoparticle films are considered: (*i*) substrate-supported particles, so-called discontinuous films, and (*ii*) particles dispersed three dimensionally in a matrix material. Again through the use of EMTs, it will be shown how the optical constants of gold can be determined from a nanoparticle film. This format eliminates the influence of surface roughness, void content, and grain boundary material, allowing for the observation of other factors that influence  $\epsilon_m$ , namely, strain-induced lattice deformation.

## 2. EXPERIMENT

The gold thin films were deposited on glass and quartz slides by radio-frequency (RF) magnetron sputtering from a 50 mm diameter gold target at 60 mTorr of Ar using an RF power of 100 W for a self-bias of -350 V. The discontinuous films<sup>12</sup> were obtained simply from shorter (< 1min) deposition times. These films were cladded with an overlayer of SiO<sub>2</sub> deposited by plasma-enhanced chemical vapor deposition (PECVD) using SiH<sub>4</sub>/N<sub>2</sub>O chemistry.<sup>13</sup> Dispersion of the nanoparticles in a matrix was obtained by simultaneous sputtering of the gold target and PECVD of SiO<sub>2</sub> from a separate RF electrode.<sup>14</sup>

Ellipsometric measurements were made using a variable-angle spectroscopic ellipsometer (model VASE from J. A. Woollam Co., Inc.). Additional normal-incidence transmission measurements were made on the nanoparticle films using a Perkin-Elmer Lambda 19 spectrophotometer. The particle size and concentration of the cladded discontinuous films were determined using transmission electron microscopy (TEM) with a Phillips CM30 microscope.

## 3. OPTICAL MODELING

An ellipsometric measurement consists of measuring the quantities  $\Psi$  and  $\Delta$  which are used to determine the optical properties of the sample through the standard equation<sup>15</sup>

$$\rho = \tan \Psi \exp i\Delta \quad (1)$$

where the complex amplitude ratio,  $\rho$ , gives the absolute amplitude attenuation and phase change of each component of the incident electric field upon reflection, regardless of the multilayer structure of the sample. The simple case of reflection from a substrate,  $\rho$  is related to the dielectric function of the substrate,  $\epsilon_s$ , through<sup>16</sup>

$$\epsilon_s = \left[ 1 - \tan \phi \sqrt{1 - 4\rho \sin^2 \phi / (\rho + 1)^2} \right]^2 \quad (2)$$

where  $\phi$  is the angle of incidence. In the case of a film-covered substrate (or any multilayer structure), a unique solution for the dielectric function of the film does not exist due to the unknown film thickness.<sup>17,18</sup> In this case, one makes use of parametric

dispersion models within the multilayer optical model which are applied to spectroscopic data together with fitting algorithms to extract the dielectric function. Measurements at multiple angles of incidence as well as addition of photometric data is used to constrain the solution.

#### 4. THIN FILM

Typical ellipsometric data ( $\Psi$  and  $\Delta$ ) measured for an opaque gold film is shown in Fig. 1 for incidence angles  $55^\circ$ ,  $65^\circ$  and  $75^\circ$ . Being opaque, it can be considered a substrate and, assuming a plane-parallel surface, the dielectric function of the gold film,  $\epsilon_m = \Re[\epsilon_m] + i\Im[\epsilon_m]$ , is simply obtained from Eq. (2) and is also shown in Fig. 1.

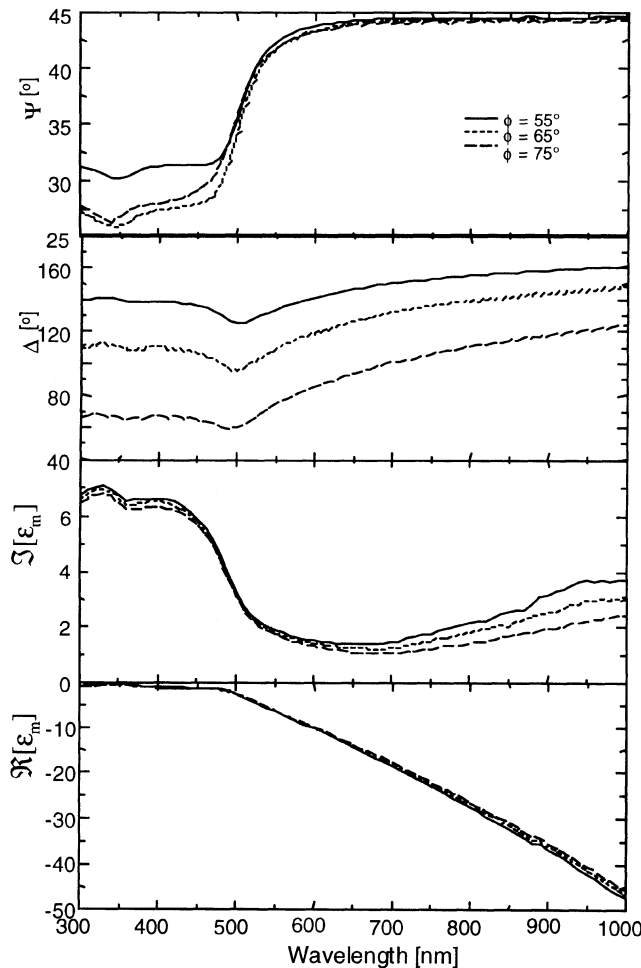


**Figure 1.** Ellipsometric spectra  $\Psi$  and  $\Delta$  and calculated  $\epsilon_m$  for an RF sputtered gold film.

In the analysis of the dielectric function of gold, in particular, its relation to the electronic band structure, it is more informative to consider  $\Im[\epsilon_m]$ . The low energy part of the  $\Im[\epsilon_m]$  spectrum is determined by intraband transitions, for which the resulting absorption is well described by the Drude equation

$$\epsilon_{Drude} = 1 - \frac{\omega_p^2}{\omega(\omega + i\Gamma)} \quad (3)$$

where  $\omega_p$  is the plasma frequency and  $\Gamma$  is the collision frequency arising from electron scattering processes. By fitting Eq. (3) to the low energy part of the spectrum, the Drude absorption,  $\Im[\epsilon_{Drude}]$  can be subtracted from  $\Im[\epsilon_m]$  leaving the contribution to the absorption due to interband transitions from the d-bands to the Fermi surface,  $\Im[\epsilon_{core}]$ , shown in Figure 2. The interband absorption has contributions from a weak transition near symmetry point X in the Brillouin zone with an onset energy of 1.94 eV, and a stronger transition near point L with an onset energy of 2.45 eV.<sup>19</sup> The latter is the dominant absorption edge in gold and is responsible for the peak at  $\lambda \sim 425$  nm. There is also a contribution to  $\Im[\epsilon_{core}]$  from interconduction band transitions (6sp conduction band to the higher energy 7sp band) which is responsible for the absorption feature at  $\lambda \sim 325$  nm.<sup>20</sup>

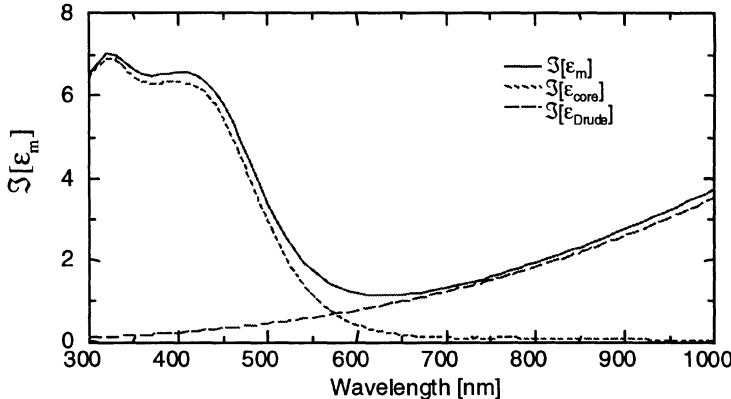


Figure 2. Imaginary part of the dielectric function of gold showing Drude and core contributions.

In general, the magnitude of both the core and Drude absorption are found to vary depending on sample preparation, low values of  $\Im[\epsilon_{Drude}]$  and high values of  $\Im[\epsilon_{core}]$  being associated with high quality samples. The variation in the calculated constants results from differences in grain morphology (i.e. size, packing, stress), as well as different levels of impurities, both in and on the film.<sup>9,19</sup> These effects will influence the dielectric function either fundamentally (i.e. changes in electron scattering and crystal lattice constant) or by rendering the assumptions made in the optical model used to calculate  $\epsilon_m$  invalid. For example, surface roughness and very thin surface films renders the assumption of a plane-parallel substrate incorrect, while void content or grain boundary material affects the amount and type of polarizable material per unit volume. We will

concentrate on the effects which can be incorporated within the optical model under the assumption that the dielectric function given in Figure 1 corresponds to a high quality sample.

Consider first the effect of surface roughness: If the roughness is macroscopic (i.e. having dimensions comparable to the incident wavelength), the light will be scattered out of the field of the detector, and, since ellipsometry is not sensitive to intensity fluctuations, will have no effect. Microscopic roughness, on the other hand, results in depolarization of the analyzed light and will affect the calculated optical constants. It can be included in the optical model by considering a thin surface layer having a dielectric function,  $\epsilon_{eff}$ , given by an effective medium with contributions from the substrate,  $\epsilon_s = \epsilon_m$ , and the ambient,  $\epsilon_h$ . The Bruggeman EMT, or effective medium approximation, EMA, is generally used:

$$0 = p_m \frac{\epsilon_m - \epsilon_{eff}}{\epsilon_m + 2\epsilon_{eff}} + (1 - p_m) \frac{\epsilon_h - \epsilon_{eff}}{\epsilon_h + 2\epsilon_{eff}} \quad (4)$$

with the volume fraction of metal,  $p_m$ , set to 50%.

If a surface roughness layer is present and is not taken into account (i.e. Eq. (2) is used for  $\epsilon_m$ ), an artificially low value of  $\Im[\epsilon_{core}]$  is obtained as shown in Figure 3a. (Note

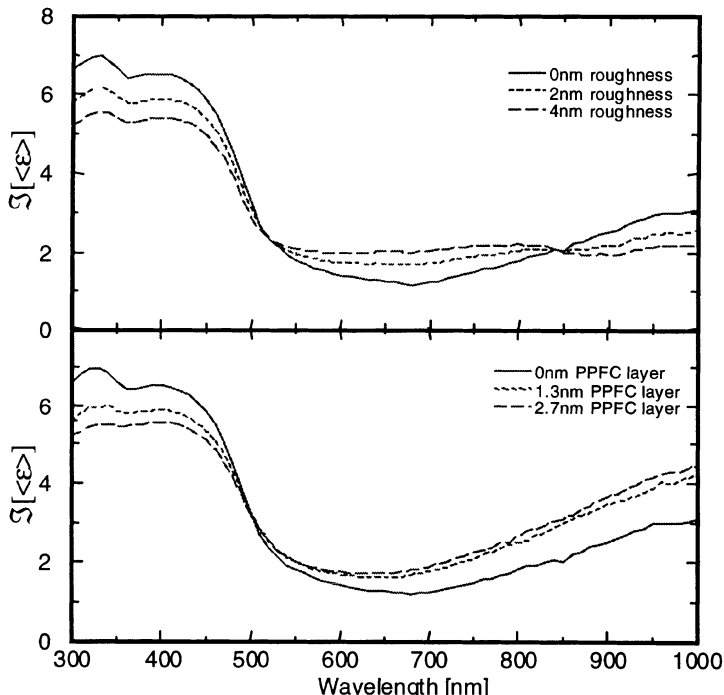


**Figure 3.** (a)  $\Im[\epsilon_m]$  determined using Eq. (2) applied to model spectra calculated considering  $\epsilon_s = \epsilon_m$  from Figure 1 with EMA roughness layers of 2nm and 4nm. (b)  $\Im[\epsilon_m]$  calculated using Eq. (2) for a Au film coated with thin layers of fluoropolymer (1.3nm and 2.7nm).

that if Eq. (2) is applied to a multilayer structure, the resulting dielectric function is generally referred to as the pseudo-dielectric function,  $\langle \epsilon \rangle$ .)

The effect of microscopic surface roughness is similar to the presence of a thin surface film of reduced index. If such a film is deliberately deposited on top of the gold, the same decrease in  $\Im[\epsilon_{\text{core}}]$  is observed. This is demonstrated in Figure 3b where thin layers ( $< 4 \text{ nm}$ ) of plasma polymerized fluorocarbon, PPFC, ( $\epsilon \sim 1.7$ ) have been deposited on the gold.<sup>21</sup> The pseudo-dielectric function was calculated using Eq. (1), that is, neglecting the surface film, and a similar decrease in  $\Im[\epsilon_{\text{core}}]$  as observed for the surface roughness layers is obtained.

The influence of voids within the film can be modeled, as with surface roughness, using the EMA. In this case  $\epsilon_{\text{eff}}$  replaces  $\epsilon_s = \epsilon_m$  in Eq. (1) instead of the  $\epsilon_m/\epsilon_{\text{eff}}$  multilayer structure. Again, the predominant effect is a decrease in  $\Im[\epsilon_{\text{core}}]$  (see Fig. 4a), in this case due to a decrease in the amount of polarizable material per unit volume. This type of effect can be easily observed experimentally using films deposited by simultaneous RF sputtering of a gold target and plasma polymerization of a fluorocarbon monomer which has been added to the gas mixture.<sup>22</sup> The amount of fluoropolymer incorporated within the growing film can be controlled by the glow discharge parameters. The effect of a 10% fluoropolymer content is shown in Figure 4b, demonstrating a similar decrease in  $\Im[\epsilon_{\text{core}}]$  as predicted by the EMA model for voids.

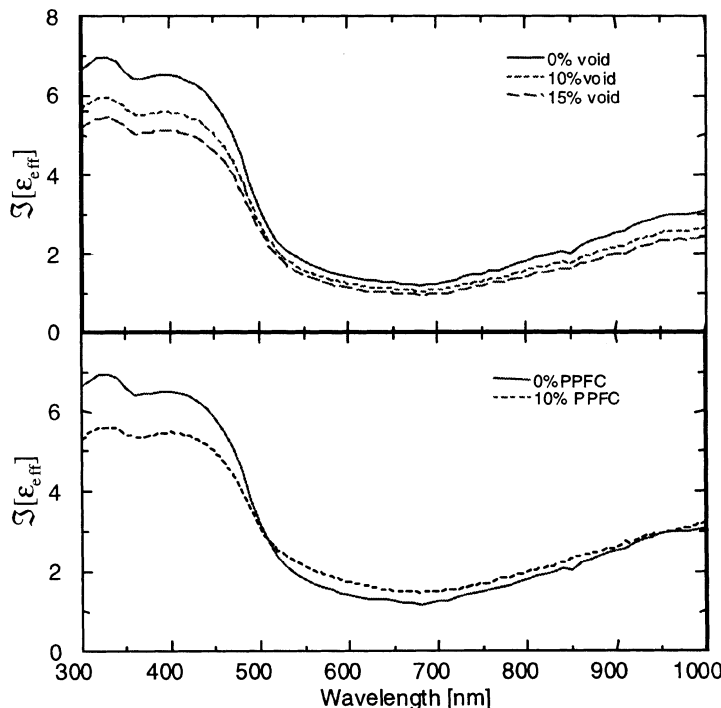


**Figure 4.** (a)  $\Im[\epsilon_{\text{eff}}]$  calculated using the EMA with Au plus 10% and 15% void. (b)  $\Im[\epsilon_{\text{eff}}]$  for a film deposited by simultaneous sputtering of a gold target and plasma polymerization of  $\text{C}_4\text{F}_8$ .

In the approach used to account for voids (i.e. mixing  $\epsilon_m$  from Figure 1 and  $\epsilon_h = 1$  using the EMA), changes in  $\epsilon_m$  itself, which are expected from changes in the frequency of electron scattering events (i.e.  $\Gamma$ ), were not considered. Changes in  $\Gamma$  are evident from the slight increase in the long wavelength absorption upon addition of 10% PPFC to the gold (Figure 4b). A more accurate model would use  $\epsilon_m(\Gamma)$ , as in Figure 5, within the EMA.

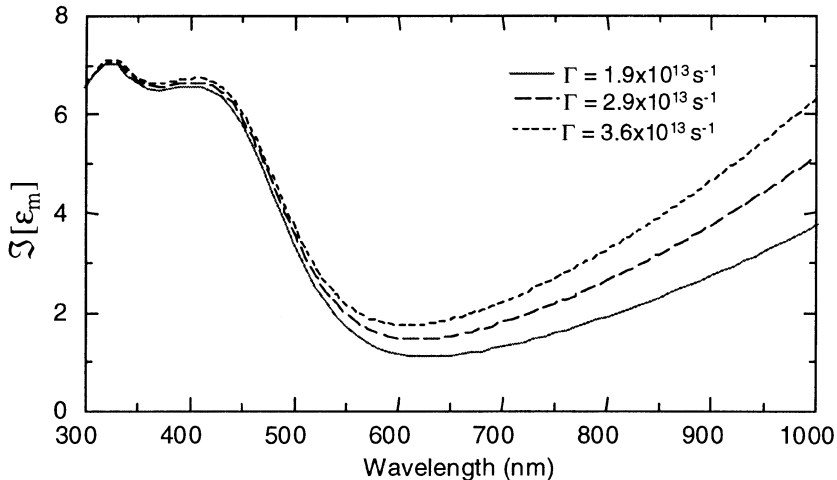


**Figure 5.** (a) Dependence of  $\Im[\epsilon_m]$  on  $\Gamma$  from Eq. (3).

## 5. DISCONTINUOUS FILMS

Using EMTs, one can also model the optical response of very thin metal films having a thickness insufficient to form a continuous layer. At the later stages of the film growth, where the effective medium is comprised predominantly of metal (i.e. past percolation,  $p_m > 50\%$ ), the optical response of the discontinuous film is the same as in the case of a thick film with a high void content. For smaller metal volume fractions and particle sizes (see Figure 6), the optical response is dominated by the collective excitations of the free electrons within the particles, so-called surface plasmon polaritons.

For small enough particles, only the dipole or surface plasmon mode is excited, and the film can be considered as a 2-D array of dipoles. The appropriate effective medium is given by the theory of Yamaguchi<sup>23</sup> which describes two effective dielectric functions, one in the plane of the film,  $\epsilon_{||}$ , and one perpendicular,  $\epsilon_{\perp}$ , since a 2-D array will have an anisotropic response:

$$\epsilon_{||} = \epsilon_h \left[ 1 + \frac{p_m (\epsilon_m - \epsilon_h)}{\epsilon_h + F_{\perp} (\epsilon_m - \epsilon_h)} \right] \quad (5a)$$

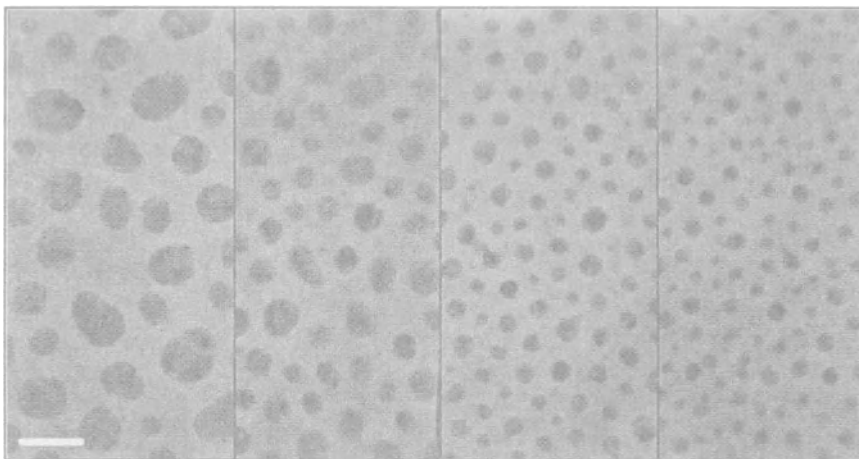


**Figure 6.** TEM of discontinuous gold films having different  $p_m$  and  $R$ . Bar indicates 20nm.

$$\frac{1}{\varepsilon_{\perp}} = \frac{1}{\varepsilon_h} \left[ 1 - \frac{p_m (\varepsilon_m - \varepsilon_h)}{\varepsilon_h + F_{\perp} (\varepsilon_m - \varepsilon_h)} \right]. \quad (5b)$$

$F_{\parallel}$  and  $F_{\perp}$  are effective depolarization factors which take into account the particle shape, image charge interaction, and dipole-dipole interaction.

To apply this model to discontinuous films where the particle size is smaller than the free electron mean free path, one has to take into account the scattering of electrons from the particle surface. This can be done by replacing  $\Gamma$  in Eq. (3) with an effective collision frequency:<sup>24</sup>

$$\Gamma_{eff} = \Gamma + A v_F / R \quad (6)$$

where  $v_F$  is the Fermi velocity,  $R$  is the particle radius, and  $A$  is a broadening parameter equal to 1 for isotropic scattering. The parametric model given by Eq. (5) was applied to ellipsometric data of a series of discontinuous films (shown in Figure 6) having different  $p_m$  and  $R$  values and cladded with a SiO<sub>2</sub> film (i.e.  $\varepsilon_h \sim 2.2$ ). Transmission data was included in the fitting procedure to minimize correlations between the fit parameters. The calculated  $\Im[\varepsilon_{\parallel}(p, R)]$  is shown in Figure 7.

The imaginary part of the effective dielectric function of a discontinuous film has a much reduced core absorption (as expected from such a low concentration of gold, see Figure 4). Also, there is no free electron absorption, instead one sees the large absorption band at ~525nm arising from the excitation of surface plasmons, the width and position of the band depending on  $p_m$  and  $R$  through Eqs. (3), (5), and (6). In order to extract the

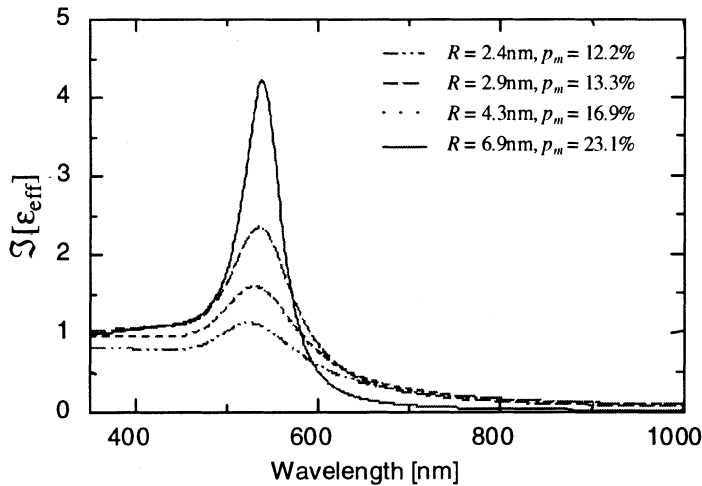


**Figure 7.** Imaginary part of the effective dielectric function of discontinuous Au films corresponding to TEM images in Figure 6.

correct particle size when comparing with the TEM images of the films, a value of  $A$  equal to 0.15 was needed. This reduced value (compared to  $A = 1$  for isotropic electron scattering) indicates that the classical interpretation of electron scattering at the particle surface (Eq. (6)), is not adequate in describing the width of the surface plasmon resonance (which is determined by  $A$ ). A more careful interpretation of the broadening of the resonance with decreased particle size considers quantum size effects which will eventually lead to a discrete conduction band. In this interpretation, the broadening is caused by Landau damping<sup>25</sup> and the band is expected to be narrower for a given particle size (i.e. smaller  $A$ ).

## 6. 3-D FILMS

In the case of particles dispersed in 3-D, there are no image charge interactions and no substrate-induced particle shape deformation, providing a much simpler format for studying particle size dependencies of  $\epsilon_m$ . The appropriate effective medium for well-isolated spherical particles in 3-D matrix is the simple Maxwell-Garnett model:

$$\frac{\epsilon_{eff} - \epsilon_h}{\epsilon_{eff} + 2\epsilon_h} = p_m \frac{\epsilon_m - \epsilon_h}{\epsilon_m + 2\epsilon_h}. \quad (7)$$

3-D films were prepared by simultaneous sputtering of gold and PECVD of  $\text{SiO}_2$ .<sup>14</sup> The particle size was controlled by post-deposition annealing at 900°C. The effective dielectric function calculated from ellipsometric measurements is similar to the response

of the discontinuous films shown in Figure 7. However, since only  $p_m$  is a fit parameter (as opposed to  $p_m$  and  $F$  for the discontinuous films) one can fit directly for  $\epsilon_m$  as a function of  $R$ , as shown in Figure 8.

Three distinct particle size dependencies are apparent: First, with decreasing size, the long wavelength absorption increases due to an increasing  $\Gamma_{\text{eff}}$  (see Eq. (6)). Second, the interband absorption edge arising from 3d and 4d to 6sp transitions near L changes form. This is more evident if Figure 8 is replotted as  $\Im[\epsilon_{\text{core}}]$  versus  $(\omega - \omega_0)^{1/2}/(\hbar\omega)^2$  (i.e. with the Drude absorption subtracted). In the vicinity of the absorption edge this should yield a straight line since the transition is like an  $m_c$  critical point and, hence, should have a  $\Im[\epsilon_{\text{core}}] \sim (\omega - \omega_0)^{1/2}/(\hbar\omega)^2$  dependence,  $\hbar\omega_0$  being the onset energy. Figure 9 shows this linear dependence and, from a least squares fit, demonstrates a decreasing bandedge slope and onset energy with decreasing particle size (see inset). The last particle size dependence in Figure 8 concerns the interconduction band transitions. The feature due to these transitions (at  $\lambda \sim 325\text{nm}$ ) decreases and broadens dramatically with decreasing particle size.

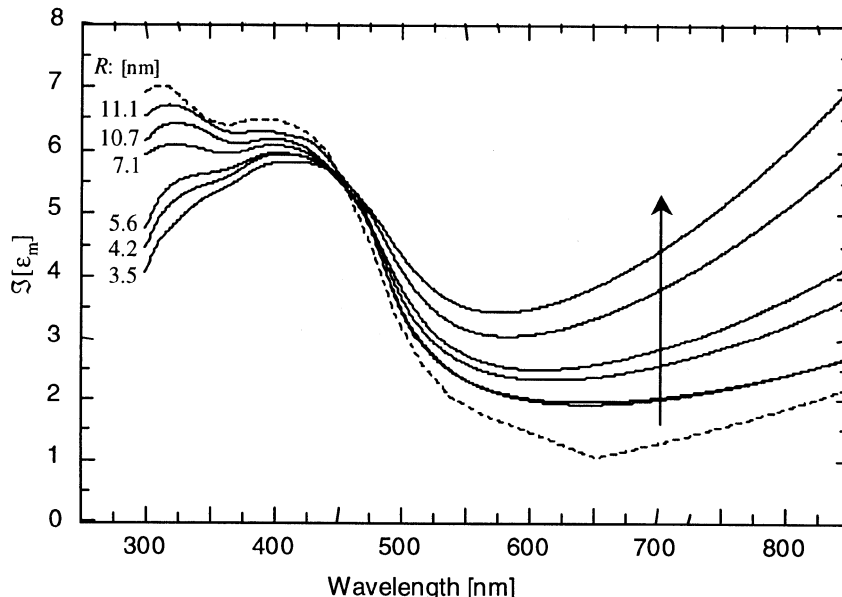


**Figure 8.** Imaginary part of the effective dielectric function of gold as a function of particle size. The dashed line corresponds to Théye's values determined from a thin film sample.<sup>2</sup>

The observed decrease in the onset energy suggests contracted lattice, with  $\Delta\hbar\omega_0 = 0.03\text{eV}$  calculated for a  $0.053\text{\AA}$  change in lattice constant.<sup>20</sup> Such a severe surface stress-induced contraction is, however, not expected for particles of this size.<sup>26</sup> Alternatively, the decrease in the bandedge slope suggests lattice distortion as opposed to simple contraction. Similar disorder-induced changes in the bandedge are observed from transmission measurements made at temperatures at and above the melting point.<sup>27</sup> Disorder will also affect the interconduction band transitions, in particular, the observed

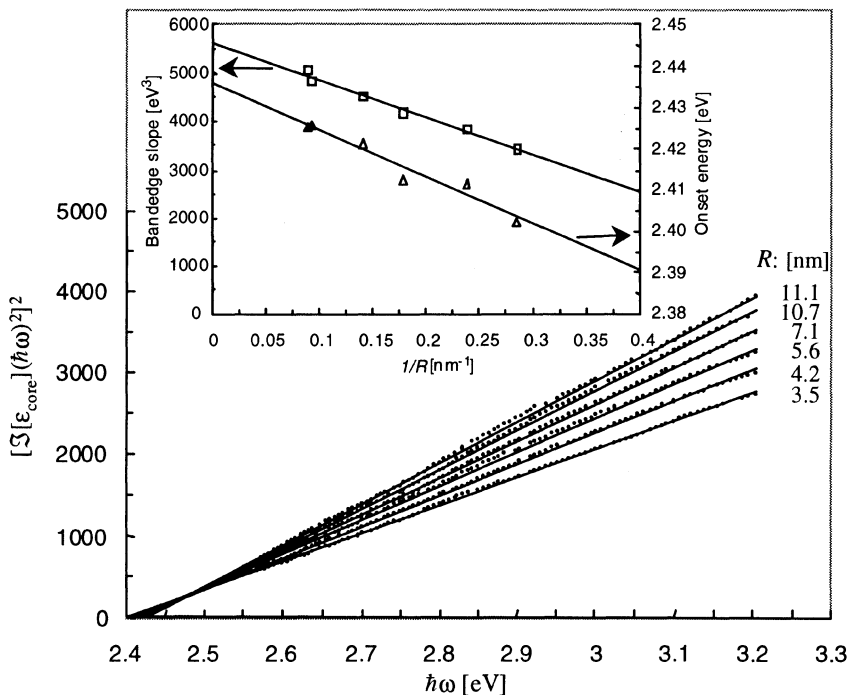


Figure 9. Particle size dependence of the interband absorption edge in gold.

lowering and broadening of the peak at  $\lambda \sim 325\text{nm}$  has been described in terms of a distribution of lattice spacings<sup>20</sup> and used to account for a similar behavior of  $\Im[\epsilon_{core}]$  for a thin film during annealing.

## 7. Conclusion

Some factors affecting the calculations of the optical constants of gold using ellipsometric measurements on a thin film sample were demonstrated. These include: (i) an incorrect optical model assumed in the calculation (i.e. surface roughness, surface layers) and (ii) calculation of an effective dielectric function as opposed to the true optical constants of the metal (i.e. void content and grain boundary material). In each case, the use of effective medium theories can be used to recuperate a more representative metal dielectric function.

Effective media were also used to describe the optical response of gold in a nanoparticle format. In this case, the response is dominated by an absorption band in the visible arising from the excitation of surface plasmons. Using nanoparticle films allows the observation of fundamental changes in the optical response of gold, namely changes in the core response arising from stress-induced lattice distortion and changes in the Drude response arising from electron scattering by the particle surface.

## 8. REFERENCES

1. P. O. Nilsson, Optical properties of metals and alloys, *Solid State Phys.* **29**, 139-234 (1974).
2. M.-L. Thèye, Investigation of the optical properties of Au by means of thin semitransparent films, *Phys. Rev. B* **2**, 3060-3078 (1970).
3. P. B. Johnson and R. W. Christy, Optical constants of the noble metals, *Phys. Rev. B* **6**, 4370-4379 (1972).
4. M. Otter, Optische Konstanten massiver Metalle, *Z. Phys.* **161**, 163-178 (1961).
5. G. P. Pells and M. Shiga, The optical properties of copper and gold as a function of temperature, *J. Phys. C* **2**, 1835-1846 (1969).
6. D. E. Aspnes, Fourier transform detection system for rotating-analyzer ellipsometers. *Opt. Commun.* **8**, 222-225 (1973).
7. G. Jungk and A. Röseker, Optical Properties of Metals: Au, *Phys. Stat. Sol. B* **137**, 117-123 (1986).
8. Y. Wang, L.-Y. Chen, B. Xu, W.-M. Zheng, R.-J. Zhang, D.-L. Qian, S.-M. Zhou, Y.-X. Zheng, N. Dai, Y.-M. Yang, K.-B. Ding, X.-M. Zhang, The medium-related optical constants of noble metals observed by ellipsometric study, *Thin Solid Films* **313-314**, 232-236 (1998).
9. D. E. Aspnes, E. Kinsbrorn, and D. D. Bacon, Optical properties of Au: sample effects, *Phys. Rev. B* **21**(8), 3290-3299 (1980).
10. D. E. Aspnes in: *Handbook of Optical Constants of Solids*, edited by E. D. Pallik (Academic Press, New York, 1985) pp. 89-112.
11. S. Berthier and J. Lafait in *Handbook of Optical Properties: Thin Films for Optical Coatings*, edited by R. E. Hummer and K. H. Guenther (CRC Press, Boca Raton, Fla., 1995) pp. 305-352.
12. D. Dalacu and L. Martinu, Optical properties of discontinuous gold films: finite size effects, *J. Opt. Soc. Amer. B* **18**(1), 85-92 (2001).
13. J. E. Klemburg-Sapieha, O. M. Kuttel, L. Martinu, and M. R. Wertheimer, Dual microwave-RF plasma deposition of functional coatings, *Thin Solid Films* **93-94**, 965-972 (1990).
14. D. Dalacu and L. Martinu, Spectroellipsometric characterization of plasma-deposited Au/SiO<sub>2</sub> nanocomposite films, *J. Appl. Phys.* **87**, 228-235 (2000).
15. H. G. Tomkins and W. A. McGahan, *Spectroscopic Ellipsometry and Reflectometry: A User's Guide* (John Wiley & Sons, New York, 1999).
16. F. L. McCrackin, E. Passaglia, R. R. Stromberg, and H. L. Steinberg, Measurement of the thickness and refractive index of very thin films and the optical properties of surfaces by ellipsometry, *J. Res. Natl. Bur. Sect. A* **67**, 363- (1963).
17. O. S. Heavens, *Optical Properties of Thin Solid Films* (Dover Publications, New York, 1965).
18. R. M. A. Azzam and N. M. Bashara, *Ellipsometry and Polarized Light* (North-Holland Publishing, Amsterdam, 1977).
19. M. Guerrisi, R. Rosei, and P. Winsemius, Splitting of the interband absorption edge in Au, *Phys. Rev. B* **123**, 557-563.
20. P. Winsemius, H. P. Jengkeek, and F. F. van Kampen, Structure dependence of the optical properties of Cu, Ag and Au, *Physica B* **79**, 529-546 (1975).
21. D. Dalacu, A. P. Brown, J. E. Klemburg-Sapieha, L. Martinu, M. R. Wertheimer, S. I. Najafi, and M. A. Andrews, Characterization of Au/fluoropolymer nanocomposite films for nonlinear optical application, *Mat. Res. Soc. Proc.* **544**, 167-172 (1999).
22. D. Dalacu and L. Martinu, Spectroellipsometric characterization of plasma-deposited Au/fluoropolymer nanocomposite films, *J. Vac. Sci. Technol. A* **17**, 877-883 (1999).
23. T. Yamaguchi, M. Takiguchi, S. Fujioka, and H. Takahashi, Optical absorption of submonolayer gold films: size dependence of  $\epsilon_{\text{bound}}$  in small island particles, *Surf. Sci.* **138**, 449-463 (1984).
24. H. Hovel, S. Fritz, A. Hilger, U. Kreibig, and M. Vollmer, Width of cluster plasmon resonances: bulk dielectric function and chemical interface damping, *Phys. Rev. B* **48**, 18178-18188 (1993).
25. C. Yannouleas and R. A. Broglia, Landau damping and wall dissipation in large metal clusters, *Ann. Phys. N.Y.* **217**, 105-141 (1992).
26. C. Solliard and M. Flueli, Surface stress and size effects on the lattice parameter in small particles of gold and platinum, *Surf. Sci.* **156**, 487-494 (1985).
27. D. Dalacu and L. Martinu, Temperature dependence of the surface plasmon resonance of Au/SiO<sub>2</sub> nanocomposite gold films, *Appl. Phys. Lett.* **77**, 4283-4285 (2000).

# **ULTRA THIN FILM ANALYSIS USING THERMO VG SCIENTIFICS THETAPROBE INSTRUMENT**

R.K. Champaneria, J. Wolstenholme\*

## **1. INTRODUCTION**

Thin films and the ability to produce them are part of our every day lives. For example, thin films are widely used to provide passivation (insulating films between conductors), and diffusion barriers for faster processing speed in electronic circuits. Hardness coatings for scratch resistance, antireflection coatings, magnetic media, metallisation on polymers and even printing on polymers for the packing industry are also thin films.

To perform the function for which they were designed , thin films must have the proper thickness, composition, roughness and other characteristics important to the particular application. These characteristics must often be measured, both during and after thin-film fabrication.

Films typically used in thin-film applications range from a few atoms thick (<10 Å) to 100um. They can be formed by many different processes, including spin coating, vacuum evaporation, sputtering, vapour deposition, epitaxial growth planarisation, and dip coating.

An important emerging field is ultra thin films, for example ultra thin dielectric layers in transistor technology. To provide the correct capacitance of the ultra thin films for the next generation of transistors, a new generation of dielectrics with high dielectric constants would be required. These new materials will have a chemistry which is more complex than silicon dioxide on silicon making chemical characterisation an important part of the process. The interface chemistry between the silicon and the new material is also important and will need to be understood. Traditional ellipsometric methods will not provide sufficient information.

Smaller devices geometry also mean that p-type and n-type dopants need to be implanted into silicon at smaller depths. SIMS profiling is the traditional technique for measuring these profiles but this is not ideal for very shallow implants and other methods are being sought.

\*R.K. Champaneria and J. Wolstenholme. Thermo VG Scientific. The Birches Industrial Estate.  
Imberhorne Lane. East Grinstead. West Sussex RH19 1UB. England

*Metallization of Polymers 2.*  
Edited by Edward Sacher, Kluwer Academic/Plenum Publishers, 2002

23

Using angle resolved or angle dependent XPS, it is possible to obtain concentration profile information from thin film samples without sputtering. In most cases angle resolved XPS (ARXPS) can be considered to be a non-destructive technique. It therefore has the potential to probe chemical states beneath the surface which would be destroyed by sputtering.

The information that can be derived from ARXPS is dependent upon the fact that the electrons are not only emitted from the solid sample surface but also from a range of depths beneath the surface.

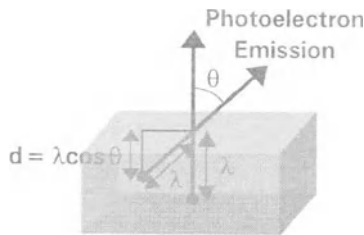


*Figure 1* Greater surface specificity is achieved by collecting electrons at more grazing emission angles

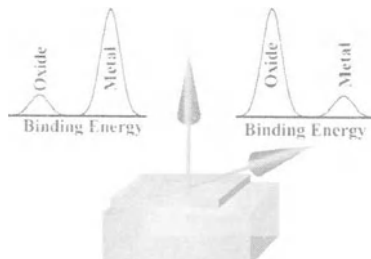


*Figure 2* An illustration of the analysis of a thin metal oxide on a metal. The diagrammatic spectra show the effect of the collection angle on the elemental and oxide peaks of the metal.

If electrons are collected from angles other than normal to the sample surface ( $0^\circ$ ), depths from which electrons leave the surface decreases by a factor of  $\cos\theta$  (figure 1). Equation (1) shows the relationship between the signal detected and the depth from which the photoelectrons originated from where  $I$  is the signal intensity from a depth  $d$ ,  $I'$  is the intensity from an infinitely thick clean substrate, and  $\lambda$  is a constant known as the attenuation length of the electron within the solid and is related to the inelastic mean free path.

$$I = I' \exp(-d/\lambda \cos\theta) \quad (1)$$

If XPS signal is collected over a range of angles from near normal emission to near grazing emission then the analysis depth changes also.

Figure 2 shows schematically the analysis of a thin metal oxide on a metal substrate. In this example XPS data are collected from the metal at two angles, near normal (the “bulk angle”) and near grazing (the “surface angle”). Near normal emission produces a spectrum in which the metal peak dominates while the oxide peak dominates in the spectrum from the grazing emission. This is the basis for angle resolved XPS measurements.

## 2. CONVENTIONAL ANGLE RESOLVED XPS

In conventional ARXPS data, the angular acceptance range of the spectrometer is reduced to provide the required angular resolution. Clearly, there must a compromise between angular resolution and sensitivity (acquisition time). Spectra are then collected at each of a number of take off angles by tilting the specimen. An example of this type of experiment is shown in Figures 3 for a sample of GaAs which has a thin oxide layer at its surface.

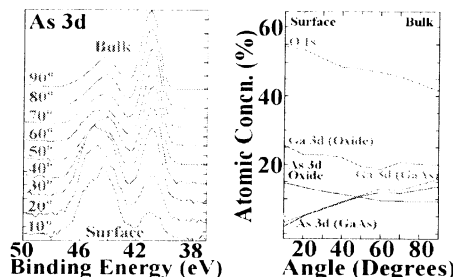
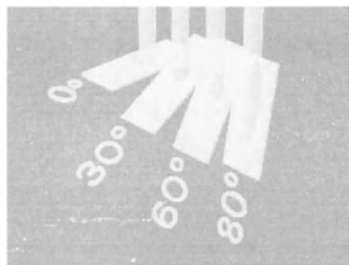


Figure 3 ARXPS experiment acquired by tilting the specimen. In this case the specimen is gallium arsenide.



*Figure 4 The analysis area changes as a function of angle, especially when using lens-defined small area analysis.*

In this set of data the angles were measured with respect to the sample surface. It is clear from the montage of As 3d spectra that the oxide peak is dominant at the surface whereas the peak due to As in the form of GaAs is more dominant at near normal analysis angles. This phenomenon is repeated in the gallium spectra, as can be seen from the atomic concentration curves in Figure 3.

The main limitation with the conventional method of ARXPS are:

- a) the analysis area changes as a function of angle as shown in figure 4.
- b) For Small Area ARXPS experiments :
  - i) at all angles, the analysis position would have to be accurately aligned with the feature to be analysed. This is difficult, especially if the analysis position is at some distance from the tilt axis and the required analysis area is very small.
  - ii) the analysis area changes as a function of angle, as can be seen in Figure 4. A worst case occurs when the transfer lens is used to define the analysis area.
- c) if an insulating sample is tilted the charge compensation conditions also change. Changes in peak position or shape may then be due to changes in the efficiency of charge compensation.
- d) it would be difficult to tilt large sample in a typical XPS system, especially if data is required from a region near the edge of the sample.

To over come these problems a new instrument, the Theta Probe has been developed by Thermo VG Scientific

### 3. THETAPROBE – PARALLEL COLLECTION OF ANGLE RESOLVED DATA

The Theta Probe is a major advance in analysis of Ultra Thin films by ARXPS. It features :

- 1 a two dimensional detector for multi-channel snap shot spectra
- 2 a Microfocus x-ray monochromator for maximum sensitivity in small area XPS
- 3 Parallel collection of angle resolved data for thin film analysis without tilting the sample
- 4 Chemical state and depth information at every analysis point, even from maps

Apart from the development of the high performance microfocus x-ray monochromator, the development of the Radian Spectrometer is a significant step forward in the field of thin film analysis.

In its angle resolving mode, Theta Probe is operated such that the electron kinetic energy is dispersed in one direction on its 2-dimensional detector and angular distribution in the other direction. Figure 5 shows an image of the detector when Theta Probe is being operated in this mode.

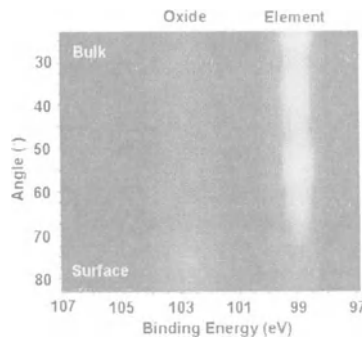


Figure 5 An image of the output from Theta Probe detector. This shows angular dispersion in one direction and energy dispersion in the other direction. The sample being analysed in this case is a silicon wafer with a thin layer of oxide on its surface.

A convenient method for illustrating the way in which Theta Probe lens operates is by means of an optical analogy.

#### **Analyser Energy Dispersion Plane**

Figure 6 shows the optical analogy for a two-lens system. Lens combinations of this type are frequently used as XPS transfer optics.

Photoelectrons emitted from the sample are focused by Lens 1 and form an image at Image Plane 1. A second lens, Lens 2, forms a photoelectron image of the sample at the analyser input slit. Electrons reach the slit plane at a point which is dependant upon their initial position at the sample. In this mode of operation the analyser slit plane is a second image plane.

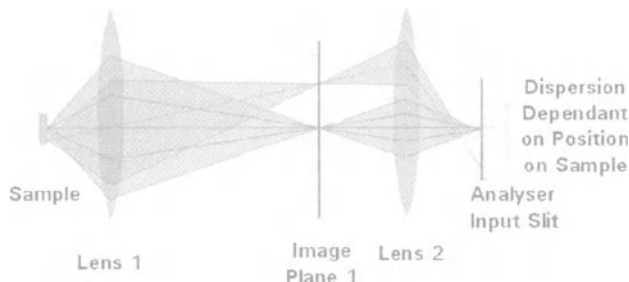


*Figure 6 The optical analogy for the energy dispersive plane of the transfer lens in the in Theta Probe.*

#### **Analyser Angular Dispersion Plane**

To obtain angular dispersion at the analyser slit plane, the focal length of Lens 2 must be changed. Figure 7 shows the requirement.

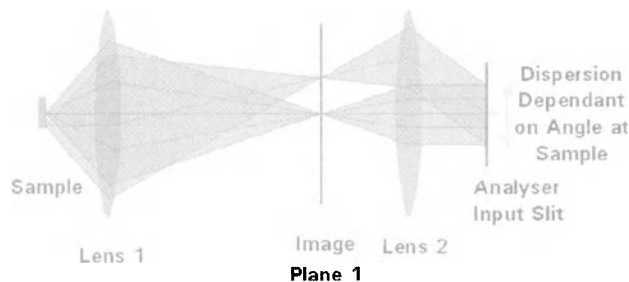


*Figure 7 The optical analogy for the angle dispersive plane of the transfer lens in Theta Probe.*

The focal length of Lens 2 needs to be set such that it is equal to the distance between Image Plane 1 and Lens 2. As can be seen from Figure 7, this means that the position at which the electrons reach the slit plane is independent of their initial position on the sample but is dependent upon the angle at which they leave the sample surface, i.e. a diffraction image is formed at the analyser slit plane.

This is the means by which the angular distribution of the electrons as they leave the sample surface is converted to spatial distribution at the input to the analyser in the angular dispersive plane.

The hemispherical analyser on Theta Probe is a focusing element as well as an energy filter and so the angle and position of the electrons as they enter the analyser is mirrored at the exit plane.

#### **Practical Implementation**

When Theta Probe is operated in its angle resolving mode, the electron optical system is similar to Figure 6 in the energy dispersive plane and similar to Figure 7 in the non-dispersive plane.

For optimum performance, Lens 1 in Theta Probe is designed to have two important features.

1. It must collect photoelectrons over a wide angular range to allow angular measurements to be made from near normal to near grazing angles. This also maximises sensitivity.
2. It must be operated at high magnification to keep the angle of the electrons into Lens 2 as small as possible.

For these reasons Lens 1 has a large diameter and a maximum collection angle of 60°. It is designed to operate with a magnification of 4 so that the angular range of electrons into Lens 2 is  $\pm 7.5^\circ$ .

Lens 2 is designed to be capable of providing a different focal length in each plane.

Taking into account the focusing properties of the analyser, the electrons are then dispersed onto the two-dimensional detector such that in one direction the position on the detector is determined by the kinetic energy of the electrons and, in the other direction the position on the detector is determined by the angle at which the electrons left the sample surface in the angular dispersive plane.

### ***Compound Angles***

A photoelectron emitted at an angle  $\gamma$  with respect to the surface normal, see Figure 8, is likely to have components of its direction in both the energy dispersive plane ( $\alpha$  in Figure 8) and the angular dispersive plane ( $\beta$ ). This electron will reach the detector at position which depends upon its total kinetic energy and the angle  $\beta$ . The position of the detected electron is totally independent of  $\alpha$ .

The maximum value for  $\beta$  is 30° and for  $\alpha$  is about 2.5° when Theta Probe is operated in its angle resolving mode.

### ***Example 1***

The following data were collected using Theta Probe. In this instrument ARXPS can be performed without tilting the sample. Using its two-dimensional detector energy dispersion can be obtained in one direction and angular dispersion can be obtained in the other.

A set of angle resolved data was collected using Theta Probe from a thin layer of silicon dioxide on silicon. The silicon 2p region of the spectra is shown in Figure 9.

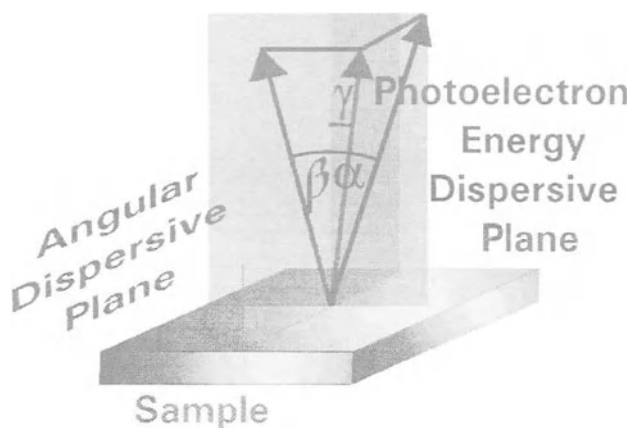


Figure 8 Components of the emission angle in the energy dispersive and angular dispersive planes.

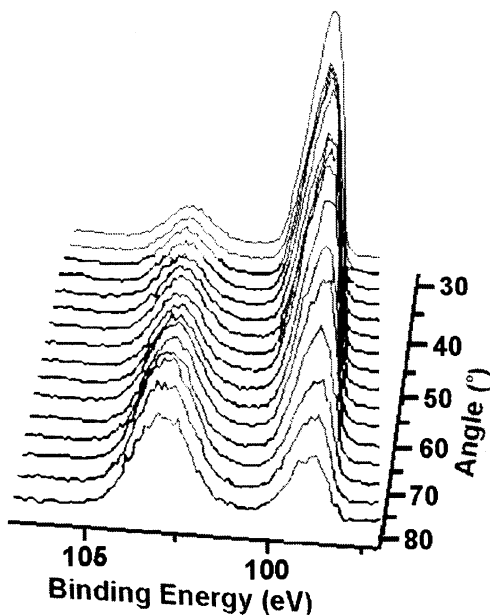


Figure 9 Montage of silicon spectra from a thin layer of silicon dioxide on silicon. Each spectrum is collected from a different angle. The low binding energy peak is due to elemental silicon and the peak at higher binding energy is due to silicon in the form of its oxide.

Data was collected from a number of samples where the oxide thickness was known, from ellipsometry, and the appropriate graph plotted, using only the angles close to normal emission. The graphs may be seen in Figure 10.

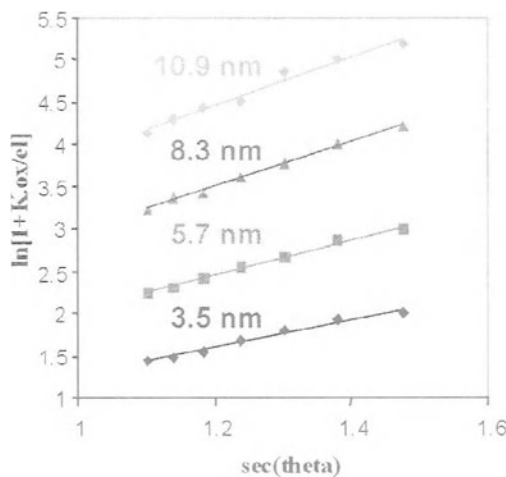


Figure 10 Graph showing linearity of the calibration plots for a set of  $\text{SiO}_2$  on Si samples which have a range of different oxide thicknesses.

If the gradients of these lines ( $d/\lambda$ ) is plotted against the known thickness of the oxide then we can calculate the attenuation length,  $\lambda$ . This is shown in Figure 11.

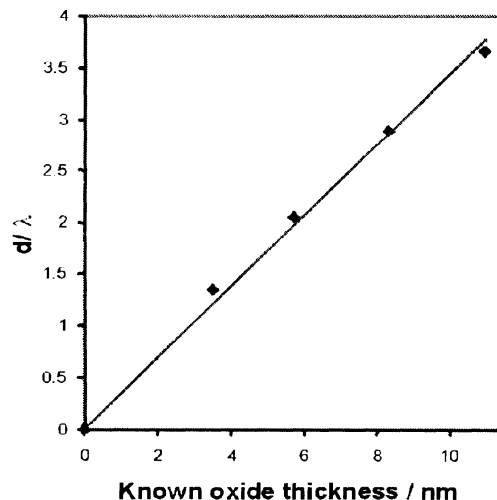


Figure 11 The gradients in Figure 8 are shown plotted against the known oxide thickness to allow the calculation of the attenuation length  $\lambda$ .

From these data  $\lambda$  is calculated to be 2.86 nm. This value can now be fed back into the expression for an unknown sample to calculate the thickness of the oxide.

### **Example 2      Measurement of Multilayers using ARXPS**

For a material with a single overlayer (e.g. silicon dioxide on silicon) :

$$\ln[1+KR] = d/\lambda \cos\theta \quad (2)$$

Where K is the ratio of the atomic densities, R is the ratio of the signal from the overlayer and substrate, d is the overlayer thickness,  $\lambda$  is the attenuation length of the electrons and  $\theta$  is the emission angle of the electrons with respect to the surface normal. If  $\ln[1+KR]$  is plotted against  $\sec\theta$  ( $1/\cos\theta$ ) then the gradient is  $d/\lambda$ .

In the case of the oxide / nitride / element we can assume a simple two overlayer structure, and extend the method to determine both the nitride thickness and the oxide thickness.

If equation (2) is applied to the signal intensity ratios of silicon nitride and elemental silicon The ratio of nitride / element gives a straight line plot with gradient =  $d_{\text{nitride}}/\lambda$ .

If the oxide / element ratio is used in the plot then a straight line plot is obtained with gradient which, to a close approximation, is given by  $(d_{\text{nitride}}+d_{\text{oxide}})/\lambda$ .

A typical spectrum from an oxide/nitride overlayer is shown in Figure 12. This is a spectrum from a single angle and one sample.

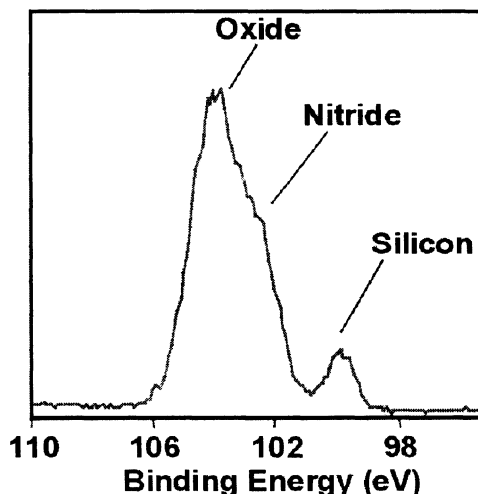
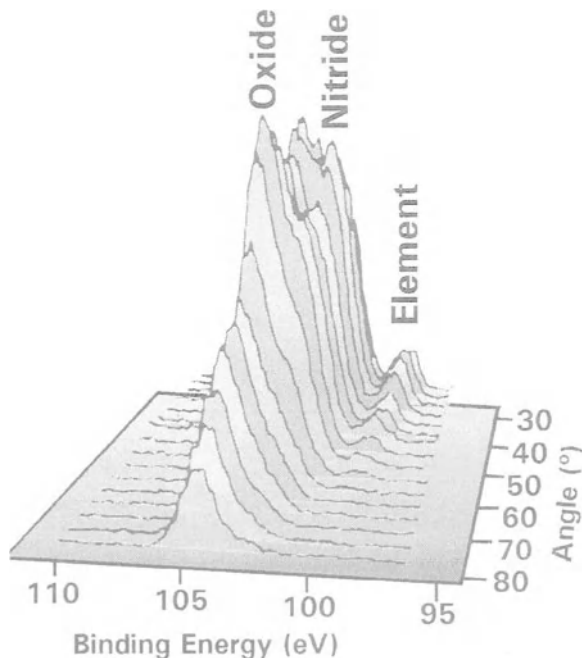


Figure 12 Example of the Si 2p region of the XPS spectrum from silicon nitride/oxide layers on silicon. The emission angle used for this spectrum was 25°.

This spectrum shows how the elemental, oxide and nitride components of the Si 2p spectrum can be resolved and therefore used to generate plots of  $\ln[1+KR]$  vs.  $\sec\theta$  where the K and R values are those corresponding to the appropriate overlayer / substrate model. The relative intensities of each of the components are obtained by peak fitting.

The montage of spectra, shown in Figure 13, is from a single sample but from the full range of angles available from Theta Probe. It illustrates how the components of the Si 2p spectrum are affected by the emission angle.



*Figure 13 Montage of Si 2p spectra from a silicon oxide / nitride sample showing how the spectrum changes as a function of angle.*

Spectra similar to those shown in Figure 13 were acquired from each of four samples.

The appropriate intensity ratios, described above can be plotted on the appropriate graph. From the gradient of these graphs the values for  $d/\lambda$  were calculated and, knowing  $\lambda$ , the layer thicknesses were calculated.

This procedure was followed for the full set of samples and the layer thicknesses are shown in Figure 14.

ARXPS, as a method for calculating layer thicknesses, is not restricted to single thin layers on a substrate. Using the correct analysis procedure, more complex samples can be measured.

All of the above angular data was collected using parallel collection which is available on Theta Probe. These oxide / nitride layers are insulators and so the data can be collected with greater confidence than if sample tilt had been employed.

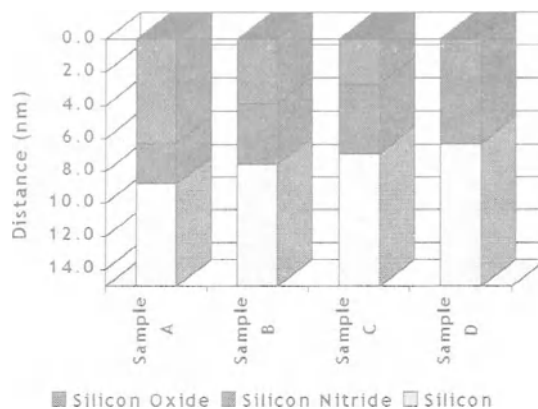


*Figure 14 Thicknesses of oxide and nitride layers for each of the four samples.*

### Conclusion

As can be seen from the above discussion, ARXPS is a technique which can provide information about near-surface layers to a depth of about 10 nm. As with conventional XPS, it also provides chemical state information. ARXPS can therefore provide information which is not available using other methods. Much of this falls into the category of non-destructive depth profiling.

When chemical state information is needed sputtering should not be used because the required information may be destroyed. ARXPS allows measurements to be made on buried interfaces without the need to sputter the sample.

For quantitative information from near surface features sputtering cannot be used. This is because there is a transient region of a few nanometers at the start of the sputtering process within which quantitative data is unreliable.

Atomic mixing causes depth resolution from sputtering methods to be insufficient unless very low energy ions are used.

Techniques such as ellipsometry and spectroscopic ellipsometry are capable of providing film thickness information but they are incapable of providing chemical state information. Indeed, using these methods it is essential to know the composition of the films before their thickness can be determined.

In the past ARXPS has not been used extensively because of the difficulty of performing the experiments. Now, using Theta Probe, most of the practical difficulties have been removed and ARXPS becomes viable as a routine analytical tool.

# NANOINDENTATION OF MICROSPRINGS AND MICROCANTILEVERS

Mary W. Seto, Brian Dick, and Michael J. Brett\*

## ABSTRACT

Unique, microstructured thin films have been fabricated with the Glancing Angle Deposition (GLAD) technique. This technique enables porous, columnar thin films with engineered microstructures to be grown with nanometer scale control. The morphology of the films tested included microsprings and microcantilevers, and some of their mechanical properties were studied using a nanoindentation technique. The geometries of the microsprings were varied, and a number of different materials were used to fabricate these films, which were typically a few micrometers thick. Arrays of slanted posts resembling micro-cantilevers were also subjected to nanoindentation tests over a range of forces. Results of initial experiments and theory show that these microstructures behave in a manner analogous to macroscopic springs and cantilevers, and may offer some insight into how materials behave at the microscale.

## 1. INTRODUCTION

For thin films grown with the GLAD technique<sup>1,2</sup> two main mechanisms dominate the growth process. Under conditions of highly oblique flux and low substrate temperature, the principal processes governing film growth are enhanced shadowing and limited adatom diffusion. Vapour atoms arriving from the source nucleate at the substrate and create an irregular topography, with higher areas physically shadowing areas behind them due to the oblique angle subtended by the substrate and source. Since the substrates are not heated, the diffusion length of the adatoms is limited, and the voided regions do not become filled. As the film evolves, the formation of nanometer scale, columnar structures occurs. Motion of the substrate then allows the growing micro-columns to be engineered with a variety of possible morphologies<sup>3-6</sup>.

---

\* Mary W. Seto, Brian Dick, and Michael J. Brett, University of Alberta, Department of Electrical and Computer Engineering, Edmonton, Alberta, Canada T6G 2V4.

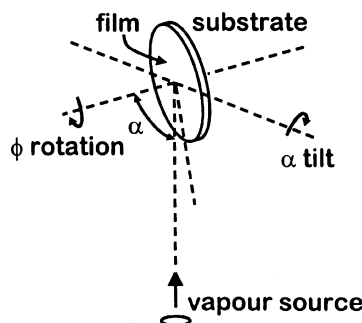


**Figure 1.** GLAD apparatus showing range of substrate motion.

The GLAD apparatus employs two computer controlled stepper motors that adjust the motion of the substrate. Rotation can occur about an axis perpendicular to the plane of the substrate, and the incident flux angle can be modified by tilting about an axis parallel to the plane of the substrate. This system can be utilized with thermal and electron beam evaporation, sputtering<sup>7</sup>, and laser ablation techniques<sup>8</sup>, allowing for a wide range of materials to be grown. Further details on the GLAD technique can be found in other literature<sup>9</sup>.

## 2. NANOINDENTATION: MICROSPRING EXPERIMENTAL DETAILS

The nanoindentations were performed with Hysitron's<sup>10</sup> Triboscope®, which employs a capacitive load-displacement transducer that allows for a wide dynamic range of forces to be utilized in sample testing. Forces from as low as 1  $\mu$ N to as high as 13 mN can be applied, using a variety of customizable force curves. The Triboscope® was operated with Digital Instrument's Dimension 3100 SPM, and enabled imaging of the sample prior to and following the indentations.

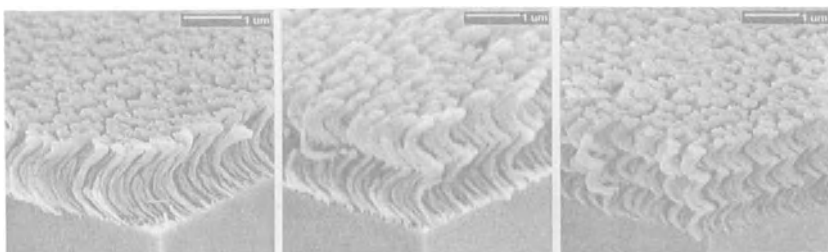


**Figure 2.** SEM images of SiO microspring thin films with one turn (a), two turns (b), and three turns (c) grown by thermal evaporation with the GLAD technique.

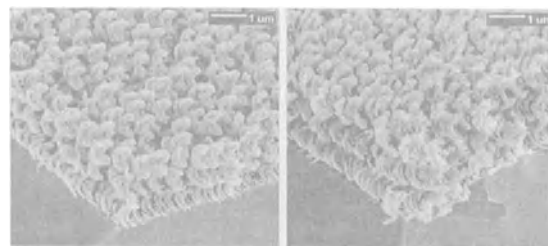


**Figure 3.** SEM images of additional three-turn microsprings of Ti (a) and Cr (b) films tested.

A number of SiO thin films were grown by thermal evaporation, with each film approximately 2  $\mu\text{m}$  in thickness. By rotating the substrate the desired number of times during the deposition (with higher rotational speeds for higher number of turns), the resulting thin films could be grown with the desired helical geometries. These included 1-, 2- and 3-turn microsprings with pitches of 1300 nm, 950 nm, and 600 nm, respectively. Other 3-turn microspring thin films of titanium (Ti) and chromium (Cr) were grown by electron beam evaporation also having thicknesses of approximately 2  $\mu\text{m}$ . Deposition rates for all of the films grown ranged between 10-20  $\text{\AA/s}$ .

The geometrical parameters of the helical films shown in Figures 2 and 3 are given in Table 1, with dimensions and areal number densities estimated from Scanning Electron Microscope (SEM) images. Tabulated values for Young's Modulus were taken from solid thin film values of the materials indicated and used as guides<sup>11,12</sup>.

For the amount of deflection that was made by the nanoindenter into the films (typically 60-70 nm), the high porosity of the films likely resulted in the microsprings that acted independently. Cross-sectional and plan view SEM images confirmed that the spacing between neighboring springs was large enough to allow low force nanoindentations to be made. These resulted in displacements that were lower than the spring spacing, and ensured that no interaction occurred between adjacent springs.

**Table 1.** Geometrical parameters of the microspring thin films tested.

Thin Film Sample	Film Height ( $\mu\text{m}$ )	Nominal Column Diameter (nm)	Nominal Coil Radius (nm)	Young's Modulus (GPa)	Poisson's Ratio	Areal Number Density (#/ $(\mu\text{m})^2$ )	Rise Angle (deg)
SiO (1 turn)	1.3	115	280	92	0.3	10	37
SiO (2 turns)	1.9	110	190	92	0.3	10	39
SiO (3 turns)	1.8	110	165	92	0.3	10	30
Ti (3 turns)	2.4	115	200	110	0.34	15	33
Cr (3 turns)	1.8	150	190	140	0.21	3.2	27

A spherical diamond indenter tip with a 100  $\mu\text{m}$  radius of curvature was used to apply forces ranging from 20  $\mu\text{N}$  to 1000  $\mu\text{N}$ . The indenter's large radius of curvature also enabled elastic deformations of these films to be studied under the low force indentations, where displacements made into the film were less than 5% of the total film thickness.

A cylindrical flat punch sapphire tip with a foot area of 0.785 ( $\text{mm}^2$ )<sup>2</sup> was used in additional nanoindentations of these films, but due to inhomogeneities in the films at the larger scales associated with this particular tip, the effect of surface irregularities and debris thwarted the assessment of microstructure properties.

### 3. RESULTS AND DISCUSSION

#### 3.1 Microspring Nanoindentations

Results from typical nanoindentations for the microspring thin films pictured in Figures 2 and 3 are shown in Figure 4. A comparison of the displacement curves for a standard, dense SiO film to those of the porous microsprings shows a marked difference in stiffness between these films. The dense film was found to be approximately  $10^3$  times stiffer than the porous microspring thin films, requiring a significantly higher amount of force to displace it by the same amount. Low force indentations performed successively at the same site in the microspring films produced the overlapping curves shown in Figure 4(b), and indicated that the indentations were reproducible and not destructive to the films.

A separation between 1-, 2-, and 3-turn microspring films for various applied forces is shown in the displacement curves in Figure 4(a), with film stiffness increasing with a greater number of turns. This scaling could be predicted from the macroscopic spring constant ( $k$ ) given by Equation 1<sup>13</sup>. A reasonable estimate of the microspring stiffness could be obtained using the macroscopic formula. Detailed SEM images allowed microspring geometries to be evaluated, and an estimated areal number density of approximately 10 microsprings per ( $\mu\text{m}^2$ )<sup>2</sup> was determined. The spring constant,  $k$ , for a helical spring is given by:

$$k = \frac{Gd^4}{64R^3n} \left[ 1 - \frac{3}{64} \frac{d^2}{R^2} + \frac{3+v}{2(1+v)} \tan^2(\alpha) \right]^{-1} \quad (1)$$

where  $G$  is the Shear modulus ( $G=E/[2(1+v)]$  where  $E$  is Young's Modulus),  $d$  is the column diameter,  $R$  is the coil radius,  $n$  is the number of turns,  $v$  is Poisson's ratio, and  $\alpha$  is the rise angle.

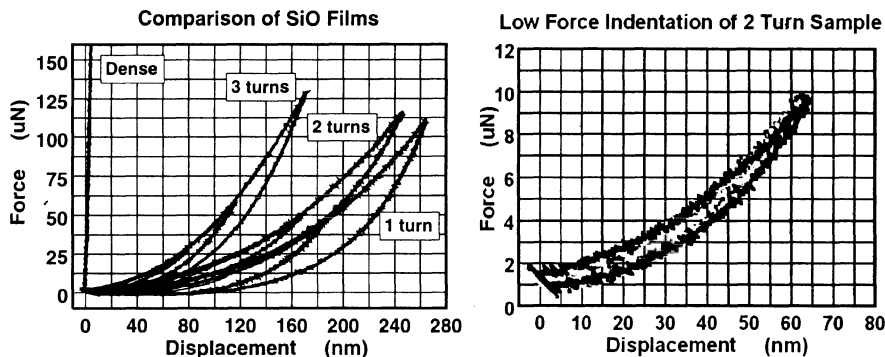


**Figure 4.** Force vs displacement results showing the trend in the curves for various microspring geometries in (a), and the results of three low force indentations carried out successively at the same site in (b).

Films with the same microspring geometry but composed of different materials were studied for 3-turn SiO, Ti, and Cr microsprings. These films did show a stiffness that was material dependent (Table 2) and could again be resolved from the macroscopic formula. The spring geometry also has a definite bearing on the resultant spring constant as shown by the results in Table 2. The trend shown is useful for determining spring geometries that may yield more easily than others, and is ultimately useful in assisting in the design of theoretically postulated devices.

There was some discrepancy in the magnitude of the experimental and theoretical areal stiffnesses present. This was likely due to inaccuracies in determining *exact* microspring dimensions from the SEM images, as a small error in determining the coil radius ( $R$ ) or column diameter ( $d$ ) would be augmented by the 3<sup>rd</sup> and 4<sup>th</sup> powers for  $R$  and  $d$  in Equation 1. The formula above also assumes a constant column diameter, whereas the actual thin film microsprings exhibit a distinctive shape anisotropy, with the column thickness increasing towards the top of the column<sup>14,15</sup>. This broadening effect was taken into account in initial simulations performed using ANSYS® finite element modeling software<sup>16</sup>. Each of the different microsprings was modeled using an initial column thickness that increased linearly to a final column thickness. The values for these thicknesses were obtained from cross-sectional SEM images of the films. Preliminary results revealed that the deflection of a thickening microspring was consistent with experimental deflections obtained for the thin film microsprings. With more accurate approximations of the real shape of the microsprings, values in better agreement with experimental results would be expected. Additional work is underway to further model the shape anisotropy of these films, and in experimental studies to eliminate the anisotropy.

**Table 2.** Comparison of experimental and theoretical areal stiffness values for various thin film samples.

Thin Film Sample	Experimental Areal Stiffness (N/m)/(μm) <sup>2</sup>	Theoretical Areal Stiffness (N/m)/(μm) <sup>2</sup>
SiO (1 turn)	10.0	27
SiO (2 turns)	11.3	32
SiO (3 turns)	17.8	42
Ti (3 turns)	19.8	47
Cr (3 turns)	21.2	56
SiO (Dense)	18500	N/A

### 3.2 Nanoindentation of Microcantilever Array

Periodic nickel (Ni) microcantilevers were grown by electron beam evaporation on a pressed plastic array having a 2 μm periodicity (Figure 5). This allowed for a film with increased porosity to be fabricated. Film growth occurred primarily on the raised plastic “seeds” and not in the areas between them due to shadowing from adjacent seeds when fabricated under oblique incidence angles. An ordered array of microstructures could then be fabricated which followed the periodicity enforced by the seeded substrate<sup>15,17,18</sup>. Some material can still be found in the areas between the artificial nucleation sites, due to the amount of shadowing received from nearby seeds. Depending on how the seeded array is positioned relative to the direction of incoming flux and on what angle of incidence is used for the deposition, the size of shadowed region may not be large enough to prevent small amounts of film growth between the seeds.

The size of the seed elements (approximately 250 nm in diameter) affected the resulting column size of the microstructure grown on it, as the typical width of the microcantilevers was found to be approximately 300 - 400 nm. The number of microstructures per (μm)<sup>2</sup> was also easily determined for this film (0.25 posts/(μm)<sup>2</sup>), and it allowed theoretical values to be calculated with better accuracy.

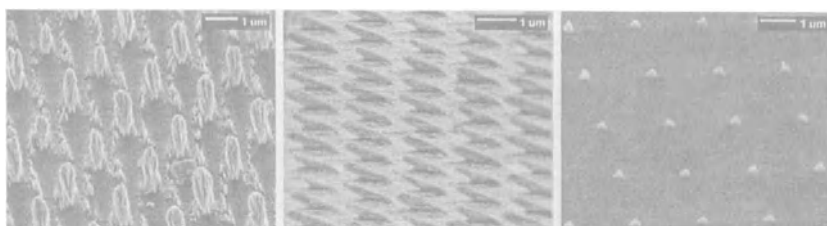


**Figure 5.** Pressed plastic array with a period of 2 μm shown in (a) and with a Ni film grown on it shown in (b) and (c).

The cross-section of the microcantilevers was assumed to be approximately rectangular, and this geometry was used to estimate the theoretical displacements using Equation 2<sup>19</sup>. Experimental displacements agreed well with the predicted displacements (Figure 6). The simplified microstructure enabled the dimensions to be determined more precisely, and no significant shape anisotropy of the slanted posts could be observed in the microcantilevers. The displacement,  $\Delta x$ , can be determined by:

$$\Delta x = \frac{FL^3 \cos^2(\alpha)}{3EI} \quad (2)$$

where F is the applied force, L is the cantilever length,  $\alpha$  is the rise angle, E is Young's modulus, and I is the moment of inertia (for a rectangular cross-section,  $I = wt^3/12$ , where w is the width and t is the thickness).

Predicted displacements for the microcantilevers corresponded well with experimental displacements (Figure 6). At higher loads, larger calculated displacements were determined in comparison to experimental ones. More stress would be placed on the microcantilevers at higher loads, and there could be issues with how it would be distributed along the microcantilever or at the substrate junction where details of attachment are not well known.

**Table 3.** Geometrical parameters of the microcantilever array tested.

Thin Film Sample	Length ( $\mu\text{m}$ )	Width (nm)	Thickness (nm)	Rise Angle (deg)	Young's Modulus (GPa)	Moment of Inertia ( $\mu\text{m}^4$ )	Experimental Spring Constant (N/m)/( $\mu\text{m}$ ) <sup>2</sup>	Calculated Spring Constant (N/m)/( $\mu\text{m}$ ) <sup>2</sup>
Ni Cantilevers on Array	1.2	500	250	27	200	6.5e-4	83	72

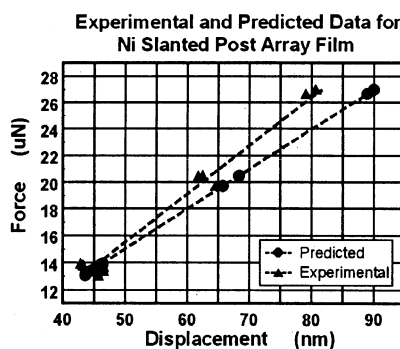


**Figure 6.** Comparison of experimental and predicted displacements for the Ni slanted post array.

## 5. CONCLUSIONS

A selection of thin film microstructures and materials were tested with nanoindentation experiments. For microsprings and microcantilevers grown using the GLAD technique, their mechanical properties could be predicted from macroscopic theory. Some divergence existed between calculated and experimental values, likely a result of difficulties in determining actual microstructure geometries, and with complexities associated with materials behavior at the size scales involved. Further work is in progress to fabricate improved microstructures and simulate non-ideal film geometries. From optimizing the material, geometry and dimensions of these films, much potential exists for developments to be made using GLAD-fabricated thin films.

## 6. ACKNOWLEDGEMENTS

The authors would like to acknowledge support from NSERC, the University of Alberta Microfab, Micralyne and Hysitron. Valuable assistance from George Braybrook for the excellent SEM images, and C. Bastiaansen and I. Votte for the provision of the imprinted plastic substrates is also recognized.

## 7. REFERENCES

1. K. Robbie, L. J. Friedrich, S. K. Dew, T. Smy, and M. J. Brett, *J. Vac. Sci. Technol. A* **13**, 1032 (1995).
2. K. Robbie, and M. J. Brett, *J. Vac. Sci. Technol. A* **15**, 1460 (1997).
3. K. Robbie, M. J. Brett, and A. Lakhtakia, *J. Vac. Technol. A* **13**, 2991 (1995).
4. K. Robbie, C. Shafai, and M. J. Brett, *J. Mater. Res.* **14**, 3158 (1999).
5. A. Lakhtakia, R. Messier, M. J. Brett, and K. Robbie, *Innovations in Materials Research* **1**, 165 (1996).
6. K. Robbie and M. J. Brett, U.S. Patent # 5,866,204.
7. J. C. Sit, D. Vick, K. Robbie, and M. J. Brett, *J. Mater. Res.* **14**, 1197 (1999).
8. D. Vick, Y. Y. Tsui, M. J. Brett, and R. Fedosejevs, *Thin Solid Films* **350**, 49 (1999).
9. K. Robbie, J. C. Sit, and M. J. Brett, *J. Vac. Sci. Technol. B* **16**, 1115 (1998).
10. Hysitron, Inc., <http://www.hysitron.com>.
11. A. Wolfenden, *Dynamic Elastic Modulus Measurements in Materials* (American Society of Testing Materials, Philadelphia, PA, 1990), P. 14.
12. B. Halg, *IEEE Micro Electro Mechanical Systems Workshop*, Napa Valley, CA, 172 (1990).
13. R. Roark, *Roark's Formulas for Stress and Strain*, 6<sup>th</sup> ed. (McGraw-Hill, New York, 1989), p. 386.
14. F. Liu, M. T. Umlor, L. Shen, J. Weston, W. Eads, J. A. Barnard, and G. J. Mankey, *J. App. Physics* **85**, 5486 (1999).
15. M. Malac, R. F. Egerton, M. J. Brett, and B. Dick, *J. Vac. Sci. Technol. B* **17**, 2671 (1999).
16. ANSYS, Inc., <http://www.ansys.com>.
17. B. Dick, M. J. Brett, T. J. Smy, M. R. Freeman, M. Malac, and R. F. Egerton, *J. Vac. Sci. Technol. A* **18**, 1838 (2000).
18. B. Dick, J. C. Sit, M. J. Brett, I. M. N. Votte, and C. W. M. Bastiaansen, *Nano Letters* **1**(2), 71 (2001).
19. F. Kreith, *The CRC Handbook of Mechanical Engineering*, (CRC Press Inc., Boca Raton, 1998), p. 1-83.

# **PHYSICAL AND INTERFACIAL PROPERTIES OF LOW PERMITTIVITY POLYMERS: SILK\* AND ULTRA-LOW K**

D.C. Frye\*\*, J.J. Waeterloos, M. Simmonds, T. Stokich, J. Im

## **1. INTRODUCTION**

In the last 5 years, the requirement for low k polymer dielectric in on-chip interconnects has resulted in a considerable effort by both material and tool suppliers in product development, thin film characterization and process integration development. The acceleration of the ITRS roadmap and company-specific integration requirements imposes very specific property requirements onto the low k dielectrics. SiLK\* Semiconductor Dielectric was developed specifically to accommodate the needs imposed by high performance interconnect systems fabricated using either a subtractive Al/W [1] and Cu [2,3] damascene architecture. Besides faster clock speeds, ICs need denser I/O to get this information on and off the chip faster and faster. Low k polymers, Cyclotene\* Advance Electronics Resin (BCB) are also being used to build these dense arrays of bond pads and bumps[4].

In this article, we will review some of the key topics related to low k's material properties, and how they can be used to their advantage during the development of integration modules for Flip Chip and Dual Damascene (DD).

There are families of for low k dielectrics but they can mostly be broken into two categories: 1. Spin on Dielectric (SOD). 2. CVD Silica glasses. In this paper we will focus on Spin on Polymer (SOP) based solutions, in particular organic polymers. The reasons we choose to focus on polymers are listed in increasing importance [5].

1. Polymers have sufficient thermal stability.
2. Polymers are compatible with current integration technology.
3. Polymers have a mature material technology.

---

\* Trademark of The Dow Chemical Co.

\*\* 1714 Building, The Dow Chemical Co., Midland, MI 48674

*Metallization of Polymers 2.*

Edited by Edward Sacher, Kluwer Academic/Plenum Publishers, 2002

4. Polymers have the lowest Cu drift rate.
5. Significant performance improvement.
6. Polymers are extendible to Ultra-Low K.

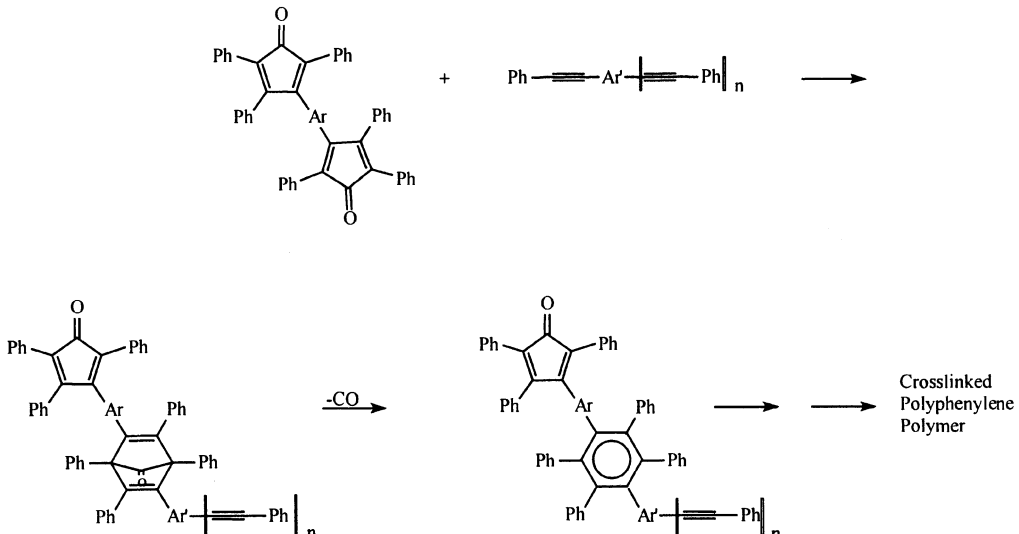
## 2. LOW PERMITTIVITY POLYMER PROPERTIES

Table one lists several potential candidates for low permittivity polymers.

**Table 1.** Potential Low permittivity polymers.

Benzocyclobutene (BCB)	2.7
Fluorinated Polyimide (FPI)	2.5 - 2.9
Perfluorocyclobutane (PFCB)	2.6 - 2.9
Polybenzoxazole (PBO)	2.6 - 2.9
Polypheylene (SiLK)	2.6

SiLK dielectric has been adopted for use in over 33% of the chips at the 0.13 micron technology nodes[6]. BCB is used in many advance packaging and LCD applications. The other materials are not currently used in any high volume applications. The SiLK polymer structure is given in Figure one. As shown in figure one, SiLK polymer is a highly crosslinked polyphenylene polymer.



**Figure 1.** The SiLK polymer structure and polymerization reaction. [7]

After the SiLK polymer is fully cured we can expect from the above structure that the polymer will be isotropic, have low moisture adsorption, be highly crosslinked and very thermally stable. Table two lists the physical properties of the fully cured SiLK

polymer. SiLK resin comes in several different versions: I, J and H. SiLK I is for damascene applications and it required a separate primer layer. SiLK J is self-priming and can be used for damascene application. SiLK H is used for gap fill applications.

**Table 2.** The SiLK polymer physical properties.

Thermal stability @ 450C	< 1% wt loss at 450C
Glass Transition	>490C
k-value @ 1MHz	2.6
Refractive index @ 633 nm	1.6278 out-of-plane
Moisture uptake at 80%RH	<0.24wt.%
CTE	62 ppm/C (50-150C)
Film stress at RT	60 MPa (tensile)
Toughness	0.62 MPa m <sup>1/2</sup>
Thermal conductivity	0.23 W/mK @ 125C
Breakdown voltage	>4MV/cm
Interline leakage current	<50pA at 1MV/cm
Modulus, indentation	3.6(3)GPa
Hardness, indentation	0.29(8)GPa
Tensile Strength	93(3.5)MPa
Elongation to break	12(1.5)%

In addition to SiLK polymer, BCB is used for LCD and advance packaging applications. Table three lists the physical properties for BCB. BCB has similar dielectric properties of SiLK, but it has lower thermal stability and lower cure temperature.

**Table 3.** Physical properties of Cyclotene.

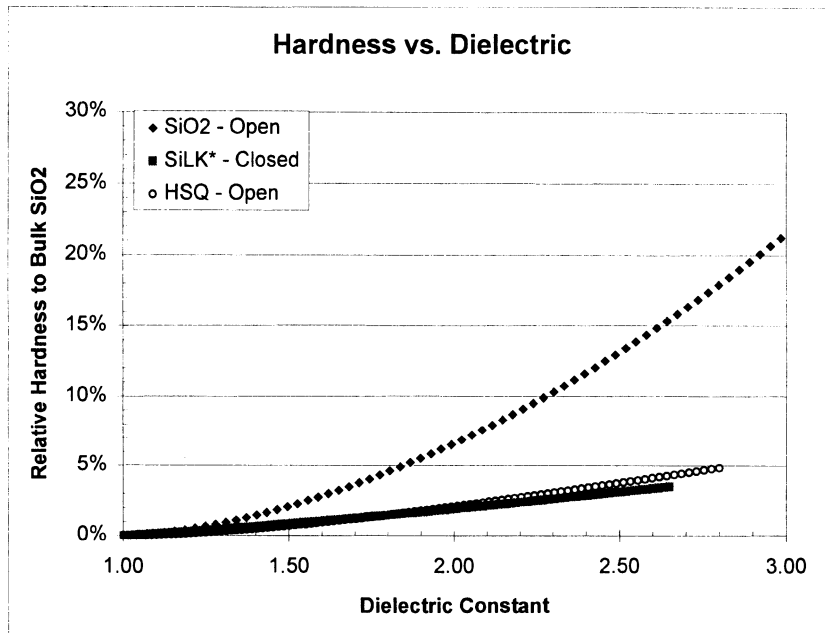
Dielectric Constant (1 KHz - 20 GHz)	2.65
Dissipation Factor (1 KHz - 1 MHz)	0.0008
Breakdown Voltage (V/cm)	$3 \times 10^6$
Volume Resistivity (ohm-cm)	$1 \times 10^{19}$
CTE (ppm/ $^{\circ}$ C)	52
T <sub>g</sub> ( $^{\circ}$ C)	>350
Tensile Modulus (GPa)	$2.9 \pm 0.2$
Tensile Strength (MPa)	$87 \pm 9$
Elongation at Break (%)	$8 \pm 2.5$
Poisson's Ratio	0.34
Residual Stress on SiO <sub>2</sub> at 25 $^{\circ}$ C (MPa)	28

### 3. CHALLENGES TO USING POLYMERS

A few of the challenges to using polymers as an intermetal or interlayer dielectric for semiconductors are:

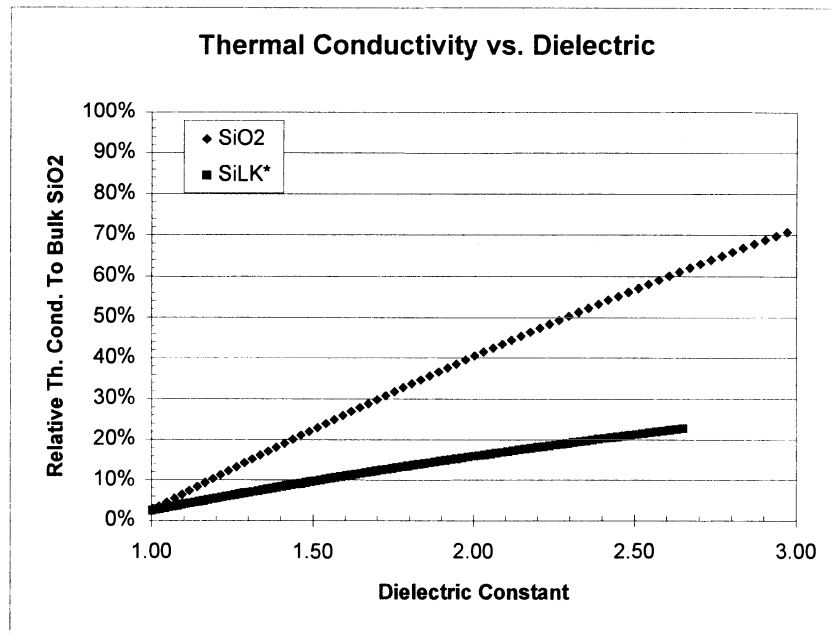
1. Lower Mechanical Properties than Oxide
2. Lower Thermal Stability than Oxide
3. Lower Thermal Conductivity
4. Higher Gas Permeation

Figure two shows the variation of hardness with dielectric constant. The dielectric constants are calculated by varying the porosity of the film.



**Figure 2.** Relative Hardness of Ultra Low K's with respect to SiO<sub>2</sub>.

In figure two we see that as you approach a dielectric constant of 2.0; SiO<sub>2</sub>, HSQ and SiLK polymer based materials have very similar hardness values. In figure three we see the same trend, that all the thermal conductivities approach the same value at low dielectric constants.



**Figure 3.** Relative thermal conductivity of low –ks with respect to SiO<sub>2</sub>.

These figures show that as the dielectric constants of these materials approach 2.0 many of the mechanical and thermal properties approach similar values for the polymer and SiO<sub>2</sub> based materials. These properties have typically been the weaker properties for polymers, but now we find them to be equivalent to the inorganic materials.

#### 4. COPPER DUAL DAMASCENE

##### 4.1. Coat & Cure

The coat and cure process is similar for SiLK H, I and J. Here we will describe the process for I and J. The process for H is very similar to the one for I. Table four lists the spin coating process for SiLK I and J.

**Table 4.** Coat & Cure step list

Process Step	SiLK I	SiLK J
Dispense Promoter	Yes	No
Bake Promoter @ 185°C for 60secs	Yes	No
Dispense SiLK	Yes	Yes
Bake SiLK @ 325°C for 90 sec	Yes	Yes
Cure SiLK on Hot plate or furnace	Yes	Yes

The cure can be done in a furnace or on a hot plate. In the furnace, the baseline Cu DD recommendation is to bring the wafers to 400°C for 30 minutes. On the hot plate you need to keep the wafer on the hotplate at 450°C for 3 to 5 minutes. The time on the hotplate can vary depending upon the hotplate design. All of the furnace and hot plate bakes above 200°C must be done in an inert environment.

#### 4.2. Hardmask Or Etchmask Deposition

Typically silane based SiO<sub>2</sub> hardmask are used adjacent to the SiLK [8] layer. Recently, SiC has also become popular as a hardmask material. Additionally, NEC recently published a paper using nitride as the etchmask directly adjacent to the SiLK [9] layer. Most companies have switch to a bilayer hardmask integration scheme [2,9].

#### 4.3. Etch & Clean

The etch of SiLK films can be done with oxidation or reduction chemistry [10,11]. Figure 5 shows a picture of an etch done with TEL's DRM etcher. The photoresist is usually striped during the SiLK etch, but can be striped by a combination dry and wet process.

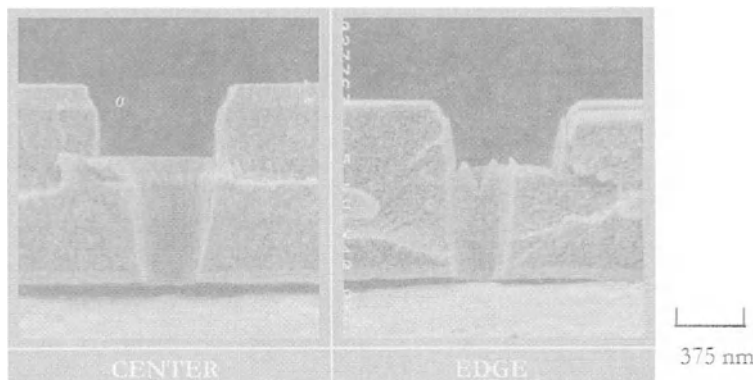
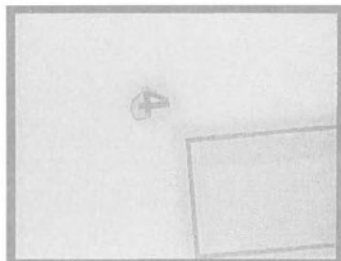


**Figure 5.** An example etch done in a TEL DRM etcher, photograph courtesy of TEL.

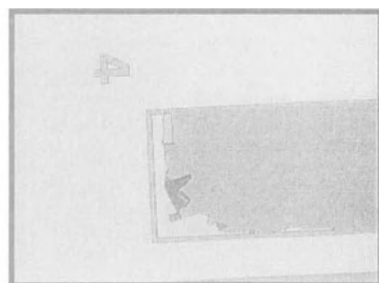
The wet clean process can be done with many different chemistries. Most can be made to work. There are two key steps: A.. Add a post bake after solvent exposure. B. Use AP4000 or SiLK J. Figure six demonstrates these two steps, A & B. The post bake will restore the film to its original thickness. The AP4000 will prevent delamination of the SiLK film.

Challenge: A. Solvent Swelled the Film.



Solution: A. Post Clean Bake.

B. Loss of Adhesion.



B. Use AP4000 or SiLK J resin.

**Figure 6.** Wet Clean Demonstrations.

**Table 5.** A chart of hardmask adhesion after wet clean.

Wafer ID	OX	SiON	SiLK	SiN	OX	SiON	SiLK	SiN	OX	SiON	Kc, MPa-m <sup>1/2</sup>		Wet Clean (ST-250)
											Avg	St. Dev.	
2			x	x							0,31	± 0,02	survived
3			x		x						0,24	± 0,01	delaminated
4			x			x					0,22	± 0,01	discolored
5	x		x	x							0,31	± 0,02	survived
6		x	x	x							0,32	± 0,02	survived
7			x	x			x	x			0,33	± 0,02	survived
8			x	x			x		x		0,19	± 0,02	delaminated
9			x	x			x			x	0,33	± 0,03	discolored

**Table 6.** Atomic percent values measured by XPS

Sample	Side	O(1s)	N(1s)	C(1s)	Si(2p)	[pi-pi*]/C(1s)	Assignment
Std. SiLK	-	2.3	0	97.6	0	0.104	SiLK
3	Substrate	12.2	0.0	87.8	0.0	0.080	SiLK Si oxide
	Thin Film	44.7	1.3	34.2	19.8		
8	Substrate	4.1	0.4	95.4	0.1	0.091	SiLK Si oxide
	Thin Film	44.7	1.3	34.2	19.8		
11	Substrate	5.8	0.6	93.3	0.1	0.084	SiLK Si oxide
	Thin Film	51.2	1.6	24.2	23.1		
14	Substrate	3.6	0.1	96.2	0.0	0.092	SiLK Si oxide
	Thin Film	51.0	1.2	25.0	22.8		

In Table five we see that oxide containing hardmask films delaminate after wet clean. The oxide deposition recipes used in this study were not optimal and it was found that the early stages of the depositions lead to oxidation of the SiLK surface. From the data in Table five we see that the films made using reduction chemistry did not delaminate during wet clean and had high adhesion. Table six shows the XPS atomic percent values from the two surfaces of the hardmask polymer interface after delamination. In Table six we see the proof that the Oxide CVD process caused surface oxidation. This was fixed by the proper CVD recipe, and the adhesion stayed high for oxidation and reduction chemistries. Many papers have shown the good adhesion between SiLK and inorganic hardmask [12].

## 5. ULTRA LOW K, POROUS SILK

Many challenges exist for integrating porous materials into a standard semiconductor process. Figure seven illustrates a few of the challenges[13].

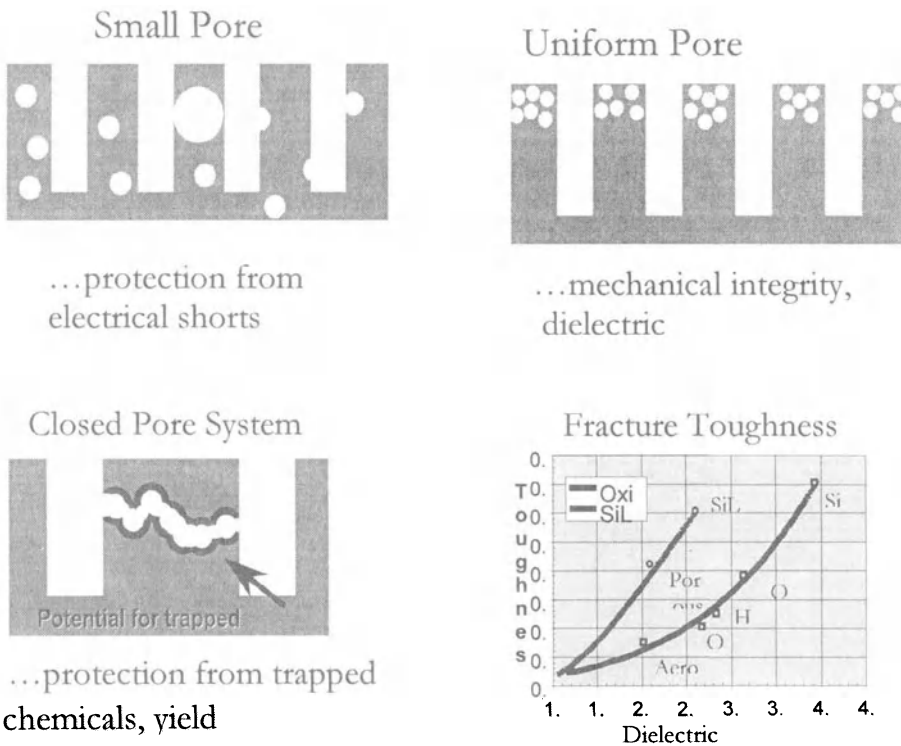


Figure 7: Challenges of Porous Dielectrics

In figure 7 we see the need for small pore sizes, or a large pore could cause a short between the metal lines. Plus, we see that uniform porosity is needed to ensure that each metal line sees a uniform dielectric. In addition we see that an open pore system provides a path for shorts to form and a site for trapped process chemicals. Finally we see that a low k polymer based matrix will always lead to better fracture toughness than a SiO<sub>2</sub> based matrix.

Porous SiLK was shown to be integratable. In particular they found good electricals and survivability after CMP[14].

## 6. CONCLUSIONS

In this paper we have shown that polymers have a blend of properties that make them integratable into semiconductor processes. We have shown examples from several unit operations in the process to make semiconductor chips using the current version of SiLK. Not only do polymers provide good dielectrics today, but also provide a good route to the ultra-Low-K<sub>s</sub> dielectrics of tomorrow. As materials are scaled to lower dielectrics many of the mechanical properties become equivalent between the classes of materials, except the toughness where the polymers always retain their advantage.

## 7. REFERENCES:

1. J. Waeterloos et al, AVS 99 Proceedings, San Francisco.
2. R.D. Goldblatt et al, IITC 2000 Proceedings, San Francisco.
3. J. Waeterloos et al, European Semiconductor, August (1999).
4. J. Im et al, SEMI Technical Symposium, Semicon Korea (2001).
5. M. Mills et al, SEMI Technical Symposium, Semicon West (2001)
6. Klein Report, Low K Dielectrics (2001).
7. S. Martin et al, Development of a Low k Polymer for Fabrication of IC Interconnects, *Advance Materials* 12 (23) p. 1769-1778 (2000).
8. S. Allada, IITC 99 Proceedings, San Francisco.
9. K. Kinoshita et al, IEDM 2000 Proceedings, San Francisco.
10. S. Vanhaelemeersch et al, IITC 99 Proceedings, San Francisco.
11. TEL, IITC 2000 Dow Chemical Technical Showcase, San Francisco.
12. J. Waeterloos et al, AMC 2000 Proceedings, San Diego.
13. M. McClear et al, AVS Proceedings, February (2001)
14. J. Waeterloos et al, IITC 2001 Proceedings, San Francisco.

# MECHANICAL PROPERTIES OF CURED SiLK LOW-K DIELECTRIC FILMS

J. Im, P. H. Townsend, J. Curphy, C. Karas, E. O. Shaffer II

## 1. INTRODUCTION

SiLK (trademark of The Dow Chemical Company) semiconductor dielectric is a low-k organic polymer, based on the synthesis of crosslinked polyphenylenes by the reaction of polyfunctional cyclopentadienone- and acetylene-containing materials<sup>1</sup>. SiLK dielectric is used for high performance integrated circuits with subtractive Al/W<sup>2-4</sup> or Cu damascene<sup>5-7</sup> wiring technology. The properties of cured SiLK enable integration with current interlayer dielectric (ILD) processes: for example, high thermal stability, high T<sub>g</sub>, low dielectric constant, no fluorine, spin-on application, good adhesion and mechanical durability, low moisture absorption, and solvent resistance. Some of these properties are listed in Table 1.

**Table 1.** Summary of SiLK dielectric properties<sup>8,9</sup>

Property	Value
Dielectric constant	2.65
Voltage breakdown	4 MV/cm
Leakage current at 1 MV/cm	0.33 nA/cm <sup>2</sup>
Refractive index at 632.8 nm	1.63
Moisture uptake at 20°C, 80 %RH	0.24 %
Thermal stability	> 425°C
Weight loss at 450°C	0.7 wt-%/hr
Glass transition	> 490°C
Hardness	0.38 GPa
Toughness	0.62 MPa m <sup>1/2</sup>
Residual stress at room temperature	56 MPa

---

J. Im, P. H. Townsend, J. Curphy, and C. Karas, The Dow Chemical Company, Advanced Electronic Materials, 1712 Building, Midland, MI, 48674, USA, E. O. Shaffer II, The Dow Chemical Company, CRAFT Shared Services, 433 Building, Midland, MI, 48674, USA

*Metallization of Polymers 2.*

Edited by Edward Sacher, Kluwer Academic/Plenum Publishers, 2002

53

In addition, adhesion within integrated structures containing SiLK coatings and their mechanical reliability in general were reported previously using a modified edge lift-off test (m-ELT) method<sup>10,11</sup>. It should be noted for this method, however, that the epoxy backing layer on the test piece undergoes stress relaxation with elapsed time between preparation and testing<sup>12</sup>. This complicates accurate assessment of residual stress at break. The problem can be overcome by heating the sample at the start of the test up to  $T_g$  of epoxy to reset the mechanical state in the epoxy, immediately followed by cooling down to termination of the measurement.

In this paper, we present some other results of SiLK films: tensile properties of strength, modulus, and elongation at break, dynamic mechanical analysis (DMA) below room temperature for storage modulus, loss modulus and  $\tan\delta$ , and temperature dependent coefficient of thermal expansion (CTE) from thermal mechanical analysis (TMA).

## 2. EXPERIMENTAL

For tensile properties, free-standing film strips, ca. 10  $\mu\text{m}$  in thickness, were tested. Testing of free-standing films underestimates the true capability of on-wafer film performance due to flaw and edge crack generation during sample preparation, handling, and testing. Special care is needed to minimize these artifacts. Therefore, the strips were prepared by a clean room procedure as follows.

- Plasma clean  $\text{SiO}_2$  wafers.
- Metallize wafers with 0.2  $\mu\text{m}$  Cu (Polymer/Cu adhesion should be optimum to survive processing, but to be lifted off easily into strips in a Cu etch bath.).
- Coat and cure 1  $\mu\text{m}$  layer, 9 total layers of SiLK-I resin, with 400°C/10 min. initial cure between layers and 450°C/6 min. final cure.

The remainder of the strip preparation was:

- Laser ablation of coating to define individual strips of 1/4" width.
- Lift off the strips by immersing the patterned wafer in a Cu etch bath of 0.15-M ammonium persulphate for an hour, and rinse in DI water.
- Dry the strips overnight – between clean room wipes.
- Attach the strip to a paper tab having a rectangular hole in middle (ref. Fig. 1).
- Precondition the tabbed strips for 24 hours at 23±2°C, 50±5 %RH per ASTM D882-88.

Tensile tests were performed on an Instron machine equipped with air-actuated film grips. Tabbed specimens were carefully aligned, then mounted in the Instron grips. The paper tabs were then cut on both sides using sharp scissors with minimum disturbance (Figure 1) so that the film strip would only be stressed upon loading. The strain rate was fixed at 10 %/min, but the gage length was varied 1 to 3" for system compliance correction per ASTM D3379-75, from which corrected Young's modulus and elongation at break could be obtained. In addition, the separation of the ink dots placed near the top and bottom of the gage section was monitored with video taping to spot check the accuracy of elongation at break obtained by the system compliance correction method. Video taping also helped to confirm that there was no slippage of the specimen from the grips. Approximately 150 specimens were tested for greater accuracy of the data.

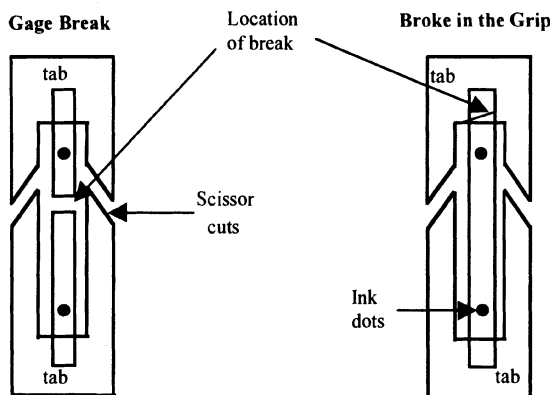


**Figure 1.** Tabbed film strips after tensile failure. Note that the paper tabs were cut prior to film testing.

Specimens for assessment by dynamic mechanical analysis (DMA) and thermal mechanical analysis (TMA) were prepared in the similar manner as the aforementioned tensile specimens, except their width was 1/8". A Rheometrics Model RSA-2 was used for DMA and a TA Instrument Model 2940 was used for TMA.

### 3. RESULTS

In tensile testing, the specimens sometimes broke in the grip region as depicted schematically on the right hand side of Figure 1. These results were discarded, and only the data for specimens broken in the gage region were used for analysis. The fracture surface of the specimens revealed one simple cleavage plane without individual layer delineation, demonstrating good interlayer adhesion regardless of the varying degrees of repeated thermal exposure imposed on the multilayer stack during the coating process (Figure 2).

Since we used a small load cell (10 N) as well as small grips and accompanying attachments so as to enhance the resolution of testing thin films, the system compliance became substantial, and had to be corrected to obtain accurate modulus and elongation at break. The system compliance was determined following ASTM D3379-82 (Figure 3). The intercept with the vertical axis in Figure 3 represents the amount of 'extension' of the testing system per kg of applied load. This amount was taken out, to obtain the net extension of the film as well as the corrected properties. Tensile modulus, corrected for the system compliance vs. uncorrected, is compared in Figure 4. The corrected modulus was independent of the gage length, as expected, whereas the uncorrected modulus varied with the gage length. The discrepancy between the corrected and uncorrected modulus was more pronounced for a shorter gage length, where the system compliance was more dominant. If one opts to omit the compliance correction step, but a reasonable estimate of modulus is still desired, the use of as large a gage length as practical is recommended. The compliance correction was similarly applied to elongation at break.

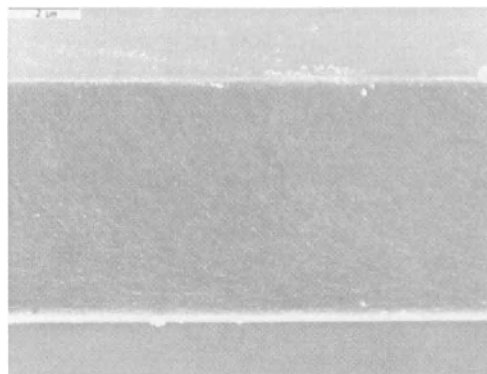


Figure 2. Tensile fracture surface of multiple layered SiLK film, showing no evidence of layer delamination

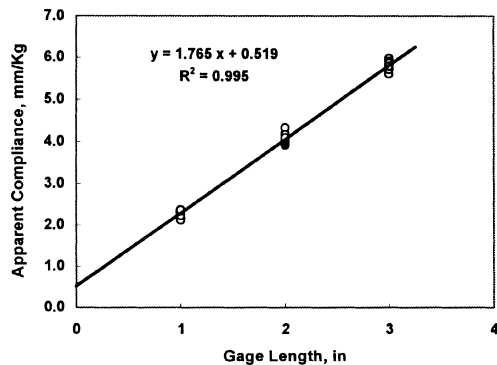


Figure 3. Apparent compliance vs. gage length. The y-axis intercept represents the system compliance

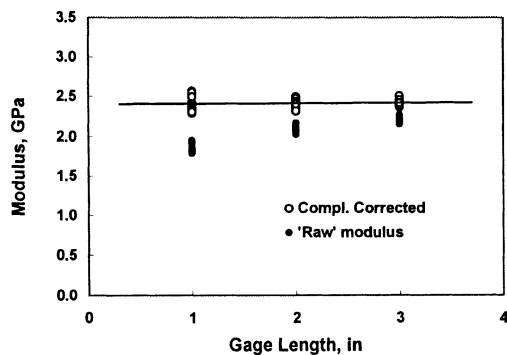
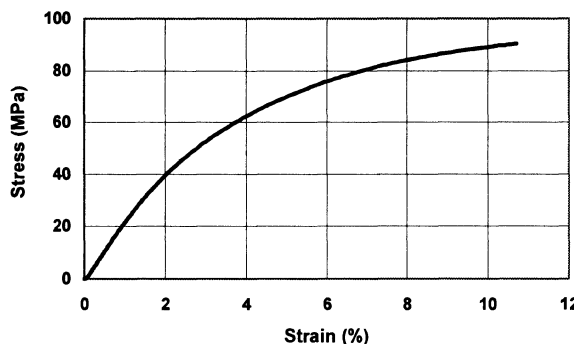


Figure 4. Comparison of modulus vs. gage length before and after the system compliance correction

Table 2 shows the tensile properties of SiLK films, which underwent a final cure at 450°C/6 min.. Figure 5 shows a representative stress-strain curve. Although not reported in detail, a film with a final cure at 400°C/30 min. yielded the same tensile properties.

**Table 2.** Tensile properties of SiLK film

Strength (MPa)	Strain at break (%)	Modulus (GPa)
90±4	11.5±2	2.5±0.1



**Figure 5.** Typical stress-strain curve for SiLK film

The DMA sweep of SiLK film from room temperature up to 490°C was reported previously (Figure 6)<sup>8</sup>. To expand the temperature range, the present DMA study covered room temperature down to -125°C (Figure 7).

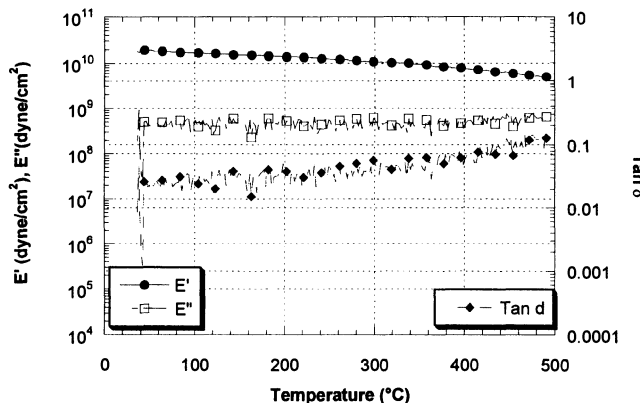


**Figure 6.** DMA plot of 12 μm free-standing SiLK film from room temperature to 490°C (from [8])

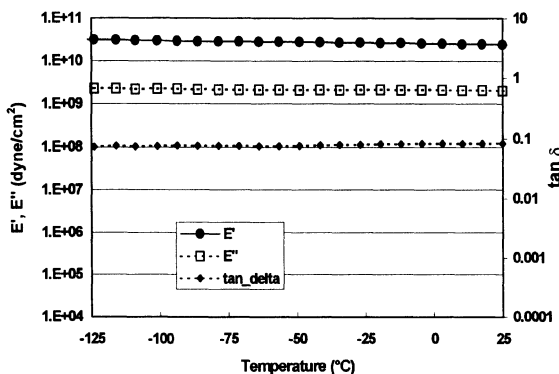


Figure 7. DMA plot of SiLK film from -125°C to room temperature

No appreciable transition for any of the properties of storage modulus, loss modulus, and loss tangent is noted in Figures 6 and 7 in the entire temperature range from -125°C up to 490°C. Therefore, the  $T_g$  of SiLK is in excess of 490°C while there is no secondary transition below  $T_g$ .

In the TMA study, a SiLK film strip was thermally cycled between 270°C and -75°C under nitrogen purge. The resulting plot for dimensional changes with temperature demonstrates the reversible nature of each sweep (Figure 8). The CTE may be obtained by taking the slope of these curves as follows: length of dimensional change per length of gage length per unit temperature change (cm/cm/°C). However, the TMA curves exhibit a slight curvature, indicating that the CTE would be slightly temperature dependent. Figure 9 shows the plot of CTE obtained from the slope of the curves in Figure 8. The temperature dependence of CTE in the glassy state below  $T_g$  is common for other network polymers such as epoxy<sup>13,14</sup>.

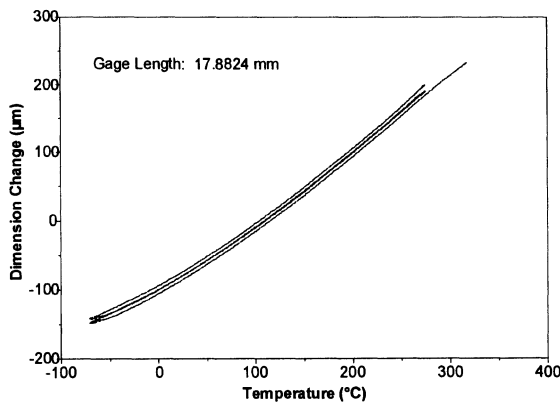
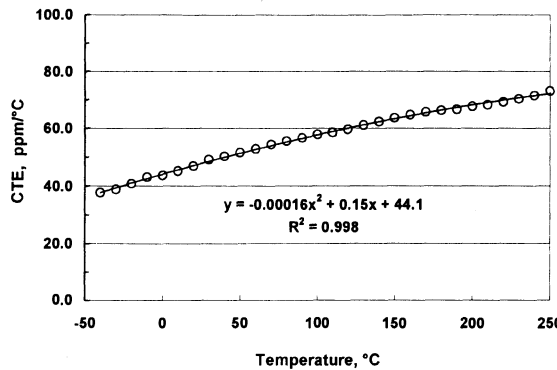


Figure 8. Dimension change of SiLK strip with temperature



**Figure 9.** Coefficient of thermal expansion of SiLK film at the temperature of measurement

The evolution of film stress with temperature is related to the product of film modulus and CTE mismatch between the film and substrate, as below.

$$\sigma = [\{E(T)/(1-v)\} \{\alpha(T) - \alpha_s\}] \Delta T \quad (1)$$

where  $\sigma$  is the residual stress,  $T$  is the temperature,  $E(T)$  and  $\alpha(T)$  are the temperature dependent modulus and CTE of SiLK film, respectively, and  $\alpha_s$  is the CTE of Si substrate. The increase in CTE with temperature and the opposing decrease in modulus (Figure 6) result in a nearly linear rate of residual stress variation with temperature. A previous experiment using curvature measurement reveals that the value inside the bracket [ ] in Eq. 1, ie. the slope of the stress-temperature curve, is nearly constant (Figure 10)<sup>8</sup>. Compared with inorganic dielectrics, the CTE of polymers can be as much as two orders of magnitude greater. At the same time, the other component making up the stress, elastic modulus, can be two orders of magnitude less. The net result is that the stress level in a polymer dielectric is generally close to or less than standard  $\text{SiO}_2$ .

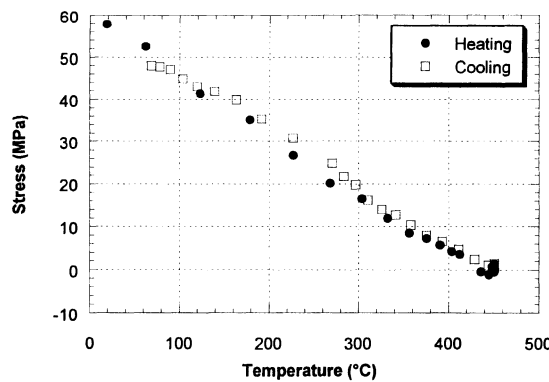


**Figure 10.** In-plane stress as a function of temperature for 1.0 um SiLK film on silicon (from [8]).

#### 4. SUMMARY

Tensile properties of free-standing SiLK film, eg. strength, modulus and elongation at break have been determined. Methods to prepare tensile specimens and test procedures including system compliance correction were described in detail. Dynamic mechanical properties extending down to -125°C have been obtained. No secondary transition was observed anywhere below 490°C. Coefficient of thermal expansion (CTE) has been determined from the TMA sweep. Although the CTE of SiLK film below  $T_g$  was somewhat temperature dependent, the counteracting temperature effect of modulus resulted in nearly a constant rate of residual stress variation in the SiLK coating on a Si wafer.

#### 5. ACKNOWLEDGEMENTS

The authors thank Joan Marshall for fracture surface microscopy, and Chuck Broomall for dynamic mechanical analysis.

#### 6. REFERENCES

1. J. P. Godschalk, D. R. Romer, Y. H. So, Z. Lysenko, M. E. Mills, G. R. Buske, P. H. Townsend, D. W. Smith, Jr., S. J. Martin, and R. A. DeVries, US Patent 5,965,679 (1999)
2. Lee, M. Chae, H. Kim, S. Kim, C. T. Kim, J. M. Hwang, in proc. Int. Interconnect Tech. Conf., San Francisco, CA, June 5-7, 137-139 (2000)
3. J. Waeterloos, M. Simmonds, A. Achen, and M. Meier, Semicond. Eur. Aug. 26 (1999)
4. H. Maynard, C. S. Pai, C. B. Case, R. O. Adebanjo, M. R. Baker, W. Wai Tai, R. Liu, in proc. Int. Interconnect Tech. Conf., San Francisco, CA, May 24-26, 212-214 (1999)
5. R. D. Goldblatt, et al., in proc. Int. Interconnect Tech. Conf., San Francisco, CA, June 5-7, 261-263 (2000)
6. M. Ikeda, H. Kudo, R. Shinohara, F. Shimpuku, M. Yamada, Y. Furumura, in proc. Int. Interconnect Tech. Conf., San Francisco, CA, June 1-3, 131-133 (1998)
7. O. Demollien, et al., in proc. Int. Interconnect Tech. Conf., San Francisco, CA, May 24-26, 198-199 (1999)
8. P. Townsend, S. Martin, J. Godschalk, D. Romer, D. Smith, D. Castillo, R. DeVries, G. Buske, N. Rondan, S. Froelicher, J. Marshall, E. O. Shaffer II, and J-H. Im, Thermosetting Polymer Coating with Low Dielectric Constant and High Thermal Stability for ULSI Interlayer Dielectric, proc. MRS Symp. **476**, 9-17 (1997)
9. S. Martin, J. P. Godschalk, M. E. Mills, E. O. Shaffer II, and P. H. Townsend, Development of a Low-Dielectric-Constant Polymer for the Fabrication of Integrated Circuit Interconnect, *Adv. Mater.*, **12**, No. 23, 1769-1778 (2000)
10. E. O. Shaffer II, L. Hoang, and F. J. McGarry, Edge Liftoff: A New Test for Adhesion, *Polym. Sci. & Eng.*, **36**, 18, 2375-2381 (1996)
11. J. Im, E. O. Shaffer II, T. Stokich, Jr., A. Strandjord, J. Hetzner, J. Curphy, C. Karas, G. Meyers, D. Hawn, A. Chakrabarti, and S. Froelicher, On the Mechanical Reliability of Photo-BCB-Based Thin Film Dielectric Polymer for Electronic Packaging Applications, *J. Elec. PKG*, **122**, 1, 28-33 (2000)
12. J. Hay, E. G. Liniger, and X. H. Liu, Evaluation of the Modified Edge Lift-Off Test for Adhesion Characterization in Microelectronic Multifilm Applications, *J. Mater. Res.*, **16**, 2, 385-393 (2001).
13. A. S. Voloshin, P.-H. Tsao, and R. A. Pearson, In Situ Evaluation of Residual Stress in an Organic Die-Attach Adhesive, trans. ASME, *J. Elec. PKG*, **120**, 314-318 (1998).
14. S. Rzepka, M. A. Korhonen, E. Meusel, C.-Y. Lee, The Effect of Underfill and Underfill Delamination on the Thermal Stress in Flip-Chip Solder Joints, trans. ASME, *J. Elec. PKG*, **120**, 342-348 (1998)

# **PLASMA-POLYMERIZED FLUOROPOLYMER THIN FILMS FOR MICROELECTRONIC APPLICATIONS**

M. S. Silverstein, R. Chen, E. Sacher and L. Sandrin\*

## **1. INTRODUCTION**

The demand for increased signal transmission speed and device density in the next generation of multilevel integrated circuits (ICs) has placed stringent demands on materials performance for such applications as the line-to-line capacitance of interlayer dielectrics (ILD).<sup>1</sup> The ‘National Technology Roadmap for Semiconductors (NTRS) – Technology Needs’, released by the Semiconductor Manufacturing Technology Consortium (SEMATECH) and sponsored by the semiconductor industry association (SIA), has defined two critical changes needed for the development of ultra large scale integrated circuits (ULSI): the reduction of resistance ( $R$ ) and capacitance ( $C$ ). The reduction of resistance is underway with the introduction of copper interconnects to replace aluminum. The NTRS has charted the present and future ILD needs.<sup>2</sup> The current need is for a permittivity less than 3 that has compatibility with copper and copper processing. A suitable low permittivity material (low  $\kappa$  dielectric) for near future needs has yet to be found because, according to NTRS, “Materials that simultaneously meet the electrical, mechanical and thermal requirements have been elusive”. Fluoropolymers have low permittivities but are difficult to process. The authors have investigated fluoropolymer sputtering, spin-cast perfluorinated dioxole polymers, and plasma polymerization in an attempt to produce thin fluoropolymer films.<sup>3-11</sup>

Plasma polymerization is a solvent-free, room temperature process that can be used to rapidly deposit thin polymer films onto a wide variety of substrates.<sup>12,13</sup> In plasma

---

\* M. S. Silverstein and R. Chen, Department of Materials Engineering, Technion – Israel Institute of Technology, Haifa 32000, Israel. E. Sacher, Département de Génie Physique et de Génie de Matériaux, École Polytechnique de Montréal, Montréal, Québec H3C 3A7, Canada. L. Sandrin, Laboratoire Ondes et Acoustique, ESPCI, 75005 Paris, France.

polymerization, a neutral ‘monomer’ gas or vapor in a low pressure reactor is subjected to an electric field. The monomer is fragmented into reactive species which subsequently recombine, forming a crosslinked polymer. The ‘monomer’ can be a hydrocarbon, fluorocarbon, organosilicone or organometallic and need not necessarily include the functional groups typically associated with conventional polymerization techniques.<sup>12</sup> The molecular structure and properties of the plasma polymer depend on the monomer, plasma power, monomer flow rate and reactor pressure. The advantages of plasma polymerization include: the environmental friendliness of the solvent-free process; the deposition of ultra-thin films with thickness directly proportional to deposition time; the deposition of pinhole-free films without the dimensional changes associated with solvent evaporation; the deposition of highly adherent films with substrate activation in the plasma environment; the plethora of monomers available; and the simplicity of the reactor (standard microelectronics industry plasma cleaning equipment). This paper will describe the deposition of plasma polymers from octafluorocyclobutane (OFCB), evaluate their molecular structures, and describe their deposition on a copper substrates.<sup>14,15</sup> OFCB has been chosen to represent fluorocarbons which tend to undergo plasma polymerization (an F/C of 2 or less). Fluorocarbons with similar F/C’s are expected to yield similar results.<sup>14</sup>

## 2. EXPERIMENTAL

### 2.1. Materials

Octafluorocyclobutane ( $C_4F_8$ ) (Matheson) was the fluorocarbon monomer used for plasma polymerization. The substrates used were silicon wafers or glass slides.

### 2.2. Plasma Polymerization

The copper sputtering and PPOFCB plasma polymerization were carried out using an innovative reactor in which the specimen stage for copper sputtering became the upper parallel plate electrode for plasma polymerization when rotated. In this manner, a plasma polymer could be deposited on sputter-coated copper without breaking vacuum. The chamber could be evacuated to  $10^{-8}$  Pa (base pressure) and the operating pressure was regulated independently of the gas flow, using a Baratron valve. The gas flow rates were controlled using mass flow controllers. An RF generator (13.56 MHz) and matching unit were used for plasma polymerization and a DC magnetron generator was used to sputter copper.

The substrate was placed on the specimen stage. The stage was rotated such that the substrate was positioned on the upper parallel plate plasma electrode. The substrate was cleaned in an argon plasma (10 sccm, 67 Pa, 50 W) for 2 min and then the chamber was evacuated to base pressure. The stage was rotated  $180^\circ$  such that the substrate was positioned beneath the copper target. The substrate was coated with sputtered copper at  $0.1 \mu\text{m}/\text{min}$  (0.5 A, 360 V) for 3 min in an argon atmosphere (2.7 Pa, 5 sccm) and then the chamber was evacuated to base pressure. The stage was rotated  $180^\circ$  such that the copper-coated substrate was again positioned as the upper parallel plate plasma electrode. Plasma polymerization was then carried out at powers ranging from 5 to 50 W, pressures

from 2.7 to 40 Pa, and flow rates from 10 to 24 sccm. Typical conditions for OFCB were 7 W, 33 Pa, 24 sccm.

### 2.3. Characterization

The film thickness was measured using both a profilometer (model 3030ST, Dektak) and a variable angle spectroscopic ellipsometer (model 200, J. A. Woollam) in reflection. The ellipsometer was also used to characterize the refractive index,  $n$ , as a function of wavelength. The permittivity,  $\kappa$ , was taken as  $n^2$ . The molecular structure was characterized using a combination of x-ray photoelectron spectroscopy (XPS) using a non-monochromated Mg K $\alpha$  source (ESCALAB MKII, Vacuum Generators). Both low resolution survey spectra and high resolution core level spectra were taken for carbon, fluorine and oxygen. Elemental concentrations were evaluated from the high resolution peak areas following Shirley background subtraction.<sup>16</sup> The topographies were characterized using atomic force microscopy (AFM) in contact mode (model 2010, Topometrix). Scans of  $5 \times 5$ ,  $1 \times 1$  and  $0.2 \times 0.2 \mu\text{m}^2$  were conducted at 20, 5 and  $1 \mu\text{m}/\text{s}$ , respectively. The roughness was obtained from the  $0.2 \times 0.2 \mu\text{m}^2$  scan. Micro-scratch tests were performed to measure adhesion of PPOFCB to copper (CSEM Microscratch Tester, MST). An 0.8 mm radius hemispherical diamond indentor was placed on the sample surface, the sample was moved under the indentor at a constant speed of 0.5 mm/min, and a linearly increasing normal force ramp, in the range 0-3 N, was applied. The indentor-sample interaction was recorded on video tape and the adhesion was calculated from the normal force at which film-substrate debonding began.

## 3. RESULTS AND DISCUSSION

### 3.1. Deposition Rate, Topography, Permittivity and Adhesion

The plasma polymer films discussed here were all transparent and yellow. Plasma polymer deposition rates are generally relatively independent of polymerization time. A linear increase in thickness with time is observed for a typical PPOFCB (7 W, 24 sccm, 33.3 Pa), as shown in Figure 1 is  $0.03 \mu\text{m}/\text{min}$ . The variation of PPOFCB deposition rate with  $W/F_m$  in Figure 2 is typical of plasma polymerization. The low deposition rate at low  $W/F_m$  reflects deposition in an energy-poor plasma. The deposition rate increases with increasing energy per monomer mass until a plateau is reached at a critical  $W/F_m$  (approximately 25 MJ/kg). The reaction is energy saturated beyond this critical value and the deposition rate does not increase further. Based on the molecular structure of OFCB, fragmentation would tend to yield CF<sub>2</sub>, which enhances polymerization.<sup>17</sup>

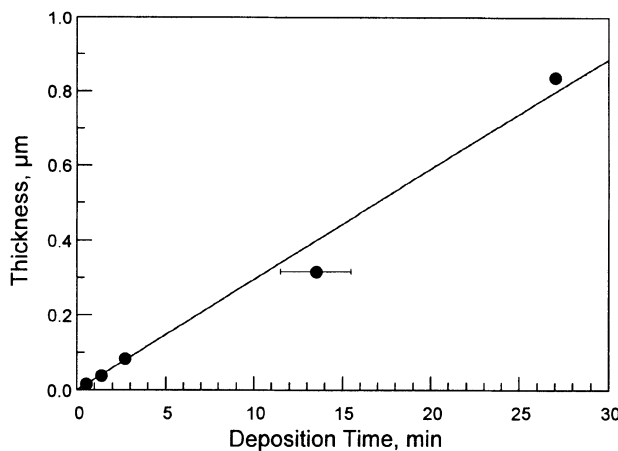


Figure 1. Thickness as a function of deposition time.

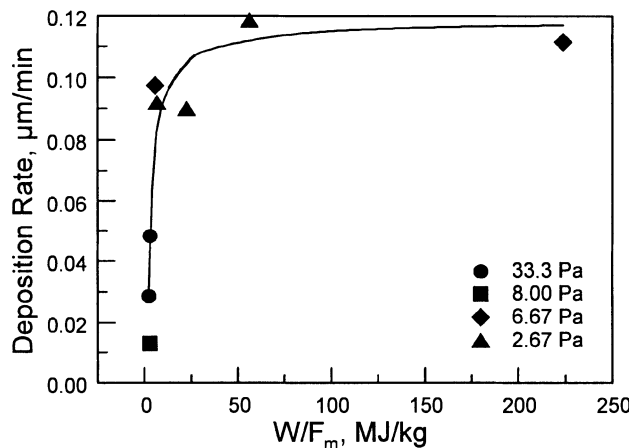


Figure 2. Deposition rate as a function of  $W/F_m$  at various pressures.

PPOFCB (7 W, 2.67 Pa, 24 sccm) has a relatively smooth topography. The RMS roughness of a copper-sputtered silicon wafer, measured using AFM, was 0.97 nm. PPOFCB deposited on the copper had a roughness of 0.46 nm. The smooth PPOFCB surface suggests that polymerization occurs predominantly on the substrate surface. The polymer film grows through reaction with the monomer fragments that reach the surface. This polymerization mechanism yields the relatively slow deposition rate seen in Figure 1.

The PPOFCB (7 W, 24 sccm, 33.3 Pa) refractive index, determined through variable wavelength ellipsometry, is 1.37 at 900 nm. This relatively low refractive index indicates that PPOFCB is a potentially attractive low  $\kappa$  dielectric with a permittivity in the neighborhood of 2.0 (i.e.,  $n^2$ ) at high frequencies.

PPOFCB adhered strongly to the copper substrate. Several attempts were made to quantify the adhesion of plasma polymers to copper. A Scotch Tape peel test could not debond the PPOFCB from the substrate. In scratch tests the indentor ploughed through the polymer but could not debond it from the copper. An attempt to propagate a crack between the layers produced a failure at the Cu/Si interface, rather than at the polymer/Cu interface.

### 3.2. Molecular Structure

#### 3.2.1. Copper Substrate

The XPS spectrum of the copper substrate (0 s deposition), following approximately one day of exposure to the atmosphere, exhibits 30.4% copper, 41.4% oxygen and 28.2% carbon (Table 1). The C<sub>1s</sub> spectrum of the copper substrate exhibits its strongest peak at the lowest binding energy. The curve fit for the C<sub>1s</sub> spectrum for the copper substrate yields 6.5% hydroxyl/ether (286.5 eV), 9.3% carbonyl (288.3 eV) and 10.8% carboxyl (289.3 eV) (Table 2).<sup>18</sup> The elemental composition of the copper substrate is affected by its exposure to the atmosphere. Exposure to a brief argon plasma prior to XPS analysis revealed a significant drop in carbon and oxygen contents, and a copper content of 61%.

**Table 1.** XPS elemental analysis of copper exposed to an OFCB plasma for various times.

Exposure Time, s	0	1	5	30	600
PPOFCB Thickness, nm	----	----	----	15	300
C, %	28.2	24.1	31.6	37.1	39.0
F, %	----	11.5	38.4	62.1	59.8
O, %	41.4	32.3	11.5	0.8	1.2
Cu, %	30.4	32.1	18.5	----	----
F/C	----	----	----	1.67	1.53

**Table 2.** Curve fit peak contributions to C<sub>1s</sub> spectra for copper exposed to an OFCB plasma for various times.

Exposure Time, s	0	1	5	30	600
PPOFCB Thickness, nm	----	----	----	15	300
Group	BE, eV	Concentration %			
C-C	285.0	73.4	72.0	37.7	----
C-O, C*-CF <sub>n</sub>	286.4 – 287.0	6.5	6.3	14.5	15.6
C=O, CF	288.0 – 288.4	9.3	8.6	14.3	8.1
O-C=O, C*F-CF <sub>n</sub>	289.1 – 289.6	10.8	11.0	8.5	17.5
CF <sub>2</sub>	290.9 – 291.3	----	2.1	20.5	38.2
CF <sub>3</sub>	293.1 – 293.4	----	----	4.5	24.2

### 3.2.2. 300 nm Thick PPOFCB Films

The atomic compositions in Table 1 for a 300 nm thick PPOFCB (7 W, 2.67 Pa, 24 sccm) is typical of the thicker PPOFCB films. The film has an F/C of 1.53, and 1.2% oxygen, resulting from the reaction of long-lived radicals in the plasma polymer with atmospheric oxygen. The F/C ratio decreases with  $W/F_m$  (Figure 3) and increases with pressure at low  $W/F_m$ . F/C is more sensitive to  $W/F_m$  than to pressure, with a 50% increase in  $W/F_m$  yielding a more significant change in F/C than a 50% increase in pressure.

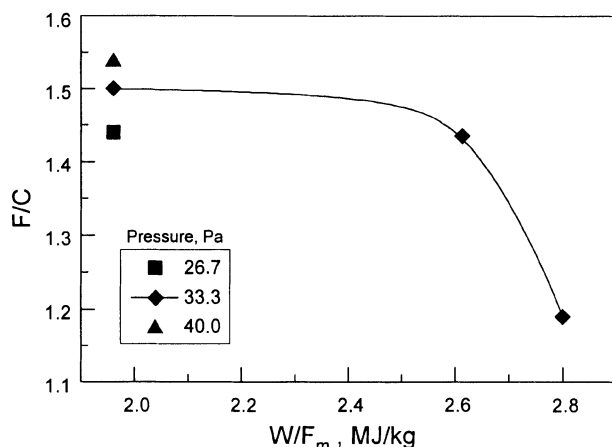


Figure 3. F/C as a function of  $W/F_m$  at various pressures.<sup>14</sup>

The variation of PPOFCB molecular structure with film thickness for relatively thick films can be described through the variation in F/C. The F/C in Figure 4 are calculated from the XPS spectra for films that were sufficiently thick for the copper substrate not to be detected. The 15 nm PPOFCB thick film from a 30 s OFCB plasma exposure had the highest F/C, 1.68. The F/C decreases rapidly in the first few minutes of OFCB plasma exposure, reaching 1.5 for an 84 nm thick PPOFCB film. It then remains relatively constant, at a value of 1.5, with further exposure to the OFCB plasma (measured up to a PPOFCB thickness of 840 nm). The initial rapid decrease in F/C with film thickness (Figure 4) may reflect the unsteady state of the plasma polymerization and plasma etching reactions in the first few minutes of plasma exposure: fluorine-rich groups are removed from PPOFCB under the influence of ion bombardment and vacuum UV.<sup>17</sup> The F/C would reach a plateau once these reactions have reached their steady states.

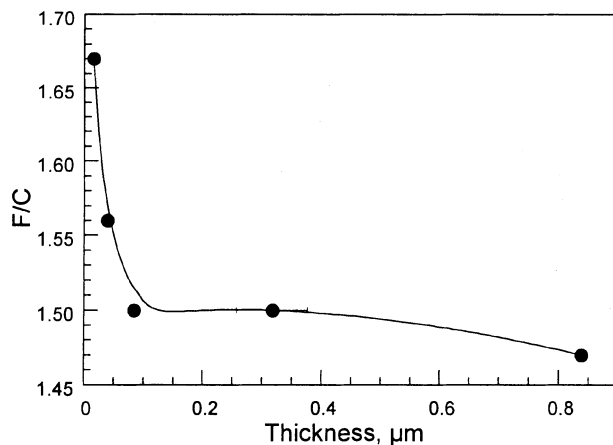


Figure 4.  $F/C$  as a function of film thickness.<sup>15</sup>

The curve fits for plasma fluoropolymer  $C_{1s}$  spectra in the literature usually includes  $\text{CF}_3$ ,  $\text{CF}_2$ ,  $\text{CF}$  and  $\text{C}^*\text{-CF}$  peaks and, in some cases, a  $\text{CH}$  peak.<sup>12,17</sup> There is no regular molecular structure in this random addition of monomer fragments and, therefore, the molecular environments of identical groups may be quite varied. This irregular molecular structure, therefore, yields especially broad binding energy peaks. Full widths at half maximum (FWHM) of 2 eV are common for plasma polymers.<sup>12</sup> The close proximity of numerous broad peaks in plasma fluoropolymers yields spectra whose interpretation can be especially challenging. An additional factor that must be taken into account in the interpretation of the spectra is the presence of  $\alpha_{3,4}$  x-ray satellites.<sup>18</sup> The  $\alpha_3$  satellite, 8.0% of the main peak area, is located -8.4 eV from the main peak; the  $\alpha_4$  satellite, 4.2% of the main peak area, is located -10.2 eV from the main peak.  $\text{CF}_3$  and  $\text{CF}_2$ , at 293.5 and 291.4 eV, respectively, will, therefore, have satellite contributions near the  $\text{CH}$  binding energy, 285 eV.

The method used to determine the binding energy peak positions for PPOFCB is described elsewhere.<sup>14</sup> The peak at the highest binding energy, 293.6 eV, was assigned to  $\text{CF}_3$ . The peak with the second highest binding energy, 291.5 eV, (and the highest magnitude) was assigned to  $\text{CF}_2$ . These peak positions and the 2.1 eV difference between them are similar to those found in the literature.<sup>18</sup> The deconvolution of the PPOFCB  $C_{1s}$  spectrum in Figure 5 was based on finding a fit that best suited the  $\text{CF}_3$  and  $\text{CF}_2$  peaks. These two prominent peaks were best fit using a 50% Gaussian/Lorenzian distribution and a FWHM of 1.9 eV. These two fitting parameters were then used to fit the entire spectrum, positioning peaks at 289.5 and 286.9 eV, the other maxima in the spectrum. The resulting fit indicated that a fifth peak must be added at 288.2 eV. The peaks at 289.5, 288.2 and 286.9 eV were assigned to  $\text{C}^*\text{F-CF}_n$ ,  $\text{CF}$  and  $\text{C}^*\text{-CF}_n$ , respectively, in accordance with other plasma fluoropolymer XPS studies in the literature.<sup>19</sup>  $\text{C}^*\text{F-CF}_n$  and  $\text{C}^*\text{-CF}_n$  represent monofluorinated carbon and non-fluorinated carbon affected by a neighborhood of highly fluorinated carbon. The tail of the spectrum at low binding

energies results from the  $\alpha_{3,4}$  satellites of the higher energy peaks. A FWHM of 1.9 eV was needed to fit the composite peaks associated with the irregular structure of the plasma polymer.

The concentrations of  $\text{CF}_3$ ,  $\text{CF}_2$ ,  $\text{C}^*\text{F}-\text{CF}_n$ ,  $\text{CF}$  and  $\text{C}^*\text{-CF}$  in Table 2 are based on the relative peak area. The total  $\text{CF}$ ,  $\Sigma\text{CF}$ , is the sum of the  $\text{CF}$  and  $\text{C}^*\text{-CF}$  in Table 2. PPOFCB had a relatively high concentration of  $\text{CF}_2$  (32.9%), about 25%  $\text{CF}_3$  and about 25%  $\Sigma\text{CF}$ .

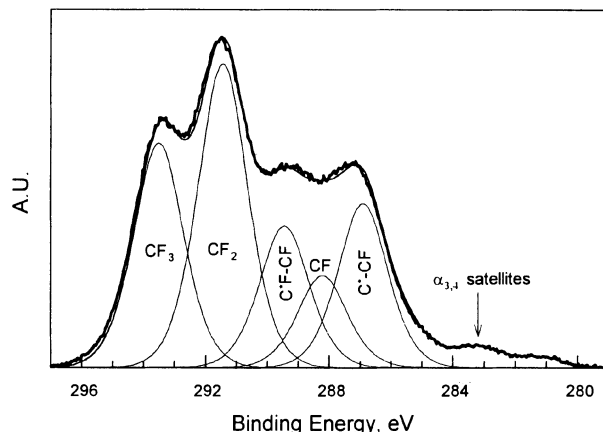


**Figure 5.**  $\text{C}_{1s}$  spectrum curve fit. Thick line: data. Thin lines: individual peaks and the sum of all peaks and satellites.<sup>14</sup>

### 3.2.3. PPOFCB Deposition

XPS reveals significant changes on the copper surface with increasing exposure to an OFCB plasma. The variations in elemental composition, as determined from the XPS spectra, are seen in Figure 6 and Table 1. The high resolution XPS spectra for each element reveal the variations in molecular structure with increasing OFCB plasma exposure time. The evolving molecular structure of PPOFCB was characterized through the curve fits for the  $\text{C}_{1s}$  spectra with the peak assignments and the curve fit results listed in Table 2.

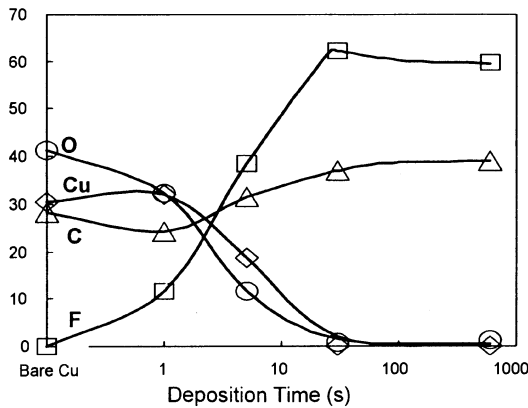


**Figure 6.** Atomic composition as a function of thickness.<sup>15</sup>

The nature of the changes on the surface are also reflected by the changes in the C<sub>1s</sub> spectra as seen through the variation in the C-C, CF<sub>2</sub> and CF<sub>3</sub> contents in Figure 7. There are distinct CF<sub>2</sub> and CF<sub>3</sub> peaks at 291.0 and 293.1 eV, respectively, after a 2 s OFCB plasma exposure. With increasing OFCB plasma exposure time, the CF<sub>2</sub> and CF<sub>3</sub> peaks become more prominent, and occur at slightly higher binding energies. The C-C peak at 285 eV associated with a hydrocarbon contaminant becomes less prominent; there is no discernable C-C peak following a 30 s OFCB plasma exposure. The variations in elemental composition and group concentrations provide a detailed description of the effects of OFCB plasma exposure on the copper substrate, beginning with the first second of OFCB plasma exposure and ending in the deposition of a smooth, planarizing PPOFCB film, with no exposed copper, following a 30 s OFCB plasma exposure.

#### 4. CONCLUSIONS

The plasma polymerization of OFCB, representative of fluorocarbons which tend to undergo plasma polymerization, was investigated with the objective of synthesizing a smooth fluoropolymer film with a low permittivity. PPOFCB had a refractive index of 1.37 at a wavelength of 900 nm, suggesting that it has potential as a low  $\kappa$  dielectric, with a high frequency permittivity in the neighborhood of 2.0. The surfaces of copper exposed to an OFCB plasma for times as short as 1 s and as long as 30 min were characterized using XPS.

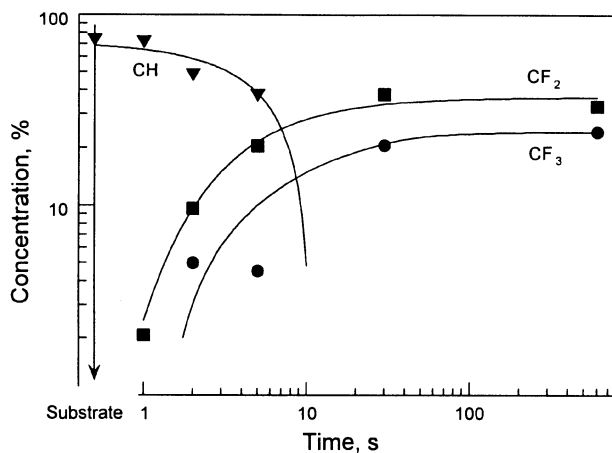


Figure 7. Concentration of various groups as a function of deposition time.<sup>15</sup>

This investigation has shown:

- Transparent, yellow fluoropolymer films that adhered strongly to the substrates were deposited at a constant deposition rate (about 0.03  $\mu\text{m}/\text{min}$ ).
- The deposition rate increased with  $W/F_m$  until a critical  $W/F_m$  of approximately 25 MJ/kg. Beyond the critical  $W/F_m$ , the deposition rate reached a plateau.
- PPOFCB was a smooth planarizing film with a roughness of 0.46 nm, less than half the 0.97 nm roughness of the copper substrate.
- F/C increases with decreasing  $W/F_m$  and, in a less sensitive manner, with increasing pressure, with a typical F/C of 1.5. The approximately 1.5% oxygen results from the reaction of long-lived radicals in the plasma polymer with atmospheric oxygen.
- The F/C for PPOFCB can be as high as 1.68 after brief deposition times (30 s), reaching a plateau value of 1.5 following several minutes of plasma exposure. This reduction in F/C is associated with ion bombardment and vacuum UV defluorination.
- The copper surface is oxidized, on exposure to atmosphere, and covered by an oxidized hydrocarbon contaminant. Following several seconds of OFCB plasma exposure, the deposited fluorocarbon begins to dominate the surface, although oxidized copper and oxidized hydrocarbon contaminant are still observed.
- The copper substrate beneath a 15 nm PPOFCB film (30 s OFCB plasma exposure) could no longer be detected via XPS nor was oxidized hydrocarbon contaminant found on the low energy PPOFCB surface.

## 5. ACKNOWLEDGEMENTS

The authors gratefully acknowledge the support of the Technion VPR Fund and the Natural Sciences and Engineering Research Council of Canada. The figures have been reprinted with the kind permission of Excerpta Media Inc.

## 6. REFERENCES

1. W. W. Lee and P. S. Ho, *MRS Bull.*, **22**(10), 28 (1997).
2. *National technology roadmap for semiconductors – Technology needs – 1998* (SEMATECH, New York 1998).
3. E. Sacher and J. E. Klemburg-Sapieha, *J. Vac. Sci. Technol.*, **A15**, 2143 (1997).
4. L. Sandrin and E. Sacher, *Appl. Surf. Sci.*, **135**, 339 (1998).
5. D. Popovici, M. Meunier and E. Sacher, *J. Appl. Phys.*, **83**, 108 (1998).
6. D. Popovici, M. Meunier and E. Sacher, *J. Appl. Polym. Sci.*, **70**, 1201 (1998).
7. D. Popovici, M. Meunier and E. Sacher, *J. Adhesion*, **70**, 155 (1999).
8. R. Chen, V. Gorelik and M. S. Silverstein, *J. Appl. Polym. Sci.*, **56**, 615 (1995).
9. R. Chen and M. S. Silverstein, *J. Polym. Sci. Part A: Polym. Chem.*, **34**, 207 (1996).
10. M. S. Silverstein, R. Chen and O. Kesler, *Polym. Eng. Sci.*, **36**, 2542 (1996).
11. M. S. Silverstein, J. Sadovsky, D. Alon and V. Wahad, *J. Appl. Polym. Sci.*, **72**, 405 (1999).
12. H. Yasuda, *Plasma Polymerization* (Academic Press, New York, 1985).
13. N. Morosoff, in: *Plasma Deposition, Treatment, and Etching of Polymers*, edited by R. d'Agostino (Academic Press, New York, 1990), p. 1.
14. L. Sandrin, M. S. Silverstein and E. Sacher, *Polymer*, **42**, 3761 (2001).
15. M. S. Silverstein, L. Sandrin and E. Sacher, *Polymer*, **42**, 4299 (2001).
16. P. M. Sherwood, in: *Practical Surface Analysis by Auger and X-ray Photoelectron Spectroscopy*, edited by D. Briggs and M. P. Seah (John Wiley & Sons, New York, 1983), p. 445.
17. R. d'Agostino, in: *Plasma Deposition, Treatment, and Etching of Polymers*, edited by R. d'Agostino (Academic Press, New York, 1990), p. 95.
18. G. Beamson and D. Briggs, *High Resolution XPS of Organic Polymers* (John Wiley & Sons, New York, 1992).
19. M. E. Ryan, J. L. C. Fonseca, S. Trasker and J. P. S. Badyal, *J. Phys. Chem.*, **99**, 7060 1995.

# FUNDAMENTAL ASPECTS OF POLYMER METALLIZATION

F. Faupel, V. Zaporojtchenko, T. Strunskus, J. Erichsen, K. Dolgner, A. Thran, and M. Kiene\*

## 1. INTRODUCTION

Metallized plastics are used extensively in applications ranging from food packing to microelectronics<sup>1, 2</sup>. Particularly the latter field has stimulated intensive research throughout the last decades<sup>1-6</sup>. In view of the great need for further miniaturization and reduction of propagation delay in future device generations aluminum will increasingly be replaced by the lower resistivity copper, and polymers are seen as potential low-permittivity (low-k) dielectrics even for on-chip interconnect<sup>5, 6</sup>. First chips involving Cu and the polymer SiLK® (DuPont<sup>7</sup>) have already been fabricated by IBM<sup>8</sup>.

Both processing and operation of microelectronics components involves exposure to elevated temperatures and thermal cycling. This may lead to crack formation and delamination induced by mechanical stress that originates from the difference in the expansion coefficients of the different materials. In chip applications diffusion of even very small amounts of copper, acting as a deep-level impurity, from the polymer into silicon is also a concern<sup>6</sup>. Therefore, much effort has been made to control the microstructure and thermal stability of metal-polymer interfaces, especially with the aim to improve adhesion and to prevent its degradation<sup>1-6, 9</sup>. In this connection it was observed that the microstructure and hence the mechanical and dielectric properties of the interface may be affected strongly by the degree of intermixing<sup>9-15</sup>.

Recently, there is also much interest in nano-sized metal clusters, which form in the initial stage of polymer metallization if the metal is not too reactive. This interest does not only arise from quantum size effects and single-electron tunneling phenomena<sup>16</sup> but is also triggered by applications in medicine<sup>17</sup> and as substrates for biomolecules<sup>18</sup>.

Irrespective of its technological background polymer metallization is also interesting from the fundamental point of view due to the strongly contrasting properties of metals

\* F. Faupel, V. Zaporojtchenko, J. Erichsen, K. Dolgner, Lehrstuhl für Materialverbunde, Technische Fakultät der Universität Kiel, Kaiserstr. 2, 24143 Kiel, Germany, E-mail: ff@tf.uni-kiel.de; T. Strunskus, now Ruhr-Universität Bochum; A. Thran, now Universität Hamburg; M. Kiene, now AMD Inc.

*Metallization of Polymers 2.*

Edited by Edward Sacher, Kluwer Academic/Plenum Publishers, 2002

and polymers. While metals are densely packed crystalline solids with a high cohesive energy, polymers are made up of large covalently bonded macromolecules held together by very weak van der Waals interactions in an open structure. The cohesive energy of metals is typically two orders of magnitude higher than the cohesive energy of polymers. Furthermore, the interaction between moderately reactive metals and polymers is generally very weak in comparison to the strong metal-metal binding forces. As a consequence, these metals are expected to exhibit a strong aggregation tendency, and their solubility in polymers should be extremely low under equilibrium conditions. Hence, practically no intermixing should occur when a piece of metal of low reactivity is brought into close contact with a polymer surface<sup>14</sup>. For the same reasons metals of low reactivity do not wet untreated polymer surfaces. They form clusters during polymer metallization, which finally coalesce and form a continuous film (Volmer-Weber growth) as discussed in Section 3.

Despite the expected extremely low solubility of metals in polymers metal clusters at polymer surfaces were found to be embedded into the polymer bulk upon heating the polymer above its glass transition temperature, where the polymer chains attain long-range mobility<sup>19, 20</sup>. Embedding was even observed below the bulk glass transition temperature<sup>21</sup>. In Section 6 we will show, how this effect can be made instrumental to measure the glass transition temperature at the surface.

It is obvious that embedding of metal clusters in polymers is a process being entirely different from ordinary dissolution, e.g., of gas molecules in polymers. Apparently, there is a driving force for embedding of metal clusters, i.e., the Gibbs free energy of a metal particle inside the polymer is lower than that of the particle at the surface. Once more this is related to the high cohesive energy of metals which gives rise to a correspondingly high surface Gibbs free energy of metal particles. The surface Gibbs free energy can be reduced by embedding if the surface tension  $\gamma_M$  of the metal particles exceeds the sum of the interfacial tension  $\gamma_{MP}$  and the polymer surface tension  $\gamma_P$ <sup>19, 20</sup>:

$$\gamma_M > \gamma_{MP} + \gamma_P \quad (1)$$

Since the cohesive energy of polymers is so much lower than that of metals  $\gamma_P$  is very small in comparison to  $\gamma_M$ .

When a metal particle is covered by polymer there is still a net van der Waals force driving it deeper into the bulk and an entropic force, due to the confinement of the polymer chains near the metal particle, pushing it back<sup>19, 20</sup> to the surface. This results in a size dependent potential minimum pinning large particles below the surface. Clusters of the order of 10 nm or less can overcome the potential barrier by thermal activation<sup>14</sup>.

While the above considerations on metal solubility and the absence of significant metal diffusion into polymers are based on equilibrium thermodynamics, the conditions, during the initial stage of polymer metallization, which are the subject of Section 2 and 3, are far from thermodynamic equilibrium. Here the virgin polymer surface is exposed to isolated metal atoms that do not have to overcome the strong metallic cohesive force to become mobile. Therefore, significant diffusion of metals into polymers is only expected to take place during the early metallization process or when the metal is deposited at a very low rate (see Section 5).

This keynote paper is mainly concerned with the fundamental processes taking place if metals are evaporated onto fully cured polymers. Readers interested in polymer-on-metal interfaces are referred to<sup>22, 23</sup>, for instance. Emphasis throughout is placed on investigations performed by the Kiel group. No attempt is made to give a comprehensive literature review. In this connection we refer to<sup>1-4, 6, 9, 14</sup>. We first treat the early deposition stages, involving metal condensation, nucleation, and growth, and address the role of metal-polymer interaction on atomic mobility. Subsequently, the interplay of atomic diffusion and aggregation and the embedding of metallic nanoclusters are discussed. It is shown that nanoclusters can be used to probe the polymer surface glass transition. Finally we cover possible approaches to improve adhesion by interface tailoring.

## 2. CONDENSATION

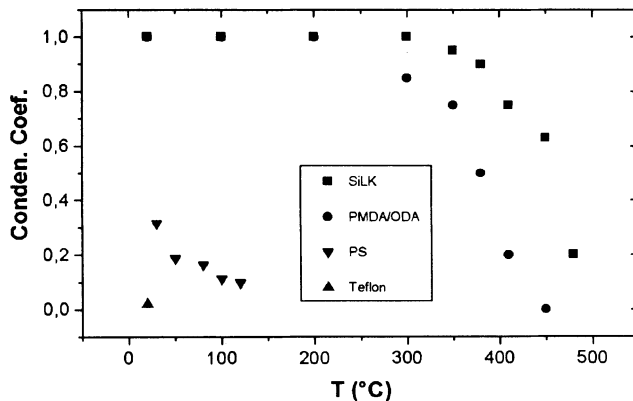
Condensation coefficients of metal atoms on metals are generally very close to unity even at elevated temperatures. The same behavior has often been assumed for metal atoms on polymer surfaces. We have recently shown, however, that the tendency of metals of low reactivity not to wet polymer surfaces can be accompanied by a very low condensation coefficient. The condensation coefficient  $C$  (often also denoted as sticking coefficient) is defined as the ratio of the number of adsorbed metal atoms to the total number of metal atoms arriving at the surface. Whereas sticking coefficients of gas and vapor molecules on solid surfaces can be determined via partial pressure measurements and have been studied extensively<sup>24</sup> little was known about  $C$  values for metal atoms on polymer surfaces. Therefore, we developed a very sensitive radiotracer method to measure condensation coefficients of metals on polymers. In this method, which is described in detail elsewhere<sup>25</sup>, radioactive metal isotopes are evaporated onto a polymer sample through an aperture, and reemitted atoms are collected on a catcher plate. After straightforward calibration the method allows to measure the fraction of reemitted metal atoms. Moreover, sectioning of the catcher plate and counting the activity deposited on each section also yields the angular distribution of the reemitted atoms.

Meanwhile, we also succeeded in measuring quantitatively metal condensation coefficients on polymers employing X-ray photoelectron spectroscopy (XPS) in conjunction with a mathematical correction procedure which takes into account the drop of the metal intensity due to inelastic scattering within metal clusters<sup>26, 27</sup>. Results from the radiotracer technique and photoelectron spectroscopy proved to be in excellent agreement under conditions where metal diffusion into the polymer bulk is negligible<sup>26</sup>. The latter condition is generally obeyed because surface diffusion of metal atoms is much faster than bulk diffusion. Therefore, most metal atoms get trapped in metal clusters at the surface before they are able to “escape” into the polymer bulk (see below).

Depending on polymer-metal combination and temperature,  $C$  varies by about three orders of magnitude. Fig. 1 illustrates the course of  $C(T)$  for Cu on different polymers. For example, condensation coefficients close to unity are observed on the polyimide PMDA-ODA and SiLK® up to temperatures as high as 200 °C and 300 °C, respectively<sup>28</sup>. Above these temperatures, however,  $C$  decreases drastically. On a polystyrene surface the condensation coefficient of Cu is only 0.26 at room temperature and drops further at higher temperatures<sup>27</sup>. For Teflon AF®, finally,  $C$  is as low as 0.02<sup>27</sup>. This means that

only two of hundred atoms impinging on the surface of this interesting low-k polymer stick to the polymer even at room temperature. At elevated temperature the fraction is much smaller.

**Figure 1:** Condensation coefficient vs. temperature for Cu evaporated onto polyimide PMDA-ODA (pyromellitic dianhydride-oxydianiline, DuPont PI-2545), SiLK® (DuPont), polystyrene (Aldrich,  $M_w = 44$



kg/mol), and Teflon AF® (DuPont 1600) (see references for experimental details).

The condensation coefficients for Ag and Au are smaller than those for Cu on all polymers. The differences are most prominent for strongly incomplete condensation. For example, we found a  $C$  value as low as 0.002 for Ag on Teflon AF®<sup>25, 26</sup>, which is about an order of magnitude smaller than the value for Cu.

The extreme differences in the metal condensation coefficients of the polymers are the subject of ongoing investigations. We note, however, that  $C$  follows the trend of the surface energies of the polymers. Since a low surface energy impedes macroscopic wetting of the surface, it does not appear unreasonable that a low surface energy also impedes atomic condensation. The increase of the condensation coefficient from Ag and Au to Cu seems to be related to the higher reactivity of Cu.

A detailed discussion on condensation of metals on polymers and a compilation of  $C$  values for various metal-polymer systems is given in the article by Zaporotchenko et al. in the present proceedings volume<sup>29</sup>. We also refer to<sup>26-28</sup>.

### 3. NUCLEATION AND GROWTH

As mentioned above, the early stages of polymer metallization are far from thermodynamic equilibrium conditions since isolated metal atoms impinge on the polymer surface. Various competing processes, illustrated in Fig. 2, have to be considered. After deposition (*a*) the metal atoms may perform a random walk at the surface (*b*) or diffuse

into the polymer (*e*). Metal atoms encountering each other on their diffusion path may form aggregates at the surface (*c*) and in the polymer bulk (*f*). These aggregates are stable if their size exceeds the size of a critical nucleus. Above the glass transition temperature metal clusters may also be embedded into the polymer (*g*, cf. Section 6). Moreover, the importance of metal atom reemission into the vacuum (*d*) has been stressed earlier. At higher metal coverages metal atoms increasingly impinge on metal clusters, and finally the condensation coefficient approaches unity, which is typical for condensation of metals on metals at moderate temperatures<sup>25</sup>.

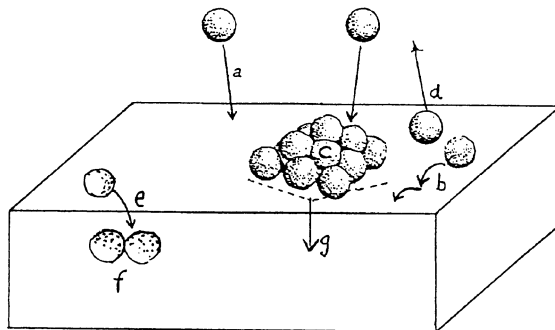


**Figure 2:** Processes taking place during the initial deposition stage where isolated metal atoms impinge on the polymer surface (see text).

In view of the very low  $C$  values observed for noble metals on some polymers the question arises whether the metal atoms are backscattered directly or whether they perform a random walk prior to reemission and are desorbed thermally. In order to address this question we have measured the angular distribution of reemitted atoms. An example is shown in Fig. 3. The measured  $\cos\Phi$  distributions, are a “fingerprint” of random emission whereas a preferred emission direction, defined by the angle of incidence, is expected for backscattering<sup>25</sup>. Although nonrandom emission is also expected for backscattering from a disordered surface we ruled out that the randomness in the emission behavior is caused by the amorphous polymer structure. This was done by demonstrating that the metal emission is independent of the angle of incidence, i.e., the reemitted atoms have no memory of their angle of incidence<sup>25</sup>. Based on these experiments we can exclude direct backscattering and conclude that the metal atoms perform a random walk on the polymer surface and a fraction ( $1 - C$ ) is thermally desorbed before it finds a nucleation site.

Two possibilities have to be taken into account for the nucleation. In so-called preferred nucleation metal atoms are trapped at preferred sites, while in random nucleation nuclei are formed by metal atom encounters. Both processes have been observed in polymer metallization<sup>25, 26, 29</sup>. Preferred nucleation was shown for Ag on TMC polycarbonate, for instance<sup>25</sup>. Here the Ag condensation coefficient is independent of the metal evaporation rate. This clearly allows random nucleation to be ruled out<sup>25</sup>. Apparently,

nucleation takes place at special surface sites. The nature of these sites is not known yet; one can, e.g., think of terminal groups of the polymer chains, impurities, or attractive local arrangements of the chains. The number of these surface defects, and hence the condensation coefficient, can be strongly increased by even moderate ion-beam treatment<sup>26, 29</sup>. Preferred nucleation at defect sites is particularly expected for low condensation coefficients and at the initial deposition stage. In all other cases random nucleation dominates .

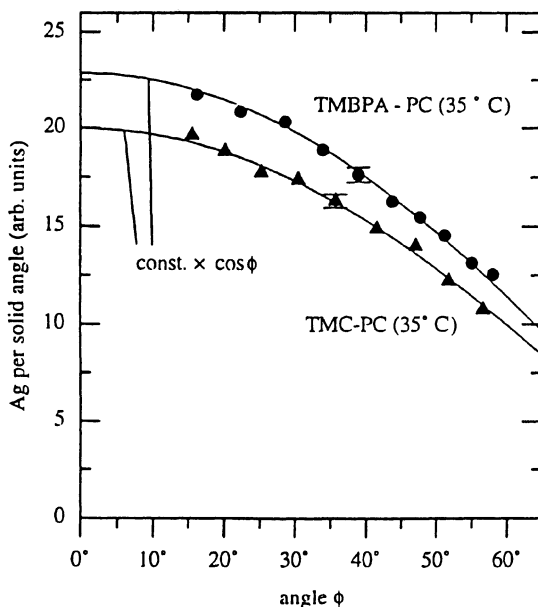


**Figure 3:** Angular distribution of reemitted Ag atoms on TMC polycarbonate and TMBPA (tetramethyl-bisphenol-A) polycarbonate (Bayer AG Leverkusen) at 308 K.  $\phi$  is the angle between the surface normal and the reemission direction.

For a detailed quantitative treatment of metal nucleation on polymers in terms of nucleation theory we refer to the article by Zaporojtchenko et al. in this proceedings volume<sup>29</sup> and to Zaporojtchenko et al.<sup>27</sup>. Here we only outline an approach for random nucleation and report essential results.

The approach is based on measurements of the deposition rate and temperature dependence of the maximum cluster density  $N_{\max}$  in the regimes of incomplete and complete condensation. The latter regime is always accessible at sufficiently low temperatures, and cluster densities can be determined from TEM measurements<sup>26</sup>. The cluster density quickly reaches a maximum during the nucleation period and drops thereafter as a result of cluster coalescence.

The dependence of the maximum cluster density on the deposition rate can be used to evaluate the size of the critical cluster. For random nucleation in the regime of complete condensation nucleation theory predicts<sup>30</sup>

$$N_{\max} \propto (R / D_s)^{\frac{i}{i+2.5}}, \quad (2)$$

where the integer quantity  $i$  is the critical cluster size. An acceptable fit to experimental data was only possible with  $i = 1^{26}$ . This means that noble metal dimers already form stable clusters on polymers. This is in accord with the high cohesive energy of metals and the calculated binding energies for dimers, e.g., 0.8 eV per atom for Ag<sup>31</sup>.

With  $i = 1$  Eq. 3 immediately yields the temperature dependence of the maximum cluster density:

$$N_{\max} \propto \exp[E_d / (3.5kT)]. \quad (3)$$

Thus, measurements of the maximum cluster density as function temperature allow one to determine the activation energy  $E_d$  of surface diffusion.

In the regime of incomplete condensation there is a competition between thermal desorption with a rate  $\tau \propto \exp(-E_a / (kT))$  and diffusion controlled nucleation. Here nucleation theory predicts<sup>30</sup>:

$$N_{\max} \propto \exp[(2/3)(2E_a - E_d)/(3.5kT)]. \quad (4)$$

Based on eqs. (3) and (4) we have determined adsorption energies  $E_a$  and activation energies of surface diffusion  $E_d$  for various noble metal polymer systems. Representative plots of  $\ln(N_{\max})$  against  $1/T$  are depicted in Fig. 4.

The adsorption energies of Cu on polyimide,  $0.6 \pm 0.1$  eV, and SiLK®,  $0.7 \pm 0.1$  eV, turned out to be surprisingly high<sup>28</sup>. They reflect a substantial interaction of the noble metal with these polymers, in accord with conclusions drawn from bulk diffusion studies discussed in Sect. 5. Ag and Au exhibit a much weaker interaction (0.3 eV for Ag on polyimide, for instance). The adsorption energies are also much lower for noble metals on polymers like polystyrene and Teflon AF®. A compilation of  $E_a$  values is given in the article by Zaporojtchenko et al. in these proceedings<sup>29</sup>.

The activation energies of surface diffusion are substantially lower than the adsorption energies, for instance,  $0.2 \pm 0.05$  eV for Cu on polyimide and  $0.3 \pm 0.05$  eV on SiLK®<sup>28</sup>. This reflects non-localized binding forces, which make it much easier to displace an atom at the surface than to remove it completely. Like for the adsorption energies  $E_d$  decreases when going from Cu to Ag and Au or from polyimide and SiLK® to polymers like polystyrene and Teflon AF®.  $E_d$  values are also given in the aforementioned article by Zaporojtchenko et al.<sup>29</sup>.

Based on the activation energies of surface diffusion we also estimated the ratio of the surface diffusivities  $D_s$  of Ag, Au, and Cu assuming that the pre-exponential factors do not differ much. For polyimide at room temperature  $D_s$  ratios for Ag/Au/Cu are  $100/2/1^{26}$ . The larger surface diffusivity of Ag compared to Au is unexpected, judging

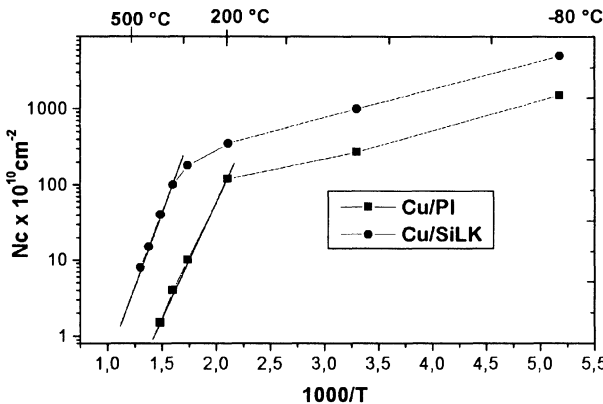


**Figure 4:** Maximum cluster density  $N_{\max}$  as function of reciprocal absolute temperature on a semi-logarithmic scale for Cu evaporated onto polyimide PMDA-ODA (pyromellitic dianhydride-oxydianiline, DuPont PI-2545) and SiLK® (DuPont). The regimes of complete condensation at low temperatures and incomplete condensation at higher temperatures as shown in Fig. 1 are clearly distinguished by two linear ranges of different slopes. The slopes are related to  $E_a$  and  $E_d$  via Eqs. (3) and (4) and allow one to determine these important microscopic quantities.

from the metal reactivity. Apparently, the general trend of the reactivity does not account for the interaction with the polymer. Deviations from the general trend are also seen, for instance, in many cases in the complex formation behavior of Ag and Au. The higher surface diffusivity of Ag compared to Cu also calls for further comments, because the opposite behavior has been observed in radiotracer measurements of bulk diffusion<sup>14,32</sup> (cf. Fig. 9). The slower diffusion of Ag in the bulk was attributed to the larger size of Ag atoms which should reduce the bulk diffusivity substantially in a glassy polymer. In contrast, diffusion at the surface should not be affected significantly by size effects because factors like availability of free volume and distortion of the polymer do not come into play here. Moreover, one cannot definitely exclude that the Ag bulk diffusion coefficients are diffusivities of very small clusters (see Section 5).

We note that the above evaluations were carried out under the assumption that metal diffusion into the polymer bulk does not significantly change the nucleation process at the surface. This does not mean that metal atoms do not diffuse into the bulk during metallization. However, surface diffusion is orders of magnitude faster than bulk diffusion, where effective activation energies are substantially higher than the values given above (e.g.,  $\approx 0.6$  eV for Cu in polyimide<sup>33</sup>). The aforementioned agreement between condensation coefficients from radiotracer and the XPS measurements<sup>26</sup> confirms that diffusion into the polymer bulk is not a major factor. Otherwise, XPS, due to its surface sensitivity would yield lower C values than the radiotracer method.

#### 4. INTERFACIAL CHEMISTRY

Despite many investigations our present knowledge of metal-polymer interaction is still rather incomplete, particularly with respect to the details of the interaction mechanisms and the early deposition stages<sup>9, 34-36</sup>. Consensus exists that Au, Ag, Cu, and Pd interact weakly with polymers. For Au no indications of a chemical interaction or site preference were found on PMDA-ODA<sup>37</sup> and Pd appears to be chemically inert, too<sup>38</sup>. For Ag and Cu purely physical<sup>39</sup> and weak chemical<sup>40-43</sup> interactions with polymers have been considered. Recently, Strunskus et al.<sup>44</sup> have demonstrated that, due to the strong aggregation tendency of noble metals on polymers, the chemical interaction at room temperature and above occurs between metal clusters and the polymer. This not only leads to a significant drop of the detectable interfacial area but may change the mode of interaction significantly because the chemistry of clusters and single atoms is not expected to be the same. The observation of chemical interactions of isolated noble metal atoms and polymer surfaces requires the deposition at much lower temperatures<sup>44</sup>.

For highly reactive metals, i.e. the transition metals Cr<sup>34, 39, 45</sup> and Ti<sup>46-48</sup>, the rare-earth metal Ce<sup>49</sup>, and Al<sup>50-52</sup>, the available experimental data show clear signs of strong chemical reactions with polymers, involving the formation of new compounds, at coverages near one monolayer and higher. It has been argued<sup>35, 36</sup> that the data for polyimide do not imply reactive metals like Cr and Ti to be bonded directly to the polymer but rather suggest a disruption of the polyimide and the formation of oxidic, nitridic, and carbidic compounds. Co was also found to react strongly with PMDA-ODA<sup>53</sup>. Ni appears to be much less reactive but more reactive than Cu<sup>11, 54</sup>.

The alkali metals K<sup>36</sup> and Cs<sup>55</sup> have been demonstrated to reduce PMDA-ODA by transferring an electron to the PMDA unit of the polymer. Dianion formation was also observed at high alkali metal concentrations.

The high reactivity of Cr, Ti, Al, and Co in the high-coverage regime does not necessarily imply that individual metal atoms are strongly bound to polymer chains. Based on recent NEXAFS measurements of the very early stages of interface formation, Strunskus et al.<sup>36</sup> ruled out purely physical interactions between Cr and polyimide and discussed  $\pi$ -complex formation<sup>44</sup> as one possible interaction mechanism. On the other hand, the fact that an intermixing layer was observed at the Al-polyimide interface in cross-sectional TEM studies<sup>9, 11</sup> points to relatively weak interactions of this reactive metal at very low coverages. XPS and TEM experiments carried out in our group in the Cr-polyimide system at very low Cr coverages also show short-range intermixing at the interface. However, the absence of long-range diffusion even after very slow deposition at elevated temperatures in conjunction with the lack of any influence of the deposition rate on the extent of intermixing (cf. Section 5) clearly point to strong chemical interactions<sup>56</sup>.

#### 5. DIFFUSION

A strong correlation between reactivity and mobility of metal atoms was found in surface spectroscopy experiments, where the metal was deposited at room temperature, and the drop of the metal intensity was measured after annealing. While substantial intensity drops, reflecting appreciable metal mobility, were observed for noble metals<sup>37, 54, 57</sup>

<sup>59</sup>, interfaces of polymers with Cr and Ti proved to be thermally stable<sup>9, 46, 54</sup>. Al showed features of some mobility<sup>9, 51</sup>, and the mobility of Ni turned out to be somewhere in between that of Al and Cu. It has to be pointed out that the metal mobility reflected in a drop of the metal intensity in surface analytical techniques can not necessarily be taken as evidence of metal diffusion into the polymer bulk but is often caused by metal clustering at the surface (see Section 5).

The above mentioned ability of K and Cs to reduce polymers proved to have drastic consequences on the diffusion behavior. Since positive ions repel each other their diffusion is not impeded by the formation of immobile clusters. Moreover, positive ions are much smaller than the neutral atoms. As a result, these ions were found to be highly mobile in polymers, and almost uniform K and Cs distributions were observed by means of angular-resolved XPS<sup>55</sup> and FT-IRAS<sup>36</sup> in polyimide films of appreciable thickness.

First direct evidence of noble metal diffusion and aggregation in the polymer bulk has been provided by cross-sectional TEM studies of interface formation between Cu and polyimide (PMDA-ODA). In these studies LeGoues et al.<sup>11</sup> observed marked clustering of Cu at considerable distances below the polyimide surface after metal deposition at elevated temperatures (but still well below  $T_g$ ) and low deposition rates. However, no clustering in the bulk was observed at high deposition rates and even elevated temperatures. After room temperature deposition and subsequent annealing no metal particles were detected, either. Investigations carried out in our group<sup>15</sup> have essentially confirmed these early results and have shown that other noble metal/polymer systems, e.g., Ag/PMDA-ODA polyimide<sup>13, 60, 61</sup> and Au/TMC polycarbonate<sup>21, 62</sup>, exhibit a similar behavior.

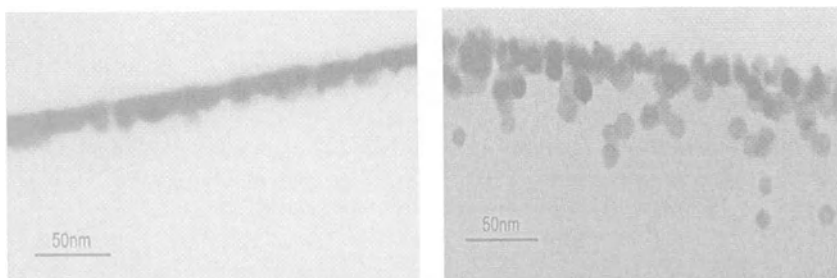


**Figure. 5** Cross-sectional TEM micrographs showing the striking differences in the copper diffusion characteristics between Cu deposition at room temperature (8 nm at 0.16 nm/min) followed by subsequent annealing at 350 °C for 30 min (left) and very slow evaporation of Cu (4 nm at 0.16 nm/min) at 350 °C (right).

A striking example demonstrating the crucial role of the metallization conditions on the interfacial structure is given in Fig. 5. While deposition of Cu at a very low rate at 350 °C produces a rather spread-out interface implying pronounced Cu diffusion (Fig. 5 right), deposition at room temperature and subsequent annealing at the same temperature results in a sharp interface without cluster formation inside the polyimide (Fig. 5 left)<sup>15</sup>. We point out that the metal films in Fig. 5 are still not continuous despite the relatively

large nominal metal coverage of about 30 monolayers. The impression of a continuous film is a consequence of the finite thickness of the samples of 40–100 nm, depending on the cutting procedure. Upon tilting, isolated and connected clusters are clearly visible.

The results depicted in Fig. 5 and corresponding results obtained for other noble metal systems (for a recent review see Ref. 14) show that metal clustering at the surface effectively impedes metal diffusion into the bulk and strongly suggests that no significant metal diffusion into the polymers is expected from a continuous film or an arrangement of large clusters. This conclusion is also corroborated by the pioneering medium energy ion scattering (MEIS) experiments of Cu diffusion in polyimide by Tromp et al.<sup>10</sup>. On the other hand, the absence of clusters in cross sectional TEM images does not allow one to rule out diffusion of metal atoms into polymers and the formation of small clusters that are not detectable in TEM.

To study atomic diffusion we have employed a very sensitive radiotracer technique in conjunction with ion-beam microsectioning. A very high depth resolution of typically 3 to 4 nm can be achieved by use of argon ions of energies as low as 100–200 eV<sup>63</sup> (as opposed to several keV in secondary ion mass spectrometry).

Representative penetration profiles are shown in Fig. 6. Here the logarithm of the activity of <sup>198</sup>Au is plotted versus the square of the penetration depth  $x$ . On this scale ordinary diffusion of the tracer according to the thin-film solution of Fick's second law,

$$c(x) = \text{const.} \exp\left(-\frac{x^2}{4Dt}\right), \quad (5)$$

leads to a straight line of slope  $1/4Dt$ . In eq. (5)  $D$  is the tracer diffusivity and  $t$  the diffusion time. It is obvious from Fig. 6 that Au diffuses deeply into polyimide during deposition at elevated temperatures. However, the profiles are not Gaussian. A nearly Gaussian profile has only been obtained after evaporation of Ag onto a hot polymer sample at an extremely low rate, where metal aggregation does not play a dominant role. At higher deposition rates all penetration profiles obtained so far exhibit the feature seen in Fig. 6 that most of the metal deposit is located at, or very close to, the surface, and the fraction of atoms that diffuse over large distances and contribute to the linear range is very small (note the logarithmic scale). Metal diffusion into the bulk is only detectable because of the high sensitivity of the radiotracer technique. Nevertheless, diffusion of traces of Cu into Si devices may cause damage in ultra large scale integrated chips if it is not effectively blocked by a barrier. Penetration profiles of a similar shape have been recorded in various measurements for noble-metal tracers in polyimides<sup>14, 61, 64, 65</sup> and polycarbonates<sup>66, 67</sup>. Only the ratio of metal in the near surface region and in the tail varied from case to case.

Monte Carlo simulations have shown that the dominant role of the deposition rate, which is not observed in ordinary diffusion, is a direct consequence of the interplay of atomic diffusion and aggregation<sup>14, 68, 69</sup>. Simulated metal concentration profiles and simulated “TEM images” were found to exhibit the characteristics observed Monte Carlo simulations have shown that the dominant role of the deposition rate, which is not observed in ordinary diffusion, is a direct consequence of the interplay of atomic diffusion and aggregation<sup>14, 68, 69</sup>. Simulated metal concentration profiles and simulated “TEM im-

ages" were found to exhibit the characteristics observed in the experiments if one incorporated the condition that stable clusters form whenever metal atoms encounter each other on their diffusion path. This condition is implied by our observation of a critical cluster size of  $i = 1$  (see Section 3).

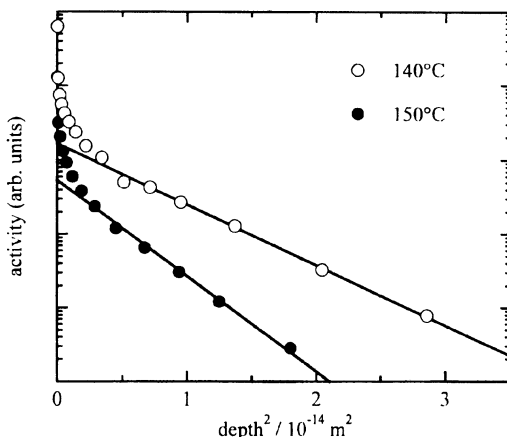


**Figure 6.** Typical penetration profiles for  $^{198}\text{Au}$  in bisphenol-A polycarbonate at 140 °C and 150 °C (for details see Ref. 14 or 66).

An example is given in Fig. 7. The Monte Carlo simulations also reflect the experimental observation that the total metal concentration found at large concentration depth decreases strongly with increasing deposition rate due to the metal immobilization through clustering <sup>14</sup>. This is illustrated in Fig. 8, where the fraction of metal atoms at depths of 3 nm and 30 nm is plotted against the deposition time ( $\propto 1/\text{rate}$ ). One can draw the conclusion that at industrial metallization rates only traces of noble metal are to be expected in the polymer bulk. As mentioned earlier these trace amounts can still cause device failure in chip interconnects involving organic low-k dielectrics and, hence, call for diffusion barriers.

Based on the notion, suggested by the Monte Carlo simulations and the experiments described in this article, that metal diffusion into polymers is an interplay between atomic diffusion and aggregation the extended linear tails in the low-concentration range of the radiotracer profiles (see Fig. 6) were attributed to diffusion of isolated metal atoms. Tracer diffusivities for noble metals in polyimides and polycarbonates, determined from the linear tails of penetration profiles similar to those in Fig. 6, are summarized in Refs. 14 and 33. An Arrhenius plot for diffusion of Cu and Ag in the polyimide PMDA-ODA and of Cu in the polyimide BPDA-BDA is shown in Fig. 9, together with diffusivities of O<sub>2</sub>, CO<sub>2</sub>, and H<sub>2</sub>O. Our first results from ion-beam depth profiling in conjunction with X-ray photoelectron spectroscopy on Cu diffusion in SiLK® indicate that Cu diffusion is more than an order of magnitude slower in SiLK® than in the polyimide PMDA-ODA at

315 °C<sup>28</sup>. This is in accord with the higher adsorption energy of Cu on SiLK®, discussed in Section 3, which indicates stronger interaction.

One notes that the diffusivities of noble-metal atoms are many orders of magnitude smaller than those of simple gas molecules of comparable size. This points to important contributions from metal interactions with the polymer even for noble metals. Substantial interaction between noble metal atoms and polymers are also reflected in the relatively high adsorption energies discussed in Section 3. Based on a detailed analysis of the diffusion behavior we have attributed the drastic slowing down of atomic mobility of metals in comparison to non-interacting gas molecules to metal-atom-induced temporary crosslinking<sup>14, 66</sup>. As discussed in Refs. 14 and 66 this is consistent with several observations reported in the literature. It was reported, for instance, that polyimide-polyamide copolymers could no longer be dissolved in typical solvents after fine dispersion of Ag and Pd had been incorporated (by reduction of the corresponding metal salts)<sup>70</sup>.

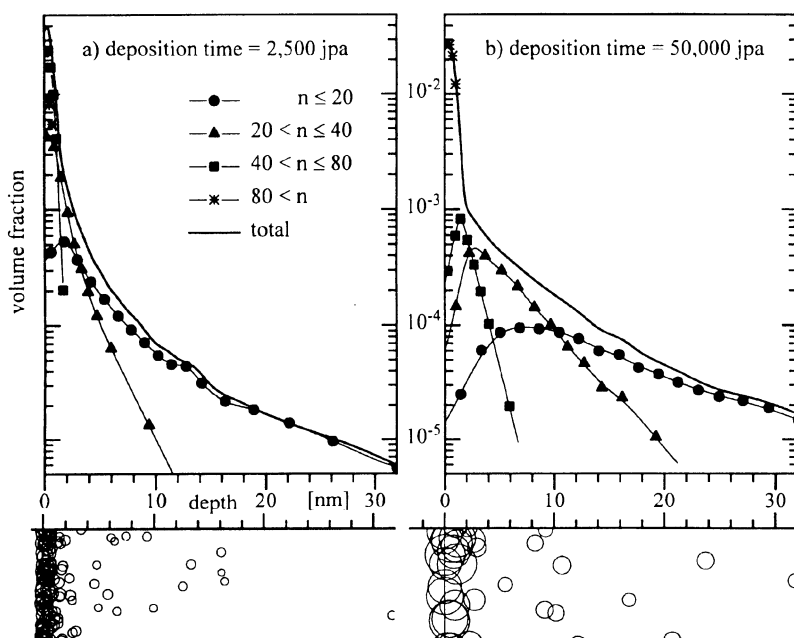


**Figure 7** Simulated penetration profiles for the total metal concentration and for metal clusters of different size ranges, indicated by the number  $n$  of atoms, after deposition during (a) 2,500 jpa and (b) 50,000 jpa and subsequent annealing. The total annealing time of  $5 \times 10^5$  jpa (jumps per free atom), the nominal metal coverage of 0.2 monolayers, and the ratio of surface and bulk diffusivity of  $D_s/D_b = 60$  are equal for both runs. The figures at the bottom are cross-sectional views showing clusters that have formed in a section of the simulated volume. The calibration of the deposition rates depends on the experimental diffusion temperature. For diffusion of noble metals in polyimides and polycarbonates a deposition rate of the order of 1 ML/min typically corresponds to 100 jpa in the vicinity of the glass transition temperature (see Ref. 14 for details).

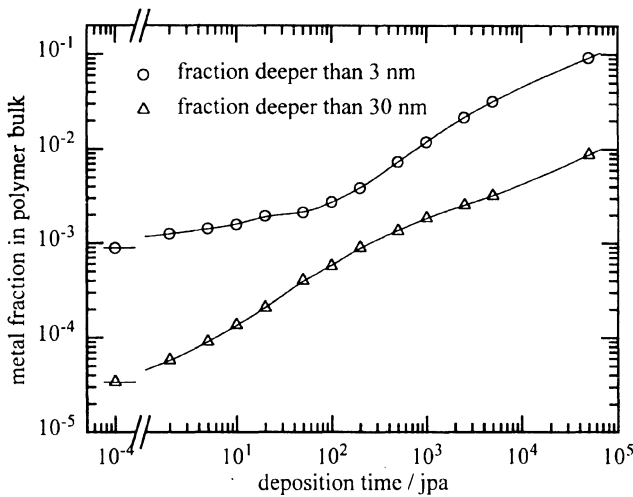


**Figure 8.** Total metal concentration found in the computer simulations at penetration depths > 3 nm and > 30 nm, respectively, as function of the metal deposition time in units of jpa (see Fig. 7 for conversion of jpa in actual deposition rates).

Despite the available evidence of substantial interaction of noble metal atoms with polymers one cannot exclude that the diffusivities determined from the linear tails of the radiotracer profiles reflect diffusion of small clusters rather than atomic diffusion. This particularly holds for the measured Ag diffusivities because the tracer concentration in the experiments with Ag typically corresponds to several monolayers (while only  $\approx 1/4$  monolayer was used in the Cu tracer studies). As discussed in Section 3 the differences in the ratios of  $D_{\text{Cu}}/D_{\text{Ag}}$  for surface and bulk diffusion also point to this possibility. This view is further corroborated by our recent radiotracer measurements of  $^{110m}\text{Ag}$  in TMC polycarbonate<sup>71</sup>. These measurements indeed suggest that the diffusivities reported in Ref. 67 are those of small clusters and that single Ag atoms, which are only present in trace amounts, are mobile even at room temperature.

For reactive metals like Cr and Ti long-range diffusion appears to be blocked completely after chemical interactions resulting in the formation of strong bonds to the polymer chains (see Section 4). As discussed above, interfaces of polymers with Cr and Ti proved to be sharp and thermally stable<sup>9, 46, 54</sup>, and these metals were shown to act as diffusion barriers for Cu diffusion. No indications of Cr diffusion into polyimide were found in XPS studies even after very slow evaporation near the glass transition temperature<sup>56</sup>. Al showed features of some mobility<sup>9, 51</sup>, and the mobility of Ni turned out to be somewhere in between that of Al and Cu.

In contrast to the numerous investigations demonstrating the very effective impediment of metal diffusion into polymers after metal aggregation there are many publications reporting strong diffusion from continuous metal films into polymers. For instance, the drop of the metal intensity in XPS<sup>46, 75, 76</sup> and the broadening of metal spectra in Rutherford backscattering (RBS)<sup>75, 77</sup> upon annealing have been taken as evidence for metal

diffusion, and it has been concluded from angle-resolved XPS measurements that Cu diffuses strongly into the low-k fluoropolymers Teflon-AF1600<sup>TM</sup><sup>78</sup> and FLARE<sup>TM</sup><sup>76</sup>. We have shown, however, that XPS results on metal diffusion into polymers can be rather misleading without complementary microstructural observations and careful investigation of the long-time behavior of the metal intensity<sup>15</sup>. Concerning the RBS results, it was recently demonstrated that metal clustering at the polymer surface may mimic metal diffusion into the polymer bulk<sup>79</sup>. Clustering is driven by the reduction in surface energy and may even take place after annealing of continuous thin metal films<sup>79</sup>.

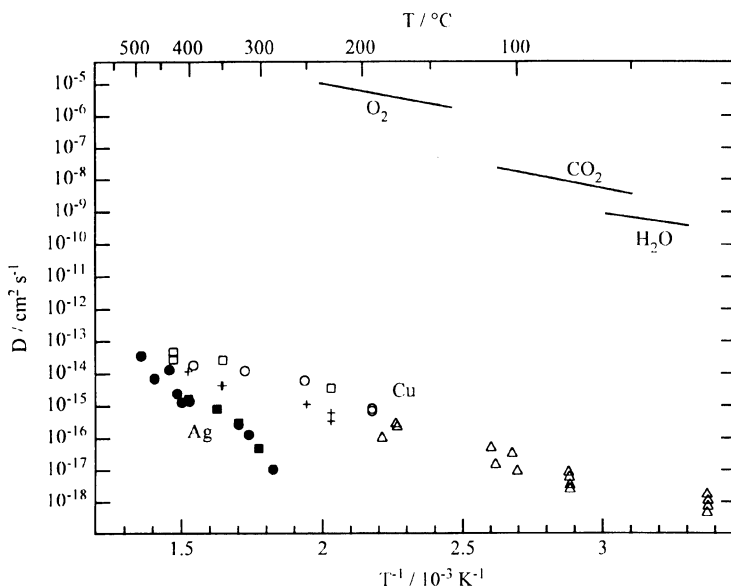


**Figure 9.** Diffusion coefficients versus reciprocal temperature for diffusion of <sup>67</sup>Cu (open circles from Refs. 61, 64, open squares from Refs. 65, 72) and <sup>110m</sup>Ag (solid squares from Ref. 32, solid circles from Ref. 73) in PMDA-ODA polyimide, Cu in Kapton (open triangles, from RBS in combination with ion implantation<sup>74</sup>) and of <sup>67</sup>Cu in BPDA-PDA polyimide (crosses, from Refs. 65, 72). Arrhenius plots for diffusion of O<sub>2</sub>, CO<sub>2</sub>, and H<sub>2</sub>O in Kapton<sup>33</sup> are shown for comparison.

In order to demonstrate the absence of significant diffusion from a continuous metal film we have evaporated Cu, e.g., with nominal coverages of several monolayers (ML) onto polyimide at room temperature. Subsequently, the samples were annealed at high temperatures, and the Cu 2p<sub>3/2</sub>/C 1s peak intensity ratio was measured as function of the annealing time. An example is given in Fig. 10. Similar measurements were also performed for Au on TMC polycarbonate<sup>62</sup>. Without further quantitative evaluation the occurrence of the plateau in the intensity ratio unambiguously demonstrates Cu immobilization. Any significant copper diffusion into polyimide would lead to a drop of the Cu

$2p_{3/2}$  intensity because of the very short inelastic mean free path of the photoelectrons. Moreover, the C 1s intensity would increase if Cu disappeared from the surface. The inset in Fig. 10 demonstrates that no deviations from the plateau value were detected even after prolonged annealing for 30 h at 350 °C. TEM investigations show that the Cu immobilization is due the formation of Cu clusters, which already form during metal deposition at room temperature. Annealing at 350 °C causes the clusters to grow. As discussed above Cu clustering at polymer surfaces arises from the high cohesive energy of the metal and the low metal-polymer interaction energy. Apparently, the cohesive energy is high enough to immobilize the Cu atoms by preventing their dissociation from the clusters at temperatures far below the metal boiling point. Cluster growth does not appear to occur by ordinary Ostwald ripening, but by a temperature-induced mobility of smaller clusters and cluster coalescence, thus causing a plateau in the Cu  $2p_{3/2}$ /C 1s peak intensity due to the decrease in the cluster mobility and the increase in the cluster distance with increasing cluster size<sup>57</sup>.

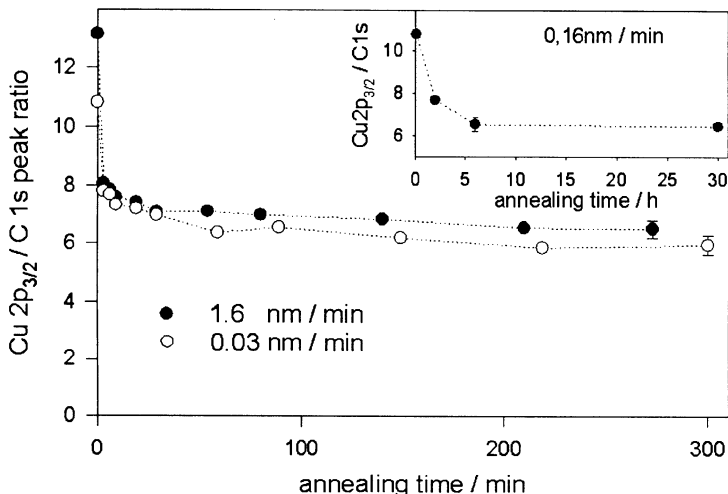


**Figure 10.** Evolution of the Cu  $2p_{3/2}$ /C 1s peak intensity ratio in XPS upon annealing at 350 °C after deposition of 1.6 nm Cu (7 ML nominal coverage) onto polyimide at room temperature at rates of 1.6 nm/min and 0.03 nm/min. The inset shows results from a separate experiment involving room temperature deposition (1.6 nm, 0.16 nm/min) and prolonged annealing for 30 h at 350 °C. The leveling off is a clear indication of Cu immobilization.

Simple calculations<sup>15, 80</sup> show that the cluster growth observed in TEM is the main reason for the small drop of the Cu  $2p_{3/2}$ /C 1s peak intensity ratio of about 40 % during annealing in Fig. 10. Obviously, even in the initial annealing stages prior to complete Cu immobilization Cu diffusion into the polymer plays at best a minor role.

On the other hand, recent capacitance-voltage measurements involving Cu/oxide/polymer/oxide/Si capacitors suggest drift of Cu<sup>+</sup> ions into poly(arylene ether)

and fluorinated polyimide at elevated temperatures in strong electric fields of the order of  $10^6$  V/cm<sup>81, 82</sup>. The drift current turned out to drop rapidly within several minutes and was not observed after incorporation of thin nitride barrier layers<sup>82</sup>. Benzocyclobutene proved to be much less prone to Cu<sup>+</sup> ion drift<sup>81-83</sup>. While the drift of Cu<sup>+</sup> ions through the polymers has not yet been demonstrated directly, the interpretation of the drift experiments does not seem to be in conflict with the present view of metal diffusion in polymers, since no drift was observed at zero and low electric fields. Moreover, the oxide layer between Cu and the polymer most likely acts as a catalyst for the formation of Cu<sup>+</sup> ions, which are injected into the polymer in the electric field. These Cu<sup>+</sup> ions are expected to be highly mobile and, unlike neutral Cu atoms, unable to form immobile clusters because of their repulsion. This interpretation is supported by the aforementioned strong diffusion of K<sup>+</sup> and Cs<sup>+</sup> ions into the polyimide PMDA-ODA<sup>36, 55</sup>. Unlike noble metals, K and Cs are both able to reduce polyimide.

## 6. EMBEDDING OF NANOCLUSTERS AND SURFACE GLASS TRANSITION

As discussed in Section 1 there is a driving force for embedding metal clusters at the polymer surface into a polymer if inequality (1) holds. However, while diffusion of metal atoms into the polymer bulk can occur in the glassy state, embedding of clusters of some nm should certainly require long-range chain mobility. Therefore, the onset of embedding is expected to take place at the surface glass transition temperature of the polymer.

During the last years there has been much interest in the effects of the free surface and confinement on polymer dynamics particularly on the liquid to glass transition<sup>84-86</sup>. Concerning the glass transition at the surface, conflicting results have been reported. For instance, a pronounced depression of the glass transition temperature of 20 – 60 K was seen for polystyrene by means of positron annihilation Doppler broadening<sup>87</sup>, scanning viscoelasticity microscopy<sup>88</sup>, and by studying the  $T_g$  as function of film thickness variation<sup>89</sup>. In contrast, thermal expansion data measured via X-ray reflectivity indicate a pronounced increase in  $T_g$ <sup>90</sup>. Theoretical work also resulted in conflicting conclusions<sup>85, 86</sup>.

We have recently demonstrated that the embedding of noble metal nanoclusters into polymers can indeed be made instrumental as a potential probe of the surface glass transition temperature<sup>91</sup>. Spherical clusters in the range of 1 – 4 nm, for instance of Cu, were produced by thermal evaporation onto the polymer films at room temperature. Embedding of the clusters upon heating was monitored *in situ* by means of X-ray photoelectron spectroscopy. The size of nanoclusters was determined by an indirect method based on the measurement of the ratio of two XPS lines of the same metal with different kinetic energies and hence different attenuation lengths of the photoelectrons in the metal. Details of this method are given in Ref. 27. The actual particle embedding depth was determined from the XPS intensity ratio C1s/Cu2p in case of Cu by assuming that self-attenuation of the Cu2p intensity due to cluster coalescence is negligible compared to the attenuation by embedding near the surface glass transition temperature. The XPS measurements were complimented by microstructural investigations based on cross-sectional TEM and atomic force microscopy as well as by ion-beam depth profiling in conjunction

with XPS monitoring of the Cu intensity<sup>91</sup>. These investigations clearly confirmed all conclusions drawn from XPS on cluster size and the embedding process.

An example is shown in Fig. 11, where the Cu2p intensity, normalized to its value at room temperature, is plotted as function of the inverse absolute temperature for two polycarbonates. In both cases embedding of the Cu clusters starts well below the bulk glass transition temperature (48 K for TMC-PC and 20 K for BPA-PC). This suggests a considerable depression of the glass transition temperature at the surface.

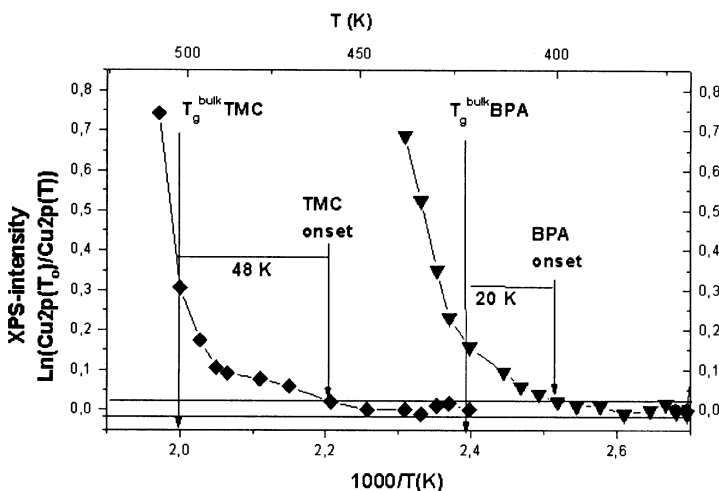


**FIGURE 11.** Change in the XPS Cu2p( $T_0$ )/Cu2p( $T$ ) intensity ratio for the systems Cu/TMC-, BPA-polycarbonate as a function of the annealing temperature (heating rate 0.5 K/min,  $T_0=298$  K).  $\ln(\text{Cu2p}(T_0)/\text{Cu2p}(T))$  is proportional to embedding depth of the Cu clusters. The solid line represents the  $1\sigma$  deviation from the base line in the glassy state.

There are various indications that the onset temperature of cluster embedding can indeed be identified as the surface glass transition temperature<sup>91</sup>. The embedding temperature correlates with the bulk  $T_g$  and has a molecular weight dependence in accord with expectations. Moreover, the quantitative evaluation of the embedding kinetics yields a viscosity of the right order of magnitude for an amorphous polymer close to but above the glass transition. We also showed that the noble metal nanoclusters do not significantly affect the polymer dynamics by going from Cu clusters to non-interacting Au clusters without seeing changes in the onset temperatures of embedding.

A plausible explanation of the  $T_g$  depression at the surface can be given in terms of the enhanced molecular motion resulting from the additional degrees of freedom.

## 7. INTERFACE TAILORING AND ADHESION

In the previous sections we have shown that the morphology of metal-polymer interfaces can vary in a very wide range, e.g., from almost step-like to spread out over large distances, depending on the preparation conditions. This know-how can be used to tailor the interfacial morphology for particular purposes<sup>92</sup>. In this section we report on some experiments on the enhancement of adhesion of Au and Cu on polycarbonates, for example. The noble metals Cu and particularly Au were chosen because their adhesion to untreated polymer surfaces is expected to be very poor as a result of the low reactivity. The main objective of the ongoing studies is to explore the enhancement of adhesion that can be achieved without chemical pretreatment of the polymer surface by maximizing the contact area between metal and polymer and by taking advantage of mechanical interlocking.

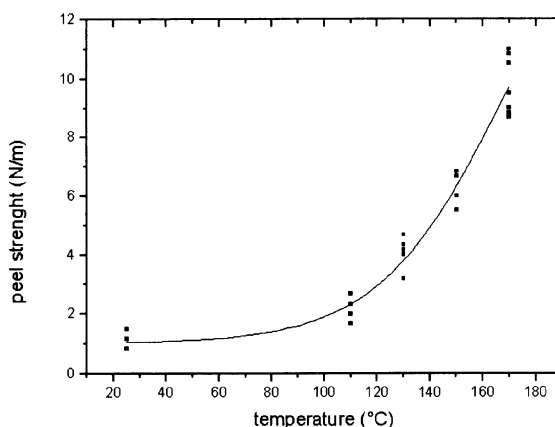


**FIGURE 12.** Peel strength of Cu, deposited at room temperature, on BPA-PC as function of annealing temperature. The annealing time was 30 min.

After evaporation at room temperature both metals exhibited peel strengths of typically  $< 2 \text{ N/m}$ , reflecting indeed very poor adhesion<sup>21, 92</sup>. Annealing of the samples after metal deposition well below the glass transition temperature, did not affect the peel strength significantly. However, the peel strength was found to increase strongly upon annealing above the glass transition temperature. An example is depicted in Fig. 12. In accord with the aforementioned reduction of  $T_g$  near the surface an improvement of adhesion can already be achieved by annealing close to but still below the bulk glass transition temperature. Investigations of the kinetics have shown that the adhesion enhancement is a very slow process occurring on a time scale of hours in the rubbery state near the glass transition temperature.

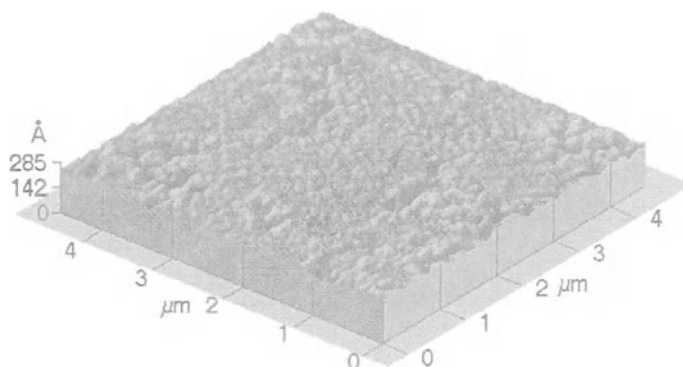


**FIGURE 13.** AFM image of a Cu surface originally in contact with BPA-PC after peeling and dissolution of polymer residues. The sample was annealed at 200 °C for 200 min.

Atomic force microscopy and XPS investigations of the samples after peeling revealed small polymer residues on the metal side and no metal on the polymer side, indicating that the failure occurred at least partially within the polymer layer close to the interface. A considerable roughness on the metallic side and the occurrence of channels was observed by means of AFM after removal of the polymer residues by dissolution.

We interpret the strong adhesion enhancement as a combination of increase in metal-polymer contact area and mechanical interlocking. After preparation at room temperature the metal and the polymer are expected not to be in perfect contact with each other because the metal growth is mainly controlled by metal-metal interactions leading to the observed cluster formation and coalescence. Therefore, the initial contact area should be small on a microscopic scale. In particular, the formation of small voids and channels is expected at the metal-polymer interface, since at room temperature, well below the glass transition temperature, the polymer chains have no long-range mobility. Heating above  $T_g$  results in long-rang mobility of the polymer chains, which can now increase the contact area and fill the voids and channels. We attribute the improvements in adhesion at long annealing times to latter process. The time dependence of the increase in peel strength also provides evidence that the adhesion enhancement is caused by the increased mobility of the polymer chains and not just by a chemical reaction occurring at the elevated temperatures. In the latter case, we would expect an increase in peel strength to its maximum value within a few minutes or less.

## 8. SUMMARY AND CONCLUSIONS

In this review we discuss investigations that have contributed to the present understanding of metal-polymer interface formation. Emphasis is placed on work carried out by our group in Kiel involving surface spectroscopy, radiotracer measurements, electron and atomic force microscopy, Monte Carlo simulations, and a novel technique to determine condensation coefficients.

For noble metals their relatively weak interaction with polymers gives rise to very small condensation coefficients on all polymers at elevated temperatures and on untreated low-k fluoropolymers such as Teflon AF even at room temperature. The weak interaction of noble metals and other metals of low reactivity with polymers together with the high metal cohesive energy and the much lower polymer cohesive energy lead to a very strong aggregation tendency. Therefore, these metals exhibit a Volmer-Weber surface growth mode with a critical nucleus consisting of only one atom. The strong aggregation tendency effectively impedes metal diffusion into polymers. In particular, no significant diffusion of noble metal into polymers is expected from continuous metal films unless conditions like interfacial reactions, the presence of an oxide layer between metal and polymer, or an external electrical field promote the formation of metal ions. On the other hand, noble metals have a high atomic mobility, and diffusion of metal atoms into polymers occurs at very low deposition rates, and cannot be avoided during the initial deposition stage. This calls for barriers in chip applications. Reactive metals like Cr and Ti form relatively sharp interfaces with polymers and are candidates for diffusion barriers.

The strong variability of the interfacial structure as a result of the preparation conditions can be instrumental in tailoring interface properties. Post-deposition annealing near and above the polymer glass transition temperature, for instance, leads to a strong improvement of noble metal adhesion, which was attributed to an increase in the metal-polymer contact area and mechanical interlocking. Interface tailoring may also involve the formation of metallic nanoclusters on the polymer surface and embedding of these clusters into the polymer. This process lends itself as a probe of the glass transition temperature  $T_g$  at the surface. A pronounced depression of  $T_g$  was observed at surfaces of polycarbonates and interpreted in terms of the additional degrees of freedom for molecular motion at the surface.

## ACKNOWLEDGMENTS

We gratefully acknowledge financial support by the Volkswagen-Stiftung, Deutsche Forschungsgemeinschaft, and Technologie-Stiftung Schleswig-Holstein.

## REFERENCES

1. Metallized Plastics: Fundamentals and Applications, edited by K. L. Mittal (Marcel Dekker, New York, 1998).
2. S.P. Kowalczyk, in Metallization of Polymers, edited by E. Sacher, J. Pireaux and S.P. Kowalczyk (ACS Symposium Series **440**, American Chem. Soc., Washington DC, 1990) p. 10.
3. Polymers for Electronic and Photonic Applications, edited by C. P. Wong (Academic Press, Boston, 1993).
4. Polyimides: Fundamental Aspects and Technological Applications, edited by M. Ghosh and K. L. Mittal (Marcel Dekker, New York, 1996).
5. M. T. Bohr, IEEE IEDM, 241 (1995).
6. Low-Dielectric Constant Materials and Applications in Microelectronics IV, edited by C. Chiang, P. S. Ho, T.-M. Lu and J. Wetzel, Mat. Res. Soc. Symp. Proc. **511** (1998).

7. P. H. Townsend, S. J. Martin, J. Godschalk, D. R. Romer, D. W. Smith, Jr., D. Castillo, R. deVries, G. Buske, N. Rondan, S. Froelicher, J. Marshall, E. O. Shaffer, and J-H. Im, *Mat. Res. Soc. Symp. Proc.*, **476**, 9 (1997).
8. European Smiconductor, May 2000, 7.
9. P. S. Ho, R. Haight, R. C. White, B. D. Silverman and F. Faupel, in *Fundamentals of Adhesion*, edited by L. H. Lee, (Plenum Press, New York, 1991) p. 383.
10. R. M. Tromp, F. K. LeGoues and P. S. Ho, *J. Vac. Sci. Technol. A* **3**, 782 (1985).
11. F. K. LeGoues, B. D. Silverman and P. S. Ho, *J. Vac. Sci. Technol. A* **6**, 2200 (1988).
12. S. P. Kowalczyk, Y. H. Kim, G. F. Walker and J. Kim, *Appl. Phys. Lett.* **52**, 375 (1988).
13. F. Faupel, in *Polymer-Solid Interfaces*, edited by J. J. Pireaux, P. Bertrand and J. L. Brédas (IOP Publishing, 1992) p. 171.
14. F. Faupel, R. Willecke and A. Thran, *Mater. Sci. Eng. R* **22**, 1-55 (1998).
15. M. Kiene, T. Strunskus, R. Peter, and F. Faupel, *Adv. Mater.* **10**, 1357 (1998).
16. Y. Inoue, M. Inata, M. Fujii, S. Hayashi, K. Yamamoto, *Thin Solid Films* **372**, 169 (2000).
17. R. M. Joyce-Wöhrmann, T. Hentschel, H. Müntstedt, *Adv. Eng. Mater.*, **2** (6), 380-386, (2000).
18. S. Nie, S. R. Emory, *Science*, **275**, 1102 (1997).
19. G. J. Kovacs and P. S. Vincett, *J. of Colloid and Interface Sci.*, **90**, 335 (1982).
20. G. J. Kovacs and P. S. Vincett, C. Tremblay and A. L. Pundsack, *Thin Solid Films*, **101**, 21(1983).
21. C. v. Bechtolsheim, V. Zaporjchenko, and F. Faupel, *Appl. Surf. Sci.*, **151** (2000), 1-2, 119 - 128.
22. S. P. Kowalczyk, Y. H. Kim, G. F. Walker, and J. Kim, *Appl. Phys. Lett.* **52**, 375 (1988).
23. D. J. Godbey, L. J. Buckley, A. P. Purdy, and A. W. Snow, *Thin Solid Films* **308-309**, 470 (1997).
24. see, e.g., K. D. Rendulic, *Surface Science* **272**, 34 (1992).
25. A. Thran, M. Kiene, V. Zaporjchenko, and F. Faupel, *Phys. Rev. Lett.* **82**, 1903 (1999).
26. V. Zaporjchenko, K. Behnke, A. Thran, T. Strunskus, and F. Faupel, *Appl. Surf. Sci.* **144-145**, 355 (1999).
27. V. Zaporjchenko, K. Behnke, T. Strunskus, and F. Faupel, *Surf. a. Interf. Anal.* **30**, 439-443 (2000).
28. V. Zaporjchenko, J. Erichsen, T. Strunskus, K. Behnke, F. Faupel, M. Baklanov and K. Maex to be published in *MRS Proceedings Symposium L* (2001).
29. V. Zaporjchenko, J. Erichsen, J. Zekonyte, A. Thran, T. Strunskus, and F. Faupel, in this proceedings
30. J. A. Venables, *Surf. Sci.* **299-300**, 798 (1994).
31. R. Poteau, J. L. Heully, and F. Spiegelmann, *Z. Phys. D* **40**, 479 (1997).
32. F. Faupel, *Adv. Mater.* **2**, 266 (1990).
33. F. Faupel and G. Kroll, in: *Diffusion in Non-Metallic Solids*, Landolt-Börnstein, New Series, W. Martenssen (Ed. in Chief), Volume III/33B1, D. L. Beke (Ed.), Springer-Verlag, Berlin, Heidelberg, New York 1999.
34. N. J. DiNardo, *Metallized Plastics 1: Fundamental and Applied Aspects*, edited by K. L. Mittal and J. R. Susko (Plenum Press, New York, 1989).
35. L. J. Matienzo and W. J. Unertl, in *Polyimides: Fundamental Aspects and Technological Applications*, edited by M. Ghosh and K. L. Mittal (Marcel Dekker, New York, 1996).
36. T. Strunskus, M. Grunze, G. Kochendoerfer and Ch. Wöll, *Langmuir*, **12**, 2712 (1996).
37. H. M. Meyer, S. G. Anderson, Lj. Atanasoska and J. H. Weaver, *J. Vac. Sci. Technol. A* **6**, 30; 1002 (1988).
38. N. J. DiNardo, J. E. Demuth and T. C. Clarke, *Chem. Phys. Lett.*, **121**, 239 (1985).
39. J. L. Jordan-Sweet in *Metallization of Polymers*, edited by E. Sacher, J. Pireaux and S.P. Kowalczyk (ACS Symposium Series **440**, American Chem. Soc., Washington DC, 1990).
40. A. R. Rossi and B. D. Silverman in J. H. Lupinski and R. S. Moore (eds.), *Polymeric Materials for Electronic Packaging and Interconnection*, ACS Symposium Series **407**, American Chemical Society, Washington DC (1989).
41. L. J. Gerenser, *J. Vac. Sci. Technol. A* **8**, 3682 (1990).
42. A. J. Pertsin, Y. M. Pashunin, *Appl. Surf. Sci.*, **47**, 115 (1991).
43. G. D. Davis, B. J. Rees, P. L. Whisnant, *J. Vac. Sci. Technol. A* **12**, 2378 (1994).
44. T. Strunskus, M. Kiene, R. Willecke, A. Thran, C. v. Bechtolsheim and F. Faupel, *Materials and Corrosion* **49**, 180 (1998).
45. J. J. Pireaux, C. Grégoire, M. Vermeersch, P. A. Thiry, M. R. Vilar and R. Caudano in E. Sacher, J. Pireaux, and S.P. Kowalczyk (eds.), *Metallization of Polymers*, ACS Symposium Series **440**, American Chem. Soc., Washington DC, p.47 (1990).
46. F. S. Ohuchi and S. C. Freilich, *J. Vac. Sci. Technol. A* **4**, 1039 (1984); *A* **6**, 1004 (1988).

47. W. N. Unertl, *High Performance Polymers* **2**, 15 (1990).
48. S. C. Freilich and F. S. Farnsworth, *Polymer* **28**, 1912 (1987).
49. J. G. Clabes, *J. Vac. Sci. Technol. A* **6**, 2887 (1988).
50. L. Atanasoska, S. G. Anderson, H. M. Meyer, Z. Lin and J. H. Weaver, *J. Vac. Sci. Technol. A* **5**, 3325 (1987).
51. P. S. Ho, P. O. Hahn, J. W. Bartha, G. W. Rubloff, F. K. LeGoues and B. D. Silverman, *J. Vac. Sci. Technol. A* **3**, 739 (1985).
52. J. J. Pireaux, M. Vermeersch, C. Grégoire, P. A. Thiry, R. Caudano and T. C. Clarke, *J. Chem. Phys.* **88**, 3353 (1988).
53. S. G. Anderson, H. M. Meyer, and J. H. Weaver, *J. Vac. Sci. Technol. A* **6**, 2205 (1988).
54. P. O. Hahn, G. W. Rubloff, J. W. Bartha, F. K. LeGoues and P. S. Ho, *Mat. Res. Soc. Symp. Proc.*, **40**, 251 (1985).
55. J. G. Clabes, M. J. Goldberg, A. Viehbeck and C. A. Kovac, *J. Vac. Sci. Technol. A* **6**, 985 (1988).
56. M. Kiene, H. Kiesbye, T. Strunskus, and F. Faupel, to be published.
57. M. Kiene, T. Strunskus, and F. Faupel in *Metallized Plastics: Fundamentals and Applications*, edited by K. L. Mittal (Marcel Dekker, New York, 1998).
58. R. G. Mack, E. Grossman and W. N. Unertl, *J. Vac. Sci. Technol. A* **8**, 3827 (1990).
59. M. Fontaine, J. M. Layet, C. Grégoire and J. J. Pireaux, *Appl. Phys. Lett.* **62**, 2938 (1993).
60. A. Foitzik and F. Faupel, *Mater. Res. Soc. Symp. Proc.* **203**, 59 (1991).
61. F. Faupel, *phys. stat. sol. (a)* **134**, 9 (1992).
62. C. v. Bechtolsheim, V. Zaporotchenko, and F. Faupel, *J. Mater. Res.*, **14**, 9 (1999).
63. F. Faupel, P. W. Hüppé, K. Rätzke, R. Willecke and T. Hehenkamp, *J. Vac. Sci. Technol. A* **10**, 92 (1992).
64. F. Faupel, D. Gupta, B. D. Silverman and P. S. Ho, *Appl. Phys. Lett.* **55**, 357 (1989).
65. D. Gupta, F. Faupel and R. Willecke, in *Diffusion in Amorphous Materials*, edited by H. Jainand and D. Gupta (The Minerals, Metals & Materials Society, 1994) p. 189.
66. R. Willecke and F. Faupel, *Macromolecules* **30**, 567-573 (1997).
67. R. Willecke and F. Faupel, *J. Polym. Sci. Polym. Phys. Ed.* **35**, 1043 (1997).
68. A. Thran and F. Faupel, *Defect and Diffusion Forum* **143-147** (1), 903 (1997).
69. B. D. Silverman, *Macromolecules* **24**, 2467 (1991).
70. L. Tröger, H. Hünnefeld, S. Nunes, M. Oehring, and D. Fritsch, *J. Phys. Chem. B* **101**, 1279 (1997).
71. A. Thran, F. Faupel, to be published.
72. D. Gupta, in *Diffusion in Thin Films*, *Encyclopedia Appl. Phys.*, **5**, (VCH Pub. Inc., New York, 1993), p 75.
73. R. Willecke, PhD thesis, University of Göttingen, 1993.
74. J. H. Das and J. E. Morris, *J. Appl. Phys.* **66**, 5816 (1989).
75. N. Y. Kim, H.-S. Yoon, S. Y. Kim, C. N. Whang, K. W. Kim, and S. J. Cho, *J. Vac. Sci. Technol. B*, **17**, 380 (1999).
76. M. Du, R. L. Opila, V. M. Donnelly, J. Sapjeta, and T. Boone, *J. Appl. Phys.* **85**, 1496 (1999).
77. J. H. Das and J. E. Morris, *IEEE Transactions on Components, Packaging and Manufacturing Technology B* **17**, 620 (1994).
78. D. Popovici, K. Piyakis, M. Meunier and E. Sacher, *J. Appl. Phys.* **83**, 108 (1998).
79. N. Marin, Y. Serruys and P. Salmon, *Nuclear Instr. and Methods in Physics Research B* **108**, 179 (1996).
80. M. Kiene, PhD thesis, University of Kiel, 1997.
81. S. S. Wong, A. L. S. Loke, J. T. Wetzel, P. H. Townsend, R. N. Vrtis, M. P. Zussman, in Ref. 9.
82. A. L. S. Loke, J. T. Wetzel, C. Ryu, W.-J. Lee and S. S. Wong, *Symposium on VLSI Technology*, Honolulu, 1998.
83. J. M. Neirynck, R. J. Gutmann, and S. P. Murarka, *Proc. CMP-MIC Conference IMIC 1999*, p. 192.
84. D.C. Allara; S. Arte and A. N. Parikh, in *Polymer Surfaces and Interfaces*, edited by W. J. Feast; H. S. Munrom, and R. W. Richards, Wiley & Sons: New York, 1993.
85. A. M. Mayes, *Macromolecules* (1994), **27**, 3114.
86. J. Baschnagel, and K. Binder, *K. Macromolecules*, **28**, 6808(1995).
87. Y. C.Jean, R. Zhang,; H. Cao, J.-P. Yuan, C.-M Huang,.. B. Nielsen, P. Asoka-Kumar, *Phys.Rev. B*, , **56**, R8459(1997).
88. N. Satomi, A. Takahara, and T. Kajiyama, *Macromolecules*, **32**, 4474 (1999).
89. J. A. Forrest, J. Mattsson, *Phys. Rev. E*, **61** (1), 53 (2000).
90. W. E. Wallace, J. H. van Zanten, and W.L. Wu, *Phys. Rev. B*, **52**, R3329 (1995).

91. V. Zaporjchenko, T. Strunkus, J. Erichsen, and F. Faupel, *Macromolecules*, **5**, 1125(2001).
92. V. Zaporjchenko, T. Strunkus, K. Behnke, C. v. Bechtolsheim, M. Kiene, and F. Faupel, *J. Adhesion Sci. Technol.*, **14**, 3, 467(2000).

# THE STUDY OF COPPER CLUSTERS ON DOW CYCLOTENE, AND THEIR STABILITY

D.-Q. Yang and E. Sacher\*

## 1. INTRODUCTION

Over the past several decades, much effort has been devoted to the study of supported metal clusters. Among the issues investigated were cluster growth mechanisms, cluster stability and electronic structure. More recently, it was found<sup>1-5</sup> that many, if not most, evaporated metals deposit onto low energy surfaces, such as low permittivity polymers, in this fashion, making this wealth of previous work<sup>6</sup> available to aid in the understanding of this process.

Here, we discuss some of our recent findings on the vapor deposition of Cu onto Dow Cyclotene, a low permittivity polymer formed by the Diels-Alder addition polymerization of (divinyl tetramethylsiloxane)-benzocyclobutene adducts<sup>7</sup>. We present our results on the growth dynamics and stability of Cu clusters, as well as their correlation with Cu film adhesion on Cyclotene whose surface has been treated in several ways so as to promote adhesion.

Clusters have been found to grow in two different ways. They may grow through the continuous deposition of new material by evaporation; this we refer to as thickness-dependence. They may also grow through the coalescence of existing clusters as they randomly diffuse by Brownian motion at any temperature; this we refer to as annealing-dependence.

## 2. EXPERIMENTAL

Cyclotene was deposited onto Si wafers and cured by raising the samples to 250°C, as previously described<sup>7</sup>. The process was carried out under N<sub>2</sub>, avoiding surface

---

\*D.-Q. Yang and E. Sacher, Groupe des couches minces, Département de génie physique, École Polytechnique, C.P. 6079, succursale Centre-Ville, Montréal, Québec H3C 3A7, Canada

oxidation. High purity Cu was evaporated in the preparation chamber of our XPS instrument, a VG ESCALAB 3 Mark II, as previously described<sup>8</sup>, and transferred to the analysis chamber without exposure to the atmosphere. Cu deposition, as measured by a deposition rate monitor, could be varied between 0.01 and 5 Å/sec. Such evaporation took place at pressures  $< 5 \times 10^{-9}$  torr, after the evaporator was stabilized and preconditioned.

XPS spectra were obtained, at pressures  $< 2 \times 10^{-10}$  torr, using non-monochromated Mg K $\alpha$  radiation, at a perpendicular take-off angle; the conditions used give a spectral resolution of  $\sim 0.7$  eV. After Shirley background removal, the peaks were separated by an in-house, nonlinear least mean squares program, using previously determined peak parameters<sup>7,8</sup>. No radiation damage was observed.

Bright field TEM images were obtained on a JEOL 2000 FX STEM, operating at 200 kV, as previously described<sup>9</sup>. AFM images were obtained on a DI Dimension 3000, in the tapping mode, as previously described<sup>9</sup>; the scan size was 500 nm and the scan rate was 1 Hz.

### 3. RESULTS AND DISCUSSION

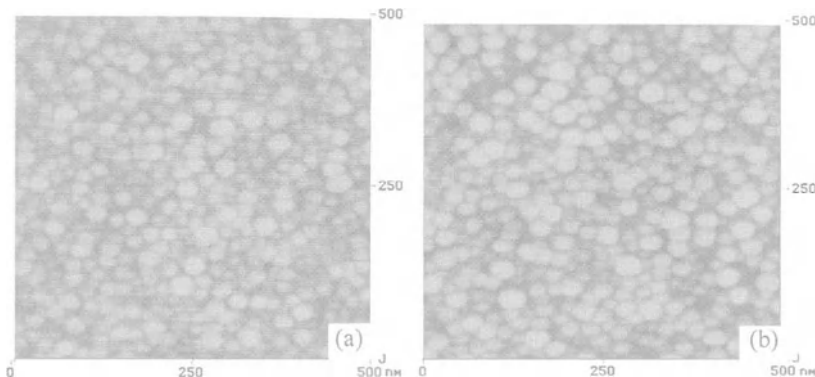


**Figure 1.** Tapping mode AFM images of Cu on untreated Cyclotene, annealed at 350°C: (a)  $t = 0$ ; (b)  $t = 60$  min. The nominal thickness is 32 Å, deposited at 0.2 Å/sec.

AFM images of a nominal 32 Å of Cu, before and after annealing at 350°C, are found in Fig. 1. The Cu forms clusters on deposition and these clusters coalesce on annealing. Cross-sectional TEM images are found in Fig. 2, where no diffusion into the bulk appears to have taken place. After deconvoluting the effect of the AFM tip<sup>10</sup>, the values obtained by both techniques are in agreement.

We obtained Cu cluster diameters and number densities from XPS Cu 2p<sub>3/2</sub>/Cu 3d intensity ratios, as previously described<sup>11</sup>. In this way, we could follow these parameters as a function of thickness (short time values), or as a function of annealing time for a given thickness. Both values were found to fit the general equation

$$d = kt^\alpha \quad (1)$$

where  $k$  and  $\alpha$  are constants and  $t$  is either the nominal Cu thickness (or deposition time) or the annealing time. This equation is based<sup>12</sup> on von Smoluchowski's approach to

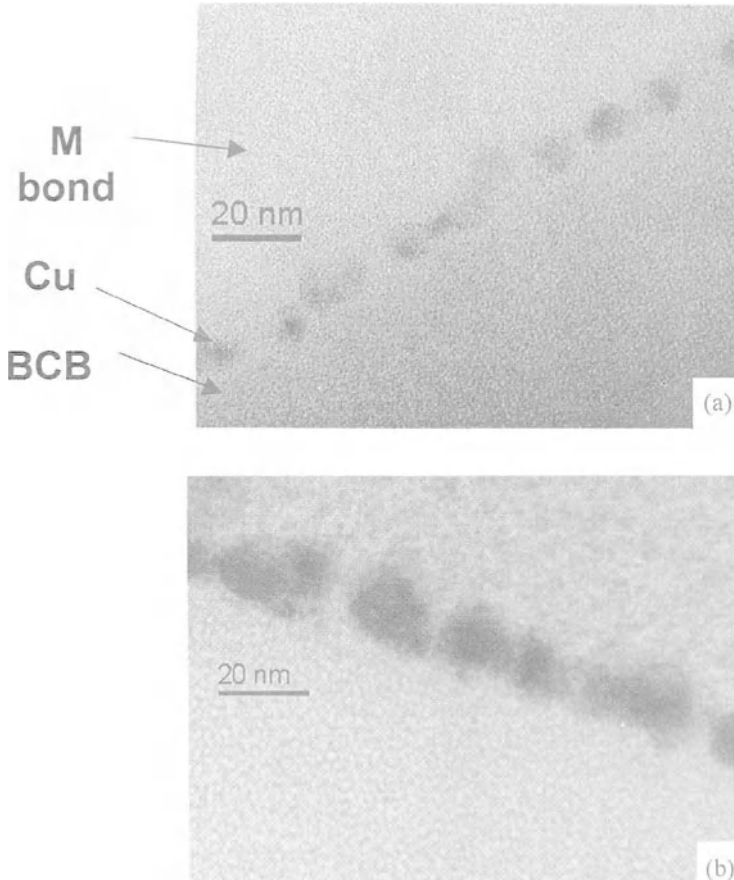


**Figure 2.** Cross-sectional TEM images of Cu on untreated Cyclotene, annealed at 350°C: (a)  $t = 0$ ; (b)  $t = 225$  min. The nominal thickness is 32 Å, deposited at 0.2 Å/sec.

binary encounters of diffusing clusters<sup>13</sup>. As seen in Fig. 3, thickness-dependent  $\alpha$  (and  $k$ ) values vary with surface treatment. Because this growth mode benefits from the constant

replenishment of Cu by evaporation rather than through coalescence, it is expected to differ from that on annealing.

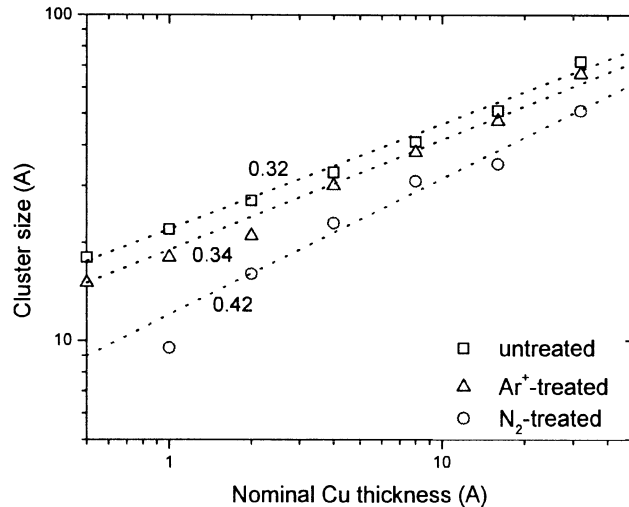


**Figure 3.** The average sizes of Cu clusters on Cyclotene at room temperature, as a function of surface treatment. The numbers are the associated  $\alpha$  values

Initial experiments have shown this to be true. Annealing data on both untreated Cyclotene (not shown) and untreated HOPG<sup>14</sup> have found identical  $\alpha$  values of 0.1, substantially lower than the thickness-dependent values. Clearly, cluster growth by annealing is slower, especially since few diffusion steps lead to cluster contact<sup>14</sup>.

This difference between thickness- and annealing-dependence is also true of coalescence coefficients. The diffusion coefficient for Brownian motion,

$$D_s = \langle x^2 \rangle / 4\Delta t \quad (2)$$

where  $\langle x^2 \rangle$  is the average square displacement of the cluster on the surface over time  $\Delta t$ . Substituting

$$\langle x^2 \rangle = \langle x \rangle^2 = 1/n \quad (3)$$

where  $n$  is the cluster surface density, we obtain<sup>14</sup> the annealing-dependent coalescence coefficient<sup>14</sup>

$$D_s = 1/4n\Delta t. \quad (4)$$

This permits us to calculate that  $D_s$  is  $7 \times 10^{-18} \text{ cm}^2/\text{sec}$  for Cu on untreated Cyclotene,  $1 \times 10^{-18} \text{ cm}^2/\text{sec}$  on  $\text{Ar}^+$ -treated Cyclotene and  $< 10^{-21} \text{ cm}^2/\text{sec}$  on  $\text{N}_2$ -treated Cyclotene at room temperature.

In the case of thickness-dependence, again using Eqn. (1), we write<sup>11</sup>

$$\langle x^2 \rangle = 1/n = \pi d^3 / 6 R_o \Delta t \quad (5)$$

where  $R_o$  is the Cu deposition rate and  $\Delta t$  is now the deposition time. Substituting in Eqn. (1), we obtain

$$D_s = \pi k^3 \Delta t^{3\alpha-2} / 24 R_o. \quad (6)$$

We see that  $D_s$  is strongly dependent on both  $k$  and the deposition time (i.e., nominal Cu thickness); as the cluster size increases in mass, its capacity to migrate decreases. This is seen in Fig. 4 for the three conditions in Fig. 3. The thickness-dependent  $D_s$  values are orders of magnitude greater than the  $D_s$  values obtained for the annealing-dependent cluster growth.

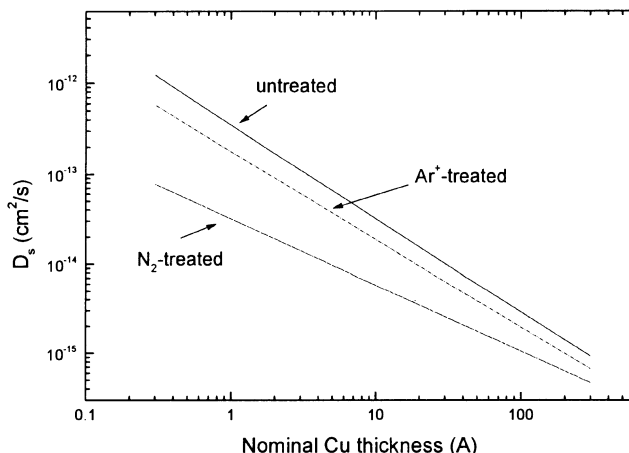


**Figure 4.** The coalescence coefficient of Cu clusters, at room temperature, as a function of surface treatment

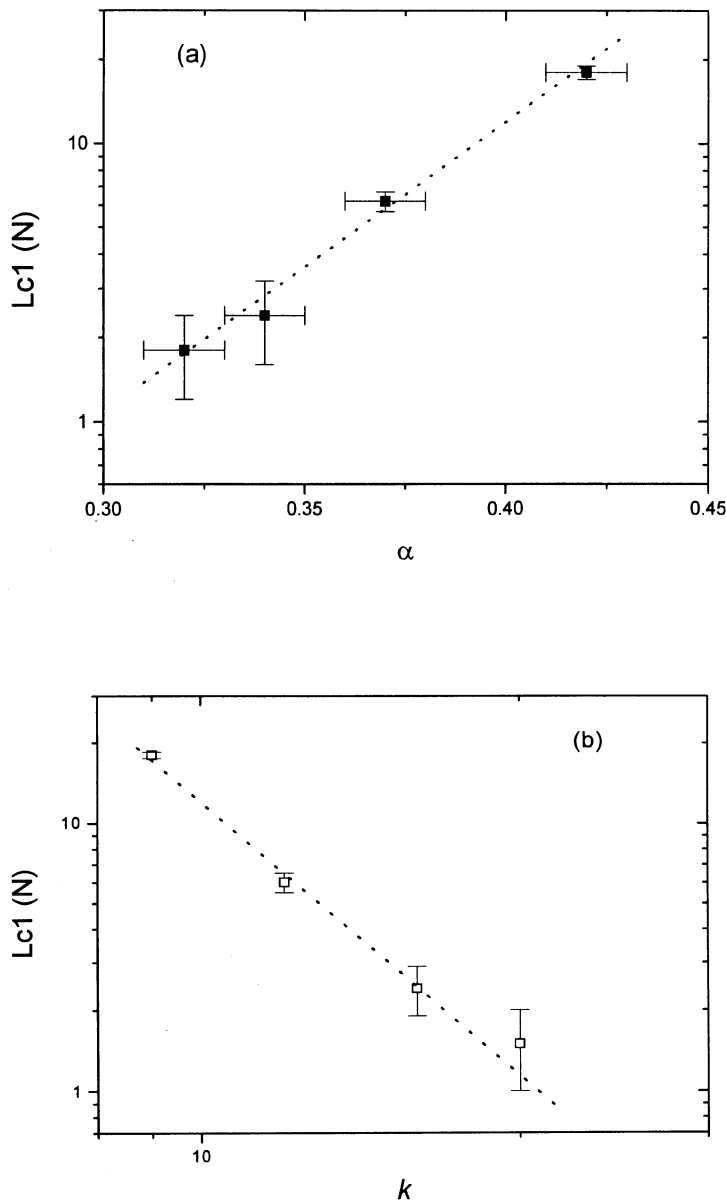


**Figure 5.** The dependence of (a)  $\alpha$ , (b)  $k$  and (c)  $D_s$  (for a nominal 4 Å of Cu) on the  $L_{c1}$  value for Cu-Cyclotene adhesion

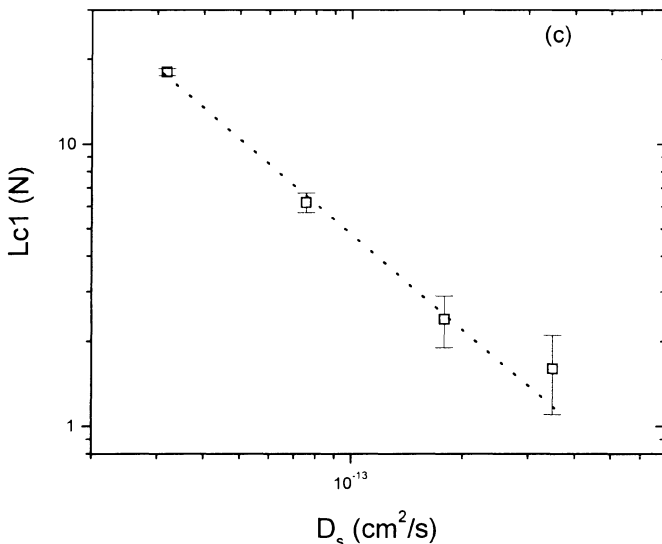


Figure 5 (continued).

The data obtained in Figs. 3 and 4 are found to be related to the adhesion of the Cu films to the Cyclotene. Our adhesion values come from microscratch test data<sup>15</sup>, in which an indenter is linearly displaced across a sample while the indenter load is linearly increased. The  $L_{c1}$  value is the load at which a 2000 Å Cu layer debonded from a 1.3 µm Cyclotene film deposited on a Si wafer. Plots of  $L_{c1}$  vs. thickness-dependent  $\alpha$ ,  $k$  and  $D_s$  are found in Fig. 5. In each case, linearity is seen:  $\log L_{c1}$  is directly linearly related to  $\alpha$  and inversely to  $\log k$ . Its inverse relation to  $\log D_s$  shows that an increased adhesion of the Cu to Cyclotene reduces  $D_s$ .

This is also true for the annealing-dependent case, as seen, in Fig. 6, for the Cyclotene samples annealed at 350°C. The  $N_2$ -treated samples, which provide greater adhesion<sup>15,16</sup>, have commensurately lower  $D_s$  values, as expected. In fact, one may determine the annealing dependence of  $D_s$  on  $d$ , and compare it with literature values. Using Eqns. (2) and (3), and the relationship previously determined<sup>11</sup> for annealing-dependence,

$$n = 6t_o/\pi d^3, \quad (7)$$

we find that

$$D_s = \pi k^{1/\alpha} d^{3-1/\alpha} / 24 t_0 \quad (8)$$

where  $t_0$  is the nominal thickness. For cluster-substrate systems with little interfacial interaction, experimental<sup>12,17</sup> and molecular dynamic simulation<sup>6,18</sup> results show that  $D_s \propto d^2$ . Eqn. (8) shows the relationship to depend on the interaction between cluster and substrate, as expressed by  $\alpha$ , as one might expect. In the case of Cu on HOPG<sup>14</sup>,  $\alpha =$

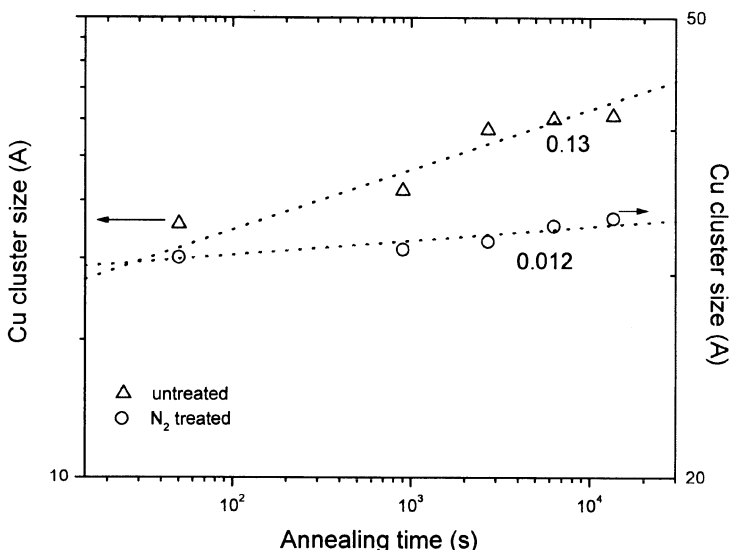


**Figure 6.** The coalescence coefficient of Cu clusters, at 350 °C, as a function of surface treatment. The numbers are the associated  $\alpha$  values

0.19, giving  $D_s \propto d^2$ , as found by these workers. However, annealing-dependent data for Cu on Cyclotene, such as seen in Fig. 8, give values of  $\alpha = 0.13$  and  $0.012$  on untreated and N<sub>2</sub>-treated Cyclotene, respectively, giving  $D_s \propto d^{-4.7}$  for untreated, and  $D_s \propto d^{-80}$  for N<sub>2</sub>-treated, Cyclotene. This is consistent with the adhesion data, and shows that, even at 350°C, the Cu clusters adhere so well to N<sub>2</sub>-treated Cyclotene as to barely coalesce.

#### 4. CONCLUSIONS

We have used data obtained by AFM, TEM and XPS to show that spherical Cu clusters are formed on both untreated and surface-modified Cyclotene. The coalescence of these clusters, whether by thickness- or annealing-dependence, follows the kinetics predicted for binary cluster collisions. We have shown that, for both types of coalescence, these kinetics depend on the cluster-substrate interaction: the greater the interaction, the slower the surface diffusion leading to cluster coalescence.

#### 5. ACKNOWLEDGMENTS

We thank the Natural Sciences and Engineering Research Council of Canada for funding. We also thank Ellen Griswold and Gerry Smith, of Nortel Networks, for furnishing the TEM and AFM images.

#### 6. REFERENCES

1. M. Keine, T. Strunskas and F. Faupel, in: *Metallized Plastics 5 & 6*, edited by K.L. Mittal (VSP, Utrecht, 1998) p. 211.
2. M. Du, R.L. Opila, V.M. Donnelly, T. Sapeta and T. Boone, *J. Appl. Phys.* **85**, 1496 (1999).
3. C. von Bechtolsheim, V. Zaporojtchenko and F. Faupel, *Appl. Surf. Sci.* **151**, 119 (1999).
4. F. Faupel, R. Willecke and A. Thran, *Mater. Sci. Eng.* **R22**, 1 (1998).
5. F. Faupel, *Phys. Stat. Sol. A* **134**, 9 (1992).
6. P. Jensen, *Rev. Mod. Phys.* **71**, 1695 (1999).
7. S. Poulin, D.-Q. Yang, E. Sacher, C. Hyett and T.H. Ellis, *Appl. Surf. Sci.* **165**, 15 (2000).
8. D.-Q. Yang, S. Poulin, E. Sacher and C. Hyett, *Appl. Surf. Sci.* **165**, 116 (2000).
9. D.-Q. Yang, E. Sacher, E.M. Griswold and G. Smith, *Appl. Surf. Sci.* **180**, 200 (2001).
10. D.-Q. Yang, Y.-Q. Xiong, Y. Guo, D.-A. Da and W.G. Lu, *J. Mater. Sci.* **36**, 263 (2001).
11. D.-Q. Yang, M. Meunier and E. Sacher, *Appl. Surf. Sci.* **173**, 134 (2001).
12. G. Rosenfeld, K. Morgenstern, M. Esser and G. Comsa, *Appl. Phys. A* **69**, 489 (1999).
13. M. von Smoluchowski, *Phys. Z.* **17**, 585 (1916).
14. D.-Q. Yang and E. Sacher, *J. Appl. Phys.* **90**, 4768 (2001).
15. A. Sadough-Vanini, D.-Q. Yang, L. Martinu and E. Sacher, *J. Adhesion* **77**, 309 (2001).
16. D.-Q. Yang, L. Martinu, E. Sacher and A. Sadough-Vanini, *Appl. Surf. Sci.* **177**, 85 (2001).
17. J.-M. Wen, S.-L. Chang, J.W. Burnett, J.W. Evans and P.A. Thiel, *Phys. Rev. Lett.* **73**, 2591 (1994).
18. L.J. Lewis, P. Jensen, N. Combe and J.L. Barrat, *Phys. Rev. B* **61**, 16084 (2000).

# ADSORPTION OF NOBLE METAL ATOMS ON POLYMERS

V. Zaporojtchenko\*, J. Erichsen, J. Zekonyte, A. Thran, T. Strunskus, and F. Faupel

## 1. INTRODUCTION

Metallized polymers are nowadays of considerable technological importance and are widely used in industry ranging from food packing to optical data storage. A detailed understanding of the metal/polymer interface properties plays a key role in most applications of metallized polymers. During the last few years, much work has been performed to study the different aspects of metal/polymer interface formation using various microscopic and surface-sensitive techniques. For recent and detailed reviews on metal/polymer interfaces, we refer the reader to refs. 1 and 2 and the article by F. Faupel et al. in the present proceedings. In this article we only consider the metal adsorption phenomena during metal/polymer interface formation by thermal evaporation of a noble metal onto a polymer.

Metals and polymers are extremely dissimilar materials. The interaction between moderately reactive metals and polymers is generally very weak and the cohesive energy of polymers is typically two orders of magnitude lower than the cohesive energy of metals. As a consequence, these metals do not wet untreated polymer surfaces and form clusters during deposition, which finally coalesce and form a continuous film at high metal coverages. Under these conditions, complete condensation as for metal deposition onto metal surfaces cannot a priori be expected at early stages of metal deposition onto polymer. Qualitatively, incomplete condensation has been observed for deposition of Mg onto polypropylene<sup>3</sup> and quantitatively it has been investigated recently for different metal-polymer combinations by our group<sup>4,5</sup>. According to atomistic models of thin film growth<sup>6</sup>, the adsorption probability of metal atoms can be described through the condensation coefficient  $C$ , which is defined as the ratio of the number of adsorbed metal atoms to the total number of metal atoms arriving at the surface. We have recently<sup>5</sup> shown that the tendency of noble metals not to wet a polymer surface is often

\*Lehrstuhl für Materialverbunde, Technische Fakultät der Christian-Albrechts-Universität zu Kiel, Kaiserstr. 2, D-24143 Kiel, GERMANY, email: [vz@tf.uni-kiel.de](mailto:vz@tf.uni-kiel.de)

accompanied by a very low condensation coefficient. Studying the condensation coefficient is useful to estimate the influence of different surface treatments on the adhesion of metals on polymers, to study the chemical interaction between metal atoms and polymers, and to understand the early stages of metal growth.

In this report, we present surface sensitive methods to determine the condensation coefficient as well as results of measurements for Ag, Au and Cu on several amorphous polymer substrates. The correlation between the morphological properties of the metal at an early stage of the deposition and C will be discussed.

## 2. METHODS AND MATERIALS

The polymer films were prepared by spin-coating or casting from solution. To obtain clean polymer surfaces and to drive off residual solvent all polymer films were cured for a few hours in ultrahigh vacuum (UHV) at a temperature close to their glass transition temperature  $T_g$  before the deposition of the metals.

The metals were evaporated from a heated Mo or alumina crucible mounted in the preparation chamber of the XPS spectrometer (Omicron Full Lab). The base pressure in the UHV system was lower than  $2 \times 10^{-8}$  Pa and increased only by an order of magnitude during metal evaporation. The deposition rate  $R$  and the nominal thickness  $Rt$  were monitored by a quartz crystal microbalance, which was calibrated gravimetrically; here  $t$  is the time of deposition. The nominal or equivalent thickness is a measure for the amount of metal evaporated onto the surface, which is not necessarily identical to the amount of metal actually deposited onto the surface. The latter can be much lower depending on the condensation coefficient, which is usually unknown, and needs to be determined within the experiment itself. As mentioned above, the condensation coefficient,  $C$ , is defined as the ratio of the number of atoms actually deposited onto the surface to the total number of atoms arriving at the surface. According to atomistic models<sup>6</sup> one distinguishes between the instantaneous condensation coefficient  $IC$ , which is defined as the ratio of the number of adsorbed atoms per unit time to the deposition rate, and the integral condensation coefficient  $C$ , which is determined for a certain nominal thickness (in our experiment for  $\sim 0.1$  ML). We have recently developed two methods to determine both parameters: a very sensitive radiotracer method<sup>4</sup> to measure  $C$  and a XPS method<sup>7</sup> in which the metal XPS intensity combined with a mathematical correction for the metal cluster formation is used to determine  $C$  and  $IC$ . In the radiotracer method, a radioactive metal isotope is evaporated onto the polymer sample through an aperture and the reemitted atoms are collected on a catcher foil. For the XPS measurements, intensities were calibrated by depositing metals onto substrates where the condensation coefficient was known to be very close to unity, i.e., for example clean metal substrates at room temperature. Determination of  $C$  for Ag on different polymer substrates have shown a good agreement between the two methods (under conditions where metal diffusion into the polymer bulk is negligible), supporting the validity of the XPS results.

Micrographs of the surface and interface region were taken with an atomic force microscope (AFM, Park CP 5) and a TEM (PHILIPS CM 30) at an accelerating voltage of 200 kV. Bright-field pictures obtained with a CCD camera were edited subsequently with standard graphic software. Thin, electron-transparent substrate films of the polymers were prepared using different methods. TEM meshes covered with a 10 nm amorphous

carbon (a-C) layer were covered with a 15 nm thick PMDA/ODA polyimide film by vapour deposition or the transparent films were obtained by cutting a thick polymer film with the help of an ultramicrotome. In the focused image the Z-contrast between metal and polymer is sufficient to resolve metal particles larger than about 1 nm.

### 3. RESULTS AND DISCUSSION

#### 3.1. Condensation coefficient of noble metals on polymer surfaces at room temperature

In the initial stages of metal/polymer interface formation single metal atoms impinge onto the polymer surface.

The metal atoms arrive at the polymer surface with the thermal energy they have gained during evaporation. This energy is usually significantly higher than the thermal energy of the polymer surface. The first question that arises is: Is the interaction between metal atom and the polymer sufficient so that metal atom will lose its translational energy and get adsorbed on the polymer surface or will the metal atoms be reflected directly back into the vacuum? In radiotracer experiments to determine the angular distribution of the reemitted atoms we found no indication for a direct reflection of the metal atoms even when the condensation coefficient was very low. It was observed that a change of the incident angle of the metal atoms by sample rotation did not cause a change of the cosine distribution of the reemitted atoms along the surface normal, i.e. the reemitted atoms have no memory of their angle of incidence. It, therefore, seems to be justified to assume that all the metal atoms get initially adsorbed onto the polymer surface even for very small condensation coefficients.

After adsorption the noble metal atoms will remain and diffuse on the polymer surface for a certain duration of time and then desorb into the vacuum or get trapped somewhere on or beneath the polymer surface. Only the trapped metal atoms contribute to the measured condensation coefficient. In order to clarify the correlation between nucleation and the adsorption probability of metal atoms on the polymer surfaces, we measured the condensation coefficient of Ag, Au and Cu on polymers with different chemical compositions<sup>4, 5</sup>. Result of this measurement for Cu on chemically different polymers are collected in Table 1.

**Table 1.** Condensation coefficients  $C$  for Cu on polymers at room temperature (evaporation rate 0.1 nm/min, nominal coverage 0.01 nm).

	PMDA/ODA Polyimide	BPA-Polycarbonade	Polystyrene $M_w = 200K$	Nylon 11	Teflon AF 1601
Cond. Coeff. Cu ( $R_t = 0.1$ nm)	0.95 ( $\pm 0.05$ )	0.95 ( $\pm 0.05$ )	0.6 ( $\pm 0.2$ )	0.3 ( $\pm 0.1$ )	0.02 ( $\pm 0.01$ )
Surface Energy (mN / m)	54.9	45	40.7	31	16

As is observed from the data in table 1, the value of the condensation coefficient varies by about two orders of magnitude depending on the polymer.  $C$  seems to follow the trend of the surface energies of the polymers. Since a low surface energy also impedes condensation, one can suppose that the large differences in the condensation coefficient may be due to differences in the chemical interaction between metal atoms and the particular polymer groups, for example, a favorable interaction of the metals with the carbonyl groups (polyimide and polycarbonate), and an unfavorable one with fluoro groups of the teflon. To gain further insight into the influence of these opposing interactions we compared  $C$  for a polyimide (PMDA-ODA) and a polybenzoxazole (PBO) which contains a relative high fluorine content (more than 10 at.%) in its repeat unit. The difference of  $C$  at room temperature was negligible. This indicates that the favorable interaction with the polymer carbonyl groups dominates the condensation of the metal on the polymer. This tendency was supported by the strong increase (more than 5 times) of the condensation coefficient of Cu on TMC polycarbonate compared to that of Ag. The increase for Cu seems to be related to the higher reactivity of Cu in the interaction with the carbonyl groups of the polycarbonates.

### 3.2 Influence of metal nucleation on C

If the deposited atoms perform a random walk at the surface prior to reemission, the condensation coefficient is closely related to the probability of finding a surface site with sufficient binding energy to remain adsorbed on the surface. This can be a preferred site on the polymer surface or it can be other metal atoms or metal clusters acting as a trap. The metal atom can also diffuse into the polymer bulk. Therefore, the considerable difference in the values of  $C$  correlates with the difference in the nucleation and growth of the noble metals on the polymers as depicted in Fig.1. Our recent TEM and AFM measurements<sup>2</sup> showed that the evaporated metals initially grow as three-dimensional spherical clusters on the polymer surface. The cluster density and size depends on the deposition parameters as well as on the particular metal-polymer combination. Early in the deposition process the cluster density increases rapidly due to formation of new metal nuclei. In a later phase of metal deposition the formation of new nuclei becomes negligible and the growth of already existing cluster dominates. The density of the nuclei depends on the nucleation process (preferred or random nucleation), the surface diffusion coefficient and the condensation coefficient. We have found that in the case of incomplete condensation at room temperature the cluster density  $N_{cl}$  was lower than  $10^{12} \text{ cm}^{-2}$  while in the case of complete condensation  $N_{cl}$  was, as a rule of thumb, higher than  $10^{12} \text{ cm}^{-2}$ .

There are two extreme cases for metal nucleation on a polymer surface: so-called preferred nucleation where metal atoms are trapped at preferred sites, and random nucleation where nuclei are formed by metal atom encounters. The cases of Au, Cu and Ag on polyimide at room temperature are typical examples of complete condensation accompanied by the random nucleation of the metal atoms on the polymer surface. For these systems it was observed<sup>2</sup> that the cluster density is deposition rate-dependent, which is strong evidence for random nucleation. The interaction of the metals with the polyimide is stronger than van der Waals (see part 3.3 of this work) and the carbonyl groups are active sites for random nucleation of the adatoms. It appears that copper shows a similar behavior on BPA-polycarbonate, which has also carbonyl groups in the repeat unit.

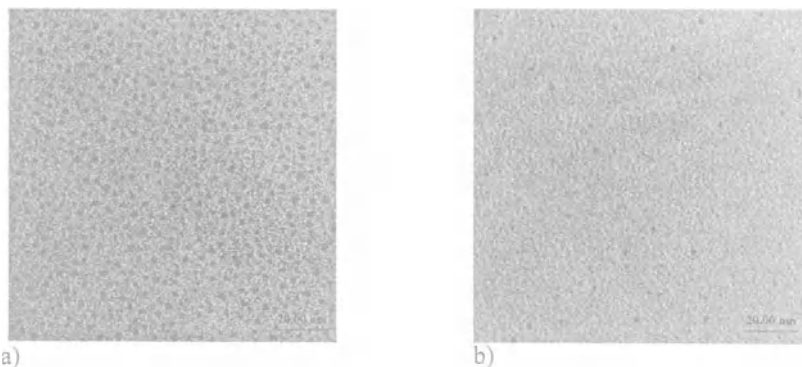


**Figure 1.** Effect of the polymer substrate on metal cluster density: 0.3 nm gold evaporated at a rate of 0.1 nm/min at room temperature onto polyimide (a) and Teflon AF (b). The condensation coefficients are  $C = 1$  for Au-polyimide and  $C = 0.006$  for Au-Teflon AF.

In contrast, polymers with incomplete condensation at room temperature show a significant lower and non deposition rate-dependent cluster density, indicating preferred nucleation at defect sites. In such a case, the interaction between metal atoms and the polymers is weak and the metal atoms easily desorb again preventing random nucleation. In the case of preferred nucleation a certain number of traps exists on the surface.  $C$  depends only on the probability for a metal atom to reach such a preferred site and is therefore independent of the deposition rate even if it is varied by an order of magnitude, cf. Fig.2.

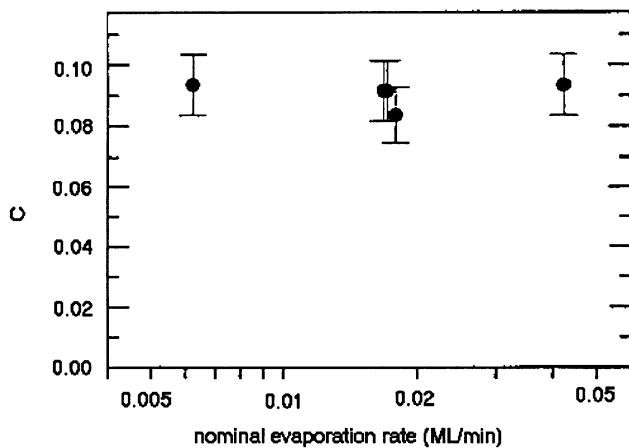


**Figure 2.** Condensation coefficient of Ag on TMC-polycarbonate as a function of evaporation rate.

The nature of these sites is not known exactly, it may be impurities, terminal groups or attractive local arrangements of the polymer chains. When an atom arrives at the surface, its probability to find a preferred site is related to the density of the defect sites  $N$

or correspondingly to the mean distance between these sites and to the diffusion length of the adatoms on the polymer surface.

To provide further evidence that heterogeneous nucleation is important for metal adsorption, a defined concentration of point defects was created by ion bombardment of the polymers, using small doses of 1 kV Ar ions. It was observed (Fig. 3) for Cu on polystyrene that the condensation coefficient and the cluster density,  $N_c$ , increase appreciably with increasing ion dose. The cluster density is approximately equal to the density of created defect sites, which was increased up to  $10^{16} \text{ cm}^{-2}$ . Certainly,  $C$  will increase with increasing cluster density due to the occupation of the new preferred sites on the polymer surface. With increasing  $N_c$  the average distance between clusters, which before treatment was larger than the surface diffusion length  $l$ , becomes comparable or even smaller than  $l$  and the condensation coefficient increases up to unity. This is the so-called steady-state regime of nucleation<sup>6</sup>, where cluster growth is dominated by surface diffusion of the adatoms to the clusters.

The same effect was observed by evaporation of Cu onto Ar<sup>+</sup>-treated Teflon AF, but in this case  $C$  increased only up to a value of 0.15, because even for a large Ar<sup>+</sup> dose the number of active sites was lower ( $10^{13}$ ) and the interaction of Cu atoms with Teflon was weaker compared to polystyrene. The same effect was observed by predeposition of a trace amount of chemically active metal atoms followed by deposition of a noble metal. For example, predeposition of 0.1 ML of Cr onto Teflon AF leads to an increase of the  $C$  value for Cu of an order of magnitude.

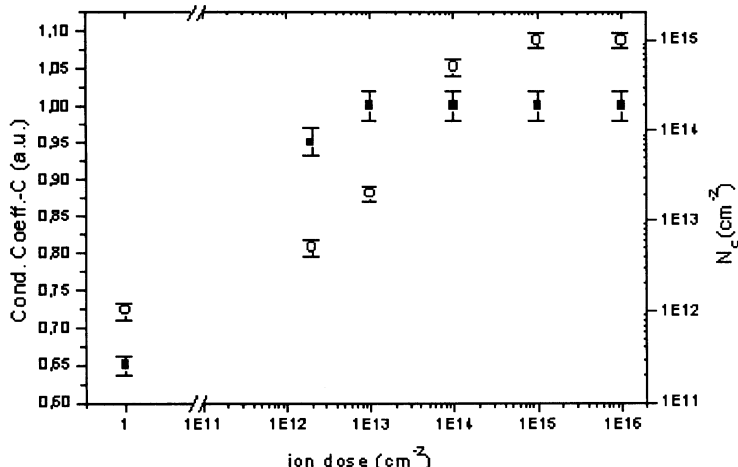


**Figure 3.** Effect of Ar ion treatment on the metal cluster density (open circles) and the condensation coefficient (solid squares) upon evaporation of 0.1 nm Cu onto polystyrene at room temperature.

### 3.3 Temperature dependence.

Previously<sup>5</sup> we reported that the substrate temperature has a strong influence on the nucleation of noble metals on polymers and on the condensation coefficient. It is seen in Fig. 4 that  $C$  decrease with the temperature and for BPA-PC the drop seems to be especially steep when the temperature approaches the glass transition temperature,  $T_g$ , of the polymer.

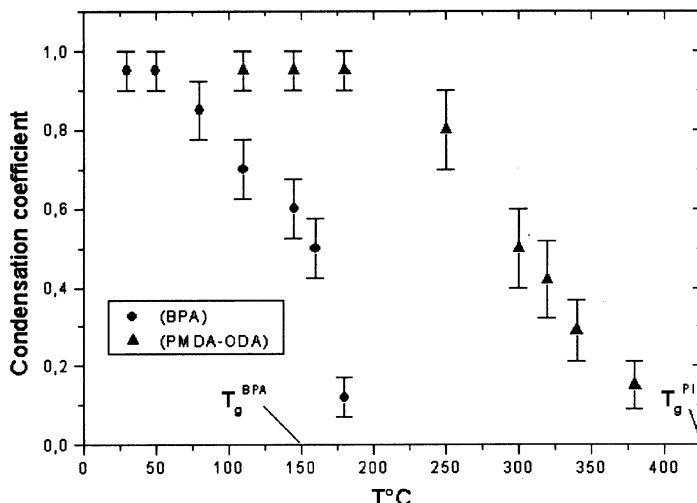
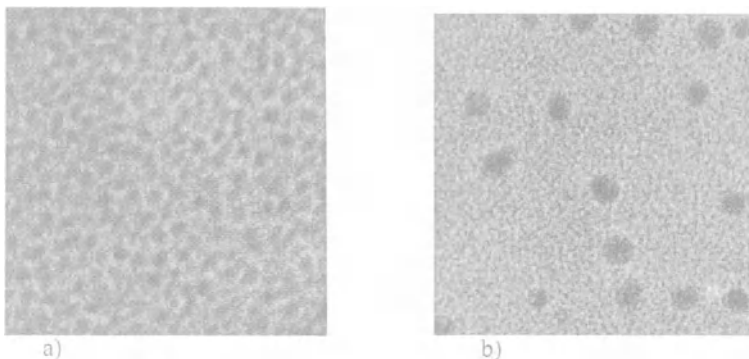


Figure 4. Condensation coefficients vs temperature for Cu evaporated onto polyimide and BPA-polycarbonate.

To understand the influence of the substrate temperature on the condensation coefficient we compare the temperature dependence for  $C$  for Cu deposited onto two different polymers, i.e., bisphenol A polycarbonate (BPA-PC) and PMDA/ODA polyimide (Fig. 4). They have a glass transition temperature of 150 °C and 420 °C, respectively. The condensation coefficient at room temperature is close to unity for both polymers due to the strong interaction of copper with the carbonyl groups. Upon heating the condensation coefficient decreases for both polymers, but at a lower temperature and more pronounced for BPA polycarbonate. One reason for a high condensation coefficient can be a high cluster density on the surface that causes all adsorbed metal atoms to be trapped by the clusters before they desorb again. However, if the clusters get embedded into the polymer the stationary concentration of clusters on the surface will be lowered enhancing the chance for desorption of the metal atoms. The drop of  $C(T)$  starts to occur below the bulk glass transition temperature of the polycarbonate at  $T_g = 150$  °C and well below the one for the polyimide at  $T_g = 420$  °C. Copper clusters formed on BPA-polycarbonate start to get embedded into the polymer at about 130 °C, i.e., already well below the bulk glass transition temperature<sup>8</sup>. But this is not sufficient to explain the steep drop of  $C$ , which starts already at a temperature as low as 100 °C.

Interesting, embedding of clusters has not been observed by us in the case of polyimide up to a temperature of 350 °C. Therefore, we looked for other reasons to explain the steep decrease of  $C$  with increasing temperature on the polyimide surface. In TEM investigations one notes a steep drop of the cluster density at elevated temperatures. In the two TEM micrographs shown in Fig. 5 a big difference in clusters density between copper deposited at 200 °C and 270 °C is observed.



**Figure 5.** Top view TEM micrographs showing the difference in the cluster density for Cu (0.3 nm) evaporated onto polyimide at 200 °C (a) and 270 °C (b). The size of the pictures is 120 x 120 nm<sup>2</sup>.

One notes from Fig. 5 that this is also the temperature range at which the decrease of the condensation coefficient starts. To gain further insight in the correlation between cluster density and the condensation coefficient we investigated the temperature dependence of the cluster density and its correlation with the temperature dependence of the condensation coefficient.

The  $\ln N_c$  vs.  $1/T$  plot, which is shown in Fig.6, exhibits two linear ranges with different slopes. Up to 200 °C one observes a relatively small decrease of the cluster density with temperature. In this temperature range the condensation coefficient is unity and the decrease in cluster density is explained by the faster surface diffusion only. For noble metals on polyimide we observed that the clusters are formed by random nucleation with a critical cluster size of  $i = 1$ , i.e., dimers and larger clusters are stable and do not dissociate again. According to nucleation theory<sup>6</sup> the change of the maximum cluster density with temperature in this case is described as:

$$N_{\max} \propto (R/v)^{1/3.5} \exp((E_d / kT) / 3.5) \quad (1)$$

where  $v$  is an atomic vibration frequency,  $R$  the deposition rate, and  $E_d$  is the activation energy of surface diffusion. This equation can be used to determine the activation energy for surface diffusion  $E_d$  [2], which amounts to  $0.2 \pm 0.1$  eV in the case of copper and to

$0.08 \pm 0.05$  eV in the case of silver. At temperatures above 200 °C one observes a steeper decrease of the cluster density, but again an Arrhenius type of behavior.

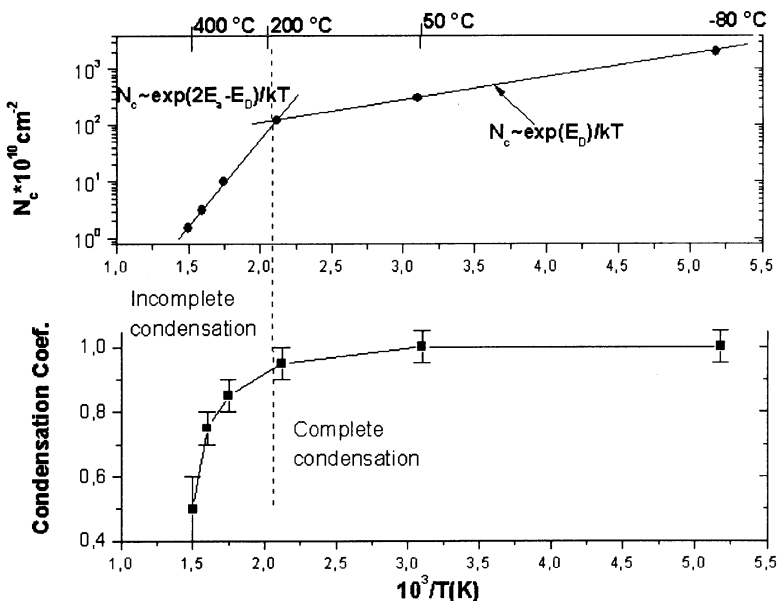


**Figure 6.** Cluster density  $N_c$  and condensation coefficient for Cu deposited on PMDA/ODA polyimide as a function of temperature. deposition rate 0.03 nm/min, nominal coverage 0.1 nm .

In this temperature range metal atoms are also reemitted into the vacuum and the change in cluster density has to be described by an equation taking desorption of metal atoms into account :

$$N_{\max} \propto (R/v)^{2/3} \exp ((2/3)((2E_a - E_d) / kT)) \quad (2)$$

With  $E_d$  known from eq. 1 it is thus possible to determine  $E_a$  from this equation, which amounts to  $0.7 \pm 0.2$  eV in the case of copper on polyimide. Note, that the value for  $E_a$  for copper on polyimide is not to different from the value of 1.02 eV calculated for the interaction of copper with the carbonyl group of acetone used as a model for the copper/polyimide interaction<sup>9</sup>.

When an atom arrives at the surface, its probability to find a trapping site is related to the density of the sites  $N$  and to the diffusion length of the adatoms on the polymer surface, which itself depends on the difference between the adsorption energy  $E_a$  (which must be overcome for desorption) and the activation energy for surface diffusion  $E_d$ . The larger the number of nucleation sites  $N$ , i.e., the smaller the average distance between the growing clusters, the larger is  $C$  since the condensation probability is controlled by surface diffusion. This leads to the following expression for the condensation coefficient  $C$ :<sup>6</sup>

$$C \propto N_C \exp ((E_a - E_d) / kT) \quad (3)$$

where  $k$  is the Boltzman constant,  $T$  is a substrate temperature and  $N_c$  is a number density of growing clusters. The number density of growing clusters is at least equal to the

number of preferred sites on the polymer surface and is in the case of random nucleation even higher because an additional number of clusters is formed on not-preferred sites. As was mentioned above, by treatment of the polymer surface with a pre-defined ion dose or by predeposition of a reactive metal it is possible to create a defined number of the preferred sites on the polymer surface. This allows us to use the Arrhenius-like temperature dependence of the condensation coefficient to estimate the metal-polymer interaction from ( $E_a - E_d$ ) also in a case of incomplete condensation. It was found that for Ag on TMC-polycarbonate ( $E_a - E_d$ )  $\sim 0.12$  eV and for Cu on Teflon AF it is  $\sim 0.08$  eV.

Judging from our results on polyimide we expect  $|E_d| \approx 1/3|E_a|$ . Thus  $E_a$  values should be about 33% larger than the given  $E_a - E_d$  values.

## CONCLUSION

It was shown that with radiotracer measurements and XPS it is possible to determine the metal atom adsorption probability, which is described through the condensation coefficients of metals on polymers. A large variation of the condensation coefficient of noble metals  $C$  is observed for different polymers.  $C$  ranges from close to unity to values of the order of  $10^{-3}$ , depending on the type of polymer and the metal. The condensation coefficient at room temperature is dominated by the most favorable interaction between the metal atoms and the polymer functional groups

It was shown that the morphology of the films and  $C$  are correlated through the nucleation process. The decrease of the condensation coefficient with temperature was related to morphological changes occurring at the metal/polymer interface. At elevated temperature the decrease of  $C$  for random nucleation is due to decrease of the cluster density.

## REFERENCES

1. P. S. Ho, R. Haight, R. C. White, B. D. Silverman and F. Faupel, in: *Fundamentals of Adhesion*, edited by L. H. Lee, (Plenum Press, New York, 1991) p. 383.
2. V. Zaporojtchenko, T. Strunskus, K. Behnke, C. von Bechtolsheim, M. Kiene and F. Faupel, *J. Adhesion Sci. Technol.*, 14, 467–490 (2000).
3. S. Nowak, R. Mauron, G. Dietler, and I. Schlapbach, in *Metallized Plastics 2; Fundamental and Applied Aspects*, edited By K. L. Mital (Plenum Press, New York, 1991)
4. Thran, M. Kiene, V. Zaporojtchenko, and F. Faupel, *Phys. Rev. Lett.* 82, 1903 (1999).
5. V. Zaporojtchenko, K. Behnke, A. Thran, T. Strunskus, and F. Faupel, *Appl. Surf. Sci.* 144–145, 355 (1999).
6. J. A. Venables, *Surf. Sci.* 299–300, 798 (1994).
7. V. Zaporojtchenko, K. Behnke, T. Strunskus, and F. Faupel, *Surf. a. Interf. Anal.* 30, 439-443 (2000).
8. V. Zaporojtchenko, T. Strunskus, J. Erichsen, and F. Faupel, *Macromolecules*, 5, 1125(2001).
9. Ouhlal, A. Selmani, A. Yelon, *J. Adhesion Sci. Technol.* 9(7),1995, 971.

# **NUCLEATION AND GROWTH OF VAPOR-DEPOSITED METAL FILMS ON SELF-ASSEMBLED MONOLAYERS STUDIED BY MULTIPLE CHARACTERIZATION PROBES**

**A.V. Walker, G.L. Fisher, A.E. Hooper, T. Tighe, R.L. Opila,  
N. Winograd and D.L. Allara\***

## **1. INTRODUCTION**

The underlying chemistry of the interaction of metal atoms with organic thin films and polymer surfaces has important implications in many areas of science and technology but uncovering critical details of the mechanisms has been difficult, primarily because of the lack of well-defined organic surfaces. Self-assembled monolayers (SAMs)<sup>1-3</sup> can now provide an approach to overcoming this problem.<sup>4-15</sup> However, in order to fully utilize these precision surfaces it is also necessary to utilize combinations of surface science techniques that can reveal information about both the nature of the metal atoms and the organic surface chemistry and structure.

In this paper we focus on the usefulness of SAMs as model substrates for the case of Al atom vapor deposition. The analysis techniques include four very complementary methods: infrared spectroscopy (IRS), x-ray photoelectron spectroscopy (XPS), time-of-flight secondary ion mass spectrometry (ToF-SIMS) and spectroscopic ellipsometry (SE).

---

\* A.V. Walker, G.L. Fisher (Present Address: Los Alamos National Laboratories; Los Alamos, NM 87545), A.E. Hooper (Present Address: Motorola Corporate Laboratories; Tempe, AZ 85284), T. Tighe, N. Winograd and D.L. Allara (Corresponding Author; dla3@psu.edu), Department of Chemistry, The Pennsylvania State University; University Park, PA 16802; R.L. Opila, Lucent Technologies/AT&T Bell Laboratories, 600 Mountain Ave.; Murray Hill, NJ 07974

The SAMs consist of terminally substituted hexadecanethiolates [ $X(CH_2)_{15}S-$ ] on Au{111} surfaces with X = -CH<sub>3</sub>, -CO<sub>2</sub>H, -CO<sub>2</sub>CH<sub>3</sub>, OH and OCH<sub>3</sub>. The substrates consist of evaporated Au. Details are described elsewhere.<sup>16</sup> A general background on the analysis methods has been reviewed.<sup>17</sup> In all the cases the Al atoms were deposited using a thermal source consisting of a heated refractory metal basket or boat.

A schematic showing the overall strategy of the approach is given in Figure 1.

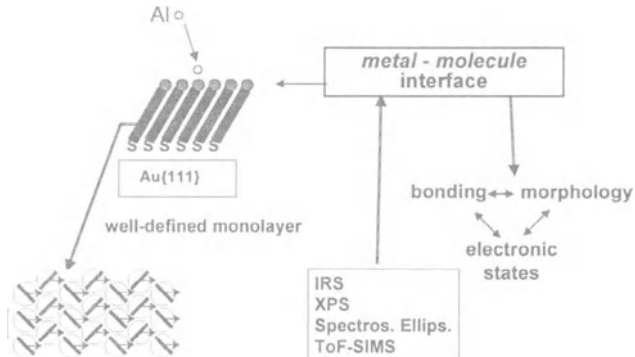


**Figure 1: Experimental Approach - Self-assembled Monolayers + Multi-technique analysis**

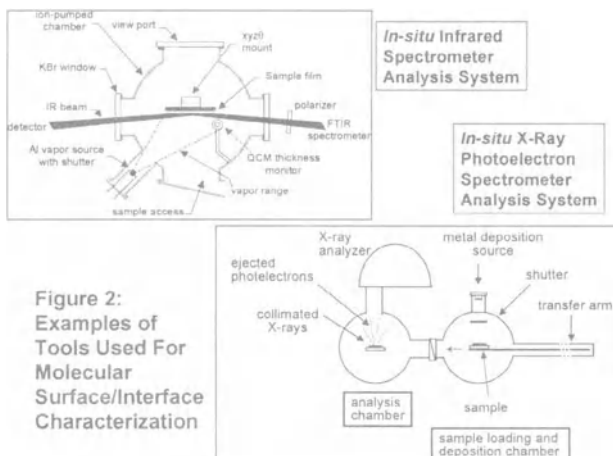


**Figure 2:**  
Examples of  
Tools Used For  
Molecular  
Surface/Interface  
Characterization

## 2. CHARACTERIZATION METHODS

Four different deposition chambers have been used, one for each type of analysis probe. The base pressure and metal deposition sources were very similar. An example of two different types of chambers is given in Figure 2. Overall, the IRS and SE chambers have fixed samples with the deposition done directly in the analysis chamber while the XPS and ToF-SIMS systems have the deposition done in a fore-chamber with sample transport via a load lock system into the analysis chamber. The type of information that one can obtain from the four analysis methods is shown in the schematic in Figure 3.

The deposition of Al onto the samples was followed directly as the mass per unit area by either QCM or the integrated flux from a controlled rate source (XPS case). For convenience in interpretation of the data the deposited amounts were converted to coverage in atoms of Al per SAM molecule, designated  $\theta_{\text{Al}}$ , on the basis that there are 4.6 molecules/nm<sup>2</sup> in a well-formed alkanethiolate/Au{111} SAM.<sup>2</sup> Thus for  $\theta_{\text{Al}} = 1.0$  there would be one Al atom deposited on average per SAM molecule.

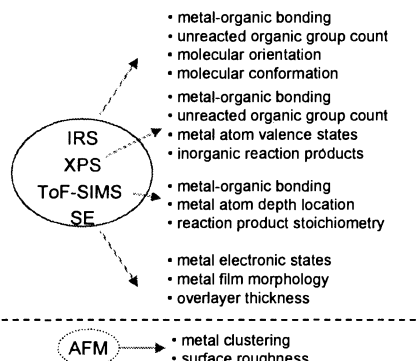


**Figure 3: Quantitative, *in-situ* Surface/ Interface Analysis**

## 3. RESULTS AND DISCUSSION

### 3.1 Studies of Al + CH<sub>3</sub>-Terminated Sam: No Molecule Reactions and Penetration of Al Atoms through The Sam

Recently, we reported on the deposition of Al atoms on the H<sub>3</sub>C-terminated alkanethiolate/Au{111} SAM.<sup>18,19</sup> Summaries of some of the IRS and ToF-SIMS data for the CH<sub>3</sub> case are given in Figures 4 and 5.

The IRS clearly shows that no reaction of the Al occurs with the alkyl chains while the appearance of Au<sub>x</sub>Al<sub>y</sub>S<sub>z</sub><sup>-</sup> ion peaks in the ToF-SIMS data show that the Al atoms were observed to penetrate through the monolayer to the S/Au interface. It was concluded that a limiting Au adlayer coverage was reached of nearly 1 Al atom per Au [on the basis of the Au surface density in a (111) terrace] after which the Al was observed

to begin depositing exclusively at the vacuum/SAM interface. Further, Au-S bonds in the adlayer were converted to aluminum thiolate species by Al insertion.

This diffusion did not appear to occur through "pinhole" defects in the SAM since the monolayers were prepared with high packing densities and were highly blocking to electrochemical processes. The diffusion was proposed to occur through thermally induced fluctuations in the monolayer chain lateral spacings that provided transient molecular-dimension channels. The shifting of a nearby S atom from a molecule to Al from Au with the presumption that the S-Al bond is stronger than the S-Au bond, could explain the cessation of the lateral chain hopping at 1 Al per Au atom. This process is summarized in the schematic in Figure 6.

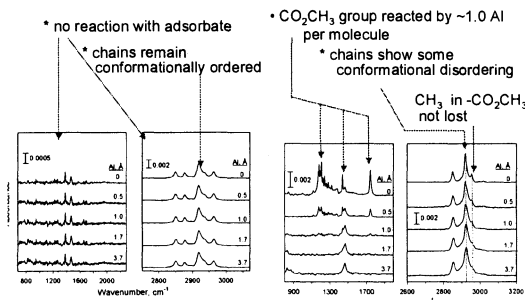


Figure 4: IRS data for  $\text{CH}_3$  and  $\text{CO}_2\text{CH}_3$  SAMs

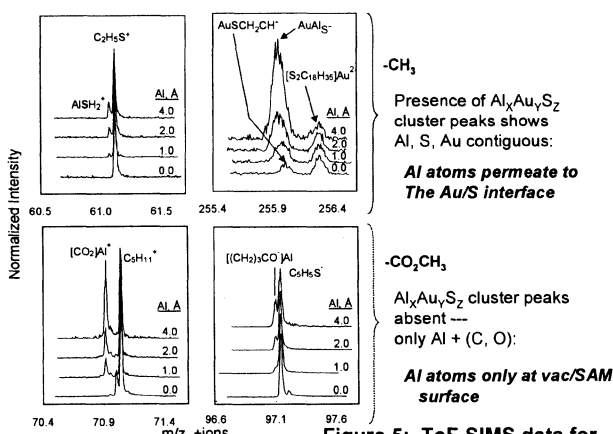


Figure 5: ToF-SIMS data for  $\text{CH}_3$  and  $\text{CO}_2\text{CH}_3$  SAMs

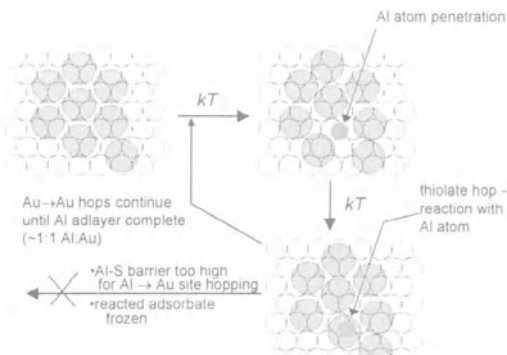
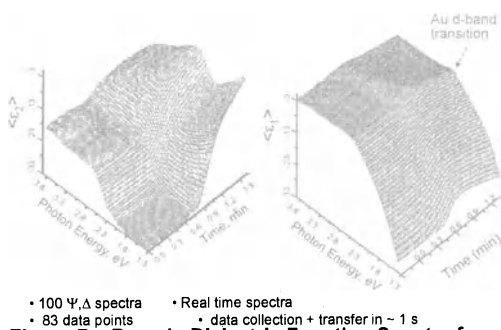
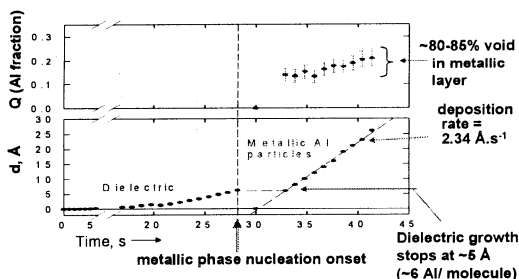


Figure 6: Schematic of Al penetration into a SAM

Figure 7: Pseudo Dielectric Function Spectra from Spectroscopic Ellipsometry Measurements of Al Deposition on a  $\text{CO}_2\text{CH}_3$ -Terminated SAMFigure 8: Al film thickness and void content evolution for a  $\text{CO}_2\text{CH}_3$ -Terminated SAM as determined from spectroscopic ellipsometry

### 3.2. Al + CO<sub>2</sub>CH<sub>3</sub>-Terminated SAM: 1:1 Surface Reaction with the CO<sub>2</sub>CH<sub>3</sub> Groups and No SAM Penetration

A summary of selected IRS and ToF-SIMS data<sup>19</sup> for the CO<sub>2</sub>CH<sub>3</sub>-terminated SAM is shown in Figures 4 and 5. A direct comparison can be made with the CH<sub>3</sub> SAM case. The ToF-SIMS data show that the deposited Al atoms do not penetrate through the SAM while the IRS data show that they react in a 1:1 stoichiometry with the carbonyl portion of the ester functionality while leaving the C-O (ether) linkage intact. The XPS data (not shown) further show that past the first deposited Al atom per group, ~4 additional Al atoms continue to undergo redox interactions with the terminal group leading to an organo-aluminum complex with non-zero Al valence states.

The SE data are useful for giving information on the dielectric and morphology characteristics of the growing Al film. The data were taken in real time as the deposition progressed. Figure 7 is a 3-D representation of the time evolution of the data in terms of the psuedo-dielectric spectra and Figure 8 shows the interpretation in terms of the time evolution of the film characteristics.

The first ~6 Å of growth produce a dielectric layer (non-metallic) while further growth is a metallic phase. However, roughly 30 Å of this phase is very porous, estimated as equivalent to ~85% voids. Subsequent film growth involves the usual dense metallic phase.

The main conclusions for the CH<sub>3</sub> and CO<sub>2</sub>CH<sub>3</sub> cases are summarized in the schematic in Figure 9.

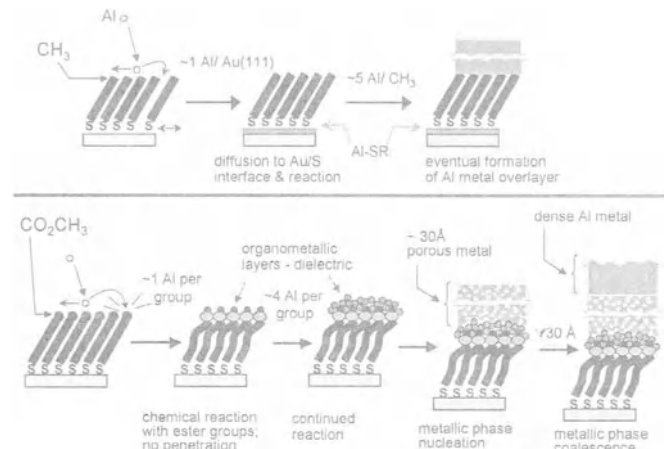


**Figure 9: Summary of results for CO<sub>2</sub>CH<sub>3</sub> and CH<sub>3</sub> SAMs**

### 3.3 Al + CO<sub>2</sub>H-Terminated SAM: ~1:1 Al:CO<sub>2</sub>H Stoichiometry but incomplete Reaction and No SAM Penetration

In a subsequent study<sup>20</sup> with a HO<sub>2</sub>C-terminated alkanethiolate/Au{111} SAM we reported that Al atoms react with the acid group in an ~1:1 average stoichiometry with no penetration into the SAM, as can be concluded from the data shown in Figure 10.

The reaction product is likely an aluminum carboxylate species that forms by insertion of Al into the O-H bond. In the IRS spectra, the new peak that forms at ~1450 cm<sup>-1</sup> after ~1 Al atom per molecule is in the typical vicinity of the symmetric stretching mode of metal carboxylates. An intriguing aspect of this study is that while the chemical degradation of the CO<sub>2</sub>H group occurs during the initial deposition of the Al atoms some 15-20% fail to react, even with continued deposition up to many Al atoms per molecule. This suggests steric blocking effects that arise as the surface continues to react with deposited Al atoms. Further evidence for steric effects comes from the C-H stretching region of the IRS spectra where the shifts to higher frequency with increasing coverage indicate an increasing degree of conformational disordering of the alkyl chains. This result is similar to that of the CO<sub>2</sub>CH<sub>3</sub>-terminated SAM and can be understood in terms of steric crowding of the organo-aluminum products at the SAM/vacuum interface. However, note that while there are steric crowding effects in the case of the CO<sub>2</sub>CH<sub>3</sub> SAM they do not affect the extent of the Al-CO<sub>2</sub>CH<sub>3</sub> group reaction since it goes to completion within experimental error.

The ToF-SIMS data shown in Figure 11 support the conclusions from the IRS data.

The Al 2p XPS data (Fig. 10) further show that the metallic state of the deposited Al atoms is not reached until ~several atoms per molecule have been deposited. This is similar to the CO<sub>2</sub>CH<sub>3</sub> result in which it was concluded that a <1 nm dielectric layer of an organo-aluminum complex forms prior to the growth of the metallic Al phase.

The main conclusions from the CO<sub>2</sub>H case are summarized in the schematic in Figure 12. Also shown in the figure is a summary from preliminary experiments with the OH SAM.<sup>21</sup>

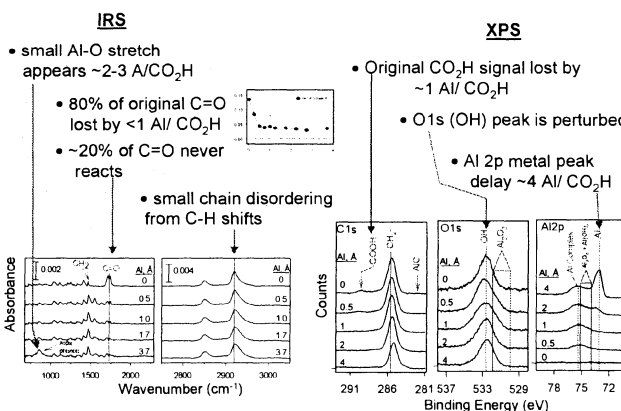


**Figure 10: IRS and XPS data for the CO<sub>2</sub>H-terminated SAM**

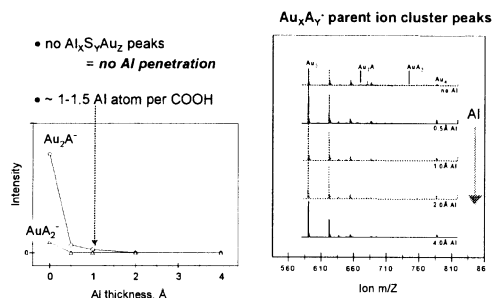


Figure 11: ToF-SIMS data for the  $\text{CO}_2\text{H}$ -terminated SAM

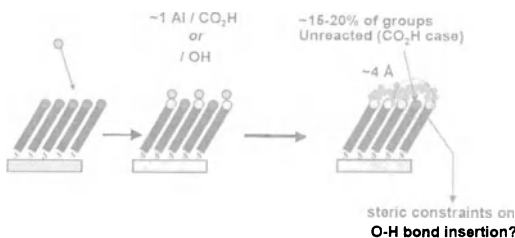


Figure 12: Summary of results for  $\text{CO}_2\text{H}$  and OH SAMs

### 3. SUMMARY AND CONCLUSIONS

Two main conclusions have emerged from these initial studies. First, when a reactive group is present at the alkyl chain terminus, nucleation and growth of a metallic film occurs only at the vacuum/film interface and the first several layers of Al atoms appear to form an organo-aluminum, dielectric layer prior to the growth of a metallic film. Second, when the chain terminus contains an unreactive  $\text{CH}_3$  group penetration through the SAM to the S/Au interface occurs. It has been proposed that this penetration occurs via a thermally activated lateral hopping process of the SAM molecules that leads to the creation of transient holes allowing transport of nearby Al atoms directly to the S/Au interface.<sup>19</sup>

In the case of the  $\text{CO}_2\text{CH}_3$  group the evidence clearly shows that the C=O carbonyl group is the critical reaction center in the metal-organic interaction. For the case of the  $\text{CO}_2\text{H}$  group the IRS data suggests that there is insertion of the Al in the O-H bond

but the data do not rigorously exclude reaction with the C=O. Recent experiments with an HO-terminated SAM<sup>21</sup> indicate from the IRS data that there is insertion of Al into the O-H bond to form an O-Al-H species.

This result establishes that O-H insertion can occur. Unfortunately, it is not possible to tell from the existing data for the CO<sub>2</sub>H SAM whether O-H insertion is the preferred pathway, relative to C=O reaction, in this case. For the CO<sub>2</sub>CH<sub>3</sub> case it also is clear from the data that the OCH<sub>3</sub> unit suffers no bond scission by the deposited Al. In recent experiments with the H<sub>3</sub>OC-terminated SAM<sup>21</sup> no evidence was seen for bond scission. Rather the results indicate Al penetration into the SAM, similar to the CH<sub>3</sub> case. There is a small but significant difference, however. In the case of the OCH<sub>3</sub> SAM only a fraction of the initially deposited Al atoms undergo penetration with some fraction remaining on the surface of the OCH<sub>3</sub> groups. Such partitioning does not occur in the CH<sub>3</sub> case. Preliminary quantum chemical calculations show that there is ~10 kcal/mol lower energy for the Al atoms to be complexed with the O of the OCH<sub>3</sub> group than to be located next to a CH<sub>2</sub> unit of the alkyl chain. This result supports the supposition that there is a weak complexing effect of the OCH<sub>3</sub> group for Al atoms that tends to keep a fraction of them on the surface while the penetration channel is open. Those atoms held at the surface eventually will undergo clustering and nucleation of a metallic over layer. A schematic summary of the proposed behavior of the OCH<sub>3</sub> SAM and its relation to the CO<sub>2</sub>CH<sub>3</sub> case is summarized in Figure 13.

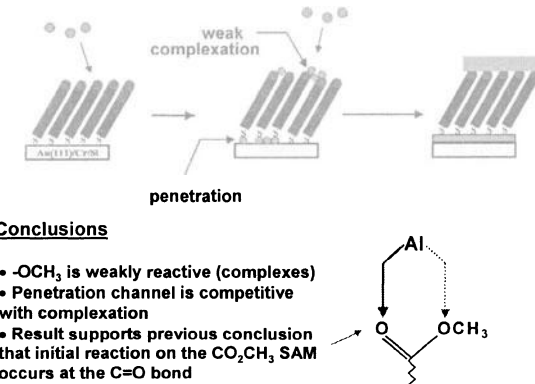


Figure 13: Schematic summary of preliminary results on the behavior of the OCH<sub>3</sub> SAM

Overall we conclude that the application to a suite of advanced surface characterization tools to the study of metal atom deposition of precisely structured self-assembled molecular films allows one to attain a very detailed, quantitative knowledge of the chemical and physical processes that can occur at an organic surface. Such information can be invaluable in assisting the understanding the complex processes that occur on many organic surfaces, particularly polymers.

#### 4. ACKNOWLEDGMENTS

The authors acknowledge financial support from the Office of Naval Research, the National Science Foundation and the National Institutes of Health.

---

#### 5. REFERENCES

1. A. Ulman, *Chem. Rev.* 96 (1996) 1533
2. L.H. Dubois and R.G. Nuzzo, *Ann. Rev. Phys. Chem.* 43 (1992) 437
3. J. Swalen, D. Allara, J. Andrade, E. Chandross, S. Garoff, J. Israelachvili, T. McCarthy, R. Murray, R. Pease, J. Rabolt, K. Wynne and H. Yu, *Langmuir* 3 (1987) 932
4. D.R. Jung and A.W. Czanderna, *Crit. Rev. Sol. St. Mat. Sci.* 19 (1994) 1
5. D.R. Jung, A.W. Czanderna and G.C. Herdt, *J. Vac. Sci. Tech. A14* (1996) 17793
6. A.W. Czanderna, D.E. King and D. Spaulding, *J. Vac. Sci. Tech. A9* (1991) 2607
7. D.R. Jung, D.E. King and A.W. Czanderna, *J. Vac. Sci. Tech. A11* (1993) 2382
8. K. Konstadinidis, P. Zhang, R.L. Opila and D.L. Allara, *Surf. Sci.* 338 (1995) 300.
9. M.J. Tarlov, *Langmuir* 8 (1992) 80
10. W.J. Dressick, C.S. Dulcey, J.H. Georger, Jr., G.S. Calabrese and J.M. Calvert, *J. Electrochem. Soc.* 141 (1994) 210
11. D.R. Jung, D.E. King and A.W. Czanderna, *Appl. Surf. Sci.* 70/71 (1993) 127
12. G.C. Herdt and A.W. Czanderna, *Surf. Sci. Lett.* 297 (1993) L109
13. Y. Hirose, A. Kahn, V. Aristov and P. Soukiassian, *Appl. Phys. Lett.* 68 (1996) 217
14. G.C. Herdt, D.E. King and A.W. Czanderna, *Z. Phys. Chem.* 202 (1997) 163
15. K. Mittal and K.-W. Lee, Eds, *Polymer Surfaces and Interfaces: Characterization, Modification and Applications*, VSP International Science Publishers, Netherlands, 1997, p. 189-224.
16. For example, see R.G. Nuzzo, L.H. Dubois and D.L. Allara, *J. Am. Chem. Soc.* 112 (1990) 558
17. D. L. Allara and P. Zhang, in *Materials Science and Technology*, R. W. Cahn, P. Haasen and E. J. Kramer, eds, VCH, Germany, 1994, 657-755
18. G.L. Fisher, A.E. Hooper, R.L. Opila, D.R. Jung, D.L. Allara and N. Winograd, *J. Elec. Spec. Rel. Phenom.* 98-99 (1999) 139
19. A.E. Hooper, G.L. Fisher, K. Konstadinidis, D.R. Jung, H. Nguyen, R.L. Opila, R.W. Collins, N. Winograd and D.L. Allara, *J. Am. Chem. Soc.* 121 (1999) 8052
20. Fisher, G.L.; Hooper, A.E.; Opila, R.L.; Allara, D.L.; Winograd, N. *J. Phys. Chem.* 104 (2000) 3267
21. G. Fisher, A. Hooper, H. Skriba, K. Bahnek, T. Tighe, M. Reinard, R. Opila, N. Winograd and D. L. Allara, manuscript in preparation

# MORPHOLOGICAL INVESTIGATIONS OF LOW-k POLYMER/DIFFUSION BARRIER INTERFACES FOR IC METALLIZATION

Sujatha Sankaran and Robert E. Geer\*

## 1. INTRODUCTION

Until recently, the performance of complementary metal-oxide semiconductor (CMOS) integrated circuits (ICs) has been driven by front-end device (i.e. transistor) size scaling. However, as the IC critical dimension (CD) shrinks, interconnect latency has emerged as a primary performance driver. This has hastened the integration of copper and low-k dielectrics in back-end processing to reduce the effective signal propagation delays associated with on-chip interconnects. With current dielectric materials, the use of Cu in CMOS processing requires a barrier layer between the Cu and the dielectric to prevent thermal and bias-induced Cu-ion diffusion. In some cases (such as low-k polymers) this barrier also serves to prevent oxidation of the Cu line due to diffusion of water vapor through the dielectric. To preserve the cross-sectional 'real estate' of the Cu interconnect, the International Roadmap for Semiconductors calls for barrier-layer thickness less than 10 nm prior to the 100 nm device node.<sup>1</sup> Consequently, new material sets are being investigated to provide chemically, electrically, and thermally stable barriers against Cu diffusion that maintain satisfactory performance at such low thickness.

Emerging barrier candidates include ternary metal-silicon-nitrides that possess reduced diffusion pathway density and increased diffusion activation energy due to their amorphous microstructure and high interatomic binding energies, respectively.<sup>2</sup> These properties are essential for adequate performance in sub-130 nm device generations. Ternary metal-silicon-nitride barriers (TM-Si-N, TM=Ti, Ta, W) have been extensively studied and have shown superior barrier performance compared to conventional barriers and hence are promising candidates.<sup>3</sup> The amorphous nature of these ternary barriers and their chemical inertness promote low Cu ion diffusivity and chemical stability respectively. Nicolet et al. showed  $Ti_{34}Si_{25}N_{43}$  films, reactively sputtered from  $Ti_5Si_3$

\* S. Sankaran and R. E. Geer, University at Albany Institute for Materials, State University of New York, Albany, NY 12203.

targets, exhibited optimal barrier performance against Cu diffusion.<sup>3</sup> Maximum temperature stability of Si/barrier/Cu and SiO<sub>2</sub>/barrier/Cu stacks was maintained up to 850 °C and 900 °C, respectively. However, more detailed investigations of these materials are required with respect to integration in a polymeric dielectric matrix. Of particular importance is the nature of the barrier/polymer interface and the stability of this interface with respect to thermally-induced stress.

In this work we present a study of the interface morphology of TiSiN diffusion barriers deposited via reactive physical vapor deposition (reactive PVD) on a low-k dielectric film consisting of SiLK® thermoset polymer. Specifically, the TiSiN/SiLK® interfacial roughness is quantitatively evaluated in as-deposited bilayer stacks using specular x-ray reflectivity (XRR) and compared to the roughness of the underlying SiLK® film determined via atomic force microscopy (AFM). Off-specular XRR is used to determine the relative roughness correlation between the buried barrier/polymer interface and the TiSiN-barrier surface. These off-specular XRR results are compared to spectra generated via numerical modeling. It is shown that the conformality of the TiSiN barrier film on the SiLK® is high. Comparisons of these results with similar data acquired from TiSiN/SiO<sub>2</sub> stacks is discussed. In the latter case, a lesser degree of TiSiN conformality with the underlying SiO<sub>2</sub> substrate is observed.

To better understand the effect of thermally-induced stress on the morphology of the barrier/polymer interface multilayer test structures consisting of TiSiN/Cu/TiSiN/SiLK® and TiSiN/Cu/TiSiN/SiO<sub>2</sub> stacks were also investigated. These particular multilayer structures were chosen to examine the effects of thermally-induced stresses (arising from the thermal expansion mismatch between the Cu, barrier and dielectric components) on the morphological stability of the barrier/polymer interface. For all the work presented here the two TiSiN layers possessed a nominal thickness of 14 nm and the Cu layer possessed a nominal thickness of 58 nm. Rutherford backscattering (RBS), specular XRR, and off-specular XRR measurements from these test structures are presented and discussed for as-deposited and annealed samples (up to 550 °C). It is shown that the multilayer stacks deposited on SiLK® exhibited a significant thermally-induced roughness compared to similar stacks on SiO<sub>2</sub> substrates. However, despite the increased roughness, the conformality of the TiSiN layers remained. This observation implies that thermally-induced morphological changes in the TiSiN/SiLK® interface are dominated by roughening and not by interdiffusion.

## 2. EXPERIMENTAL

### 2.1 SiLK® Low-k Film Deposition

Blanket thick films of SiLK® low-k polymer with a thickness of 0.73 μm were deposited via spin-casting on Si wafers previously coated with 1 μm thermal silicon oxide. X-ray photoelectron spectroscopy (XPS) measurements of as-received SiLK® films revealed an elemental composition of 98% C and 2% O. This was consistent with accepted values. SiLK® surface root-mean-square (RMS) roughness measurements (via AFM) of 0.42 nm were also in agreement with prior analysis (3).

## 2.2. Copper AND TiSiN Film Deposition

Deposition of Cu and TiSiN films utilized physical vapor deposition (PVD) and reactive PVD, respectively, in a two chamber CVC Connexion cluster tool.<sup>4</sup> Copper films were deposited from a pure Cu target. Copper deposition parameters: 5 kW DC power; 0 W RF bias power; 5 mTorr chamber pressure; 80 sccm Ar flow; 37 mm target/sample separation. TiSiN films were deposited from a Ti<sub>5</sub>Si<sub>3</sub> alloyed target. TiSiN deposition parameters: 5kW DC power; 0-100 W RF bias power; 7 mTorr chamber pressure; 80 sccm Ar flow; 0-80 sccm N flow; 37 mm target/sample separation. TiSiN film deposition times ranged from 70-150 seconds depending on desired film thickness.

## 2.3. Methods OF Characterization and Thermal Processing

Compositional analyses of as-received SiLK® films and deposited TiSiN barrier layers utilized a Perkin-Elmer PHI 550 multitechnique x-ray photoelectron spectroscopy (XPS) system. A Nanoscope III atomic force microscope (AFM) was used as a surface roughness probe for processed samples. All topography data was acquired in tapping mode. Specular and off-specular x-ray reflectivity (XRR) measurements were carried out using a 15 kW Rigaku x-ray generator and an Inel positionally sensitive x-ray detector. RBS spectra were taken using a 2 MeV He<sup>+</sup> beam calibrated with bulk samples of gold and aluminum. Care was taken to minimize the total exposure of the SiLK® films to the He<sup>+</sup> ions to mitigate the effects of ion damage. All annealing runs were performed in a quartz tube oven in Ar gas at atmospheric pressure. Sample temperature was controlled with an accuracy of 5 °C.

## 3. QUANTITATIVE MODELING OF SPECULAR XRR

The specular XRR data from multilayer stacks investigated here were quantitatively modeled using a nonlinear least squares fitting algorithm in conjunction with a slab model similar to that formulated by Parrat.<sup>5</sup> In such a model a given slab is characterized by a complex index of refraction for x-rays:  $\eta=1-\delta+i\beta$ . Here,  $\delta=\rho_e r_e \lambda^2/2\pi$ , with  $\rho_e$  the electron density,  $r_e$  the electron radius and  $\lambda$  the incident x-ray wavelength, and  $\beta=\mu\lambda/4\pi$ , with  $\mu$  the absorption length of x-rays in the medium. This method can be extended to several layers with different densities or for a single layer with variations of density along the film normal. Consider N layers where  $j=1$  refers to the air-film interface and  $j=N+1$  refers to the film-substrate interface. Each layer  $j$  is characterized by  $\delta_j$  and  $\beta_j$ , and hence  $\eta_j$ . An incident x-ray wave vector  $k_i$  of magnitude  $2\pi/\lambda$  is incident at an angle of  $\theta_i$  at the air-film interface. The normal component of the momentum transfer vector  $q$  for specular reflection is given by  $q_z = (4\pi/\lambda)\sin\theta_i$ . To account for refractive effects in each layer the wave vectors are normalized proportional to the wave vector for total external reflection relative to the layer of interest,  $q_{cj}$ . The z-component of the wave vector transfer for each individual layer is therefore given by  $q_{zj} = \sqrt{q_z^2 - q_{cj}^2}$ .

The reflectance between the  $(j-1)^{\text{th}}$  layer and the  $j^{\text{th}}$  layer is given by

$$R'_{j-1} = \frac{R_{j-1,j} + R'_{j,j+1} \exp(-iq_j d_j)}{1 + R_{j-1,j} R'_{j,j+1} \exp(-iq_j d_j)} \quad (1)$$

where  $R_{j-1,j}$  is the Fresnel reflection coefficient at the interface between layer  $j$  and layer  $j-1$  and is given by

$$R_{j-1,j} = \frac{q_{z+1} - q_z}{q_{z+1} + q_z} \quad (2)$$

To calculate the net reflectance for a given multilayer an iterative technique is used. Starting at the substrate the reflection coefficient  $R'_{j-1,j}$  for each interface is calculated and successively used to calculate the coefficient at the next interface. Thus Eq. 1 can be applied recursively until the vacuum-sample interface is reached so that

$$\tilde{R}(q_z) = R'_{01} R'_{01}^* \quad (3)$$

In this manner the scattered intensity as a function of incident angle for a set of multilayers is determined. This approach is valid over a full range of wave vectors and it takes multiple specular scattering, refraction, and absorption into account. It, however, does not take diffuse scattering into account.

Including interfacial roughness in the aforementioned model results in a decrease in the specular reflected intensity. The effective decrease can be determined by multiplying the Fresnel reflectance by a modification factor. The modification factor<sup>6</sup> most commonly chosen to describe interfacial and surface roughening is the static Debye-Waller factor<sup>7</sup> given by

$$\exp\left(-\frac{\sigma^2 q_z^2}{2}\right). \quad (4)$$

This is applicable for large lateral coherence lengths and is incorporated in the aforementioned expressions for the reflectance.

#### 4. RESULTS AND DISCUSSION

The 3D surface topography of an as-deposited SiLK® film is shown in the AFM data of Fig. 1. An amorphous surface structure is observed with a root-mean-square (RMS) roughness of 0.42 nm over a scan area of 1 μm<sup>2</sup>. Although not excessive for a thermoset polymer, the SiLK® surface RMS roughness is large compared that of the SiO<sub>2</sub> substrates employed here (~ 0.14 nm via AFM). To investigate the TiSiN/SiLK® interface Ti<sub>37</sub>Si<sub>21</sub>N<sub>41</sub>

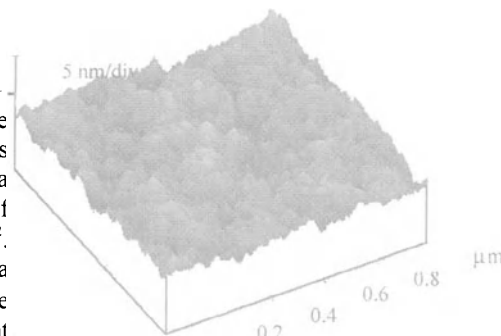


Figure 1. 3D AFM topography scan of an as-deposited SiLK® film. Surface RMS roughness is 0.42 nm. The scan size is 1 μm x 1μm.

barrier layers with a thickness of approximately 34 nm were deposited on SiLK® films and SiO<sub>2</sub> substrates via reactive sputtering as described above. X-ray diffraction measurements have previously shown that these barrier layers exhibit an amorphous or nanocrystalline microstructure.<sup>3</sup> Surface topography for the as-deposited barrier films on both substrates was examined via AFM and is shown in Fig 2. A surface RMS roughness of 0.18 nm was observed for the TiSiN/SiO<sub>2</sub> stack compared to a value of 0.70 nm for the TiSiN/SiLK® stack. Both barrier films exhibited an amorphous topography. The scan size for the data shown in Fig. 2 is 5 μm x 5 μm.

To investigate the buried TiSiN/SiLK® interface specular XRR data was collected for the TiSiN/SiLK® bilayer stack. This data was analyzed using the methodology described above. Accepted values for the density of the SiO<sub>2</sub> and SiLK® substrates were used to decrease the number of free parameters. The experimental data and modeling results are shown in Fig. 3. This XRR spectra is typical for a thin uniform film on a thick substrate. At  $q_z$  values less than 0.035 Å<sup>-1</sup> the reflected intensity is a maximum and corresponds to total external reflection. At higher values of the momentum transfer vector a series of interference fringes are observed which are related to the barrier layer thickness. The solid line in the figure corresponds to the Parrat model

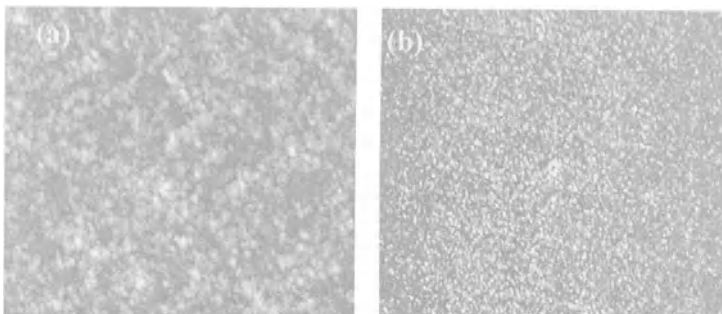


Figure 2. 2D AFM topography scans of as-deposited (a) TiSiN/SiLK® stacks and (b) TiSiN/SiO<sub>2</sub> stacks. The former exhibits an RMS roughness of 0.70 nm compared to 0.18 nm for the latter. Scan size for both panels is 5 μm x 5 μm.

result assuming a barrier layer thickness of 34.5±0.5 nm. The TiSiN surface roughness and TiSiN/SiLK® interfacial roughness determined from this fit both possess a value of 0.8±0.3 nm and correspond approximately to the topography data. It is important to note that the roughness determined from specular XRR measurements corresponds primarily to an area determined by the angular projection of the coherent portion of the x-ray beam which can encompass a significantly larger area than the AFM data of Figs. 1 and 2. Hence an exact correlation of the surface or interfacial RMS roughness values from the two measurements is not necessarily expected. For the work completed here, surface roughness determined from XRR measurements range from 10% to 25% larger than the same values determined from AFM.

Despite these comparative issues, the as-deposited TiSiN/SiLK<sup>®</sup> interfacial roughness as determined by XRR measurements is a factor of two larger than that

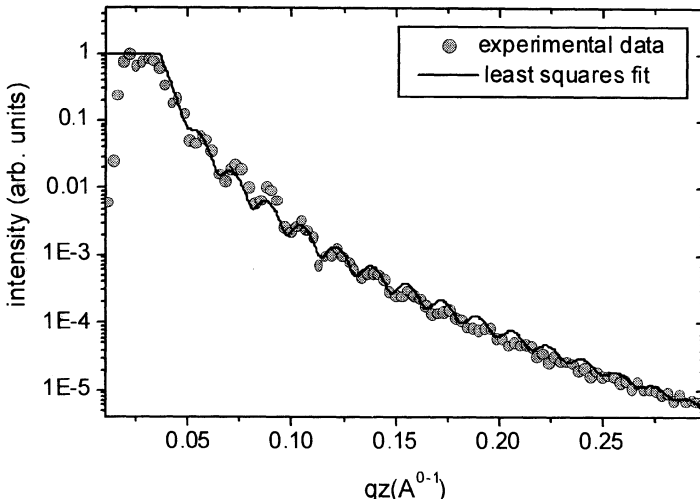


Figure 3. Specular XRR data (circles) and model (solid line) from a TiSiN/SiLK<sup>®</sup> bilayer stack. The oscillations in the XRR intensity correspond to a TiSiN film thickness of 34.5 nm. The model also provides surface and interfacial roughness values of  $0.8 \pm 0.3$  nm and  $0.8 \pm 0.3$  m, respectively.

measured from the as-deposited SiLK<sup>®</sup> surface via AFM. This raises the question of potential modification of the SiLK<sup>®</sup> surface during the reactive sputtering process. Exposure of SiLK<sup>®</sup> films to typical PVD plasma powers does not result in significant etching of the SiLK<sup>®</sup>, although plasma-induced surface roughening has been observed and presumably contributes to the enhanced TiSiN/SiLK<sup>®</sup> interfacial roughness determined from the data in Fig. 3.<sup>8</sup> To assess effects of such *in situ* interfacial roughening off-specular XRR measurements were carried out on TiSiN/SiLK<sup>®</sup> and TiSiN/SiO<sub>2</sub> stacks to determine whether the observed roughening is conformal in nature. It has been firmly established that off-specular XRR can be used as a tool to study interfacial correlations in multilayer systems.<sup>9</sup> A quantitative review of that theory is beyond the scope of this work. However, a simple qualitative argument can be made. Consider a multilayer structure comprised of layers of uniform density and possessing well-defined surface and interfacial roughness. The electron density modulation along the z-axis (average layer normal) will result in a specularly reflected x-ray intensity. The presence of roughness at the multilayer surface or interfaces will scatter photons out of the specular direction and contribute to the so-called diffuse scattering. If multiple interfaces possess a high degree of spatial correlation the off-specular scattering from each interface can actually interfere, resulting in interference fringes in the *diffuse* scattering, as well as the specular scattering. The presence of diffuse interference fringes

in off-specular XRR spectra can be modeled using the distorted wave Born approximation. This has been summarized by Sankaran.<sup>10</sup> Simulated results for the

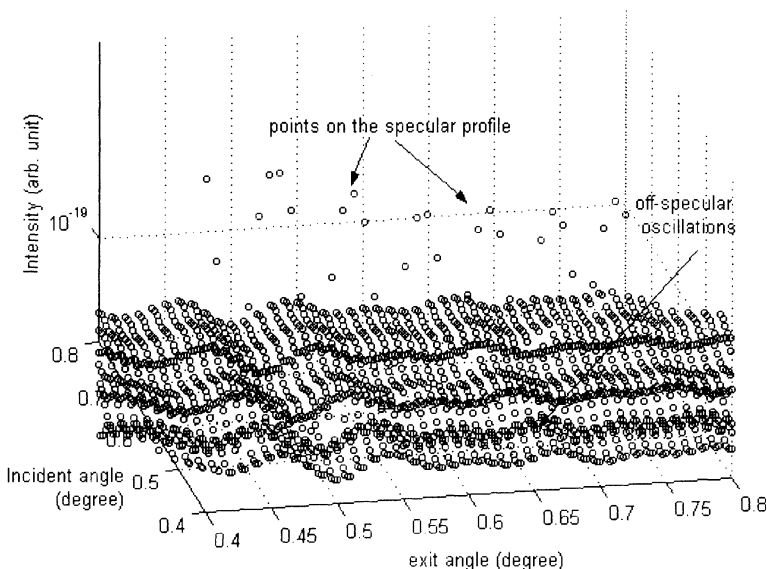


Figure 4. Simulated specular and off-specular scattered x-ray intensity from a single layer with highly correlated interfacial roughness. Note high-intensity oscillations in the specular direction and the low-intensity oscillations in the off-specular direction. The latter are a direct result of interfacial correlation.

specular and off-specular reflectivity from a single layer film with two correlated interfaces are shown in Fig. 4. In this figure the XRR intensity is plotted as a function of incident angle and exit angle. The specular 'ridge' of scattering is defined by the line at which these two quantities are equal. For the modeled data in Fig. 4 interference fringes corresponding to specular reflection are clearly evident. Note, however, at considerably lower intensities a second set of oscillations are evident. These oscillations in the off-specular, diffuse, scattering possess the same 'period' as the specular fringes. However, the intensity of these fringes is approximately constant as a function of incident x-ray angle (typically referred to as  $\theta$  in x-ray scattering). The intensity of these fringes is strongly modulated as a function of exit angle (typically referred to as  $2\theta - \theta$  in x-ray scattering where  $2\theta$  is the total scattered angle). The model used to generate the data in Fig. 4 assumed well correlated-interfaces.

To compare these simulations with experimental data, specular and off-specular XRR data from TiSiN/SiLK<sup>®</sup> and TiSiN/SiO<sub>2</sub> stacks are shown in Fig. 5. The TiSiN layer thickness is 34.5 nm for each stack. The panel in Fig. 5a represents a gray-scale intensity plot of scattered x-ray intensity as a function of incident x-ray or  $\theta$  angle (vertical axis) and exit or  $2\theta$  angle (horizontal axis). The prominent diagonal line of high scattered intensity defined by  $\theta = 2\theta/2$  corresponds to specular reflection. Nearly as prominent in Fig. 5a is a modulation in the diffuse intensity with precisely the same

period as the specular fringes. This modulation in the diffuse, off-specular scattering corresponds to the low-intensity oscillations observed in the simulation data of Fig. 4. From these data we conclude a high degree of interfacial roughness correlation exists between the TiSiN surface and TiSiN/SiLK® interface. Figure 5b shows a similar plot for scattered x-rays from a TiSiN/SiO<sub>2</sub> stack. The specular interference fringes in Fig. 5b

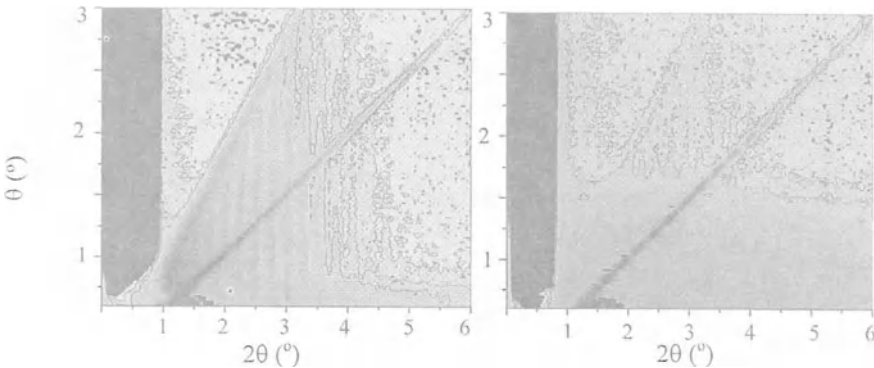


Figure 5. (a) Left panel: Reflected x-ray intensity from a 34.5 nm-TiSiN/SiLK® stack. The intense (dark) diagonal line represents the specular ‘ridge’ of scattering depicted in Fig. 3. The vertical intensity ‘stripes’ in the diffuse-scattering denote correlation of the TiSiN surface and TiSiN/SiLK® interface. (b) Right panel: Reflected x-intensity from a 34.5 nm-TiSiN/SiO<sub>2</sub> stack. The specular intensity oscillations are stronger due to the smoother SiO<sub>2</sub> substrate, but there are no off-specular intensity oscillations. This denotes a lack of correlation between the TiSiN surface and the TiSiN/SiO<sub>2</sub> interface.

are more intense compared with the data in Fig. 5a due to the reduced roughness of the SiO<sub>2</sub> substrate. However, no periodic features are present in the diffuse scattered intensity. This implies that the TiSiN surface and the TiSiN/SiO<sub>2</sub> interface are not correlated as in the case of the polymer. Presumably, the inherent roughness of the TiSiN film deposited via reactive PVD is on the same order as that of the SiO<sub>2</sub> substrate and prevents development of spatial correlation between the TiSiN surface and the TiSiN/SiO<sub>2</sub> interface during TiSiN film growth. A more detailed comparison of the specular and off-specular scattering from the TiSiN/SiLK® and TiSiN/SiO<sub>2</sub> stacks is shown in Fig. 6. The presence of oscillations in the off-specular intensity data for the TiSiN/SiLK® stack is clear, as well as its correlation to the specular interference fringes.

The capability of off-specular and specular x-ray scattering to simultaneously determine multilayer structure and interfacial correlation constitutes a powerful tool for the investigation of barrier/polymer interfaces. To further investigate interfacial stability in the TiSiN/SiLK® system, a multilayer stack test structure was fabricated for thermal annealing studies. This test structure consisted of a TiSiN/Cu/TiSiN sandwich deposited on both SiLK® and SiO<sub>2</sub> substrates. The thickness of each TiSiN layer is  $14.0 \pm 0.5$  nm. The thickness of the Cu layer is  $58.5 \pm 0.5$  nm. These particular multilayer structures were chosen to examine the effects of thermally-induced stress on the morphological stability of the barrier/polymer interface. During the anneals thermal stresses arise from the thermal expansion mismatch between the Cu, barrier, and dielectric components.

Annealing runs consisted of a 20 minute ramp and a one-hour soak. Soak temperatures were 350 °C, 450 °C, and 550 °C. The latter temperatures exceed the accepted glass transition temperature of SiLK® thermoset films (~ 425 °C).

Specular XRR data and corresponding model fits are displayed in Fig. 7 for the TiSiN/Cu/TiSiN/SiLK® stack and in Fig. 8 for the TiSiN/Cu/TiSiN/SiO<sub>2</sub> stack. Above the critical wave vector for total external reflection of x-rays (~ 0.05 Å<sup>-1</sup>) the specular

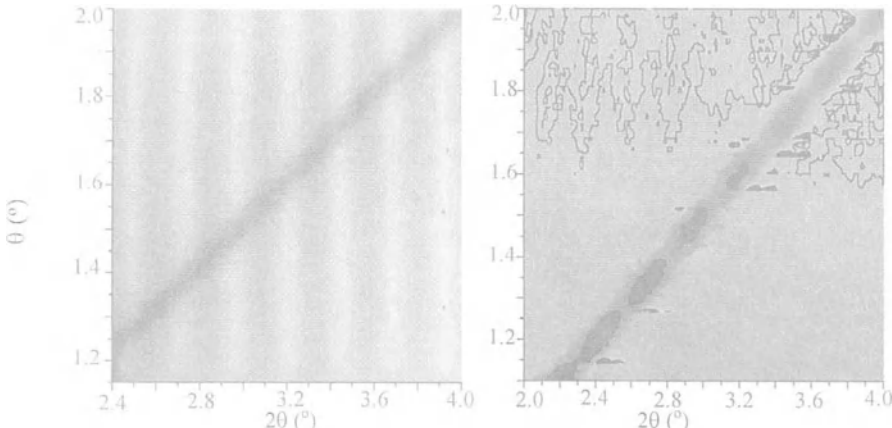


Figure 6. Expanded view of reflected x-ray intensity of Fig. 5. (a) Left panel: Reflected x-ray intensity from a 34.5 nm-TiSiN/SiLK® stack. The vertical intensity ‘stripes’ in the diffuse-scattering denote correlation of the TiSiN surface and TiSiN/SiLK® interface. (b) Right panel: Reflected x-intensity from a 34.5 nm-TiSiN/SiO<sub>2</sub> stack. The lack of off-specular intensity oscillations denote a lack of correlation between the TiSiN surface and TiSiN/SiO<sub>2</sub> interface.

XRR data for as-deposited stacks in Figs. 7 and 8 display high frequency interference fringes corresponding to the total stack thickness (~ 88 nm) and low frequency fringes corresponding to the TaSiN thickness (~ 14 nm). Upon annealing, the loss of both of these features in the XRR data of Fig. 7 implies a significant thermally-induced modification of the TiSiN/Cu/TiSiN/SiLK® stack. From quantitative modeling as described above, the TaSiN/Cu interfacial roughness parameter increases from 5±0.5nm to 8±0.5nm after annealing at 450 °C. Likewise the TaSiN/SiLK interfacial roughness parameter increases from 0.7±0.3nm to 1.9±0.3nm for the same annealing cycle. In contrast the TaSiN/Cu and TaSiN/SiO<sub>2</sub> interfacial roughness parameters determined from the analysis of specular XRR data in Fig. 8 remain unchanged upon annealing at 3.2±0.3nm and 0.3±0.2nm, respectively. The interfacial stability of the stacks on the SiO<sub>2</sub> substrates is clearly evident by the insensitivity of the high- and low-frequency interference fringes in the specular XRR data of Fig. 8 to annealing temperature. This stability is in stark contrast to the corresponding XRR data from the stacks deposited on SiLK structures. In addition, the specular XRR data of Fig. 7 displays a greater thermal effect on the specular intensity following an anneal at 350 °C compared to annealing at 450 °C. This effect is reproducible and is currently under investigation. It is presumably related to the glass transition temperature of the SiLK® resin which is approximately 425 °C for the formulation studied here.

Presumably the large modification of the interfacial morphology in the barrier stack on SiLK originates from stresses arising from the large mismatch between the thermal expansion coefficients of Cu (17 ppm/ $^{\circ}$ C), Si (5 ppm/ $^{\circ}$ C), and SiLK<sup>®</sup> (66 ppm/ $^{\circ}$ C). Thermal expansion coefficients for TaSiN films of the composition studied here are not available. The question remains whether the increased interfacial roughness parameters calculated from the XRR data of Fig. 7 originate from a true roughening of the interfaces or rather result from interfacial density gradations or interfacial diffusion. Specular XRR is sensitive only to the normal component of the electron density variation. It is not sensitive to the nature of this electron density variation, i.e. whether it results from correlated roughening or interfacial compositional gradation. Two sets of experiments were carried out to address this question. Firstly, off-specular XRR was measured for the same structures and annealing schedules as the specular XRR to evaluate the evolution of interfacial correlation. Secondly, RBS measurements of the same stacks were carried out to investigate compositional stability of

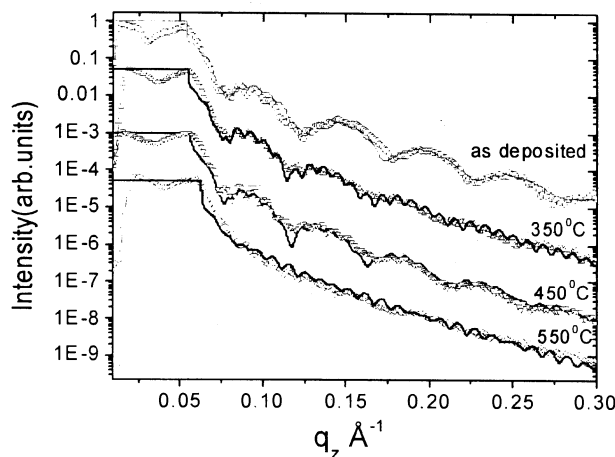


Figure. 7 Specular XRR for a TiSiN/Cu/TiSiN stack on SiLK<sup>®</sup>. The solid lines denote a best fit to the model described in the text. The high and low frequency oscillations in the data correspond to the overall stack thickness and barrier thickness, respectively. The loss of these oscillations with annealing indicate interfacial disorder.

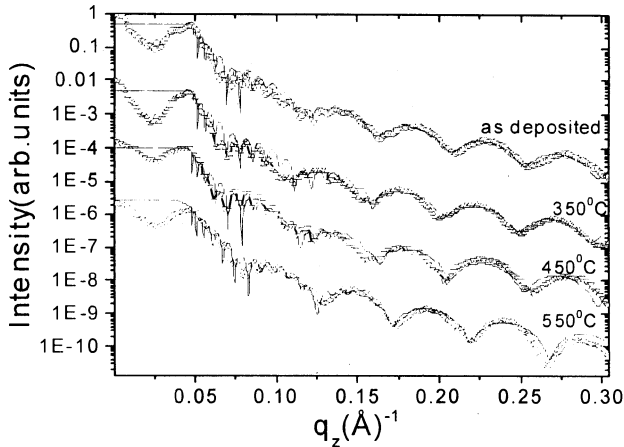


Figure. 8 Specular XRR for a TiSiN/Cu/TiSiN stack on SiO<sub>2</sub>. The solid lines denote a best fit to the model described in the text. The high and low frequency oscillations in the data correspond to the overall stack thickness and barrier thickness, respectively. The consistency of these oscillations with annealing indicate a much higher interfacial stability compared to the SiLK<sup>®</sup>-based stacks.

the interfaces.

The off-specular data for the TaSiN/Cu/TaSiN/SiO<sub>2</sub> stack reveal no interfacial correlations, similar to the data of Fig. 6, above. In contrast, off-specular XRR from TaSiN/Cu/TaSiN/SiLK® stacks do reveal an evolution with annealing. These data are shown in Fig. 9. The presence of oscillations in the off-specular XRR occur for the as-deposited stack, the stack annealed at 350 °C, and the stack annealed at 450 °C. Few discernible off-specular oscillations are evident for the stack annealed at 550 °C. Note

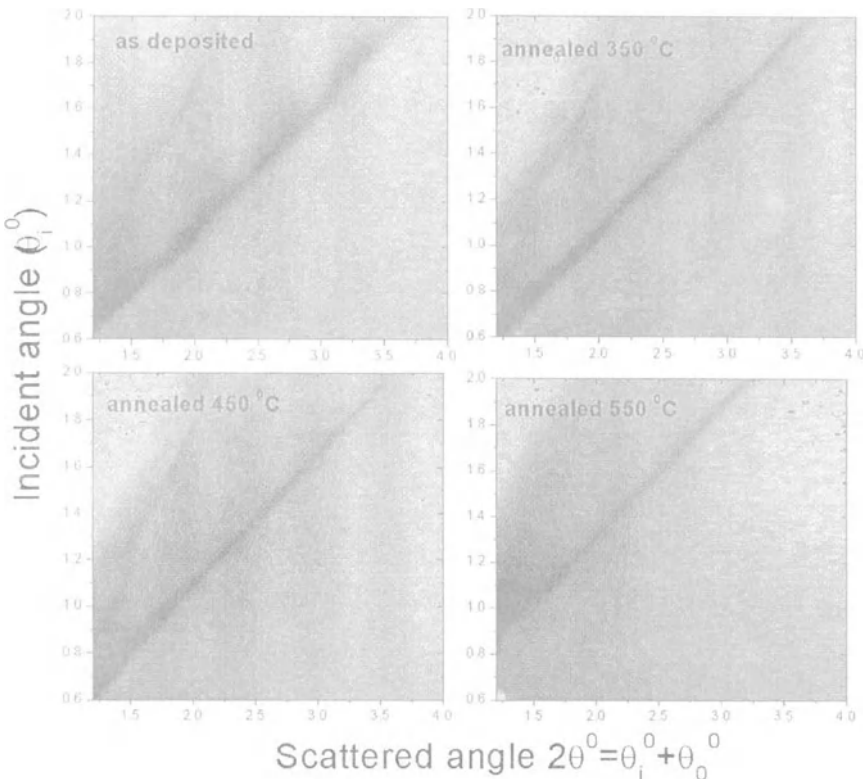


Figure 9. Off-specular XRR gray-scale plots for TaSiN/Cu/TaSiN/SiLK® stacks (as-deposited and annealed). At least four oscillation periods in the off-specular scattering measured from the as-deposited, 350 °C annealed, and 450 °C annealed samples. The off-specular scattering from the 550 °C annealed stacks displays much weaker oscillations. These data imply a significant loss in interfacial correlation at the highest annealing temperature.

that the period of these off-specular oscillations correspond to the thickness of the TaSiN barrier layers. The correlation contributing to the off-specular oscillations thus corresponds to the barrier interfaces. These data imply that up to 450 °C significant interfacial correlation remains between the barrier interfaces. However for samples annealed at 550 °C the correlations are reduced. The data in Fig. 9 suggest that the barrier interfaces are still well-defined with respect to the electron density gradient.

Barrier interfaces undergoing significant interfacial diffusion would not be expected to yield off-specular scattering.

Rutherford backscattering data for the  $\text{SiO}_2$  and SiLK®-based test structures are shown in Figs. 10 and 11, respectively. In each RBS plot the inset shows detail in the region corresponding to the backscattering of  $\alpha$ -particles from the Ti atoms resident in the barrier layers. Data are shown for as-deposited as well as annealed samples. For both figures the large peak in the backscattered intensity at channel number 815 results from the Cu layer. The rightmost Ti peak corresponds to the topmost barrier layer and the leftmost Ti peak corresponds to the buried barrier layer. The former Ti peak is stable for both the  $\text{SiO}_2$  and SiLK® substrates for as-deposited, 350 °C annealed, and 450 °C annealed samples. However, for samples annealed at 550 °C RBS data exhibit a significant smearing of the region between the Ti and Cu peaks. This occurs for stacks on  $\text{SiO}_2$  as well as SiLK®. This smearing results primarily from a broadening of the Cu peak and is attributed to compositional diffusion at the upper barrier/Cu interface. The FWHM of the Ti peak is relatively unchanged.

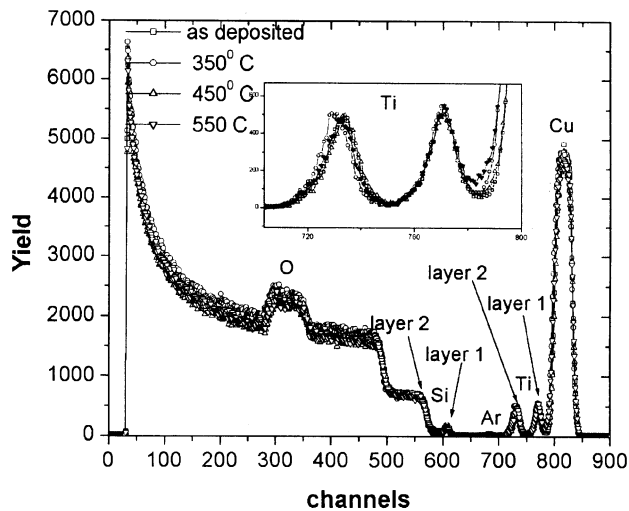


Figure 10. RBS spectra from the  $\text{TaSiN}/\text{Cu}/\text{TaSiN}/\text{SiO}_2$  stack. The inset shows expanded detail in the region of the two Ti peaks corresponding to the outer barrier layer (layer 1) and the inner barrier layer (layer 2).

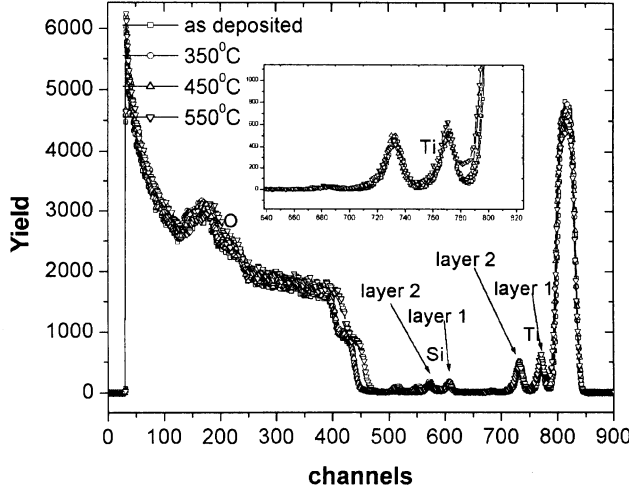


Figure 11. RBS spectra from the  $\text{TaSiN}/\text{Cu}/\text{TaSiN}/\text{SiLK}^\circledR$  stack. The inset shows expanded detail in the region of the two Ti peaks corresponding to the outer barrier layer (layer 1) and the inner barrier layer (layer 2).

More importantly it is evident for both  $\text{SiO}_2$  and SiLK® substrates and thus is less likely to be related to the interfacial roughening which occurs preferentially in the SiLK® structures.

Taken in their entirety the data in Figs. 7-11 sketch a clear picture of the thermally induced disorder in the TaSiN/Cu/TaSiN test structures on SiLK® and  $\text{SiO}_2$ . Compositionally, the TaSiN/Cu/TaSiN/SiLK® and TaSiN/Cu/TaSiN/ $\text{SiO}_2$  stacks are stable for both 350 °C and 450 °C anneals. Even at an annealing temperature of 550 °C the only compositional change evident via RBS occurs in a single interfacial region between the Cu and topmost barrier layer and is independent of the substrate. Thus we conclude that compositionally, the stack is stable with respect to the barrier at the dielectric interface. In addition, interfacial correlations are evident for barrier layers in all films except those annealed at 550 °C. Since no significant interfacial gradation is occurring, and interfacial correlations are still present in the stacks we conclude that the roughening in the SiLK® test structure implied by the specular XRR data of Fig. 7 results from a correlated interfacial morphology. The layer becomes rougher, but the thickness and composition remain approximately constant.

## 5. CONCLUSIONS

A study of the interface morphology of TiSiN diffusion barriers deposited via reactive physical vapor deposition (reactive PVD) on a low-k dielectric thermoset polymer was presented. It was shown that the conformality of the TiSiN barrier film on the SiLK® is high in contrast to similar barrier layers on  $\text{SiO}_2$  substrates. The effects of thermally-induced stress on the morphology of the barrier/polymer interface in multilayer test structures consisting of TiSiN/Cu/TiSiN/SiLK® and TiSiN/Cu/TiSiN/ $\text{SiO}_2$  stacks were also investigated for as-deposited and annealed samples (up to 550 °C). It was shown that the multilayer stacks deposited on SiLK® exhibited a significant thermally-induced roughness compared to similar stacks on  $\text{SiO}_2$  substrates. However, despite the increased roughness, the conformality of the TiSiN layers remained. This observation implies that thermally-induced morphological changes in the TiSiN/SiLK® interface are dominated by roughening and not by interdiffusion.

## ACKNOWLEDGEMENTS

The support of the Dow Chemical Company and the New York State Center for Advanced Thin Film Technology is gratefully acknowledged.

## REFERENCES

1. *The International Technology Roadmap for Semiconductors*, (Semiconductor Industry Association, San Jose, 1999).
2. P. J. Pokela, E. Kolawa, M.-A. Nicolet, and R. Ruiz, *J. Elec. Soc.* **138**, 2125-2129 (1991).
3. X. Sun, J. S. Reid, E. Kolawa, and M.-A. Nicolet, *J. Appl. Phys.* **81**, 664-671 (1996).

4. S. Sankaran, W. Harris, G. Nuesca, E.O. Shaffer, S.J. Martin, and R. E. Geer in *Proceedings of the 3rd International Interconnect Technology Conference*, (IEEE, San Francisco, CA), 40-42 (2000).
5. L. G. Parrat, Phys. Rev., **95**, 359 (1954).
6. D.G. Stearns, J. Appl. Phys. **65**, 491 (1995).
7. A. P. Payne and B. M. Clemens, Phys. Rev. B, **47**, 289 (1993).
8. Z. Bian, University at Albany, unpublished results.
9. S. K. Sinha, E. B. Sirota and S. G. Garoff, Phys. Rev. B, **38**, 2297 (1998).
10. S. Sankarn, Ph.D. Thesis, University at Albany.

# CHEMISTRY IN THE INITIAL FORMATION OF NITRIDE BARRIERS ON LOW-K DIELECTRICS

Peter Abramowitz, Junjun Liu, Michael Kiene, Paul S. Ho, Jay Im\*

## ABSTRACT

*In-situ* X-ray Photoemission Spectroscopy (XPS) has been employed in our lab to study the initial formation of tantalum (Ta) and titanium (Ti) nitride barriers on low dielectric constant (low-k) materials. The effects of low energy (100/500eV) nitrogen ion bombardment were examined in order to understand how the interface could be modified or controlled. This paper summarizes recent results on SiLK\* in comparison with Bisbenzocyclobutene (BCB\*) (\*trademark of the Dow Chemical Company). *In-situ* XPS studies showed that tantalum or titanium reacted with SiLK very strongly. Carbides and sub-oxides formed immediately upon the deposition of tantalum on SiLK. Compared with BCB, SiLK was found to have both similar binding to tantalum nitride and a similar amount of nitride incorporation near the interface. Moreover, the addition of a low-energy nitrogen ion beam can slightly increase the chemical bonding between the barrier and the low-k without inducing significant intermixing.

## INTRODUCTION

Copper diffuses easily into and adheres poorly onto most low-k dielectrics in the interconnect structures. An intermediate layer of highly reactive metal, or its nitride equivalent, which strongly binds to both dielectric and copper and thus acts as both a diffusion barrier and adhesive, has to be deposited between the copper and low-k dielectric. The diffusion barrier is usually grown by chemical vapor deposition (CVD), plasma deposition, or a combination of these techniques. These deposition processes

---

\* Peter Abramowitz, Advanced Products Research and Development Laboratory, Motorola, 3501 Ed Bluestein Blvd., Austin, Texas 78721

Junjun Liu, Paul S. Ho, Laboratory for Interconnect and Packaging, Microelectronic Research Center, The University of Texas, PRC/MER 2.206, Mail Code R8650, Austin, Texas 78712, liujj@mail.utexas.edu, Tel: (512)-471-8966, Fax: (512)-471-8969

Michael Kiene, AMD/Motorola Alliance, 3501 Ed Bluestein Blvd., Austin, Texas 78721  
Jay Im, the Dow Chemical Company, Midland, Michigan 48674

*Metallization of Polymers 2.*

Edited by Edward Sacher, Kluwer Academic/Plenum Publishers, 2002

change the surface chemistry of the low-k material, and the chemical bonding between the barrier layer. Therefore, the low-k substrate needs to be analyzed to see if the material can be successfully integrated into an interconnect structure.

In this paper, tantalum nitride and titanium nitride barriers were grown on SiLK by evaporating metal under two different conditions. By "reactive growth", we refer to the evaporation in a nitrogen ambient, and by "ion-assisted growth", the evaporation done with low energy nitrogen ion bombardment. Ion-assisted deposition is generally not used in the production line. However, it greatly simplifies the possible deposition variables by solely focusing on how low-energy ions affect the development of the interface and the growth of the barrier layer.

Low-energy ion bombardment is well known to be able to mediate reactions, modify substrate and densify film deposited. As far as polymer substrate is concerned, grafting of chemical groups, inducing cross-link and increasing surface functionality have already been observed. The studies presented in this report closely follow the methodology of previous work.<sup>1,2,3</sup> Three main issues are focused on:

1. The apparent chemical bonding at the interface,
2. The chemical homogeneity of the nitride film near the interface, and
3. The amount of ion-induced intermixing.

SiLK is also compared with another common low-k material, bisbenzocyclobutene (BCB), which provides a baseline for comparison in this report.

## EXPERIMENT

### A. Instrumentation

X-ray photoemission (XPS) measurements were done in an ultra-high vacuum chamber following a procedure described in a previous paper<sup>2</sup>. To summarize, the typical base pressure was  $1 \times 10^{-10}$  torr, and a nonmonochromatized Mg  $\text{k}\alpha$  x-ray source combined with a Leybold hemispherical analyzer operating at 38.45eV pass energy was used to collect the data. This gave a nominal energy resolution of 0.9 to 1.0eV<sup>1</sup>. Except for the angle-resolved scans, all of the measurements collected secondary electrons that came from a glancing angle (19°) to the sample surface. The binding energy scale was calibrated by matching the carbon contamination of a silicon wafer to -285.0eV<sup>4</sup>. The ion source was an ultra-high vacuum compatible differential ion gun. The ion current, as measured with a Faraday cup, was 0.1  $\mu\text{A}/\text{cm}^2$  for 100eV ions and 0.15  $\mu\text{A}/\text{cm}^2$  for 500eV ions. During the growth of tantalum and titanium nitride, the ion to metal ratio was kept at a ratio of about one to one. The incident angle of the ions was 40° from the sample's normal. The tantalum and titanium growths were done with home built electron beam evaporators and the thickness of the sample was measured *in situ* by a crystal quartz monitor. This was calibrated by measuring the thickness of thick films *ex situ* with an atomic force microscope.

## B. Dielectrics

The 100-nanometer thick SiLK films were provided by Dow Chemical. The SiLK films were kept in a vacuum storage and taken out only when new samples were prepared. The ~50nm BCB films were spin coated on a silicon wafer and cured at 300°C for 30 min. in a nitrogen ambient. Prior to growth and analysis, all samples were placed in an introduction chamber and outgassed at 250°C for at least one hour. The samples were then transferred to the analysis chamber without breaking vacuum. Note that the very thin films on highly doped Si wafer usually do not charge up during XPS measurements, so no electron flood gun was used in these experiments.

## RESULTS

### A. Nitrogen Ion Bombardment of SiLK

The chemical structure of SiLK is partially disclosed by Dow Chemical to be a cross-linked polyphenylene polymer<sup>5</sup>. Previous XPS measurement verifies that it is primarily an aromatic carbon and oxygen structure<sup>1,6</sup>. Similar results are seen here except that the atomic concentration of oxygen is slightly higher at ~6% due to the higher concentration of oxygen at the top few monolayers of SiLK. Figure 1 shows the dependence of the oxygen concentration with the electron emission angle with respect to the tangent of the sample's surface. At normal emission, the oxygen content was ~3%, in agreement with the previous work<sup>6</sup>.

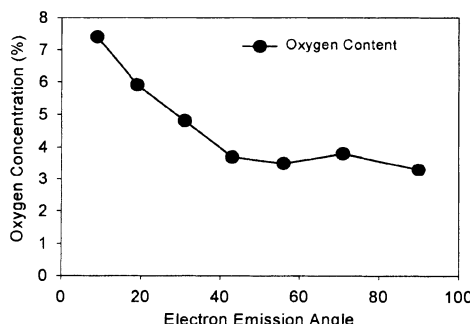


Figure 1. Oxygen enriched surface of clean SiLK

Previous studies<sup>2</sup> have also shown that nitrogen implanted into a polymer can greatly influence the growth of a nitride layer on top of it. SiLK samples were exposed to both 100eV and 500eV nitrogen ions with a total flux of  $1.5 \times 10^{15}$  ions/cm<sup>2</sup>. Angle resolved measurements of the atomic concentration of nitrogen versus electron emission angle are shown in figure 2. The hump in the nitrogen concentration at low emission angle with 100eV bombardment indicates implantation of nitrogen atoms in the top few monolayers

of SiLK. In contrast, the 500eV ion bombardment shows nearly a uniform concentration versus electron emission angle, corresponding to a much more uniform nitrogen concentration in the top several nanometers of SiLK. Increase of the amount of nitrogen embedded in SiLK with ion dosage implies that either more reactive sites, such as nitrogen-containing functional groups, or more reactive forms of nitrogen, are created inside SiLK by the low energy nitrogen ions.

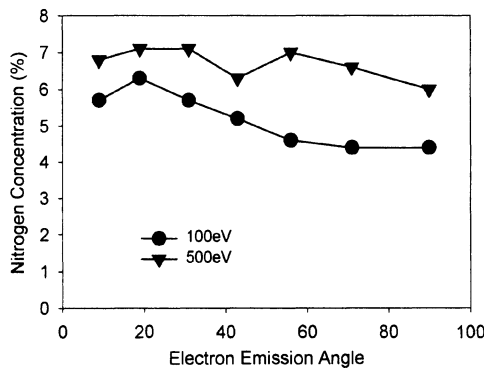


Figure 2. Implantation of Nitrogen in SiLK

## B. Initial Reactions between Refractory Metal and SiLK

Tantalum is a highly reactive material, and it needs to be in order to act as adhesion promoter with SiLK. Figure 3 shows XPS spectra of the carbon 1s peak for various different tantalum and tantalum nitride growths on SiLK.

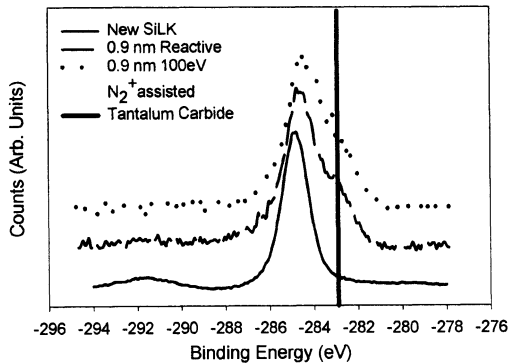
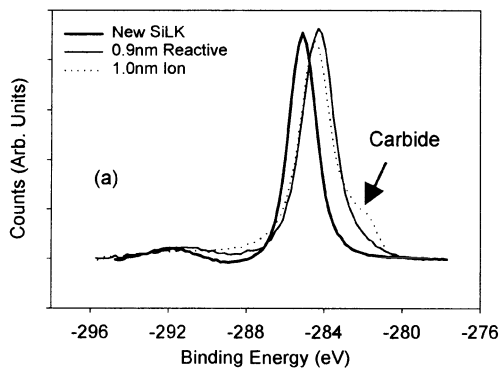


Figure 3. Reaction of Ta and Carbon in SiLK. Spectra are shifted apart for clarity.

All three growths show the development of a peak at a lower binding energy around -283.0eV. That is consistent with the development of tantalum carbide, which was confirmed at -282.9eV by measurements of thick tantalum samples. This most likely means that tantalum by itself can effectively disrupt the aromatic carbon compounds, and the nitrogen beam does not increase the bonding between SiLK and tantalum nitride. The lack of the  $\pi-\pi^*$  shakeup at -291.8eV is a further evidence of the disruption of the polymer by tantalum. The oxygen spectra can also elucidate the nature of the chemical bonding; however, oxide contamination during the evaporation of tantalum prior to deposition on the polymer compromises the validity of any interpretation of the oxygen 1s spectra.

Similar but weaker reactions occurred following the deposition of titanium on SiLK, as evidenced by smaller amount of carbide formed at similar metal coverage shown in figure 4(a). The weaker reactions enabled us to look at the effect of low energy ion bombardment. C1s spectra indicated more carbide formed with ion bombardment. Because titanium by itself does not attack the aromatic bond as strongly as tantalum, the  $\pi-\pi^*$  shakeup is still visible after the reactive growth of 0.9 nm titanium, even though it has shifted over 0.7eV to -291.3eV, and decreased in relative amplitude from 7.7% to 2.5% of the main carbon peak. With the help of 100eV nitrogen ions, the  $\pi-\pi^*$  shakeup has completely disappeared while another small carbide peak at -281.8eV has developed. Ion bombardment is clearly able to enhance the reactions of the refractory metal with the carbon in SiLK. The oxygen peaks do not show too much variation between the 0.9nm reactive and 1.0nm ion-assisted growths. Both spectra show the formation of a large amount of titanium oxide (65% for the reactive growth, 60% for the ion-assisted growth).



**Figure 4(a).** Initial Reactions of Titanium with SiLK: C 1s

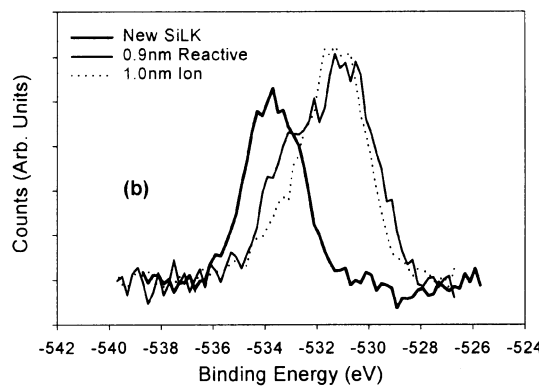


**Figure 4(b).** Initial Reactions of Titanium with SiLK: O1s

### C. Nitride Incorporation in the Ion-Assisted Growth

Previous work<sup>1</sup> has shown that the nitride incorporation in the ion-assisted growth is not uniform near the Low-k/diffusion barrier boundary. To study this effect, 100eV and 500eV ion-assisted tantalum nitride growth were performed at room temperature and nitride incorporation was monitored during film growth. The nitrogen ions penetrate more than a few monolayers into SiLK, as figure 2 implies. Therefore, it is necessary to de-convolute the nitrogen spectra using PeakFit<sup>7</sup> program to separate the amount of nitrogen implanted in SiLK from nitrogen that has reacted with tantalum to form tantalum nitride. An example of de-convolution of the nitrogen 1s spectrum is shown in figure 5, and the methodology is as follows.

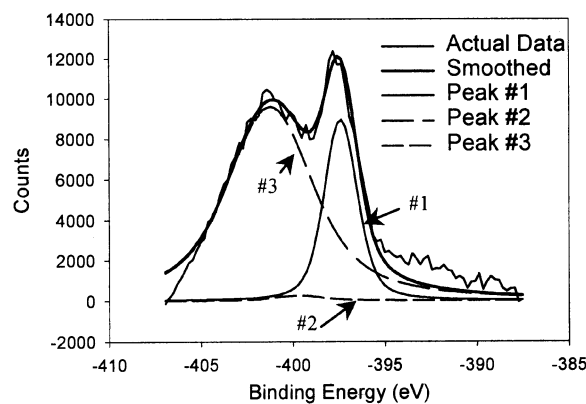


**Figure 5.** De-convolution of N 1s spectrum

Tantalum has a secondary peak located near -401eV that also needs to be deconvoluted from the nitrogen 1s spectra. This was done by assigning three peaks to each spectrum with the highest binding energy peak, peak #3, corresponding to the secondary tantalum 3p peak. Both the peak's width and peak position are allowed to move during peak fitting. The second peak, which is fixed at -399.0eV, corresponds to nitrogen embedded in SiLK. The width and binding energy are assumed to be exactly the same as for a new SiLK sample that is bombarded by 100eV nitrogen ions. The first peak corresponds to nitride, and is allowed to shift slightly during peak fitting, but is not allowed to stray more than 0.4eV from -397.0eV. Fitting nitride data for BCB is done exactly the same way except that nitrogen embedded in BCB is located at -399.7eV, and the second peak is adjusted accordingly.

The concentration of nitride with increasing thickness is plotted in figure 6. The exact ratio was determined by integrating the nitride peak (the first peak in fig. 5) and dividing by the integral number of counts for the main tantalum 4f peaks. This ratio was then multiplied by 0.42/2.4 which are the corresponding atomic sensitivities for nitrogen and tantalum. Both BCB and SiLK show a similar behavior at 500eV with the growth of near stoichiometric  $Ta_2N$  after less than 1.0 nanometer of growth. The 100eV ion-assisted growth on SiLK is not as successful as with the growth on BCB and very little nitride is incorporated initially in the tantalum nitride film.

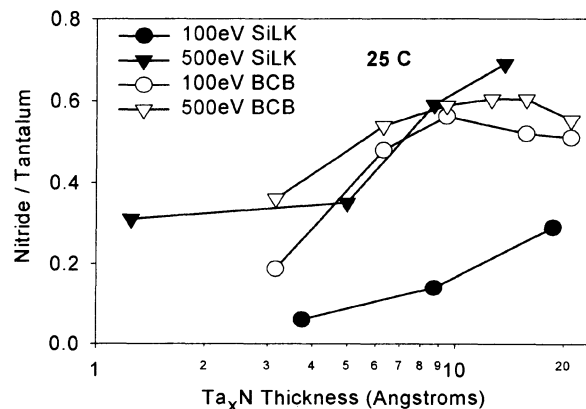


**Figure 6.** Nitride formation in nitrogen ion-assisted PVD Ta deposition on SiLK and BCB

Similar results were observed for Titanium nitride formation on SiLK and BCB, as shown on figure 7. No nitride appeared in the first few monolayers of reactive growth, and only a slight enhancement with 100eV nitrogen ions.

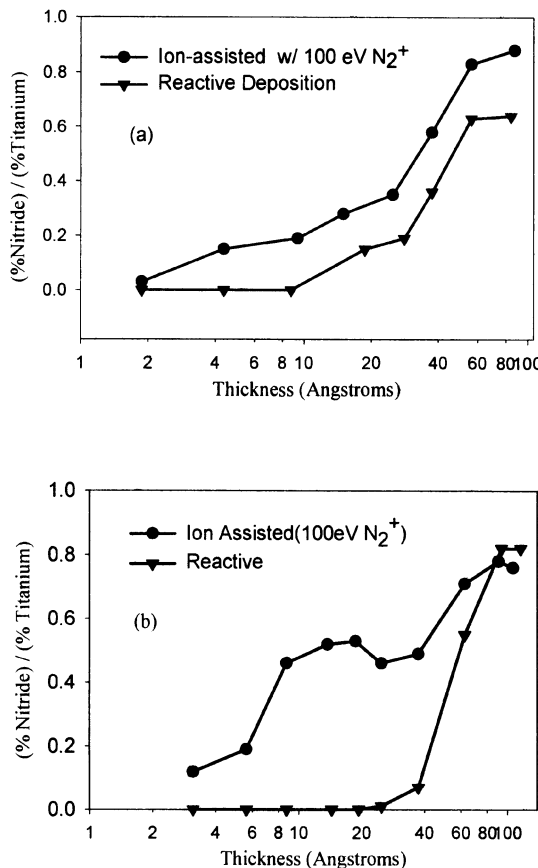


Figure 7. Effect of low energy ion bombardment on Titanium nitride growth: (a) SiLK, (b) BCB

#### D. Ion-induced Metal Intermixing

One effect of concern about low energy ion bombardment is physical intermixing between the initial nitride layer and SiLK. Although strong chemical bonding between the tantalum nitride and SiLK layers is desired, it is important that this effect does not come from isolated tantalum atoms or small tantalum clusters inside SiLK. Embedded tantalum atoms in SiLK will most likely increase the apparent binding between tantalum and SiLK, but it will have little effect on the adhesion. Previous results<sup>1,3</sup> with titanium nitride on various Low-k dielectrics have shown that nitrogen ions with energy greater than 500eV, with an ion fluence used in this study, can cause a significant amount of

intermixing and/or sputtering. Tantalum has a much greater atomic mass than titanium so intermixing is expected to be less with tantalum.

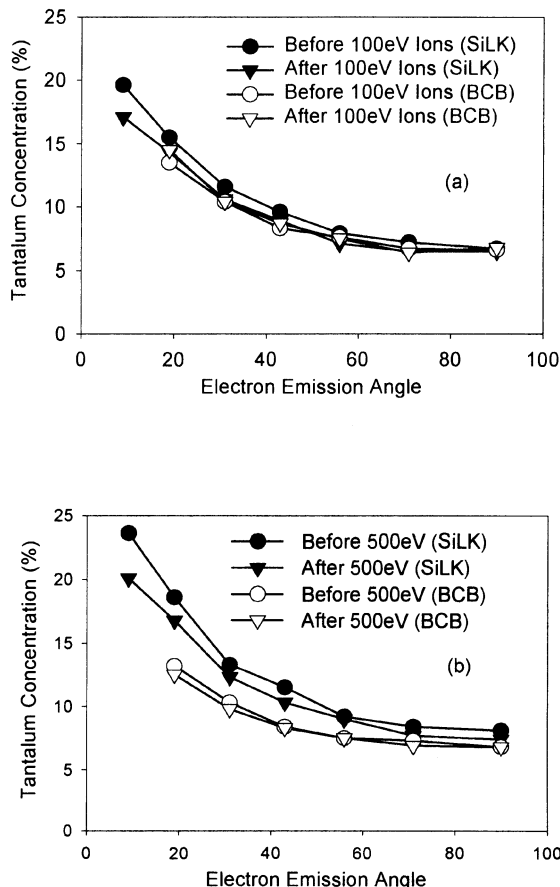


Figure 8. Ion-induced sputtering and/or intermixing: (a) 100 eV N<sub>2</sub><sup>+</sup>, (b) 500 eV N<sub>2</sub><sup>+</sup>

Figure 8 plots angle-resolved XPS scans for 1.0nm of tantalum on SiLK before and after a 1.5 \* 10 ions/cm ion fluence of 100eV and 500eV nitrogen ions. In both cases there is a slight nearly uniform decrease in the tantalum concentration with electron emission angle. This corresponds to a slight amount of ion-induced intermixing and sputtering with both 100eV and 500eV ion bombardment. For example, if the loss in signal at 90° electron emission angle were solely due to sputtering, this would correspond to a sputtering loss of approximately 0.5 angstroms or 5% of the original amount.

However, it is impossible to quantify the angle-resolved data for depth profiling since it is hard to tell the initial tantalum concentration due to the island-like growth of tantalum on SiLK at this low coverage.

As a reference, the same type of experiment was performed with tantalum on BCB, although the thickness of the film is only 0.75nm, and the result is shown in figure 8. The same qualitative result is seen with slightly less sputtering and intermixing occurring after a 100 and 500eV nitrogen ion bombardment with a fluence of  $1.5 \times 10^14$  ions/cm<sup>2</sup> when compared with SiLK.

In previous studies, larger amount of nitride was observed to form near the interface in the ion-assisted growth. To examine the possibility that this nitride formation is due to metal intermixing into SiLK, we used argon instead of nitrogen as the ion source to repeat the experiments.

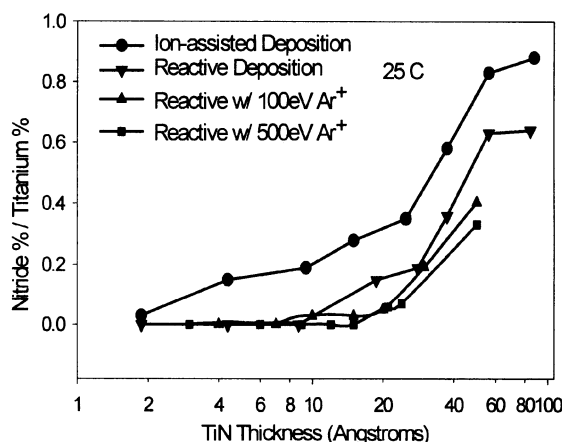


Figure 9. Effect of metal intermixing on nitride formation

Figure 9 shows the results in comparison with those of experiments with and without nitrogen ions. It can be concluded that metal intermixing didn't play a significant role in nitride incorporation near the interface in our experiments.

## DISCUSSION

Both tantalum and tantalum nitride are currently developed as diffusion barriers for low-k/Copper interconnect structure. The purpose of the studies done in this report is to identify how much control there is in producing such barrier layers near the SiLK interface. Like most metal reactive with polymers, tantalum strongly reacts with the polymer, which alters how different growth mechanisms work when compared to bulk tantalum. In this study, the effectiveness of tantalum nitride or tantalum as a diffusion barrier is not investigated. Rather the study focuses on how well growth can be controlled

to produce either a homogeneous tantalum or tantalum nitride layer. The interfacial effects can occur in the first few nanometers and becomes increasingly important as the diffusion barrier scales down in length to less than 10 nanometers.

With 500eV nitrogen ions, tantalum nitride is able to form quickly on top of SiLK. Although no significant ion-induced intermixing at 500eV was observed, the possibility that a highly mixed interfacial region occurs with higher ion energy or higher dosage can not be eliminated based only on the present results. Furthermore the carbon spectra of SiLK show a strong affinity between SiLK and tantalum, indicating most likely that the adhesion between tantalum nitride and SiLK is as good or better than tantalum and SiLK.

## ACKNOWLEDGEMENTS

The authors would like to thank the Semiconductor Research Corporation (SRC) for support of this project and Ed Shaffer from the Dow chemical company for the BCB. P.A. would like to thank the SRC for his graduate fellowship

## REFERENCES

1. P. Abramowitz, "Forming Nitrides with Low Energy Ions on Low-k Dielectrics", Ph.D. Dissertation, the University of Texas at Austin, April, 2000.
2. P. Abramowitz, M. Kiene, P. S. Ho, Effects of a low-energy ion beam on the growth of titanium nitride layers near the interface of a polyimide[Journal Paper], Applied Physics Letters, vol.74, no.22, 31 May 1999, p. 3293-5.
3. P. Abramowitz, M. Kiene, P. S. Ho, How low-energy ions can enhance depositions on low-k dielectrics[Journal Paper], Journal of Vacuum Science &Technology A-Vacuum Surfaces & Films, vol.18, no.5, Sept.-Oct. 2000, p.2254-61.
4. D. Briggs and M. Seah, *Practical Surface Analysis* (Wiley, New York, 1990), p. 606-637.
5. S. J. Martin, J. P. Godschalx, M. E. Mills, E. O. Shaffer II, and P. H. Townsend: Development of a Low-Dielectric-Constant Polymer for the Fabrication of Integrated Circuit Interconnect, Advanced Materials, Dec., No. 23, 2000, p. 1769-1778.
6. A. Rajagopal, C. Gregoire, J. J. Lemaire, J. J. Pireaux, M. R. Baklanov, S. Vanhaelemeersch, K. Maex, J. J. Waeterloos. Surface characterization of a low dielectric constant polymer-SiLK polymer, and investigation of its interface with Cu. [Conference Paper] AIP for American Vacuum Soc. Journal of Vacuum Science &Technology B, vol.17, no.5, Sept. 1999, p.2336-40.
7. PeakFit<sup>TM</sup>, version 4.05, AISN Software Inc., 1991.

# CAPABILITIES AND LIMITATIONS OF RBS TO CHARACTERIZE HYPER-THIN SILICON COMPOUND LAYERS ON VARIOUS POLYMERIC SUBSTRATES

G. Dennler, A. Houdayer, P. Raynaud, Y. Ségui, M.R. Wertheimer\*

## 1. INTRODUCTION

Transparent barriers, such as SiO<sub>2</sub> and SiN against oxygen and/or water vapor permeation through polymers are the object of increasing interest in the food and pharmaceutical packaging industries [1,2], and more recently in encapsulation of organic-based displays [3]. Their usual purpose is to act as gas barriers, reducing by up to three orders of magnitude (or even more) the undesirable permeation of gases and vapours (O<sub>2</sub>, CO<sub>2</sub>, H<sub>2</sub>O) through polymer substrates on which the layers are deposited [4]. Previous work performed in our laboratory proved that the growth of such layers deposited by Plasma-Enhanced Chemical Vapor Deposition (PECVD) behave in a layer-by-layer mode [5]. This phenomenon is attributed to a "pretreatment" of the polymer surface induced by the active species present in the plasma phase (such as Vacuum UV, energetic ions, atomic oxygen), which occurs during the first milliseconds of the deposition [5].

The objective of the work presented here is, first, to study the kinetics of the growth, that is, the evolution of the Silicon surface concentration versus time of deposition. Second, we aim to investigate the presence of an "interphase" between the polymeric substrate and the coating. We have chosen to use Rutherford Backscattering Spectroscopy (RBS), since its sensitivity is known to be great for the case of "heavy" elements combined with a "light" matrix [6]. Here, we report the strengths and limitations of this technique for characterizing hyper-thin silicon compound deposits on organic polymer substrates.

---

\* G. Dennler and M.R. Wertheimer, Dept. of Engineering Physics, Ecole Polytechnique, C.P. 6079, Station Centre-Ville, Montréal, QC H3C 3A7, Canada; e-mail : mwertheimer@courriel.polymtl.ca A. Houdayer, Groupe des Couches Minces (GCM) and Department of Physics, Université de Montréal, Montreal, QC H3C 3J7 Canada. P. Raynaud and Y. Ségui, Laboratoire de Génie Électrique de Toulouse (LGET), Université Paul Sabatier, 118 route de Narbonne, 31062 Toulouse, France.

## 2. EXPERIMENTAL METHODOLOGY

The two types of silicon compounds were deposited using a radio-frequency (RF : 13.56 MHz), capacitively-coupled PECVD reactor, described in detail elsewhere [4]. To deposit  $\text{SiO}_2$  layers, we used hexamethyldisiloxane (HMDSO), oxygen, and argon feed-gas mixture in the proportions 1:6:3, respectively. For the SiN coatings, we used silane, ammonia and argon gas mixture, in the proportions 1:3:1, respectively. The total gas pressure was kept constant at 80 mTorr (10.6 Pa), and the RF power,  $P$ , was always adjusted so as to maintain the d.c self-bias voltage,  $V_B$ , at the cathode (which supports the substrate) constant at  $V_B = -250$  V (i.e. :  $P=100$  W).

The depositions were performed on three different polymeric substrates, namely polyimide (PI, 50  $\mu\text{m}$ , DuPont Kapton-H®), polyethyleneterephthalate (PET, 50  $\mu\text{m}$ , DuPont Mylar®) and polycarbonate (PC, 175  $\mu\text{m}$ , GE Lexan®). Before each deposition, the polymer surfaces were exposed to a forced flow of dry nitrogen, so as to remove large dust particles from them.

The RBS experiments were performed using 1 and 1.5 MeV  $\alpha$  particle ( $\text{He}^{2+}$  ion) beams, with a diameter of approximately 2.5 mm, produced by a 1.6 MV Tandem accelerator (Tandetron, Université de Montréal). These particles were made to impinge at normal incidence on the sample surface. Two “IBM” geometries were used : the first one uses a 150° scattering angle and a silicon lithium drifted [Si(Li)] detector, which has a Full Width at Half Maximum (FWHM) energy resolution of 13 keV for the  $^{241}\text{Am}$   $\alpha$  line; the second geometry uses a 95° scattering angle (grazing angle) and a 18 keV FWHM [Si(Li)] detector. All the irradiations were performed at room temperature, in a vacuum of  $5.0 \times 10^{-6}$  Torr, with beam currents varying between 1 and 90 nA depending on the nature of the sample.

## 3. RESULTS

### 3.1 Kapton® PI

In order to investigate the evolution of the surface concentration of Si during film growth, we used the first geometry described above, with 1 MeV  $\alpha$  particles. Since the RBS peak area of a given element depends on the  $\alpha$  particle fluence used to perform the measurement, and since this fluence is not trivial to measure during irradiation of insulating materials like polymers, we evaluated the  $A_{\text{Si}}/A_C$  ratio,  $A_{\text{Si}}$  being the area under the silicon peak, and  $A_C$  that of a window of constant width chosen in the carbon signal coming from the substrate. As the substrate was found not to lose any significant amount of carbon during irradiation [7], the ratio  $A_{\text{Si}}/A_C$  is precisely equivalent to the number of silicon atoms per dose unit.

Figure 1 shows the evolution of  $A_{\text{Si}}/A_C$  versus the PECVD deposition time,  $t$ , for the case of  $\text{SiO}_2$  on Kapton.®. The surface concentration of Si is seen to be a linear function of  $t$ , for  $0.5 \text{ s} < t < 100 \text{ s}$ . Since the separately-measured  $\text{SiO}_2$  deposition rate was 1 nm/s, we can affirm that the sticking coefficient of Si precursors was constant during the entire growth process ( $0.5 \text{ nm} < d < 100 \text{ nm}$ ). Figure 2 shows the results for the same experiment in the case of SiN on Kapton®; the same linear evolution of the surface concentration of Si is observed for  $2 \text{ s} < t < 180 \text{ s}$ , that is,  $0.6 \text{ nm} < d < 60 \text{ nm}$  (the measured deposition rate of SiN having been 0.3 nm/s).

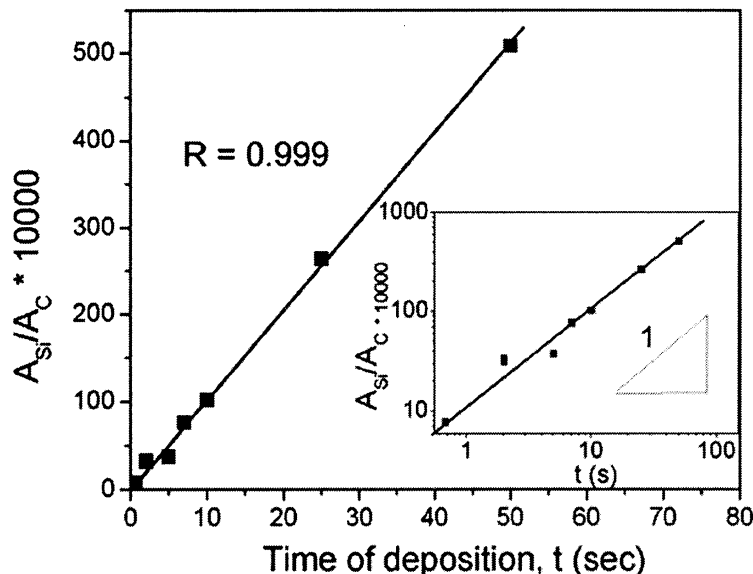


Figure 1.  $A_{Si}/A_C$  (see text) versus deposition time,  $t$ , evaluated by RBS, in the case of  $\text{SiO}_2$  deposition on Kapton®.

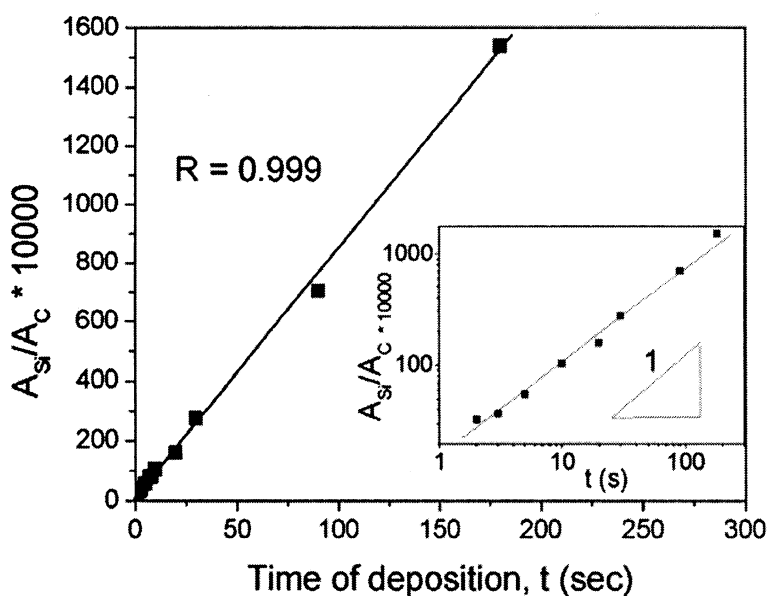
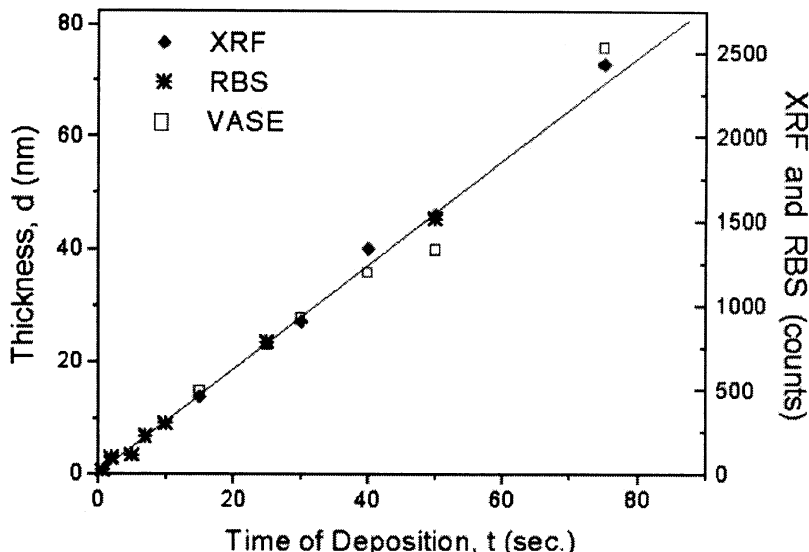


Figure 2.  $A_{Si}/A_C$  (see text) versus deposition time,  $t$ , evaluated by RBS, in the case of  $\text{SiN}$  deposition on Kapton®.



**Figure 3.** Superposition of (■) XRF and (▲) RBS ( $A_{Si} / A_C$  multiplied by 16400 to match the scale of this plot) signals, and (□) thicknesses evaluated by VASE directly on the polymer, versus time of deposition,  $t$  (in seconds).

As it was previously shown that for these Silicon compounds growth behaves in a layer-by-layer mode [5], RBS can be used as a very precise means for measuring hyper-thin film thicknesses, the sensitivity of which was evaluated to be about 1 Å (1/3 of mono-layer): since the Si surface concentration is a perfectly linear function of  $t$ , and since the chemical composition of the  $\text{SiO}_2$  was observed to be constant since the first layer deposited [8], one only needs to calibrate this linear plot versus thickness,  $d$ , using other precise means to measure  $d$ . Figure 3 comprises data evaluated by Variable Angle Spectroscopic Ellipsometry (VASE), X-Ray Fluorescence (XRF) and RBS, which are all seen to align perfectly after normalization.

The second (grazing angle) geometry, described earlier, was used to investigate the possible presence of an “interphase” [9] between the coating and the substrate. This region, sometimes exceeding 50 nm (for example in the cases of PET [9] and PC [10]), was found to consist of a cross-linked polymer with an “organosilicon” overlayer of varying chemical composition. It is thought to result from chemical modifications of the substrate surface and ablation / re-deposition of volatile organic fragments induced by VUV radiation [11], energetic ions and active species (such as AO) [12] coming from the plasma.

This grazing angle geometry allowed us to greatly enhance the depth resolution since the emerging particles lose more energy per unit of depth [6, 13], as illustrated in Fig. 4 : using RUMP software [14], we have simulated the RBS spectra of  $\text{SiO}_2$  coatings on Kapton® for three different cases, namely 40 nm of  $\text{SiO}_2$  films without an interphase, and with two different interphase thicknesses, 15 nm and 30 nm respectively. The interphases were simulated here by a layer of composition which evolves linearly from that of Kapton® to that of  $\text{SiO}_2$ .

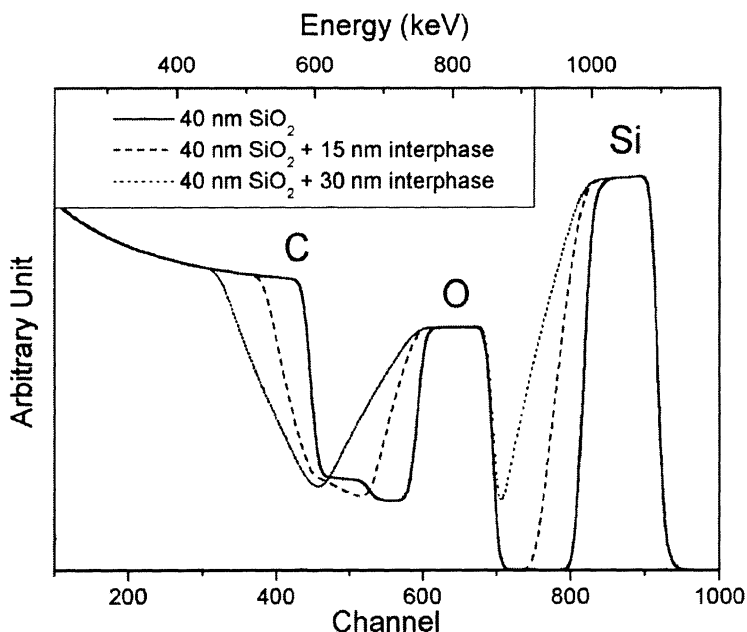


**Figure 4.** Illustration of the sensitivity of RBS at the geometry chosen : spectra produced using the RUMP code software.

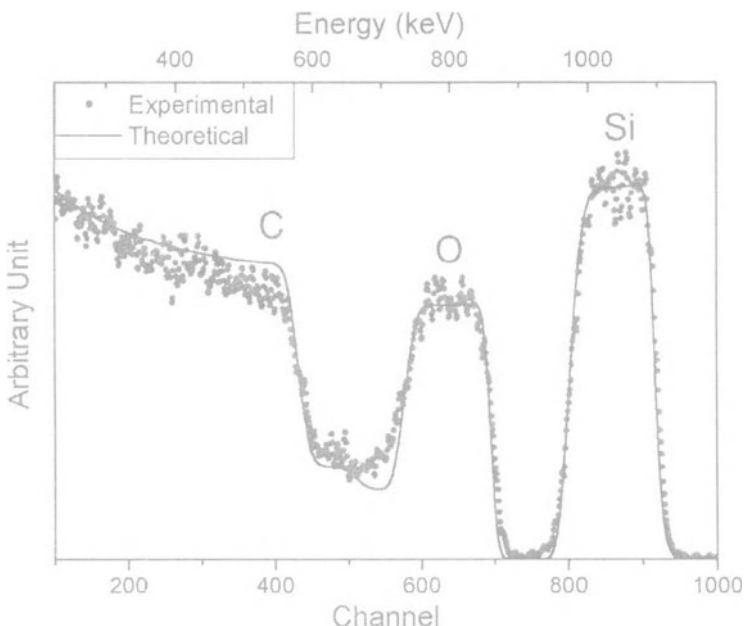


**Figure 5.** Experimental RBS spectrum of a 51 nm  $\text{SiO}_2$  coating on Kapton® fitted with RUMP (see text).

One notes that the slopes of the low energy (low channel number) edges of the Si and O peaks change, as does the high energy edge of the C peak. We estimate that this method is sensitive enough to detect an interphase thickness of less than 5 nanometers. Figure 5 shows the experimental RBS spectrum of a 51 nm (evaluated by VASE) SiO<sub>2</sub> coating on Kapton®, and the corresponding RUMP simulation : the best fit was obtained for the case of a 40 nm SiO<sub>2</sub> film and a 7 nm thick interphase, the latter value being close to the above-mentioned sensitivity limit.

We can therefore conclude that the interphase of PECVD SiO<sub>2</sub> on Kapton® is much thinner than in the cases of PET or PC substrates, which suggests that PI is much less susceptible to form volatile fragments than PET and PC. This latter statement appears to be confirmed by our recent mass-spectrometric investigations [15].

### 3.2 Lexan® PC and Mylar® PET

We tried to perform the same experiments using the two other polymer substrates, namely Lexan® PC and Mylar® PET. As these polymers are presumed to be readily damaged by energetic He<sup>2+</sup> particles, we used a 4 nA beam, that is, approximately 8 times less intense than in the case of Kapton®. However, after irradiation, we observed light scattering from the surfaces (not in the case of Kapton®), resulting from increased surface roughness directly on the black spot, which usually appears for all types of polymers (even Kapton®) at the very place where the beam had struck the sample (clear signs of drastic chemical modifications : hydrogen loss, creation of double bonds -C=C- and partial graphitization, which all modify the material's optical properties [16-19]).

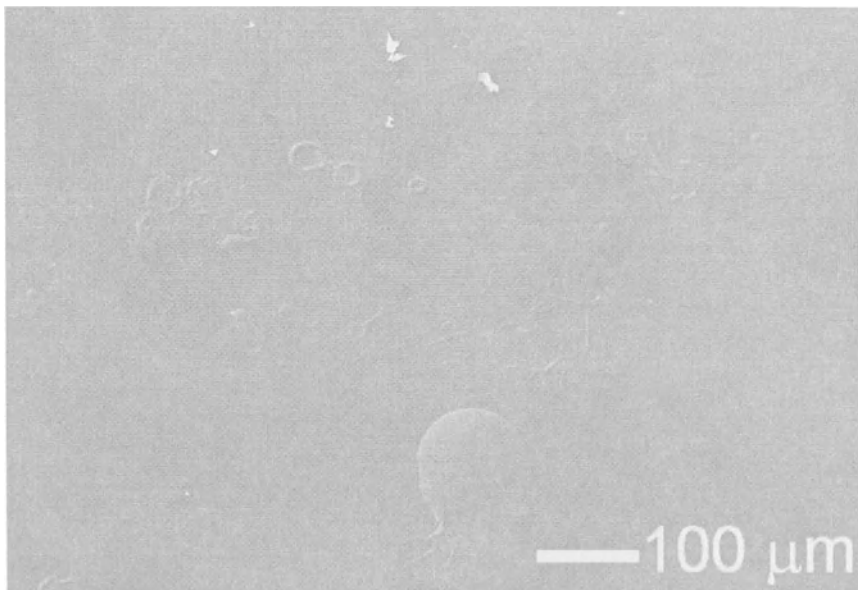


**Figure 6.** Scanning electron micrograph of a 30 nm thin SiO<sub>2</sub> coating on PC, irradiated with  $8.0 \times 10^{13}$  ions/cm<sup>2</sup> (10 nA, 125 s) of 1 MeV He<sup>2+</sup>.

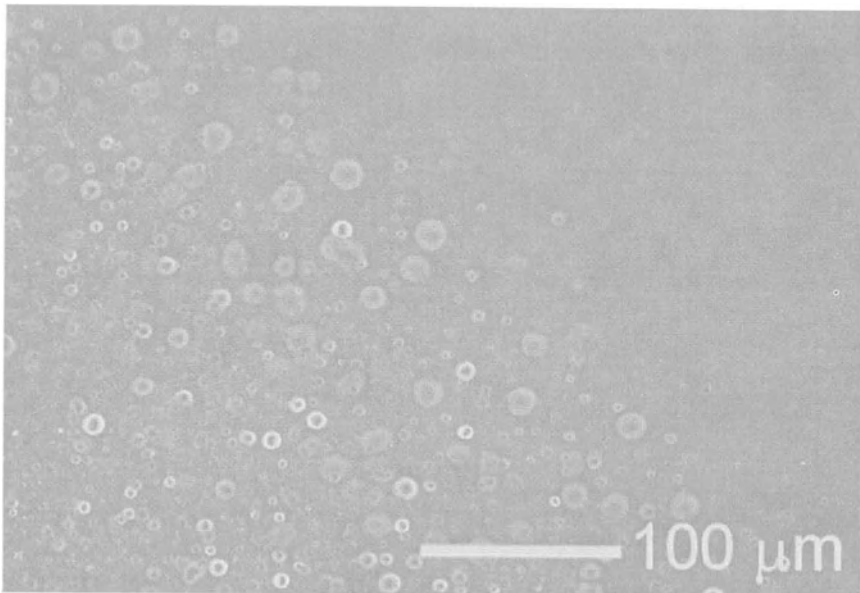
Figure 6 shows a Scanning Electron Microscope (SEM) image of a 30 nm SiO<sub>2</sub> layer on PC following irradiation by  $8.0 \times 10^{13}$  ions/cm<sup>2</sup> (10 nA, 125 s) of 1 MeV He<sup>2+</sup>. One can clearly distinguish round, dark-gray shapes on a light-gray background, and a “bubble”. X-ray fluorescence (EDX) observations performed in the SEM showed that the round shapes are devoid of Si, contrary to the light background.

Numerous previous studies reported the creation of hydrogen and other volatile molecular fragments in the bulk of polymers during irradiation by energetic ions [20-22], including He<sup>2+</sup> ions at low MeV energies [23-25]. The precise mix of these volatile fragments depends on the polymer, on the beam energy and type of ions, that is, on the Linear Energy Transfer (LET, in eV/nm) [26]. While H<sub>2</sub> is the main component, less abundant alkanes, alkenes and alkynes are also present [21, 27]; under suitable conditions, these can be detected by Residual Gas Analysis (RGA) with a quadrupole mass filter [27, 28], or by Fourier Transform Infrared (FTIR) techniques performed inside the irradiation chamber [27]. These fragments are created along the entire ion track, due to chain scission and cross-linking reactions resulting from electronic and/or nuclear energy-loss processes, and they subsequently diffuse out of the sample under thermal activation [29].

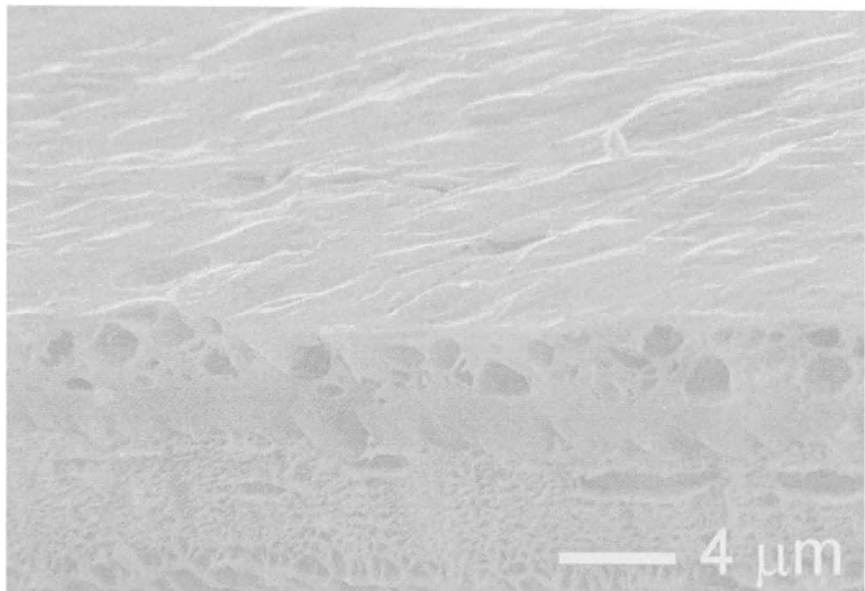
If the polymer is not coated, volatile fragments do not give rise to major artifacts during Ion Beam Analysis (IBA): for example, many authors reported depth profiling of implanted polymers using by RBS with 2 MeV He<sup>2+</sup>, but they mention no anomalies [30-32]. However, when a gas barrier layer is present on the top surface of the irradiated polymer, the volatile species cannot escape; instead, as seen in Fig. 6, they agglomerate and form bubbles at the polymer/coating interface, thereby causing delamination (as mentioned very briefly in [29]). Finally, when the differential pressure between the outside vacuum and the gas inside the bubble becomes excessive, the coating ruptures: this explains the dark-gray round shapes in Fig. 6, the polymeric substrate rendered visible after bubbles had burst.

Figure 7 is a SEM image of a 10 nm SiO<sub>2</sub> layer on PET : on the left part, which had been irradiated by  $3.0 \times 10^{16}$  ions/cm<sup>2</sup> (90 nA, 1800 s) of 1 MeV He<sup>2+</sup>, one observes many bubbles, while the right-hand (unirradiated) portion is seen to be perfectly smooth. When further increasing the fluence to  $6 \times 10^{16}$  ions/cm<sup>2</sup> (90 nA, 3600 s), some cracks appear through the entire sample thickness. Finally, Fig. 8 shows that the gas-filled cavities are located within a 4 μm thick layer below the polymer surface, corresponding to the penetration depth of 1 MeV He<sup>2+</sup> ions in PET, calculated using SRIM-2000 [33] (3.81 μm). We believe that the smooth sublayer is due to cross-linking [34], which increased its hardness before the sample cracked [35]. Cross-linking is presumably also responsible for the fact that gas bubbles can form within the polymer itself.

By the way, all these signs of sample destruction induced by the impinging particle beam introduce major artifacts on Ion Beam Analysis (IBA) results : increase of the surface roughness or even changes in the sample morphology and chemical composition modify the scattering conditions. Figure 9 illustrates the appearance of these artifacts when using the second IBM geometry with 1 MeV He<sup>2+</sup> to characterize a 40 nm SiO<sub>2</sub> film on PC. The upper and lower spectra, obtained using 9 and 90 nA beam currents, respectively, are seen to be totally different despite the fact that they were obtained for the very same sample. The silicon and oxygen peaks, which appear to be quite unsymmetrical on the lower spectrum, might lead one to infer the presence of a broad interphase (of width near 30 nm, see Fig. 4), while the upper spectrum suggests only a narrow interphase. However, since both samples displayed bubbles after irradiation, more pronounced in the case of higher current, no objective conclusion should be drawn about the existence or width of a possible interphase.



**Figure 7.** Scanning electron micrograph of a 10 nm thin  $\text{SiO}_2$  coating on PET, irradiated with  $3.0 \times 10^{16}$  ions/ $\text{cm}^2$  (90 nA, 1800 s) of 1 MeV  $\text{He}^{2+}$ .



**Figure 8.** Cross-sectional scanning electron micrograph of a 10 nm thin  $\text{SiO}_2$  coating on PET, irradiated with  $6.0 \times 10^{16}$  ions/ $\text{cm}^2$  (90 nA, 3600 s) of 1 MeV  $\text{He}^{2+}$ .

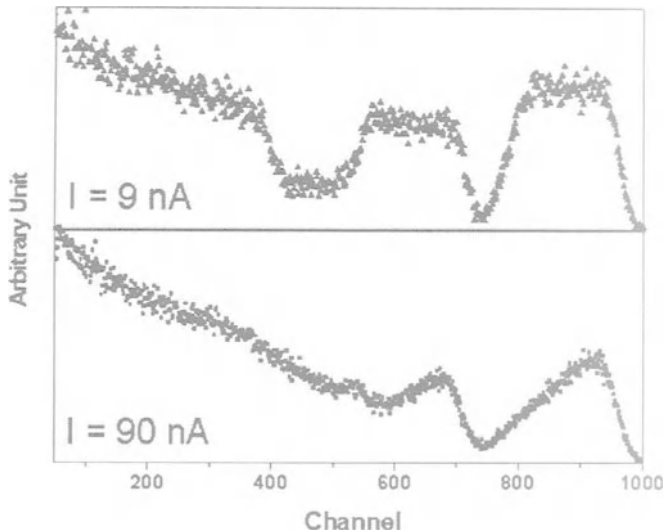


**Figure 9.** RBS spectrum of 40 nm  $\text{SiO}_2$  on PC obtained with a 9 nA (upper) and 90 nA (lower) 1 MeV  $\text{He}^{2+}$  beam current.

#### 4. CONCLUSION

We have performed RBS measurements using 1 and 1.5 MeV  $\text{He}^{2+}$  ions in order to study PECVD  $\text{SiO}_2$  and  $\text{SiN}$  gas barrier layers on various polymeric substrates. In the case of Kapton® PI, no artifacts were observed despite chemical modifications of the polymer, induced by the incident particles. The surface concentration of Si was found to be proportional to the time of deposition,  $t$ . For the case of  $\text{SiO}_2$  films, the study was performed for  $0.5 \text{ s} \leq t \leq 100 \text{ s}$ , which corresponds to thicknesses  $0.5 \text{ nm} \leq d \leq 100 \text{ nm}$ ; for  $\text{SiN}$ ,  $2 \text{ s} \leq t \leq 180 \text{ s}$ , corresponds to thicknesses  $0.6 \text{ nm} \leq d \leq 60 \text{ nm}$ . This result also shows that the sticking coefficient of precursor species is constant during the growth process. Moreover, since the growth mode is known to be layer-by-layer (Frank-van der Merwe) and the composition remains constant starting with the very first deposited layer [5], one can use RBS as a very precise method for thickness measurement, with  $\approx 1 \text{ \AA}$  sensitivity. Then, using the grazing angle geometry and RUMP simulations, we inferred a 7 nm thick “interphase” between the coating and the polymer substrate. However, for the two other polymers investigated here, Lexan® PC and Mylar® PET, both known to be more fragile than Kapton® PI, major artifacts appeared during RBS measurements. The high concentrations of volatile molecular fragments liberated by chain scission and cross-linking reactions during irradiation by energetic ions, even under very mild beam conditions (1 nA,  $8.0 \times 10^{12} \text{ ions/cm}^2$ ), appeared to be the cause of these artifacts. Scanning Electron Micrographs (SEM) revealed that these volatile fragments formed gas bubbles under the top surface of the samples, in their attempts to diffuse out of the polymer but impeded by the coating. These bubbles resulted in greatly increased surface roughness and in many cracks in the layer. Therefore, no

valid RBS studies could be performed on these particular coated materials, which probably represent the majority of commercially-important polymers. This suggests that general use of Ion Beam Analysis techniques on polymeric substrates with inorganic (ceramic, metallic,...) coatings should be undertaken only with very great prudence.

## ACKNOWLEDGMENTS

The authors wish to thank Drs. G. Czeremuszkin and M. Latrèche for numerous valuable discussions and comments. They are also grateful to Remi Poirier for his valuable assistance on the RBS measurements. This work is being supported by grants from the Natural Sciences and Engineering Research Council of Canada (NSERC). One of us (G.D.) gratefully acknowledges a post-graduate scholarship from CNRS (France).

## REFERENCES

1. H. Chatham, *Surf. Coat. Technol.* **78** (1996) 1.
2. P. Fayet, C. Holland, B. Jaccoud, and A. Roulin, *Soc. Vac. Coaters, Proc. 38<sup>th</sup> Annu. Tech. Conf.* (1995) 15.
3. A. Yalisis, M. G. Mikhael, and R. E. Ellwanger, *Soc. Vac. Coaters, Proc. 43<sup>rd</sup> Annu. Tech. Conf.* (2000) 404.
4. A.S. da Silva Sobrinho, M. Latrèche, G. Czeremuszkin, J.E. Klemburg-Sapieha, and M.R. Wertheimer, *J. Vac. Sci. Technol.* A **16** (1998) 3190.
5. G. Dennler, A. Houdayer, Y. Séguí, and M.R. Wertheimer, *J. Vac. Sci. Technol.*, in press.
6. W. K. Chu, J. W. Mayer, and M. A. Nicolet, *Backscattering Spectroscopy*, Academic Press, New York (1978).
7. G. Dennler, A. Houdayer, P. Raynaud, Y. Séguí, M.R. Wertheimer, *Nucl. Instrum. and Meth.*, in press.
8. G. Dennler, A. Houdayer, Y. Séguí, and M.R. Wertheimer, *Proc. of the 15<sup>th</sup> Int. Symp. Plasma Chem.* (2001) 109.
9. A.S. da Silva Sobrinho, N. Schüller, J.E. Klemburg-Sapieha, M.R. Wertheimer, M. Andrews, and S. C. Gujrathi, *J. Vac. Sci. Technol.* A **16** (1998) 2021.
10. A. Bergeron, J.E. Klemburg-Sapieha, and L. Martinu, *J. Vac. Sci. Technol.* A **16** 3227 (1998).
11. A. C. Fozza, J. E. Klemburg-Sapieha, and M. R. Wertheimer, *Plasmas and Polymers* **4**, 183 (1999).
12. C. Bichler, M. Bischoff, H.C. Langowsky, and U. Moosheimer, *Soc. Vac. Coaters, Proc. 39<sup>th</sup> Annu. Tech. Conf.*, 378 (1996).
13. R. Hübler, *Surf. Coat. Technol.* **116-119** (1996) 1116.
14. L. R. Doolittle, *Nucl. Instrum. and Meth.* B **9** (1985) 344.
15. J. Hong, L. Martinu, and M. R. Wertheimer, *Plasmas and Polymers* **6** (2001), in press.
16. H-S. Jeong and R. C. White, *Mat. Res. Soc. Symp. Proc.* 235 (1991) 787.
17. T. Terai, T. Kobayashi, *Nucl. Instrum. and Meth.* B **166-167** (2000) 627.
18. A. De Bonis, A. Bearzotti, G. Marletta, *Nucl. Instrum. and Meth.* B **151** (1999) 101.
19. Y. Q. Wang, R. E. Giessd, M. G. Moss, J. Kaufmann, *Nucl. Instrum. and Meth.* B **127/128** (1997) 710.
20. M. B. Lewis and E. H. Lee, *Nucl. Instrum. and Meth.* B **61** (1991) 457.
21. V. Picq, J. M. Ramillon, E. Balanzat, *Nucl. Instrum. and Meth.* B **146** (1998) 496.
22. D. K. Avasthi, J. P. Singh, A. Biswas, S. K. Bose, *Nucl. Instrum. and Meth.* B **146** (1998) 504.
23. L. J. Matienzo, F. Emmi, D. C. Van Hart, and T. P. Gall, *J. Vac. Sci. Technol.* A **7** (1989) 1784.
24. M. Braun, Emmoth, G. M. Mladenov, and H. E. Sätherblom, , *J. Vac. Sci. Technol.* A **1** (1983) 1383.
25. A. L. Evelyn, D. Ila, R. L. Zimmerman, K. Bhat, D. B. Poker, D. K. Hensley, *Nucl. Instrum. and Meth.* B **127-128** (1997) 694.
26. E. H. Lee, *Nucl. Instrum. and Meth.* B **151** (1999) 29.
27. V. Picq, E. Balanzat, *Nucl. Instrum. and Meth.* B **151** (1999) 76.
28. A. L. Evelyn, D. Ila, R. L. Zimmerman, K. Bhat, D. B. Poker, D. K. Hensley, C. Klatt, S. Kalbitzer, N. Just, C. Dreven, *Nucl. Instrum. and Meth.* B **148** (1999) 1141.
29. M. P. de Jong, L. J. van Ijzendoorn, M. J. A. de Voigt, *Nucl. Instrum. and Meth.* B **161-163** (2000) 207.
30. Z. Iskanderova, J. Kleiman, Y. Gudimenko, W. D. Morison, R. C. Tennyson, *Nucl. Instrum. and Meth.* B **127-128** (1997) 702.
31. Y. Q. Wang, *Nucl. Instrum. and Meth.* B **161-163** (2000) 1027.

32. Y. Wu, T. Zhang, Y. Zhang, H. Zhang, X. Zhang, G. Zhou, *Nucl. Instrum. and Meth. B* **173** (2001) 292.
33. J. F. Ziegler, J. P. Biersack, and U. Littmark, *The Stopping and Range of Ions in Solids*, vol. 1, Pergamon Press, New York, 1985.
34. V. Herden, S. Klaumünzer, W. Schnabel, *Nucl. Instrum. and Meth. B* **146** (1998) 491.
35. H. Dong and T. Bell, *Surf. Coat. Technol.* **111** (1999) 29.

# **SURFACE MODIFICATION BY ION ASSISTED REACTION**

S. K. Koh, Y. W. Beag, W. K. Bang, S. Han, J. S. Cho, and K. H. Kim

## **1. INTRODUCTION**

Surface characteristics of polymers determine their interfacial properties and technological applications. There have been many attempts to modify the surface of polymers to improve wettability, dye printing and adhesion to other materials. Plasma technology, high energy ion beam irradiation, corona discharge and other techniques have been used. However, rough surface and/or surface damage such as bond scission, carbonization, crosslinking, etc. are produced by the above methods. A coating of a surfactant was found to be relatively successful in enhancing the wettability of polymers, but a lifetime of the surfactant is too short for practical use. Therefore, new surface modification method is demanded to get the polymer surfaces free of the surface damage and having good wettability with a long lifetime. Koh et al<sup>1-3)</sup> successfully modified hydrophobic surface of polymers into hydrophilic one by the combination of a low energy ion beam and reactive gas environment, and they named this surface modification method “Ion Assisted Reaction (IAR)”. They also reported that the activated polymer

S.K. Koh<sup>1,2</sup>, Y.W. Beag<sup>1</sup>, W.K. Bang<sup>2</sup>, S. Han<sup>1</sup>, J.S. Cho<sup>1</sup>, and K.H. Kim<sup>1</sup>, <sup>1</sup>Thin Film Technology Research Center, Korea Institute of Science and Technology, P.O. Box 131, Cheongryang 130-650, Seoul, Korea. <sup>2</sup>P&I Corporation, Shinnae Technotown #405, Sangbong-Dong 485, Jungrang-Gu, 131-221, Seoul, Korea.

*Metallization of Polymers 2.*

Edited by Edward Sacher, Kluwer Academic/Plenum Publishers, 2002

**165**

surfaces irradiated by energetic ions induce a chemical reaction with reactive gas, and new formed bonds such as carboxyl, carbonyl, hydroxyl, and ester radicals improve wettability and adhesion to other materials.

Commercialization of IAR treatment has been executed by P&I Corp, which have manufactured IAR treatment apparatuses for mass production.

In this study, we review the experiment results of IAR treated polymer surfaces, and investigate a chemical reaction mechanism of IAR treatment. Based on these results, we also propose the adhesion enhancement mechanism between metal and polymer. Possible industrial applications of the IAR are to be discussed.

## 2. EXPERIMENTAL

Schematic diagram of the IAR treatment equipment is shown in Fig. 1. Polymer surfaces are irradiated by ion beam with reactive gas environment. It is composed of ion source, environmental gas supplier, substrate holder and vacuum pump. The  $\text{Ar}^+$  ion beam was generated by a cold hollow cathode-type ion source equipped with 5 cm convex grid. The range of ion beam energy was 0.5 keV to 1.5 keV. Ion doses were controlled by exposure time at a fixed ion beam current density from  $5 \times 10^{14}$  to  $1 \times 10^{17}$  ions/cm<sup>2</sup>. Reactive gas was blown on the polymer samples and its flow rate was changed from 0 ml/min (sccm) to 8 ml/min during the energetic ion beam irradiation. Each sample is cleaned by conventional method of ultrasonic cleaning with proper solution for the samples.

Contact angles of specimens were measured by a static contact angle meter (Tantec Co.; CAM-micro), which contained a screen, a rotation angrometer, a goniometer for specimen positioning, and a syringe equipped with micrometer normal to the specimen. In the measurement, 0.025 ml of triply distilled water and formamide (Junsei Chemical Co. Ltd) were dropped on six different places on the sample surfaces and the average value of contact angles was calculated. From the contact angle data of water and formamide, dispersion and polar components were calculated, and the change in surface energy was investigated quantitatively. The contact angle was measured within 15 second

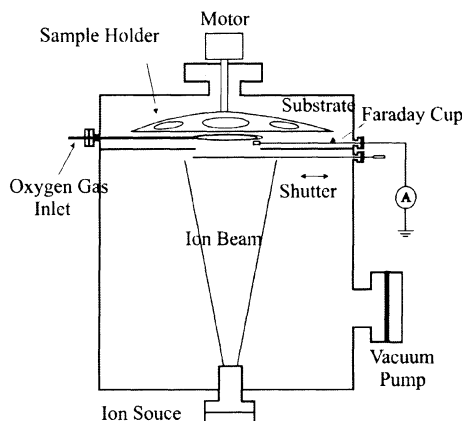


Figure. 1 Schematic diagram of ion assisted reaction (IAR).

after dropping the water drop. The standard deviation of the contact angles was about  $2^\circ$  to  $3^\circ$ .

Scanning electron microscope (SEM; Hidachi S 420) and atomic force microscope (AFM; Park Instrument) were used to examine the surface morphology. The newly formed chemical bonds on the IAR treated polymer surfaces were identified by X-ray photoelectron spectroscopy (XPS; Perkin Elmer PHI5700ESCA) using Al K $\alpha$  line ( $h\nu = 1486.6$  eV) and Mg K $\alpha$  line ( $h\nu = 1253.6$  eV). The pass energies of 187.85 and 23.5 eV were used for low and high-resolution studies. Peak positions were calibrated by 4f core level spectra of Au dots on the polymer surface. The base pressure was  $1 \times 10^{-10}$  Torr and the working pressure was  $2 \times 10^{-9}$  Torr in the process of acquiring the XPS spectra.

### 3. RESULTS AND DISCUSSION

#### 3.1. IAR Treatment

##### 3.1.1 Wettability Improvement

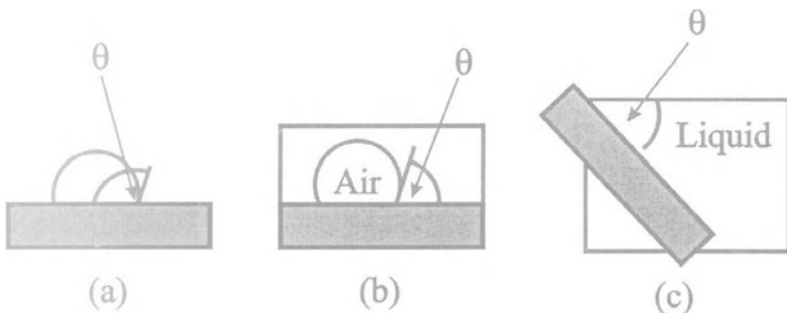


Figure 2 Techniques for contact angle measurement: (a) sessile drop, (b) captive bubble, and (c) tilting plate.

Contact angle measurement is probably the most common method of wettability measurement. Contact angle data, especially in the case of polymer, can be obtained with low price instruments and with simple techniques. The most common direct methods of contact angle measurement (Fig. 2) are the sessile drop (a), the captive bubble (b), and the tilting plate (c). In this work, the sessile drop method is used to measure contact angle of the polymer surface modified by IAR. In the sessile drop experiment, a droplet of a properly purified liquid is put on the solid surface by means of a syringe or a micropipette. The droplet is generally observed by a low magnification microscope, and the resulting contact angle is measured by a goniometer fitted in the eyepiece. Figure 3 shows the examples of contact angle measurement by sessile drop method. In the case of polycarbonate (PC), the contact angle of water to pristine polymer is as large as  $70^\circ$  on the pristine polymer, but decrease to  $20^\circ$  after IAR treatment, meaning a good wettable surface. The various cases of the IAR treatment for hydrophobic polymers will be shown.

Figure 4 shows the contact angle changes of water to polypropylene (PP) surface as a function of (a) irradiation  $\text{Ar}^+$  ion dose, (b)  $\text{Ar}^+$  ion beam energy with and without oxygen gas flow, and (c) oxygen gas flow rate, respectively. The contact angles of water to PP surface irradiated without flowing of oxygen gas are reduced from  $86^\circ$  to  $40^\circ$ , while those to PP surface irradiated with flowing of oxygen gas decrease to  $22^\circ$  at optimum condition ( $\text{ion dose} = 5 \times 10^{16} \text{ ions/cm}^2$ ,  $\text{ion beam energy} = 1 \text{ keV}$ ,  $\text{oxygen gas flow rate} = 8 \text{ ml/min.}$ ). The contact angles of PP modified without oxygen gas flowing are similar to

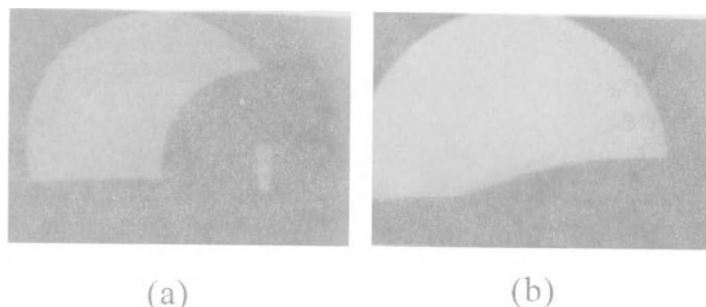


Figure 3 Example of contact angle measurement for polymer samples: (a) pristine PP and (b) PP treated by IAR.

those of previous results obtained by other methods such as high energy ion irradiation (several hundreds keV to several MeV), corona discharge, dc and rf plasma treatment, etc.<sup>4-10</sup>. In the processes mentioned above, the main mechanism of reducing the contact angle could be explained by the formation of the rough surface by irradiation of energetic ion<sup>11)</sup> and the hydrophilic groups by a surface chemical reaction.

Figure 5 shows the contact angle change to PC surface by  $O_2^+$  ion irradiation with or without oxygen gas flow. For comparison, the results of  $Ar^+$  ion irradiation also present. The contact angles of PC surface irradiated by  $O_2^+$  ion are less than those by  $Ar^+$  ion

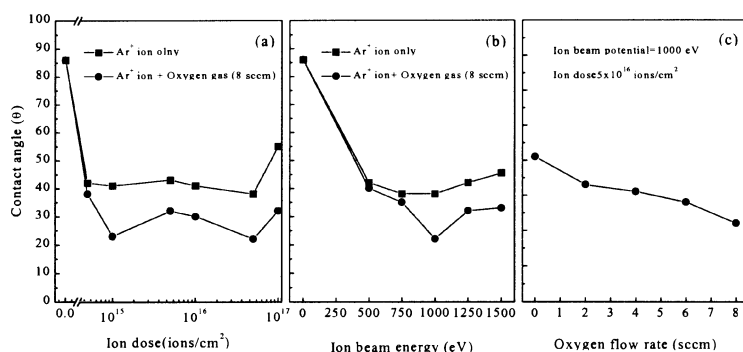


Figure 4 Changes of contact angles of water on PP as a function of (a) ion dose, (b) ion beam potential, and (c) oxygen gas flow rate.

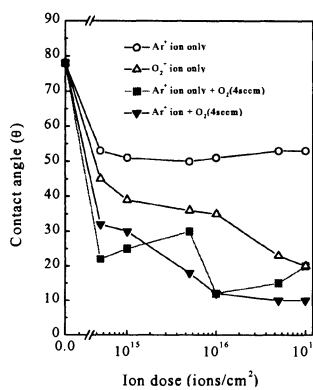


Figure 5 Changes of contact angles of water on PC modified by oxygen ion beam and Ar ion beam.

without oxygen gas flow. On the while, with oxygen gas flow, there are no remarkable differences of contact angles on PC surfaces under Ar<sup>+</sup> or O<sub>2</sub><sup>+</sup> ion irradiation for all ion doses. This means that the blowing oxygen gas near the substrate surface plays an important role in reducing the contact angle and some chemical reaction would occur between the blown oxygen gas and the surface of polymer. O<sub>2</sub><sup>+</sup> ion irradiation shows some decrease of the contact angle, but it is not enough to create chemical reaction on the polymer surface.

Figure 6 shows the contact angle variations of Ar<sup>+</sup> ion irradiated PE, PVDF and PTFE with oxygen gas flow rate of 8 ml/min and they show three different trends. As the Ar<sup>+</sup> ion doses increase with/without an O<sub>2</sub> gas environment, the contact angles on PE surface are monotonously reduced from 95° to 28°, and to 53°, respectively. The reduction of contact angle to PE surface can be explained by surface cleaning and formation of polar functional groups as mentioned above, but monotonous decrease of contact angle to PE surface is noticeable as shown in Fig. 6(a). The contact angles to IAR-treated PVDF (Fig. 6(b)) have minimum value at the low ion dose of 1 × 10<sup>15</sup> ions/cm<sup>2</sup>, and increase at the high ion dose than 1 × 10<sup>17</sup> ions/cm<sup>2</sup>. The contact angle to the irradiated PVDF is reduced from 75° to 31° at the Ar<sup>+</sup> ion dose of 1 × 10<sup>15</sup> ions/cm<sup>2</sup> with oxygen environment. After further irradiation, surface wettability is degraded and the contact angle increases to 62°.

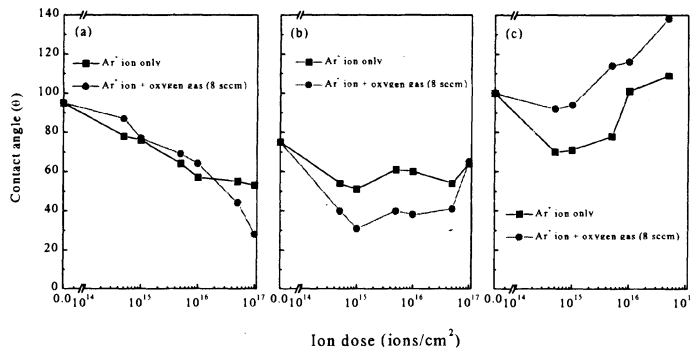


Figure 6 Changes of contact angles of water on various polymers modified by IAR: (a) PE, (b) PVDF, and (c) PTFE.

The contact angles of irradiated PVDF without an oxygen gas blowing are higher than that with introducing oxygen gas. The contact angles of irradiated PTFE with oxygen environment increase from 100° to 109° at the ion dose of 1 × 10<sup>17</sup> ions/cm<sup>2</sup> (Fig. 6(c)). The reduction of contact angle at the low ion dose could be attributed to oxygen-related bonds on the PTFE surface. The contact angle of the irradiated PTFE without oxygen gas blowing, however, increases from 100° to 140°. This result originates not from chemical change on the polymer chain, but from micron-sized, needle-type rough surface of PTFE due to ion beam bombardment. The wettability of PE and PVDF surfaces is noticeably enhanced after IAR treatment, while the wettability of PTFE is slightly enhanced at low ion dose and reduced to a contact angle of 140° at the high ion dose. It is remarkable that the contact angle of water to the irradiated PTFE monotonously increases with further irradiation than 1 × 10<sup>15</sup> ions/cm<sup>2</sup>. For PE, there was no degradation of surface wettability until the ion dose of 1 × 10<sup>17</sup> ions/cm<sup>2</sup>. Therefore, ion beam induced oxidation on PE surface determines wettability, while that of PTFE is not a main factor. For PVDF, surface oxidation strongly affects wettability at low ion dose and the carbonization of polymeric chains results in increase of contact angles at high ion dose. Consequently, the newly formed functional groups on the PTFE surface are identified as oxygen bonded

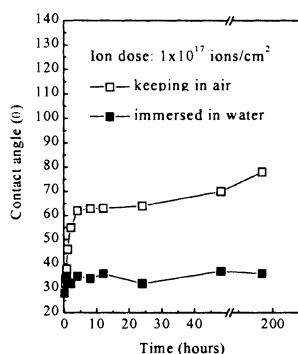


Figure 7 Contact angle of water on IAR treated PE surface immersed in water and air with keeping time.

carbon and the reduction of wettability could be due to the needle-like surface and the appearance of  $-CF_3$ - due to ion beam sputtering. This will be discussed in section 3.1.4 in detail.

The stability of hydrophilic groups formed by IAR treatment on polymer surfaces is examined in two experimental environments. As shown in Fig. 7., contact angle vs. exposure time plots are represented for irradiated specimens preserved in air and distilled water. The contact angles on the irradiated PE preserved in air (open square) increase up to  $80^\circ$  at 192 hours. It seems that in the case of atmosphere storage, the polar groups formed on the irradiated PE could be rearranged to reach equilibrium with air. Reorientation of polar groups can result in reduction of surface energy and recovery of hydrophobic surface. When immersed in water (closed square), the contact angle on the irradiated PE remains nearly constant value of  $35^\circ$ . The low contact angle on the irradiated PE immersed in water may be explained by the maintenance of hydrophilic groups in polar liquid due to electrostatic force. The trend of contact angle change on the irradiated PVDF, PS, PP, and PC preserved in air and water shows nearly same as those of PE.

Inagaki *et al.*<sup>12)</sup> reported that hydrophilic polymer surface after plasma treatment remarkably recovered hydrophobic surface increase after water washing. This means that the newly formed functional groups can be easily removed by water washing because the

chain length is shortened due to damage induced by plasma, resulting into their weak bonding to the surface. However, it is considered from the contact angle variations of IAR treated polymer immersed in water that carbon back-bonds were rarely damaged and the functional groups could not be washed out.

The surface dynamics of polymer are considerably different from those of more rigid materials such as metals and ceramics, due to the high mobility of macromolecules at the surface. Macromolecules have a high degree of freedom in determining their conformations according to the immediate neighboring phase. The introduction of surface hydrophilic groups leads necessarily to an increase of the surface energy over that of the parent polymer. This means that, when air is the interfacing medium, a driving force exists to restore the original surface composition or in general, to lower the surface energy of the treated material. This can be accomplished by reorientation of macromolecule side chains or pendant groups by which the contact angle of IAR treated and conventional plasma treated polymers stored in air increases gradually with time. When the surface treated polymers recovered hydrophobic nature are immersed in polar liquids, especially in water, the variation of contact angle of IAR treated and conventional plasma treated polymers is significantly different. In the case of IAR treated polymers, the contact angle decrease nearly to original value obtained by surface treatment. This recovery of hydrophilicity is attributed to rotation of polar groups buried in bulk to surface, due to interaction between polar liquid molecules and polar groups of treated polymer. For conventional plasma treated polymers, however, the contact angle doesn't decrease to low value. As mentioned above, the polar groups formed by conventional plasma treatment can be removed in polar liquids, which accounts for the reduced recovery of hydrophilicity. Therefore, it can be said that the ageing of hydrophilicity generally observed in conventional plasma treatment, is not happened in the IAR treated polymers. A schematic representation of the different characteristic behavior in IAR treated and conventional plasma treated polymers is given in Fig. 8.

### *3.1.2 Surface Free Energy*

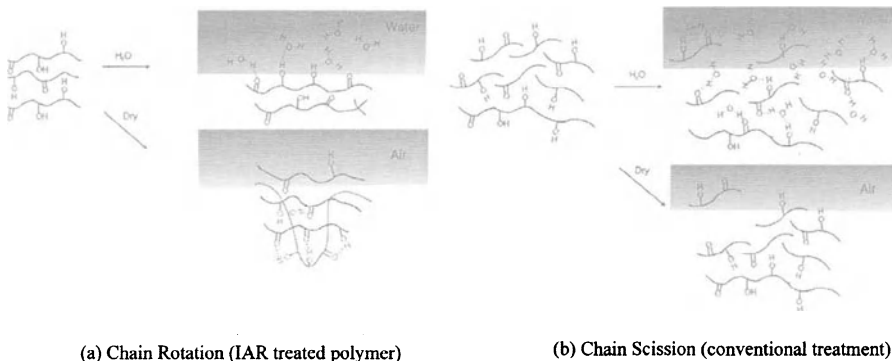


Figure 8 Schematic diagrams for characteristic behavior of IAR treated and conventional treated polymer in water and air.

Contact angles are closely related to surface free energy of the surface. The surface free energy is expressed as equation (1).

$$\gamma = \gamma^d + \gamma^p \quad (1)$$

Superscript of d and p mean dispersion force (Lifshitz-van der Waals force) and polar force, respectively. With the help of simultaneous equations (2), dispersion force and polar force can be estimated.

$$\begin{aligned} 0.5\gamma_2^W(1+\cos\theta^W) &= (\gamma_1^d \gamma_2^{w,d})^{1/2} + (\gamma_1^p \gamma_2^{w,p})^{1/2} \\ 0.5\gamma_2^F(1+\cos\theta^F) &= (\gamma_1^d \gamma_2^{F,d})^{1/2} + (\gamma_1^p \gamma_2^{F,p})^{1/2} \end{aligned} \quad (2)$$

Superscript of F and W are formamid and water, respectively. Subscript of 1 and 2 mean surface of polymer and solution, respectively. Unknown parameters in equation (2) are  $\gamma_{1d}$  and  $\gamma_{1p}$ . Equation (2) means that if the contact angle is measured with two different solutions, whose values of surface free energy, dispersion force, and polar force are known, the values of dispersion force and polar force of the polymer surface can be calculated. Also the surface free energy of that surface can be attained by equation (1).

In comparison to metals and metal oxides, all polymers are low surface energy materials, and the surface energies range between 10 and 50 ergs/cm<sup>2</sup>. The surface energy of common polymers and water is shown in Table 1.

Figure 9 shows the changes of surface energy (sum of dispersion force and polar force)

Table 1. The surface energy of various polymers and water. Polymers are divided into three classes according to their wettabilities.

Materials	Classes	Examples
Fluoropolymers, polysiloxane and polyolefins, etc.	Low wettability ( $30 \text{ ergs/cm}^2 > \gamma_c > 10 \text{ ergs/cm}^2$ )	PTFE (18.5), Electroplated PP (29)
Most vinyl polymers, e.g., poly(vinyl acetate), poly(styrene), poly(vinyl chloride), poly(methyl methacrylate), etc.	Medium wettability ( $40 \text{ ergs/cm}^2 > \gamma_c > 30 \text{ ergs/cm}^2$ )	PVA (37) PS (33) PVC (39) PMMA (39)
Most condensation polymers, e.g., poly(carbonate), polyesters, nylons, epoxy resins, etc.	High wettability ( $\gamma_c > 40 \text{ ergs/cm}^2$ )	PC (42) PET (43) Nylons (42-46)
Water	High wettability	72

of PC surface (a) irradiated by  $\text{Ar}^+$  ion without oxygen gas flow and (b) irradiated by  $\text{Ar}^+$  ion with oxygen gas flow rate of 4 sccm as a function of ion dose at a fixed ion beam energy of 1 keV. Small increase of surface free energy on the PC without oxygen environment could be explained as follows; the surface is excited by the formation of unstable radicals in polymer chain by energetic ion irradiation. Without oxygen environment, unstable radicals should be recombined each other, and thus population of unstable radicals decreases. When the sample is taken out into air, small amount of remained radicals could react with oxygen and/or nitrogen gas in air and a few polar functional groups are formed on the surface. Therefore, the surface energy on the PC without oxygen environment increases small. The surface energy of IAR treated PC increases significantly with ion dose up to  $70 \text{ erg/cm}^2$ , which is nearly same as that of water meaning that the IAR treated polymer surface is perfectly wettable. As shown in Fig. 9(b), IAR treatment increases not the dispersion force but the polar force. In a polymer, the increment of the polar force is known to be due to the formation of polar groups such as C-O, C=O, (C=O)-O and C-N. Thus we can infer that some hydrophilic groups are formed on the surface of PC by IAR treatment. Similar results for surface energy are attained for PE, PP, PS, PMMA and so on.

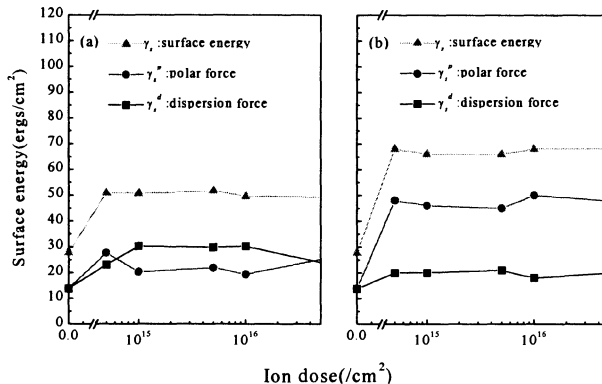


Figure 9 Changes of surface energy for PC modified by IAR: (a) Ar<sup>+</sup> ion irradiation and (b) Ar<sup>+</sup> ion irradiation with oxygen environment (4 sccm).

### 3.1.3 Surface Morphology

Momentum transfer of ion bombardment causes sputtering of atoms and/or molecules on the polymer surface as well as free radical formation, bond scission, and chemical reactions. The ion bombardment changes the surface morphology of the substrate. The low density PE (density 0.93 g/cm<sup>3</sup>) used in experiment consists of an amorphous phase. PVDF and PTFE are composed of semi-crystalline and crystalline phases, respectively. Surface morphology could relate to these crystalline phases.

AFM images of irradiated PE surfaces are represented in Fig. 10. Root-mean-square roughness ( $\sigma_{rms}$ ) of PE surface increases from 56 to 76 Å at ion dose of  $1 \times 10^{15}$  ions/cm<sup>2</sup>. The  $\sigma_{rms}$  of PE surface increases 71 Å at ion doses of  $1 \times 10^{16}$  and  $1 \times 10^{17}$  ions/cm<sup>2</sup>. This change of roughness on PE surface by ion bombardment cannot explain the noticeable reduction of contact angles in Fig. 6(a) sufficiently. Newly formed polar groups may play an important role on the wettability improvement. The roughness change of semi-crystalline PVDF shown in Fig. 11 is similar to that of PE. The  $\sigma_{rms}$  value of the irradiated PVDF is reduced from 88 to 55.8 Å at ion dose of  $5 \times 10^{14}$  ions/cm<sup>2</sup>. This

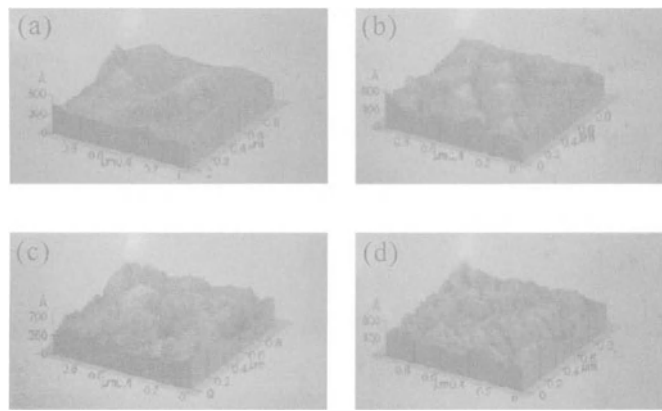


Figure 10 AFM images of PE surface irradiated by IAR as a function of ion dose: (a) pristine, (b)  $1 \times 10^{15}$ , (c)  $1 \times 10^{16}$ , and (d)  $1 \times 10^{17}$  ions/cm<sup>2</sup>.

reduction of surface roughness may result from ion beam erosion. With increasing ion dose, the  $\sigma_{\text{rms}}$  value of the irradiated PVDF increases to 77.4, 90.0, and 106.0 Å at ion doses of  $1 \times 10^{15}$ ,  $1 \times 10^{16}$ , and  $1 \times 10^{17}$  ions/cm<sup>2</sup>, respectively. Blistering, cone-like structure and cellular structure are not observed on the irradiated surface. This is because the sputtering of carbon chain itself is suppressed by double bond formation of carbon

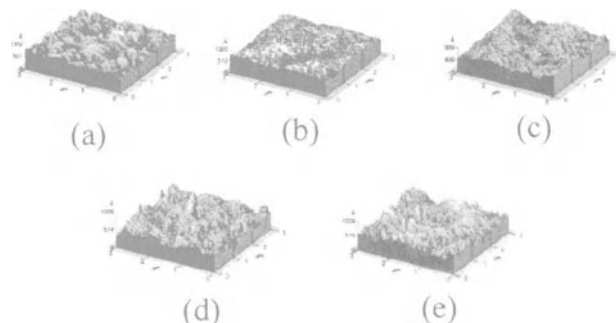


Figure 11 AFM images of PVDF surface irradiated by IAR as a function of ion dose: (a) pristine, (b)  $5 \times 10^{14}$ , (c)  $1 \times 10^{15}$ , (d)  $1 \times 10^{16}$ , and (e)  $1 \times 10^{17}$  ions/cm<sup>2</sup>.

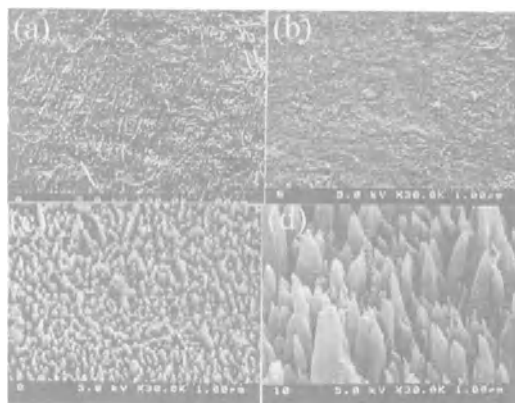


Figure 12 SEM images of PTFE surface irradiated by IAR as a function of ion dose: (a) pristine, (b)  $1 \times 10^{15}$ , (c)  $1 \times 10^{16}$ , and (e)  $1 \times 10^{17}$  ions/cm<sup>2</sup>.

radicals and crosslinking. However, the roughness change of semi-crystalline PVDF is larger than that of PE.

SEM images of the pristine and irradiated crystalline PTFE surfaces are shown in Fig. 12. The irradiated surfaces are so rough that it is impossible to observe the surface by AFM. The pristine PTFE surface is slightly rough due to preparation process and polishing. Similar to the surface of the irradiated PVDF surface at  $1 \times 10^{15}$  ions/cm<sup>2</sup>, the surface of irradiated PTFE surface at  $1 \times 10^{15}$  ions/cm<sup>2</sup> is smoother than the pristine PTFE surface. However, the needle-like structure appears on the irradiated surface at ion dose of  $1 \times 10^{16}$  ions/cm<sup>2</sup>. This sputter cone-like structure have been reported by many researchers and was explained as a result of the low thermal conductivity, high crystallinity, and dense inner structure of PTFE<sup>13-17</sup>. On the irradiated PTFE surface at ion dose of  $1 \times 10^{17}$  ions/cm<sup>2</sup>, the size and the height of the sputter cones are larger than those of irradiated surface at an ion dose of  $1 \times 10^{16}$  ions/cm<sup>2</sup>, and the surface density of cones is reduced. Michael and Stulik reported that the average density of cones was reduced with increasing ion dose and that several thin cones transformed into a large cone due to redeposition of sputtered particles<sup>17</sup>. The orientation of cones is parallel to the Ar<sup>+</sup> ion beam direction. The large roughness on the PTFE surface can result in abnormal

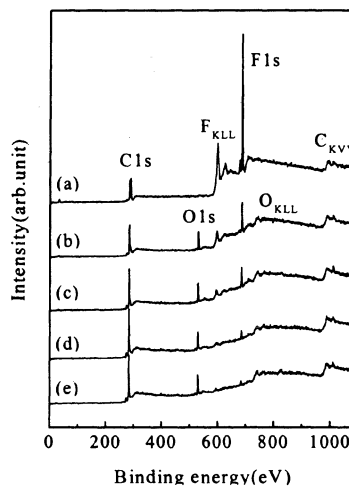


Figure 13 XPS wide scan of IAR treated PVDF samples as a function of ion dose: (a) pristine, (b)  $5 \times 10^{14}$ , (c)  $1 \times 10^{15}$ , (d)  $1 \times 10^{16}$ , and (e)  $1 \times 10^{17}$  ions/cm<sup>2</sup>.

increase of the contact angle. Subsequently, the contact angles of irradiated PE and PVDF surfaces are mainly dependent on the formation of hydrophilic functional groups, whereas those of PTFE are affected by surface roughness rather than with hydrophilic functional groups.

#### 3.1.4 XPS Study

In order to analyze the chemical state of the irradiated surface of the polymer, surfaces of IAR treated polymers were observed by XPS.

Wide-scan spectra for PVDF are shown as a function of ion dose in Fig. 13. The peak height ratios of F1s to C1s are significantly reduced from 6.30 (untreated) to 0.11 (irradiated by  $1 \times 10^{17}/\text{cm}^2$ ) with increasing ion dose. It could be inferred from this result that fluorine atoms are preferentially detached by ion irradiation. In the case of the modified PVDF in oxygen environment, the O1s peak appeared. This means that the oxygen atoms are attached at the sites of detached fluorine atoms, resulting in

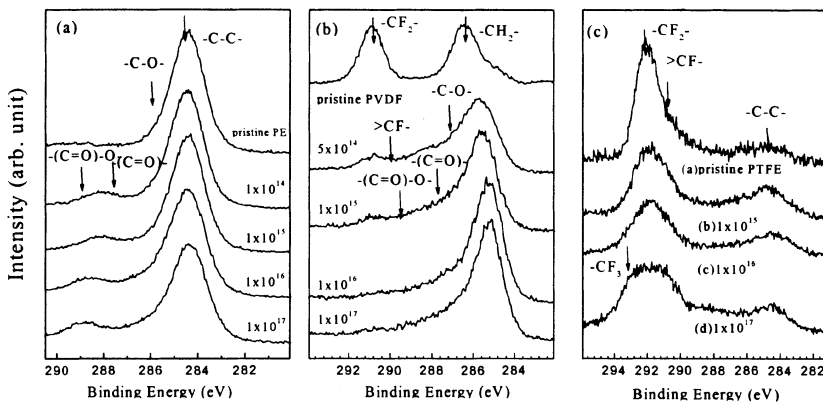


Figure 14 C1s core level spectra of various polymers by IAR as a function of ion dose: (a) PE, (b) PVDF, and (c) PTFE.

the formation of hydrophilic groups. C1s core level spectra of PE, PVDF, and PTFE are shown in Fig. 14. The irradiated PE surface shows successive broadening of peak shapes on C1s core level with increasing the ion dose. The newly formed bond species, which are located at higher binding energies than 286 eV, broaden the peak. Carbon-oxygen bond species are reported as ether  $[-(C-O)-]$ , ester  $[-(C=O)-]$ , and carboxyl  $[-(C=O)-O-]$  groups and their peak positions are 286.3, 288.2, and 289.9 eV, respectively<sup>18)</sup>. The spectra shown in Fig. 14(a) indicate that oxygen-carbon bonds are created by IAR treatment. The single peak of pristine PE at 284.6 eV originates from the simple chemical structure of PE  $[-(CH_2-CH_2)-_n]$ . In the XPS spectra of the PE irradiated by  $1 \times 10^{14}$  and  $1 \times 10^{15}$  ions/cm<sup>2</sup>, the formation of new peaks at 286.3 and 288.2 eV are related to oxidation between the activated surface induced by Ar<sup>+</sup> irradiation and oxygen environment. The main peak intensity of PE at 284.6 eV is uniform without shifting of peak position resulting in =C= bond formation after IAR treatment. This result implies that the irradiated polymeric chains of PE remain nearly same as the initial state of pristine PE during 1 keV Ar<sup>+</sup> ion irradiation, and hydrogen atoms are detached by

energetic ions. Hydrogen atoms removed from the backbone chains on a PE surface may present chemisorption sites in reaction with oxygen atoms.  $[-(C-O)-]$ ,  $[-(C=O)-]$ , and  $[-(C=O)-O-]$  groups are generated by the above process. On the while, the PE surfaces irradiated by  $1 \times 10^{16}$  and  $1 \times 10^{17}$  ions/cm<sup>2</sup> are slightly yellowish, which means that the probability of chain scission become higher than that of chemical bond formation. In XPS spectra, the main peak at 284.5 eV is broadened to lower binding energy, which means that a carbonized phase containing a double bond between carbons (nominal =C=) is formed due to hydrogen detachment by the ion irradiation exceeding  $1 \times 10^{16}$  ions/cm<sup>2</sup>. However, newly formed polar groups on the PE surface increase, and carboxyl radical is noticeably formed over  $1 \times 10^{16}$  ions/cm<sup>2</sup>. The creation of polar groups plays an important role in the wettability of PE.

Figure 14(b) shows the C 1s core level spectra of pristine and irradiated PVDF. The spectra were altered substantially compared to those of PE. The C 1s core level spectrum of pristine PVDF includes only  $-CH_2-$  (286.2 eV) and  $-CF_2-$  (290.8 eV), and shows a typical peak shape of pristine PVDF. In the spectra of PVDF irradiated by  $5 \times 10^{14}$  and  $1 \times 10^{15}$  ions/cm<sup>2</sup>, the peak intensity of  $-CF_2-$  drastically decreases, and new peaks related to oxygen and fluorine singly bonded carbon appear between  $-CH_2-$  and  $-CF_2-$  peak positions. The peak position of  $-CH_2-$  is shifted to lower binding energy of about 285 eV, which means the vicinity of  $-CH_2-$  was changed from the most electronegative fluorine atoms to other atoms, but not to =C= graphitic carbon. More interesting results are the creation of new bonds at binding energies over than 286 eV, which indicates that  $[-(C-O)-]$ ,  $[-(C=O)-]$ , etc. are formed on the PVDF surface, and remarkable reduction of  $-CF_2-$  peak intensity. Adem et al.<sup>19)</sup> reported that the peak positions of carbonized, singly oxygen bonded, and singly fluorine bonded carbon are located at -1.2, 0.7, 3.1 eV higher than that of  $-CH_2-$ , respectively. It was also reported that there are singly fluorinated carbons and peroxidation of radicals after the exposure of MeV ion beam irradiated PVDF to air. These newly formed bonds to oxygen may be generated by a reaction between the remaining radicals and air. However, as shown in Fig. 16(b), more complex spectra are observed than the reported spectra of PVDF<sup>19)</sup>. It is considered that a deliberate reaction between free radicals and environment gas could generate oxygen

doubly bonded carbon. The newly formed bonds related to environment oxygen may be identified as  $[-(C-O)-]$  and  $[-(C=O)-]$  bonds.

In comparison with high-energy ion irradiation,  $-CH_2-$  and  $-CF_2-$  peak intensity shows different reduction and oxygen substitution in the polymeric chain arise from introduced oxygen instead of subsequent oxidation resulting from the exposure to air. The C1s spectra of PVDF irradiated by  $1 \times 10^{16}$  and  $1 \times 10^{17}$  ions/cm<sup>2</sup> represent a sharp increase of doubly bonded carbon ( $=C=$ ), and their shapes are skewed to lower binding energy. Most fluorine atoms in polymeric chains on the irradiated PVDF surface are detached as shown in the  $-CF_2-$  peak of Fig. 14(b). The carbonization of PVDF by high dose ion irradiation is similar to the results of high energy and/or heavy weight ion irradiation<sup>20-22</sup>. In the XPS spectra of PVDF irradiated by a high-energy ion beam,  $=C=$  peaks are significantly increased, while  $-CH_2-$  and  $-CF_2-$  peaks are remarkably decreased.

The pure PTFE is composed of  $-CF_2-$  bonds with a binding energy of 291.6 eV (Fig.14(c)). When the ion dose increases, the intensity of the C1s core level spectra is reduced and the width of C1s peak is broadened. This broadening originates from chain scission, cross-linking, carbonization, and chemical reaction. The peak at 285 eV would be assigned to the C1s peak for the C-C bond because its binding energy is about 6.5 – 7.0 eV lower than that of the C-F<sub>2</sub> bond. This assignment of the binding energy of C-C bond is in good agreement with a previous report<sup>23</sup>. A small ridge was formed at the energy position between 285 and 292 eV in C1s spectra of the irradiated PTFE. The appearance of the ridge may be attributed to the formation of various types of C-F bonds or C-O bonds having different environment. Peaks of C1s bonded to an oxygen rise between 285 eV and 288 eV, and peaks bonded to a fluorine rise between 286 eV and 294 eV, depending on the bond types of neighboring sites. The increment of intensity level of the ridge between 285 and 292 eV with ion dose means that the irradiation severed the C-C and bonds randomly C-F<sub>2</sub> in the  $(-CF_2)_n$  chains and produced active sites. The active sites reacted with other carbon atoms to form crosslinks or with the introduced oxygen atoms to form hydrophilic groups.

Figure 15 shows (a) pristine PP, (b) IAR treated PP before washing, and (c) IAR treated

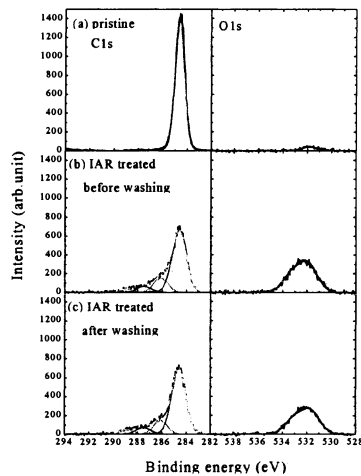


Figure 15 C1s core level spectra of (a) pristine PP, (b) IAR treated PP before washing, and (c) IAR treated PP after washing.

PP after washing. IAR treatment is performed at ion beam energy of 1 keV with ion dose of  $1 \times 10^{16}$  ions/cm<sup>2</sup>, and oxygen flow rate of 8 sccm. C1s and O1s spectra rarely change after washing, which means that hydrophilic groups formed by the IAR treatment are not washed out. Many research results to form hydrophilic surface on the polymer surface have been published<sup>24, 25</sup>. In most case, the concentration of formed hydrophilic groups decreased after washing due to the increment of solubility. Energetic ions result in reducing the chain length and these macromolecules of small chain length easily dissolve into water. While, the hydrophilic groups formed by the IAR treatment did not dissolve in water, which means that the polymer surface treated by the IAR was not severely damaged. This XPS result is in a good agreement with that of contact angle in previous section.

### 3.2 Adhesion Improvement

Applications of metallized polymer on magnetic tape, computer technology, and

flexible printed circuit require different properties. The adhesion of metal film to polymeric substrate is the most basic property. In the electronics industry, fluorine contained polymers such as PTFE and PVDF, have gained increased attention. PTFE has good thermal and dielectric properties for flexible printed circuits and capacitors. PVDF exhibits pyroelectric and piezoelectric characteristics useful for electronic devices. However, their practical application has been hampered by their poor adhesion coming from chemical inertness due to low surface energy. As mentioned in introduction, the adhesion between polymer and metal thin film is closely related to the surface energy of the polymer. High surface energy of the polymer results in good adhesion and wettability.

In this section, we report the adhesion improvement between metal films and IAR treated polymers, especially PTFE and PVDF.

Adhesion tests using the Scotch tape peeling method were conducted on Al/PTFE and Cu/PTFE. Al and Cu films are partially or completely detached from the PTFE surfaces that are irradiated without oxygen environment, whereas Al and Cu films are completely adhered on the PTFE surfaces modified by IAR. The enhancing adhesion between metal films and PTFE samples modified by IAR is attributed not only to a mechanical interlocking caused by the microscopic fiber textured surface, but also to an interfacial chemical bond.

PVDF has been used as a sensor and speaker since it has a piezoelectric property. If the electrode with high work function is deposited on PVDF with good adhesion, it increases the dielectric constant of PVDF leading to good efficiency of sensors and speaker. Up to now, however, it has been problem to make an electrode, especially Pt that has high work function value among the metals, on the PVDF because of chemical inertness of Pt. Therefore, many application using PVDF have been restricted until now.

Pt thin films were deposited on the pristine and the IAR treated PVDF surfaces by ion beam sputtering up to 100 nm. Figure 16 presents optical microscope photographs of Pt overlayers on the PVDF after a boiling test, in which the Pt/PVDF systems were kept in hot boiling water for 4 hours. The buckling of Pt layer is observed over the whole area on the pristine PVDF. This is due to stress induced at the interface between Pt thin film and PVDF surface by different thermal expansion rate of Pt and PVDF in hot water.

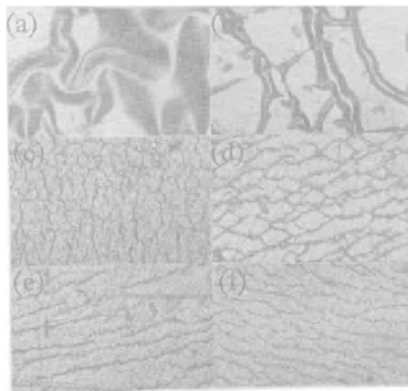


Figure 16 Optical microscope of Pt films on IAR treated PVDF immersed in boiling water during 4 hours: (a) pristine, (b)  $5 \times 10^{14}$ , (c)  $1 \times 10^{15}$ , (d)  $1 \times 10^{16}$ , (e)  $5 \times 10^{16}$  ions/cm $^2$ , and (e)  $1 \times 10^{17}$  ions/cm $^2$ .

The induced stress is released by buckling mode of Pt film, which is leaded by bad adhesion between Pt film and PVDF.

Significant reduction of the buckled, however, is shown on the PVDF irradiated by  $5 \times 10^{14}$  ions/cm $^2$  with an oxygen flow rate of 8 sccm. The stress release mode in Fig. 16 (c) is converted from the buckling of Pt layers to crack propagation within the Pt layer. The crack propagation mode of the Pt layer indicates the stress applied to the Pt layer is released by a formation of the crack. Crack propagation was still prevalent within the Pt layer of Fig. 16 (d)-(f) after the boiling test. These trends suggest that Ar $^+$  ion irradiation in an oxygen environment enhances adhesion of Pt/PVDF system as increasing ion dose, but the relationship between the crack density and the adhesion strength is still unclear.

Adhesion enhancement of metal/polymer system has been explained by three mechanisms: (1) Formation of intermetallic compounds like carbide, (2) Interlocking between metal layer and rough polymer surface formed by ion irradiation, and (3) Formation of charge transfer complex between electropositive metal and electronegative hydrophilic groups. Pt/polymer system cannot be explained by the first mechanism because Pt dose not form intermetallic compounds with polymers. The interlocking mechanism dose not sufficiently explain the adhesion enhancement because the surface

roughness of the IAR treated polymer surface seldom increases compared with that of the untreated polymer surface. The possible mechanism is the formation of charge transfer complex between the metal layer and the electronegative hydrophilic groups formed by the IAR. When the hydrophilic groups contact with metal layer, electrons are transferred from metal to electronegative hydrophilic groups resulting in forming charge transfer complex, which enhances adhesion between metal and polymer. From the adhesion test, we found that good adhesion between metal and polymer is achieved by the IAR, and the metallized polymers modified by the IAR are suitable in the practical application.

### 3.3 IAR Equipments For Mass Production

Figure 17 shows the photographs of the IAR treatment pilot systems. The roll-to-roll chamber is designed to treat the surfaces of films or foils with width of 600 mm continuously (Fig. 17(a)) and this chamber consisted of three parts, i.e., unwinding, IAR treatment, and winding chambers. The continuous surface modification chamber also has an advantage of being capable of controlling the film speed, ion dose, ion beam energy, and gas species leading to control of the degree of the surface modification.

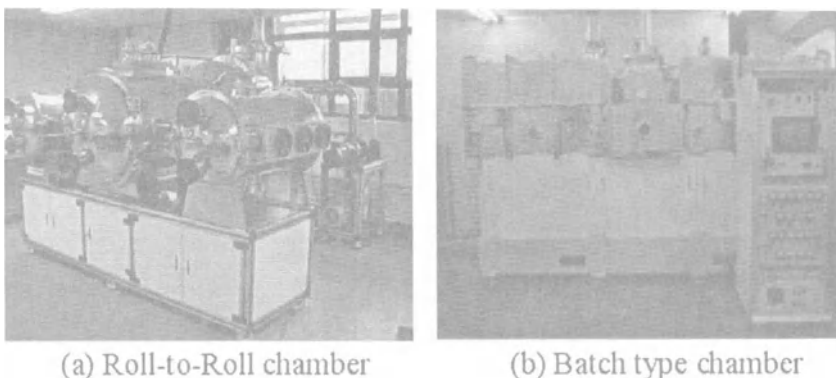


Figure 17 Photographs of pilot system for IAR treatment: (a) roll-to-roll chamber and (b) batch type chamber.

Figure 17(b) shows the batch type surface modification chamber, in which the 30 sheets type samples with size 600 mm × 900 mm can be modified continuously. The above surface modification chambers are used to produce the PTFE tapes with adhesive, silicon rubber sheets with adhesive for heat transfer between panel and Al heat sink in Plasma Display Panel (PDP), and Petri dishes for cell culturing, etc., which are made by Silion Co.Ltd, Smart Co. Ltd, and Ion Meditec in Korea receiving a license from KIST and P&I.

Figure 17 is the schematic diagram of in-line IAR treatment system, which is composed of a loading, an unloading chamber, an IAR treatment chamber and two buffer chambers. This system can treat the polymer sheets with size 600 mm × 900 mm continuously without breaking vacuum, and time for treating one sheet is at most 30 sec.

### 3.4 Applications

IAR technique can be devised in a lot of industrial applications. Immiscible materials e.g., PE and PP can be blended through IAR treatment, and new materials having advantages of each component can be made without adhesive. In the case of electronic applications, the metal backed PTFE treated by IAR can be used as printed circuit board (PCB) for microwave and RF application. IAR technique can be also applied successfully to biomedical fields such as blood contact devices, contact lens, implants, etc., in biomedical materials demanding an affinity to living body. The applications of IAR technique are summarized at Table 2.

### 4. Conclusions

New surface treatment method, so called Ion Assisted Reaction (IAR) in which the polymer surface is irradiated by low energy ion beam in a reactive gas environment, has been developed to improve wettability of polymer and adhesion between metal thin film

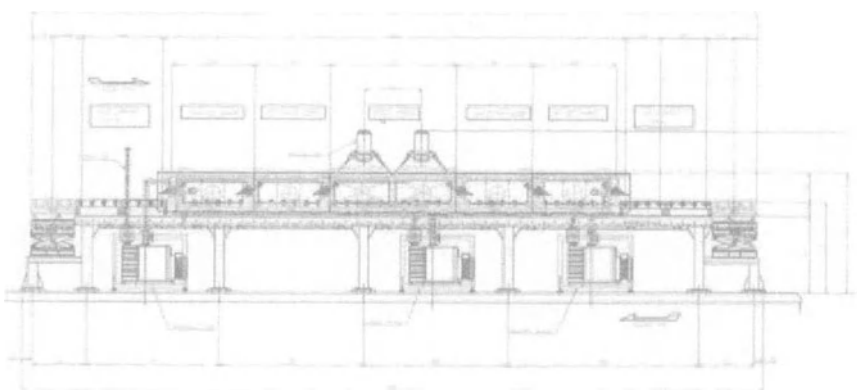


Figure 17 Schematic diagram of in-line system for IAR treatment.

and polymer surface. The mechanism of IAR treatment can be explained by two-step model as follows; Surface is activated by energetic ion irradiation by creation of unstable chains. Simultaneously, new hydrophilic functional groups are formed by the chemical reaction between environmental reactive gases and activated surface. This process can modify hydrophobic surface into hydrophilic surface.

IAR treatment increases the surface energy of polymers up to  $70 \text{ erg/cm}^2$ , which is similar as that of water. Wettability improvement is due to change of surface roughness and formation of polar component related to the hydrophilic groups. From the results in section 3.1.1, it is clear that hydrophilic groups formed on the polymer surface plays more important role in reducing the wetting angle than surface roughness.

It is revealed that the hydrophilic functional groups are  $[-(\text{C}-\text{O})-]$ ,  $[-(\text{C}=\text{O})-]$ , and  $[-(\text{C}=\text{O})-\text{O}-]$  by XPS study in section 3.1.4. Carbonized phase containing a double bond between carbons,  $=\text{C}=$ , is formed on the polymer surfaces at the high dose ion irradiation.

These hydrophilic functional groups formed by the IAR treatment are not washed out, meaning that the polymer surface treated by the IAR is not severely damaged. Excellent adhesion between metal and IAR treated polymer surface is achieved even between the noble metals and most stable polymers. Adhesion strength of IAR treated PTFE increase

Table 2. Summation of industrial applications expected by IAR technique

Fields	Applications
New composite	Blend of immiscible materials, mixture of nonadhesive materials, etc.
Electronics	PCB for microwave and RF application, Flexible PCB, Packaging, etc.
Medical appliance	Artificial heart, contact lens, Petri-dish for cell culture, implant, etc.
Environment	Membrane for treatment of waste water, green house without surfactant, etc
Miscellany	Goggle, heat exchanger, dye, etc.

significantly compared to unmodified PTFE. Stress release mode change from buckling mode to crack propagation mode because of good adhesion in the system of Pt/PVDF.

It will be expected that usage of IAR treatment become enlarged in various industrial applications, demanding wettability and adhesion. The IAR equipments have been fabricated in a scale of pilot and mass production.

## REFERENCES

1. S.K. Koh, W.K. Choi, J.S. Cho, S.K. Song, *J. Mater. Res.*, **11**, 2933 (1991)
2. S. Han, S. K. Koh and K. H. Yoon, *J. Electrochem. Soc.* **146**, 4327 (1999).
3. S. C. Choi, S. Han, W. K. Choi, H. J. Jung and S. K. Koh, *Nucl. Instr. And Meth. B* **152**, 291 (1999).
4. R. P. Livi, *Nucl. Instr. And Meth. B* **10/11**, 545 (1985).
5. S. Jacobson, B. Johonson, B. Sundqvist, *Thin Solid Films* **107**, 89 (1982).
6. J. E. Griffith, Y. Qiu, T. A. Tombrello, *Nucl. Instr. And Meth.* **198**, 607 (1982).
7. T. A. Tombrello, *Nucl. Instr. And Meth.* **218**, 679 (1983).
8. R. Flitsch, D. Y. Shi, *J. Vac. Sci. Technol. A8(3)*, 2376 (1990).
9. C. R. Wie, C. R. Shi, M. H. Mendenshall, R. P. Livi, T. Vreeland, T. A. Tombrello, *Nucl. Instr. And Meth. B9*, 20 (1985).
10. I. V. Mitchell, J. S. Williams, P. Smith, R. G. Elliam, *Appl. Phys. Lett.* **44(2)**, 193 (1984).
11. A. M. Wrobel, M. Kryszewski, W. Rakowski, M. Okoniewski, Z. Kubacki, *Polymer* **19** 908 (1978).
12. N. Inagaki, S. Tasaka, T. Horiuchi, and R. Suyama, *J. Appl. Poly. Sci.*, **68**, 271 (1998)

13. C. Chang, J. E. E. Baglin, A. G. Schrott, and K. C. Lin, *Appl. Phys. Lett.*, **51**, 103 (1987).
14. S. K. Koh, W. K. Choi, J. S. Cho, and S. K. Song, *J. Mater. Res.*, **11**, 2993 (1996).
15. G. A. Ingemarsson, M. P. Keane, and U. Gelius, *J. Appl. Phys.*, **66**, 3548 (1989).
16. G. A. Hishmeh, T. L. Bar, A. Sklyarov, and S. Hardcastle, *J. Vac. Sci. Technol.*, **A13**, 1330 (1996).
17. R. Michael and D. Stulik, *J. Vac. Sci. Technol.*, **A4**, 1861 (1986).
18. D. T. Clark and A. Dilks, *J. Polym. Sci.*, **17**, 957 (1979).
19. E. H. Adem, S. J. Bean, C. M. Demanet, A. Le Moel, and C. M. Duraud, *Nucl. Instrum. Meth.*, **B32**, 182 (1988).
20. L. Torrisi and R. Percolla, *Nucl. Instrum. Meth.*, **B117**, 387 (1996).
21. L. Torrisi, G. Ciavola, R. Percolla, and F. Benyaich, *Nucl. Instrum. Meth.*, **B116**, 473 (1996).
22. L. Torrisi, G. Ciavola, G. Foti and R. Percolla, *Nucl. Instrum. Meth.*, **A382**, 361 (1996).
23. C. R. Ginnard and W. M. Riggs, *Anal. Chem.*, **44**, 1310 (1972).
24. B. M. Callen, M. L. Ridge, S. Lahooti, A. W. Neumann, and R. N. S. Sohdi, *J. Vac. Sci. Technol.*, **A13**, 2023 (1995).
25. Yu. I. Mitchenko, V. A. Frmin, and A. S. Chegolya, *J. Appl. Polym. Sci.*, **41**, 2561 (1990).

# **PLASMA AND VUV PRETREATMENTS OF POLYMER SURFACES FOR ADHESION ENHANCEMENT OF ELECTROLESSLY DEPOSITED NI OR CU FILMS**

Maurice Romand, Marlène Charbonnier, and Yves Goepfert\*

## **1. INTRODUCTION**

Metallized polymer or polymer-based materials are used in a large range of electronics applications including the fabrication of ohmic contacts, chip-level interconnects, printed circuit boards and shielded materials.<sup>1-7</sup> For such technological applications, electroless deposition is the most widely used method in practice today.<sup>8</sup> Basically, electroless plating is an autocatalytic redox process occurring in aqueous solution between ions of the metal to be deposited (generally Ni or Cu) and a strong reducer. Typical procedures involve a variety of multi-step sequences for the preparation of the surfaces to be coated. Conventionally, substrates are cleaned with solvents to remove surface contaminants, chemically etched to obtain a micro-roughened oxidized surface, and then seeded with a catalyst such as palladium. Chronologically, the seeding process was first accomplished by using a two-step procedure involving substrate treatment successively in dilute SnCl<sub>2</sub> (sensitization step) and PdCl<sub>2</sub> (activation step) acidic solutions. Further, a one-step procedure using a colloidal suspension containing both Sn and Pd species (a SnCl<sub>2</sub>/PdCl<sub>2</sub> acidic solution) has been developed and is presently in common use in industrial environments. In this last case, the Pd/Sn colloidal particles adsorbed on the polymer surface must be exposed (acceleration step) to a solubilizer (a HCl or NaOH solution) to remove the excess of Sn<sup>+2</sup> species surrounding the catalytic Pd-based core of the colloidal particles. As can easily be inferred from the details of such multi-step procedures, it is today highly desirable to develop alternative approaches for making the insulating surfaces catalytically active. These approaches should require no chemical surface etching, reduce the number of process steps, and provide a highly selective, well-defined interaction between the catalytic species and the surface to be coated.<sup>9</sup> Obviously, these alternative approaches should be technologically reliable as well as economically and ecologically attractive.

---

\* Maurice Romand, Marlène Charbonnier, and Yves Goepfert, Laboratoire de Sciences et Ingénierie des Surfaces, Université Claude Bernard - Lyon 1, 69622 Villeurbanne cedex, France, E-mail: Maurice.Romand@univ-lyon1.fr, Phone: +33 4 72 44 81 68, Fax: +33 4 72 43 12 06.

In the present paper, special attention has been focused on the development of simplified procedures which consist in creating a sufficiently high surface density of strong chemical Pd-N bonds at the metal-polymer interface. For this purpose, seeding of palladium species is performed on polymer surfaces which are previously plasma or UV/VUV treated in nitrogenated ( $N_2$  and/or  $NH_3$ ) environments.<sup>10-21</sup>

## 2. EXPERIMENTAL

In the present work, surface pre-treatments and subsequent electroless metallization were carried out on polyimide (PI) substrates (Kapton<sup>®</sup> 500 HN foils, 125  $\mu m$  in thickness) produced by DuPont, USA. Before processing, these foils were ultrasonically cleaned in ethanol.

The plasma processing was performed in a parallel plate RF reactor operating in the Reactive Ion Etching mode (RIE 80 reactor from Plasma Technology, England). The samples to be surface-modified were placed on the powered electrode. Unless otherwise stated, experiments were conducted under the following conditions: working pressure: 100 mTorr, gas-flow: 100 sccm, power density: 0.5 W  $cm^{-2}$ .

The VUV processing was carried out using an  $Xe_2^*$  excimer source (Excivac Laboratory System from Heraeus Noblelight, Germany) which is mounted in an experimental setup already described.<sup>20, 21</sup> Briefly, the latter consists of two contiguous chambers which can be evacuated individually under primary vacuum. The upper chamber which contains the excimer lamp is separated from the reactor by a 5 mm thick  $CaF_2$  window. In these studies, the experimental conditions were the following: working pressure: 3.5 Torr, window-sample distance: 1 cm, photon flux estimated between 30 and 40 mW  $cm^{-2}$ .<sup>20</sup>

The seeding of the PI surfaces with palladium species was based on the use of two methods. The former consisted in immersing the plasma or VUV-treated substrates for 2 min in a solution containing 0.1 g/liter  $SnCl_2$  and 0.1 ml/liter concentrated HCl, rinsing them in DI water (sensitization step), then immersing them for 2 min in a solution containing 0.1 g/liter  $PdCl_2$  and 3.5 ml/liter concentrated HCl and rinsing (activation step). The latter consisted in immersing the pre-treated substrates in a simple solution containing 0.1 g/liter  $PdCl_2$  and 3.5 ml/liter concentrated HCl for 2 min and rinsing them (direct activation step).

The Ni plating bath contained  $NiSO_4 \cdot 6H_2O$  (0.14 M),  $NaH_2PO_2 \cdot H_2O$  (sodium hypophosphite) (0.09 M), lactic acid (0.27 M) and worked at 85°C, pH 5. The Cu plating bath contained five volumes of the following solution  $CuSO_4 \cdot 5H_2O$  (0.28 M),  $KNaC_4H_4O_6 \cdot 4H_2O$  (0.6 M), NaOH (0.14 M) and EDTA (0.03 M) and one volume of formaldehyde HCHO 37 %.

XPS analyses were performed with a Riber SIA 200 spectrometer using a non-monochromatic Al  $K\alpha$  photon source and a take-off angle of 65° with respect to the sample surface. Spectra were referenced to the C 1s signal at a binding energy of 285.0 eV characteristic of the C-C and C-H bonds.

Adhesion of thin metallized films to their substrates was first characterized using a simple adhesive tape peel test (cross-cut tape test of type-ASTM D 3359). In addition, a stretch deformation test (also known as a fragmentation test) was employed in conjunction with electrical measurements in order to distinguish the influence of the conditioning of the polymer surface. To reach this end, dog-bone shape metal-polymer systems were

strained under uniaxial elongation at a constant strain rate of 0.05 mm min<sup>-1</sup> using a DY 25 Adamel Lhomargy machine. Some details about the approach using electrical measurements can be found in a recent paper.<sup>22</sup> In these experiments an Europlate Ni 520 electroless nickel bath (Frappaz, Neyron, France) was employed (bath temperature = 90°C, pH = 5.1-5.2) for obtaining the Ni based deposit (in fact a Ni film containing a phosphorus content comprised between 5 and 7 %). This bath contains sodium hypophosphite as reducing agent.

### 3. RESULTS AND DISCUSSION

Nitrogen-containing plasmas have widely been used in the two last decades to introduce basic groups on a variety of polymer surfaces and thus to improve their wettability, dyeability, printability, bondability or biocompatibility characteristics. For this purpose, surface modifications have mainly been carried out using ammonia (NH<sub>3</sub>) or nitrogen (N<sub>2</sub>) gases (e.g. see<sup>23-27</sup>). However, a clear understanding of the plasma-assisted interactions of such gases with polymer surfaces has not rigorously been established, due to the different treatment conditions and equipments used by many investigators, as well as to the fact that various oxygenated functionalities are also incorporated during and after the plasma treatment itself. In addition, it should be noted that XPS spectrometry, even performed with high resolution apparatus, and commonly used as characterization technique in the field has not a sufficient spectral resolution to assign unambiguously the different N-functionalities (primary, secondary, and tertiary amines, amide, imide, etc.) which can be created under nitrogenated-plasma treatments. Concerning the use of such treatments prior to metallization, most of the published works have dealt with thermal or electron beam evaporation and ion sputtering processes operating in high vacuum and with the deposition of metals such as Ag, Al, Cu (e.g. see<sup>23, 27-30</sup>).

On the other hand, the use of nitrogen-containing plasmas for carrying out the direct conditioning of polymer surfaces and their subsequent "activation" prior to electroless metallization has been the subject of many investigations in our own laboratory.<sup>10-21</sup> In the following, polyimide (PI) substrates are taken as samples to be surface-modified and metallized.

Figure 1 represents XPS wide-scan spectra of Kapton® substrates after ultrasonic cleaning in ethanol (a), then after plasma treatment for 1 min in NH<sub>3</sub> at reduced pressure (b), and lastly after an immersion in a simple PdCl<sub>2</sub> acidic solution. These spectra show that the NH<sub>3</sub> plasma leads to the chemisorption of nitrogenated species while the subsequent "activation" in the PdCl<sub>2</sub> solution causes a significant grafting of palladium species on the PI surface. In this example, the plasma treatment is responsible for a noticeable increase of the nitrogen surface concentration (from 6.4 to ca 11.5 at. %) while the oxygen surface concentration remains approximately constant around 18 at. %. After "activation", water rinsing and drying, the relevant palladium surface concentration is ca 1.4 at. %. As smartly demonstrated by Egitto and Matienzo,<sup>31</sup> and confirmed by other authors,<sup>32</sup> the vacuum-ultraviolet (VUV) radiation emitted in plasma reactors (obviously at the same time as reactive radicals and ions are formed) plays an essential role in the surface reactions which occur when the polymer material is directly immersed in the plasma phase. In other words, VUV photons are energetic enough to contribute to the

breakage of many organic bonds at the polymer surface and thus lead to a rapid free-radical

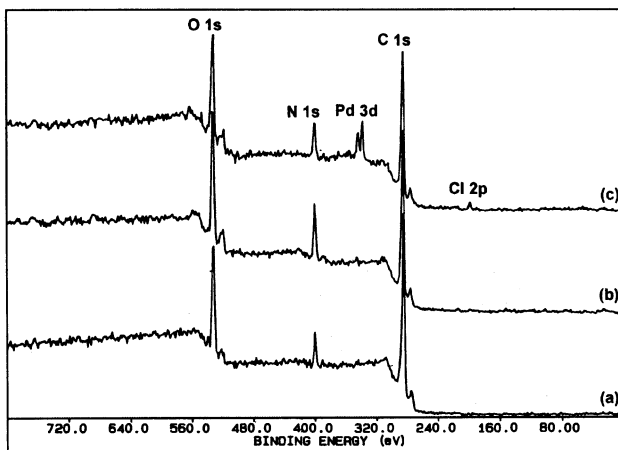


**Figure 1.** XPS survey spectra of Kapton® 500 HN samples (a) ethanol-cleaned, (b) the same as (a) after a plasma treatment in NH<sub>3</sub> for 1 min, and (c) the same as (b) after immersion in a PdCl<sub>2</sub> acidic solution.

chemistry. As a result, irradiation by photons in the same wavelength range ( $\lambda < 200$  nm) can be used to chemically modify polymer surfaces. Figure 2 is relative to XPS wide-scan spectra of Kapton® substrates which were VUV-irradiated using an Xe<sub>2</sub>\* excimer lamp emitting an incoherent radiation at 172 nm. Spectrum (a) is characteristic of an ethanol-cleaned sample while spectrum (b) is obtained after VUV irradiation for 1 min in NH<sub>3</sub>. In addition, spectrum (c) is recorded for a sample (b) subsequently to its immersion in a PdCl<sub>2</sub> acidic solution. Clearly, these spectra show that results similar to those obtained with NH<sub>3</sub>-plasma treatments can be got. In this example, the nitrogen surface concentration is increased from 6.4 to 10.0 % while that of the oxygen remains constant around 18 at. %. After "activation", water rinsing and drying, the palladium surface concentration is then of 0.6 at. %. It should now be noted that N<sub>2</sub>-plasma treatments can also be carried out for grafting nitrogenated species and attaching palladium species to the polymer surface while similar experiments cannot be performed through an VUV-irradiation in a N<sub>2</sub> atmosphere. Indeed, the VUV-photons emitted by the Xe<sub>2</sub>\* excimer lamp are not energetic enough (7.2 eV) to break the N≡N triple bond (9.76 eV) of N<sub>2</sub> molecules while they are quite able to break the N-H bonds (4.03 eV) of NH<sub>3</sub> molecules. XPS spectra recorded in Figs. 1 and 2 were obtained for PI substrates which were surface functionalized through a plasma or VUV treatment for a given treatment time, and subsequently "activated" in a PdCl<sub>2</sub> acidic solution. It is now important to determine the influence of the treatment time on both the grafting of nitrogenated species and the attachment of palladium species. Figure 3 shows the effect of the NH<sub>3</sub> or N<sub>2</sub>-plasma treatment time on the surface concentrations in oxygen (curves (a)) and nitrogen (curves (b)) for samples which have been subjected to the "activation" step. In addition, curves (d) are relative to the surface concentration in bound nitrogen just after the NH<sub>3</sub> and N<sub>2</sub> plasma treatments,

respectively. In the case of  $\text{NH}_3$  plasma treatments, comparison of curves (b) and (d) seems indicate a slight "loss" of nitrogenated species during the "activation" step in the

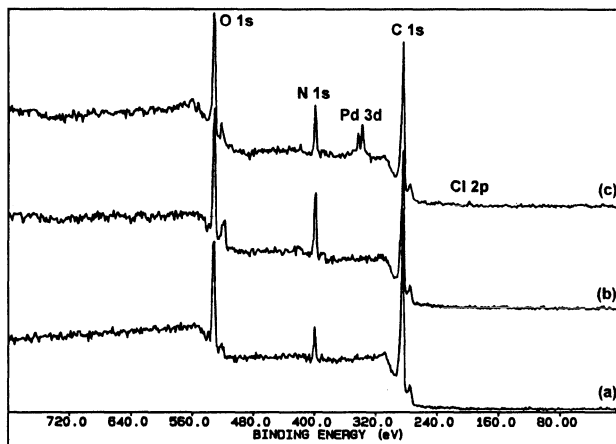


**Figure 2.** XPS survey spectra of Kapton<sup>®</sup> 500 HN samples (a) ethanol-cleaned, (b) the same as (a) after a VUV treatment in  $\text{NH}_3$  for 1 min, and (c) the same as (b) after immersion in a  $\text{PdCl}_2$  acidic solution.

$\text{PdCl}_2$  solution, unless this "loss" is only apparent and results from an analytical artifact due to the presence of palladium species at the outer surface of the probed samples. However, such an experimental discrepancy is not observed in the case of  $\text{N}_2$ -plasma treated samples. Finally, curves (c) show the influence of the plasma treatment time on the surface concentration in palladium. As can be seen from data illustrated in Fig. 3, grafting of

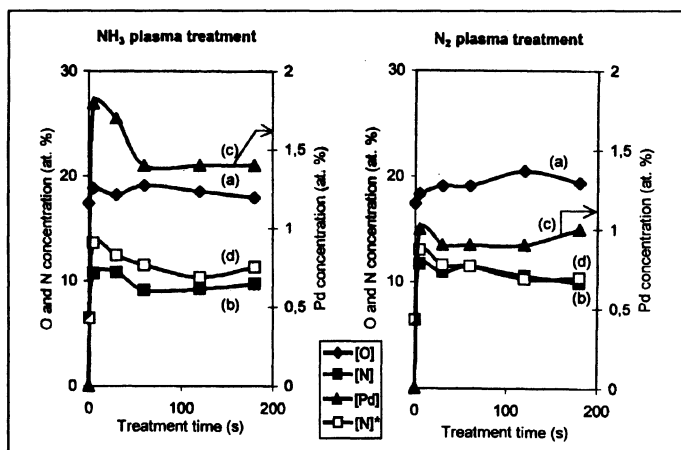


**Figure 3.** Plasma treatments of Kapton<sup>®</sup> 500 HN samples in  $\text{NH}_3$  and  $\text{N}_2$  atmospheres, respectively. Influence of the plasma treatment time on the oxygen (a), nitrogen (b) and palladium (c) surface concentrations (at. %) after the "activation" step in the  $\text{PdCl}_2$  acidic solution. For comparison, curve (d) is relative to the nitrogen surface

concentration before this step, i.e. after the plasma treatment. The other treatment conditions were: working pressure = 100 mTorr, flow-rate = 100 sccm, power density = 0.52 W cm<sup>-2</sup>.

nitrogenated functionalities increases at first as the treatment time increases, then decreases and further reaches a plateau. On the other hand, the surface concentration in oxygen increases slightly and reaches a steady-level around 19-20 at. %. In addition, it is found that, under quite similar experimental conditions, a somewhat similar nitrogen content is surface-grafted by using NH<sub>3</sub> or N<sub>2</sub> plasma treatments. More important for the subject of this paper is the fact that the change in palladium surface concentration follows that of the grafted nitrogenated species. In addition, it is noted that more Pd is attached on the polymer surface when the plasma treatment is carried out with NH<sub>3</sub>. Identically, Figure 4 depicts the effect of the VUV-treatment time in NH<sub>3</sub> on the oxygen and nitrogen surface content (curves (a) and (b), respectively) after the "activation" step, as well as the change in the palladium surface concentration (curve (c)) resulting from this operation. In addition, curve (d) is relative to the surface concentration in bound nitrogen just after the VUV irradiation in NH<sub>3</sub>. Conclusions similar to those obtained previously with plasma treatments can be drawn except that a longer treatment time (2-3 min) is necessary for grafting a similar palladium amount. Clearly, all these observations support a specific reactivity of the palladium species (which are present as Pd<sup>+2</sup> ions in the "activation" solution) towards the nitrogenated species grafted on the polymer surface during plasma or VUV treatments in a N<sub>2</sub> or NH<sub>3</sub> atmosphere. On the other hand, such a Pd<sup>+2</sup> attachment does not occur in the case of surfaces grafted with oxygenated species. Figure 5 is relative to a Kapton® substrate after plasma treatment for 1 min in O<sub>2</sub> (spectrum b), then after immersion in a simple PdCl<sub>2</sub> acidic solution (spectrum c)). In the latter case, a faint Pd 3d signal is observed only due to the attachment of Pd<sup>+2</sup> ions on the nitrogen atoms of the PI substrate still present at the polymer surface after the O<sub>2</sub> plasma treatment. However, it should be noted that, in the case of polymers containing no nitrogen atoms in their chemical structure such as polyolefins, the surface grafted with oxygenated species

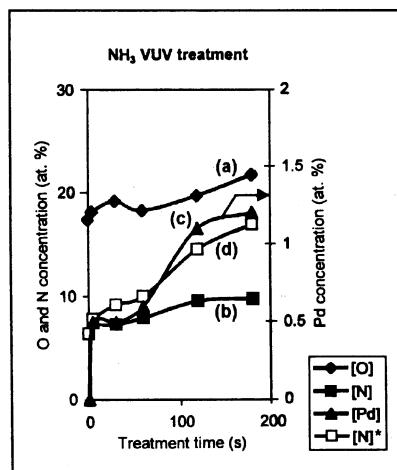


**Figure 4.** VUV treatments of Kapton® 500 HN samples in an NH<sub>3</sub> atmosphere. Influence of the treatment time on the oxygen (a), nitrogen (b) and palladium (c) surface concentrations (at. %) after the "activation" step in the PdCl<sub>2</sub> acidic solution. For comparison curve (d) is relative to the nitrogen surface concentration before this step,

i.e. after the VUV irradiation. The other treatment conditions were: working pressure = 3.5 Torr, sample-CaF<sub>2</sub>, window distance = 1 cm, power density ~ 30 mW cm<sup>-2</sup>.

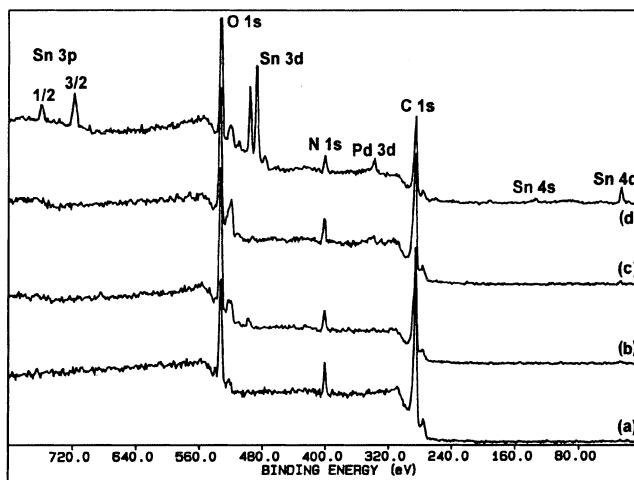


**Figure 5.** XPS survey spectra of Kapton® 500 HN samples (a) ethanol-cleaned, (b) the same as (a) after a plasma treatment in O<sub>2</sub> for 1 min, (c) the same as (b) after immersion in a PdCl<sub>2</sub> acidic solution, and (d) the same as (b) after immersion successively in SnCl<sub>2</sub> and PdCl<sub>2</sub> acidic solutions.

through O<sub>2</sub> plasma treatment does not attach any palladium species.<sup>12-19</sup> On the other hand, such oxygen-grafted surfaces have a strong propensity to adsorb tin species. Spectrum (d) in Fig. 5 is relative to a Kapton® substrate plasma-treated for 1 min in O<sub>2</sub> at reduced pressure, and then successively immersed in SnCl<sub>2</sub> and PdCl<sub>2</sub> acidic solutions (conventional two-step procedure). A strong Sn 3d signal due to Sn<sup>+2</sup> ions chemisorbed on oxygenated species appears. In addition, a Pd 3d signal can also be observed due to the palladium attachment on the tin species in agreement with the catalysis mechanism of the two-step procedure used in the present experiment. In this example, the surface concentrations in tin and palladium are 3.0 and 0.8 at. %, respectively. Lastly, it should be outlined that similar results can be obtained when the Kapton® substrate is originally VUV-irradiated in an O<sub>2</sub> atmosphere at reduced pressure. All the experimental observations previously described allow to draw the following conclusions:

- Tin (Sn<sup>+2</sup>) species have a strong chemical affinity towards oxygenated species grafted on the polymer surface through O<sub>2</sub> plasma or VUV-assisted treatments. On the other hand, tin has no chemical affinity towards nitrogenated functionalities grafted through similar techniques using NH<sub>3</sub> or N<sub>2</sub>. Under these conditions, Pd-based catalysis of the oxidized polymer surfaces requires the use of the conventional sensitization/activation processes (two-step or one-step procedure using both tin and palladium species).
- In contrast, palladium (Pd<sup>+2</sup>) species have no chemical affinity towards oxygenated species but have a strong affinity towards nitrogenated functionalities. Under these conditions, Pd-based catalysis of the polymer surfaces can be carried

out using a simplified process which involves successively its functionalization with nitrogenated species (plasma or VUV-assisted treatments in a suitable nitrogenated atmosphere) and its “activation” (immersion in a  $\text{PdCl}_2$  acidic solution).

- Grafting of nitrogenated species by plasma treatment is quasi-immediate (a few seconds). However, in this work, a 1 min treatment time was used to reach a dynamic equilibrium between grafting and etching and thus to make sure of a sufficient surface “cleaning”. Grafting of nitrogenated species by VUV treatment is as much efficient as plasma treatment but requires longer treatment times account being taken of the limited power supplied by the excimer lamp.

From a purely chemical point of view, it is important to point up the fact that:

1. the two routes described above using plasma or VUV treatments do not require the use of hazardous chemicals such as those which are conventionally used (oxidizing baths such as chromic acid / sulfuric acid or potassium permanganate / sulfuric acid mixtures) for conditioning the polymer surface prior to the sensitization / activation steps,
2. the original route using the surface functionalization with nitrogenated species has the advantage to employ a stable, dilute  $\text{PdCl}_2$  solution and to be a tin-free method which is simpler than the conventional one-step method since it allows to suppress one of its chemical steps, namely the acceleration operation. Also, remember that, in spite of its successful commercial use, the conventional method using a colloidal  $\text{Pd/Sn}$  solution presents several drawbacks. As highlighted by Brandow et al.<sup>9</sup> the acceleration step can result in an incomplete removal of the  $\text{Sn}^{+2}$  outer layer, and then leave dormant many catalytic sites. In contrast, an excessive removal of this layer can result in lowered activity of the colloidal particles by eliminating a Pd-rich part of their core provoking so, a loss of adhesion of the adsorbed colloid to the polymer surface.

Lastly, it is interesting to note that results obtained in the present work are in full agreement with the fact that  $\text{Pd}^{+2}$  ions can easily be covalently bound to ligands containing electron-donating nitrogen atoms.<sup>33</sup> As far as electroless metallization is concerned, the preference of  $\text{Pd}^{+2}$  ions for nitrogen has also been used by Calvert et al.<sup>9, 34-36</sup> to bind the catalyst on ligating surfaces. In their attractive approach, these authors have shown that surfaces which are modified with chemisorbed, self-assembled films of organosilanes containing electron-donating functional groups such as alkylamine or pyridine can be used to anchor a palladium-based electroless catalyst and that the so-bound catalyst initiates the electroless deposition. For this purpose, tin-free formulations based on aqueous  $\text{PdCl}_4^{2-}$  solutions buffered at pH 5.0 to 6.4 have been used. The process is applicable to a variety of non-conducting substrates including polymer ones. Similarly to the  $\text{Pd}^{+2}$  attachment method developed in the present study, the catalyst anchoring proposed by Calvert et al.<sup>9, 34-36</sup> is selective since it does not occur when the chemisorbed organosilane possesses no ligating nitrogenated functionality.

In the second part of this study, consider the electroless metallization process itself and more especially what occurs when the Pd-catalyzed surfaces are dipped in the electroless bath. In the case of the Ni plating bath reported in Section “Experimental”, the metal deposition starts after a certain initiation time ( $\tau \sim 12$  s) which is required to con-

vert a sufficient surface density of the chemisorbed  $\text{Pd}^{+2}$  species to the  $\text{Pd}^0$  state. On the other hand, in the case of the Cu plating bath reported in this same section, no metal deposition occurs ( $\tau = \infty$ ). Such results can be interpreted from Fig. 6. Spectrum (a) represents the Pd 3d spin-doublet of a Kapton® HN substrate plasma-treated in  $\text{NH}_3$ , and then immersed in a  $\text{PdCl}_2$  acidic solution. The binding energy of the Pd 3d 5/2 peak (338.0 eV) is characteristic of the  $\text{Pd}^{+2}$  state. Spectra (b) and (c) are relative to the same sample as (a) after immersion in the Cu electroless bath for 4 min and in the Ni electroless bath for 12 s, respectively, and spectrum (d) is characteristic of a metallic Pd sample. On spectra (b) and (c), the Pd 3d 5/2 peak is broadened towards its low-binding energy side. In addition, a small shift of the maximum of this peak is observed. This shift which is indicative of the reduction onset is more pronounced for spectrum (c). This means that some  $\text{Pd}^0$  species are rapidly formed during the initiation time in the Ni electroless bath due to the action of the reducing agent (hypophosphite ions  $\text{H}_2\text{PO}_2^-$ ), and that the kinetics of the relevant chemical reduction in the Cu electroless bath is notably smaller. Clearly, the reducing agent (formaldehyde HCHO) in this bath is not strong enough to reduce the  $\text{Pd}^{+2}$  species attached to the substrate surface. These results can easily be verified by immersing  $\text{Pd}^{+2}$ -grafted substrates in aqueous solutions containing only the reducing agents. Figure 7 represents Pd 3d XPS spectra of such samples before (a) and after immersion either in an alkaline HCHO solution at 50°C for 10 min (b) or in a 0.1 M  $\text{NaH}_2\text{PO}_2$  solution at 85°C for 12 s (c) and 3 min (d), respectively. This hypophosphite solution has a concentration similar to that used in the electroless Ni bath and operates under similar experimental conditions. Again, the widening and shifting of the Pd 3d peaks towards the low binding energy side (case of the  $\text{NaH}_2\text{PO}_2$  solutions) prove the progressive reduction of the initial  $\text{Pd}^{+2}$  species and show that it is  $\text{Pd}^0$  which operates as the actual electroless catalyst. On the other hand, a lesser change in the spectrum (b) in comparison with the spectrum (a) is observed. Under these conditions, metallization in the Cu plating bath used in this work requires an additional step which consists in immersing the  $\text{Pd}^{+2}$ -grafted surfaces in the previously cited hypophosphite solution (e.g. for

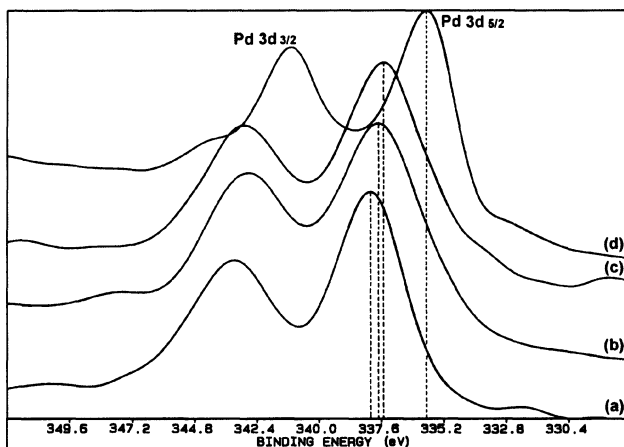


**Figure 6.** Pd 3d XPS spectra of Kapton® 500 HN samples (a) after surface functionalization by  $\text{NH}_3$ -plasma treatment and "activation" by a  $\text{PdCl}_2$  acidic solution, (b) the same as (a) after immersion in the electroless Cu

bath for 4 min, and (c) the same as (a) after immersion in the electroless Ni bath for 12 s. Spectrum (d) characteristic of the Pd<sup>0</sup> state is recorded for comparison purpose.

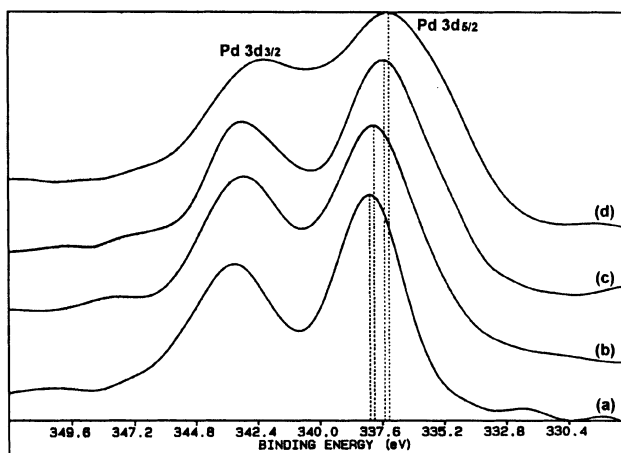


**Figure 7.** Pd 3d XPS spectra of Kapton® 500 HN samples (a) after surface functionalization by NH<sub>3</sub>-plasma treatment and activation by a PdCl<sub>2</sub> acidic solution, (b) the same as (a) after immersion in an alkaline HCHO solution at 50°C for 10 min, and (c) and (d) the same as (a) after immersion in a hypophosphite solution at 85°C for 12 s and 3 min, respectively.

1 to 3 min), before a subsequent dipping in the Cu plating bath. As a result, the metallization proceeds after an initiation time all the shorter as the immersion time in the hypophosphite solution is longer, therefore as the Pd<sup>0</sup> surface density is higher. It should be noted that some Ni industrial plating baths containing large amounts of stabilizers require a procedure similar to that employed for Cu baths, namely the reduction of the Pd<sup>+2</sup>-grafted species in an hypophosphite solution before the metallization operation itself.

Adhesion tests carried out in this work were performed on Kapton® HN substrates coated with thin electroless Ni films which were deposited from the commercial electroless bath (Europlate Ni 520). The thickness of the Ni films obtained for different deposition times was determined either by x-ray fluorescence spectroscopy (measurement of the Ni K<sub>α</sub> intensity) or by measurement of the initial electrical resistance ( $R_0$ ), the calibration being performed by gravimetry. As the Ni K<sub>α</sub> intensity and film conductance ( $1/R_0$ ) vary linearly with the thickness, a mere resistance measurement provides the film thickness, on condition that the same electroless bath is used.<sup>22</sup> In the present work, the influence of two surface conditioning processes on the level of adhesion at the metal/PI interface was studied. These processes include respectively (a) surface amination of the PI substrate (plasma treatment in NH<sub>3</sub>) and subsequent surface activation (immersion in a PdCl<sub>2</sub> acidic solution), and (b) surface oxidation (plasma treatment in O<sub>2</sub>) and subsequent surface sensitization/activation (immersion successively in SnCl<sub>2</sub> and PdCl<sub>2</sub> acidic solutions). In a first series of experiments a cross-cut peel test was carried out using a Scotch® tape. Results of this test show that no metal square or part is stripped off by the tape, and therefore that a good adhesion has been obtained at the Ni/PI interface. However, this test is proved to be unable to differentiate the effects due to the different substrate pretreat-

ments. In a second series of experiments, the coated samples were subjected to the fragmentation test. Conventionally, the coating/substrate systems are placed under uniaxial strain and the development of parallel cracks which are transverse to the straining direction is observed (optical or electron microscopy observations) as a function of the applied strain. Concerning metal/polymer systems, this test has already been used for characterizing adhesion of Ni films evaporated on ion-etched poly(ethylene terephthalate) (PET) substrates<sup>37</sup> and of electroless Pt films on PET fibers.<sup>38</sup> According to the theoretical approach proposed by Wheeler and Osaki,<sup>37</sup> the value of the maximum interfacial shear stress as it is inferred from experimental data (crack density at saturation) can be taken as a measure of the interfacial adhesion. In the present work, another experimental approach has been considered which consists in measuring the change in the electrical characteristics of the metal/substrate system under investigation.<sup>22</sup> As an example, Fig. 8 is relative to PI substrates which were subjected to the (a) and (b) conditioning processes previously described, and subsequently coated with Ni films (in fact Ni-P films) of same thickness (200 nm in this case). This figure shows how the relative electrical resistance  $\Delta R/R$  varies as a function of the applied strain (relative elongation  $\Delta L/L_0$ ). In each case (curves (a) and (b)), the first slope change indicates precisely the early stages of the fragmentation process. The instantaneous changes in the relative electrical resistance  $\Delta R/R$  provide some information on the fragmentation phenomenon. Indeed, the cracks observed on the film surface can or not reach the metal/polymer interface and, as long as  $\Delta R/R$  progressively changes, it can be concluded to the existence of bridges between the film fragments. The higher the maximum of  $\Delta R/R$ , the lesser is the number of bridges remaining between the fragments. In figure 8, the upward-sloping part of the curves (a) and (b) occurs for a very little increase in the strain applied to the substrate. This part appears to correspond to the stage for which many random cracks are formed. On the other hand, the downward-sloping part spreads out monotonically when the applied strain increases. This second stage associated with the progressive division of the largest segments at their midpoint ends when the crack density at saturation is reached. The integral curves (c) and

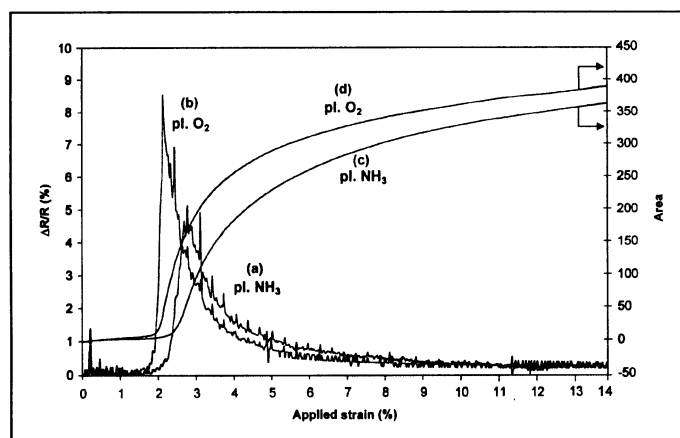


**Figure 8.** Fragmentation test. Dependence of the relative electrical resistance of a 200 nm thick Ni film on the applied strain. Curve (a) is relative to a Kapton® substrate plasma-treated in NH<sub>3</sub> and “activated” in a PdCl<sub>2</sub> acidic solution. Curve (b) is relative to a same substrate plasma-treated in O<sub>2</sub> and sensitized / “activated” by

using successively  $\text{SnCl}_2$  and  $\text{PdCl}_2$  acidic solutions. Curves (c) and (d) are obtained by integration of (a) and (b) curves, respectively.

(d) of the  $\Delta R/R = f(\Delta L/L_0)$  functions as well as curves (a) and (b) themselves tend to a plateau which characterizes the crack density at saturation. In the present case, it happens for an applied strain beyond 14 %. As an example, Fig. 9 represents a typical optical micrograph of a fragmented zone of a 200 nm thick Ni film deposited on a 125  $\mu\text{m}$  thick Kapton® HN substrate after the coated specimen has been subjected to a strain ( $\sim 15\%$ ) for which the primary process of segment division is considered as complete. In this case, the Kapton® HN substrate has been plasma treated in  $\text{NH}_3$ , then activated by immersion in the  $\text{PdCl}_2$  acidic solution, and finally metallized. As can be observed on this micrograph, a secondary fragmentation process resulting from the contraction of the film perpendicular to the straining direction begins to appear. This phenomenon which is controlled by Poisson's ratio of the polymer substrate<sup>39, 40</sup> eventually provokes (i.e. when the sample is overstrained) a buckling rupture of the coating into rectangular fragments. For the strain level ( $\sim 15\%$ ) for which the primary process of segment division is considered as complete, it is not possible at the present time, to determine if the applied strain is sufficient to produce debonding. Indeed, the adhesion of the metal film to the polymer substrate remains still actual since no metal part is removed by a Scotch® tape when a simple peel test is carried out. In addition, this is confirmed in the present examples since the resistance measurement is in the range 18-660  $\Omega$  for sample (a) and 32-1500  $\Omega$  for sample (b). Irrespective of the nature of these considerations, examination of curves provided in Fig. 8, as well as our experience in testing different series of coated specimens should indicate that the smaller the area value associated with an integral curve, the higher is the practical adhesion of the metal film to its polymer substrate. Obviously such investigations must be carried out using metal films of same thickness deposited on the same substrate from a well-defined electroless bath, the variable being the nature of the

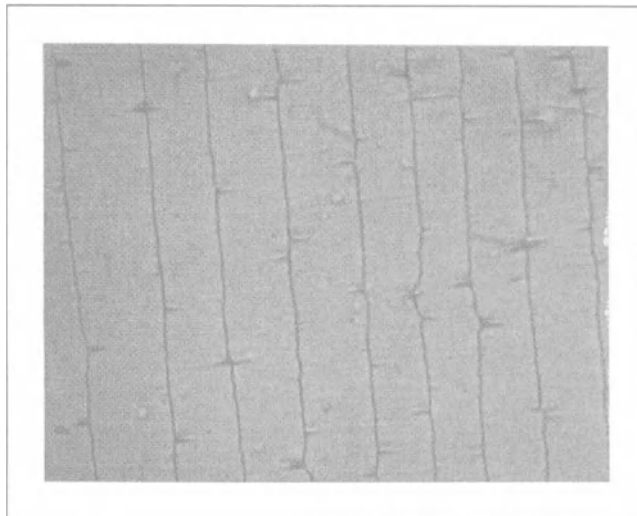


**Figure 9.** Photomicrograph (magnification  $\times 625$ ) of a fragmented zone of a 200 nm thick Ni film deposited on a 125  $\mu\text{m}$  thick Kapton<sup>®</sup> HN substrate after plasma treatment in  $\text{NH}_3$  and “activation” in a  $\text{PdCl}_2$  acidic solution. This micrograph was taken after an uniaxial straining of 15 %.

surface preconditioning step. Under these conditions and on the basis of results provided in Fig. 8 the more efficient process should involve the surface amination of the PI substrate and its subsequent “activation” in a simple  $\text{PdCl}_2$  acidic solution.

#### 4. CONCLUSION

The main conclusions of this paper may be summarized as follows:

1. Grafting of nitrogenated functionalities (through the use of plasma or VUV-assisted treatments in  $\text{NH}_3$  or  $\text{N}_2$  atmospheres at reduced pressure) confers to the surfaces (here polyimide substrates) a specific chemical reactivity. Indeed, it allows to realize a direct covalent attachment of palladium-based catalysts on polymer surfaces. The relevant chemisorption is made successful thanks to the strong chemical affinity of the  $\text{Pd}^{+2}$  species present in a dilute  $\text{PdCl}_2$  acidic solution towards the grafted nitrogenated functionalities.
2. The catalyst particles are attached to the polymer surface in the  $\text{Pd}^{+2}$  state, but the triggering of the metal deposition happens only when a sufficient amount of these bound  $\text{Pd}^{+2}$  species are chemically reduced to  $\text{Pd}^0$ . In other words, attachment of the  $\text{Pd}^{+2}$  species on the polymer surface does not really lead to its “activation” since only the reduced  $\text{Pd}^0$  species operate as the actual catalytic species capable of initiating the electroless metallization. In the case of the Ni plating bath used in the present study, the reduction is efficiently performed by the reducing agent ( $\text{NaH}_2\text{PO}_2$ ) contained in the bath. On the other hand, in the case of the Cu plating bath the reducing agent (HCHO) appears not strong enough to operate the reduction of the  $\text{Pd}^{+2}$  species attached on the nitrogen-grafted surfaces. In fact, the reaction should be thermodynamically possible at the alkaline pH of the experiments but its kinetics should be very low. To have a process compatible with a manufacturing environment, the reduction of the  $\text{Pd}^{+2}$  species attached on the polymer surfaces has to be done prior to the sample immersion in the plating bath. One simple method consists in dipping the  $\text{Pd}^{+2}$ -grafted substrates in a  $\text{NaH}_2\text{PO}_2$  solution for some seconds or tens of seconds. After rinsing, the Cu metallization initiates spontaneously in the plating bath, and then progresses thanks to the formaldehyde HCHO, only able to reduce the  $\text{Cu}^{+2}$  ions of the bath.
3. Electroless Ni or Cu films deposited on Pd-grafted surfaces exhibit good adhesion. However, peel tests with Scotch<sup>®</sup> tape do not allow to discriminate the effects of the processes used to perform the conditioning and activation of the polymer surface. On the other hand, the fragmentation test used in conjunction with electrical measurements appears to provide interesting prospects insofar as the method is not time-consuming and should be able to distinguish the effects of different surface pretreatments on the practical adhesion of metal deposits on polymer substrates.

Finally, this work shows that the tin-free method utilized here to carry out the direct attachment of the Pd-based particles and make the surface of polymer substrates catalyt-

cally active for a subsequently electroless metallization has distinct advantages in terms of ease of processing and cost over the conventional routes using especially colloidal Sn/Pd mixed particles. Indeed, the surface conditioning does not require micro-roughening and the use of strongly oxidative chemical treatments. In addition, the catalysis procedure itself is significantly simpler as it is accomplished by only dipping the N-functionalized surfaces in a dilute PdCl<sub>2</sub> acidic solution. In summary, this new approach of electroless metallization allows to reduce the number of surface preparation and activation steps and to avoid the use of several hazardous and environmentally harmful chemicals.

## 5. REFERENCES

1. E. Sacher, J. J. Pireaux, and P. Kowalczyk, *Metallization of Polymers* (ACS Symposium Series 440, American Chemical Society, Washington, DC, 1990).
2. K. L. Mittal and J. R. Susko, *Metallized Plastics I: Fundamental and Applied Aspects* (Plenum Press, New York, 1989).
3. K. L. Mittal, *Metallized Plastics 2: Fundamental and Applied Aspects* (Plenum Press, New York, 1991).
4. K. L. Mittal, *Metallized Plastics 3: Fundamental and Applied Aspects* (Plenum Press, New York, 1992).
5. K. L. Mittal, *Metallized Plastics: Fundamentals and Applications* (Marcel Dekker, New York, 1998).
6. K. L. Mittal, *Metallized Plastics 5&6: Fundamental and Applied Aspects* (VSP, Utrecht, The Netherlands, 1998).
7. K. L. Mittal, *Metallized Plastics 7: Fundamental and Applied Aspects* (VSP, Utrecht, The Netherlands, 2001).
8. G. O. Mallory and J. B. Hadju, *Electroless Plating: Fundamentals and Applications* (American Electroplaters and Surface Finishing Society, Orlando, FL, 1990).
9. S. L. Brandow, W. J. Dressick, C. R. K. Marrian, G.-M. Chow, and J. M. Calvert, The morphology of electroless Ni deposition on a colloidal Pd(II) catalyst, *J. Electrochem. Soc.* **142**(7), 2233-2243 (1995).
10. L. Deshayes, M. Alami, M. Charbonnier, N. S. Prakash, and M. Romand, in: *Proceedings of the seventeenth annual of the Adhesion Society*, edited by K. M. Liechti (The Adhesion Society, Blacksburg, VA, 1994), pp. 115-118.
11. M. Alami, M. Charbonnier, and M. Romand, in: *Proceedings of the eighteenth annual meeting of the Adhesion Society*, edited by J. W. Holubka (The Adhesion Society, Blacksburg, VA, 1995), pp. 83-85.
12. M. Charbonnier, M. Alami, and M. Romand, Plasma Treatment Process for Palladium Chemisorption onto Polymers before Electroless Deposition, *J. Electrochem. Soc.* **143**(2), 472-480 (1996).
13. M. Alami, M. Charbonnier, and M. Romand, Plasma Chemical Modification of Polycarbonate Surfaces for Electroless Plating, *J. Adhesion* **55**, 77-90 (1996).
14. M. Alami, M. Charbonnier, and M. Romand, Interest of NH<sub>3</sub> and N<sub>2</sub> Plasmas for Polymer Surface Treatment Before "Electroless" Metallization, *Plasmas Polym.* **1**(2), 113-126 (1996).
15. M. Charbonnier, M. Alami, and M. Romand, Electroless plating of polymers: XPS study of the initiation mechanisms, *J. Appl. Electrochem.* **28**(4), 449-453 (1998).
16. M. Romand, M. Charbonnier, M. Alami, and J. Baborowski, in: *Metallized Plastics 5&6: Fundamental and Applied Aspects*, edited by K. L. Mittal (VSP, Utrecht, The Netherlands, 1998), pp. 3-23.
17. M. Charbonnier, M. Romand, and M. Alami, in: *Polymer Surface Modification: Relevance to Adhesion, Vol. 2*, edited by K. L. Mittal (VSP, Utrecht, The Netherlands, 2000), pp. 29-43.
18. M. Charbonnier, M. Romand, G. Stremdoerfer, and A. Farès-Karam, Electroless Metallization of Polymers, *Recent Res. Devel. Macromol. Res.* **4**, 27-43 (1999).
19. M. Charbonnier, M. Romand, E. Harry, and M. Alami, Surface plasma functionalization of polycarbonate: Application to electroless nickel and copper plating, *J. Appl. Electrochem.* **31**(1), 57-63 (2001).
20. M. Charbonnier, M. Romand, U. Kogelschatz, H. Esrom, and R. Seeböck, in: *Metallized Plastics 7: Fundamental and Applied Aspects*, edited by K. L. Mittal (VSP, Utrecht, The Netherlands, 2001), pp. 3-26.
21. M. Charbonnier, M. Romand, H. Esrom, and R. Seeböck, Functionalization of Polymer Surfaces Using Excimer VUV Systems and Silent Discharges. Application to Electroless Metallization, *J. Adhesion* (2001) (in press).
22. Y. Goepfert, M. Charbonnier, and M. Romand, in: *Proceedings of the 24th annual meeting of the Adhesion Society*, edited by J. A. Emerson (The Adhesion Society, Blacksburg, VA, 2001), pp. 183-186.

23. L. J. Gerenser, An x-ray photoemission spectroscopy study of chemical interactions at silver/plasma modified polyethylene interfaces: correlations with adhesion, *J. Vac. Sci. Technol. A* **6**(5), 2897-2903 (1988).
24. R. Foerch, N. S. McIntyre, R. N. S. Sodhi, and D. H. Hunter, Nitrogen plasma treatment for polyethylene and polystyrene in a remote plasma reactor, *J. Appl. Polym. Sci.* **40**, 1903-1915 (1990).
25. J. R. Hollahan, B. B. Stafford, R. D. Falb, and S. T. Payne, Attachment of amino groups to polymer surfaces by radiofrequency plasmas, *J. Appl. Polym. Sci.* **13**, 807-816 (1969).
26. J. E. Klemburg-Sapieha, O. M. Küttel, L. Martinu, and M. R. Wertheimer, Dual-frequency N<sub>2</sub> and NH<sub>3</sub> plasma modification of polyethylene and polyimide, *J. Vac. Sci. Technol. A* **9**(6), 2975-2981 (1991).
27. M. K. Shi, A. Selmani, L. Martinu, E. Sacher, M. R. Wertheimer, and A. Yelon, Fluoropolymer surface modification for enhanced metal adhesion, *J. Adhesion Sci. Technol.* **8**(10), 1129-1141 (1994).
28. M. K. Shi, A. Selmani, L. Martinu, E. Sacher, M. R. Wertheimer, and A. Yelon, in: *Polymer Surface Modification: Relevance to Adhesion*, edited by K. L. Mittal (VSP, Utrecht, 1996), pp. 73-85.
29. E. Sacher, Fluoropolymer metallization for microelectronic applications, *Progr. Surface Sci.* **47**, 273-300 (1994).
30. V. André, Y. De Puydt, F. Arefi, J. Amouroux, P. Bertrand, and J. F. Silvain, in: *Metallization of Polymers*, edited by E. Sacher, J. J. Pireaux, and S. P. Kowalczyk (ACS Symposium Series 440, American Chemical Society, Washington, DC, 1990), pp. 421-432.
31. F. D. Egito and L. J. Matienzo, Modification of polytetrafluoroethylene and polyethylene surfaces downstream from helium microwave plasma, *Polym. Degrad. Stab.* **30**, 293-297 (1991).
32. J. E. Klemburg-Sapieha, L. Martinu, S. Sapieha and M. R. Wertheimer, in: *The Interfacial Interactions in Polymeric Composites*, edited by G. Akovali, Nato ASI Series, Series E: Applied Sciences - Vol. 230 (Kluwer Academic Publishers, Dordrecht, 1993), pp. 201-222.
33. F. R. Nartley, *Chemistry of the platinum group metals. Recent developments. Studies in inorganic chemistry II* (Elsevier, Amsterdam, 1991).
34. J. M. Calvert, W. J. Dressick, C. S. Dulcey, M.-S. Chen, J. H. Georger, D. A. Stenger, T. S. Koloski, and G. S. Calabrese, in: *Polymers for Microelectronics, Resists and Dielectrics*, edited by C. F. Thomson, C. G. Wilson, and S. Tagawa, ACS Symposium Series 537 (American Chemical Society, Washington, DC, 1994), pp. 210-219.
35. W. J. Dressick, C. S. Dulcey, J. H. Georger, G. S. Calabrese, and J. M. Calvert, Covalent binding of Pd catalysts to ligating self-assembled monolayer films for selective electroless metal deposition, *J. Electrochem. Soc.* **141**(1), 210-220 (1994).
36. M.-S. Chen, S. L. Brandow, C. S. Dulcey, W. J. Dressick, G. N. Taylor, J. F. Bohlend, J. H. Georger, E. K. Pavelchek, and J. M. Calvert, Channel-constrained electroless metal deposition on ligating self-assembled film surfaces, *J. Electrochem. Soc.* **146**(4), 1421-1430 (1999).
37. D. R. Wheeler and H. Osaki, in: *Metallization of Polymers*, edited by E. Sacher, J. J. Pireaux, and S. P. Kowalczyk (ACS Symposium Series 440, American Chemical Society, Washington, DC, 1990), pp. 500-512.
38. E. K. Chong and M. G. Stevens, in: *Metallized Plastics 5&6: Fundamental and Applied Aspects*, edited by K. L. Mittal (VSP, Utrecht, The Netherlands, 1998), pp. 409-422.
39. P. H. Wojciechowski and M. S. Mendolia, On the multiple fracture of low elongation thin films deposited on high-elongation substrates, *J. Vac. Sci. Technol. A* **7**(3), 1282-1288 (1989).
40. Y. Pitton, S. D. Hamm, F.-R. Lang, H. J. Mathieu, Y. Leterrier, and J.-A. Månon, Adhesion study of SiOx/PET films: comparison between scratch test and fragmentation test, *J. Adhesion Sci. Technol.* **10**(10), 1047-1065 (1996).

## INDEX

- AFM, 98, 130, 131, 176  
Adhesion, 91, 104, 183–184
- Condensation coefficients, 75, 97  
Copper on various polymers, 109
- Cyclotene (BCB), 97
- Clusters  
copper  
adhesion (critical load), 102  
annealing, 104  
condensation coefficients, 109  
deposition, 97  
growth, 76, 100  
interface tailoring, 91  
nanocluster embedding, 89  
nucleation, 76  
size, 100  
gold, 13, 87  
diffusion coefficients, 87  
silver, 78
- Crosssectional TEM, 99
- Dow cyclotene (BCB), 97  
XPS, 98
- Gold  
particles, 13  
sputtered films, 17
- HOPG (highly oriented pyrolytic graphite), 6
- Ion-assisted reactions  
adhesion improvement, 183–184  
commercialization, 186–189  
optical microscopy, 184  
polymer surface modifications, 165  
surface free energy, 174  
surface morphology, 176–178  
wettability, 166–167  
XPS, 179–183  
IR spectroscopy, 120, 123
- Metal deposition  
aluminum, 121, 125  
copper, 80, 97  
gold, 17  
silver, 78  
tantalum, 144  
titanium, 145
- Molecular structure, 65
- Nanoindentation, 36  
microcantilever array, 40  
microspring, 38
- Optical microscopy, 178
- Plasma fluoropolymers  
deposition rate, 64  
molecular structure, 65  
XPS, 68
- Polycarbonate  
gold diffusion, 87  
silver metallization, 78
- Polyimide, 80–82, 88  
copper metallization, 80  
electroless plating, 191, 194–200  
XPS, 199–200  
nickel adhesion, 201, 202  
surface treatment, 191, 194  
 $\text{N}_2$  plasma, 191, 194  
 $\text{NH}_3$  plasma, 191, 194  
sensitization  
XPS, 199–200
- Polymer metallization, 73  
condensation coefficients, 75  
interface chemistry, 81  
ion-induced metal intermixing, 148  
surface energy, 74  
XPS, 144–146
- Raman spectroscopy  
confocal, 2

- Raman spectroscopy (*cont.*)
  - confocal (*cont.*)
    - Dow cyclotene (BCB), 4
    - HOPG, 6
    - conventional, 2
  - RBS, 153, 154
  - $\text{SiO}_2$  on polyimide, 154–158
  - $\text{SiO}_2$  on polycarbonate, 158–161
  - $\text{SiO}_2$  on polyethylene terephthalate, 158–161
- SAMs (self-assembled monolayers)
  - $\omega$ -substituted hexadecanethiols, 118
  - aluminum deposition, 121, 125
  - IR spectroscopy, 120, 123
  - spectroscopic ellipsometry, 121
  - ToF-SIMS, 120, 123, 124
  - XPS, 119, 123
- SEM, 176
- SiLK, 44, 53, 141
  - copper metallization, 80
  - dual damascene, 47
  - dynamic mechanical analysis, 57, 58
  - film deposition, 128
  - in-plane stress, 59
  - ion-induced metal intermixing, 148
  - mechanical properties, 56
  - nitride incorporation, 146
- SiLK (*cont.*)
  - nitrogen ion bombardment, 143
  - physical properties, 45, 53
  - tantalum metallization, 144
  - thermal expansion, 58
  - TiSiN barrier layers, 129
    - AFM, 130, 131
    - copper deposition, 129
    - X-ray reflectivity, 129, 132, 135–138
      - quantitative modeling, 129, 133
  - titanium metallization, 145
  - ultra low K porous, 50
  - XPS, 144–146
- Spectroscopic ellipsometry, 121
  - discontinuous films, 17
  - optical modeling, 12
  - thin films, 13
  - 3-D films, 19
- Surface energy, 74
- ToF-SIMS, 120, 123, 124
- XPS, 68, 98, 119, 123, 144–146, 177
  - angle-resolved, 23
  - conventional, 25
  - multilayer analysis, 32
  - parallel collection, 26